



HAL
open science

Water Transfers in Sub-Micron Porous Media during Drying and Imbibition Transferts d'eau en milieux nano-poreux durant le séchage et l'imbibition

Jules Thiery

► **To cite this version:**

Jules Thiery. Water Transfers in Sub-Micron Porous Media during Drying and Imbibition Transferts d'eau en milieux nano-poreux durant le séchage et l'imbibition. Geophysics [physics.geo-ph]. Université Paris-Est; Harvard University, 2016. English. NNT : 2016PESC1155 . tel-01565895

HAL Id: tel-01565895

<https://pastel.hal.science/tel-01565895>

Submitted on 20 Jul 2017

HAL is a multi-disciplinary open access archive for the deposit and dissemination of scientific research documents, whether they are published or not. The documents may come from teaching and research institutions in France or abroad, or from public or private research centers.

L'archive ouverte pluridisciplinaire **HAL**, est destinée au dépôt et à la diffusion de documents scientifiques de niveau recherche, publiés ou non, émanant des établissements d'enseignement et de recherche français ou étrangers, des laboratoires publics ou privés.



Ph.D. Thesis - Jules Thiery

Water Transfers in Sub-micron Porous Media during Drying and Imbibition



HARVARD
John A. Paulson
School of Engineering
and Applied Sciences

UNIVERSITÉ —
— PARIS-EST



HARVARD
John A. Paulson
School of Engineering
and Applied Sciences

UNIVERSITÉ
— PARIS-EST

Thesis

presented by

Jules Thiery

to

The Department of Physics in fulfillment of the title of

Doctor of Philosophy in Physics

University Paris-Est, France

**Water transfers in sub-micron porous media during
drying and imbibition**

Defended on November 25th, 2016

Jury:

Prof.	Elisabeth	Charlaix	Reviewer
Prof.	Leo	Pel	Reviewer
Prof.	Stephane	Rodts	Examinator
Prof.	Dani	Or	Board President
Prof.	Philippe	Cousot	Director
Prof.	David A.	Weitz	Co-Director

Acknowledgements

These years spent as a PhD candidate were of memorable adventures and learning experiences; I will be forever grateful to the people who have driven me forward along this project and enabled me to explore freely what I was curious about.

I would like to warmly thank Philippe and Dave for accepting this collaboration, looking back, what a gamble! Thank you for spending the time, awake or asleep for Dave, to teach me how to think and build a reasoning. I am sincerely thankful for your listening, your confidence and your guidance, as well as for sharing your connections and encouraging me to meet and work with a plethora of interesting scientists throughout the globe. I hope this wasn't a way to take a mental break from the "volcano of ideas" (P. Coussot, 2016) erupting perpetually within your lab.

I would like to markedly thank Stephane for his continuous mentoring, assistance and individual NMR teaching; I particularly enjoyed working with and learning from you. Thanks for answering your phone at dinner times to trouble shoot me with MRI. I also thank Denis C. Murias for similar practice.

One of my adventures lead me to Crete where I worked with Dimitris Vlassopoulos, thank you Dimitris for having me at FORTH, for teaching me your approach and science and your exquisite culinary knowledge.

Indeed, I would like to fervently thanks, Maximilian Zieringer, Tom Kodger, Lloyd Ung, Adruian Perogaro, Ariel Amir, Emmanuel Keita, Xavier Château, Pamela Faure, Peter Lu, Christoph Muus, David Hautemayou and all members of the Weitz and Coussot Lab. for fueling this project with a large majority of good advice, great company and fruitful discussions.

I would also like to thank my friends and my family: Joce, Stephane, Nicole, my grandparents and particularly my parents, my brother and my sister for their uninterrupted love, I dedicated this work to you. Last but not least, I would like to warmly thank Lottie for helping me develop a delightful British accent and Laura for these great moments.

I acknowledge funding from Harvard University and École Nationale des Ponts et Chaussées. I am thankful to Paris-Est University and the French Academy for the awards and fundings. Eventually, I warmly thank the committee of Arthur Sachs scholarship fund, the Fulbright program as well as François Poncet-Sachs for their award, their financial support and the numerous meetings and discussions.

To whoever is looking for answers or simply fun with cool physics,

Introduction

Be it wood, rock, sand or skin, porous materials are commonly found in nature. Such materials usually contain, in their asperities, moisture in equilibrium with their surrounding environment. This liquid may be subjected to changes in atmospheric conditions such as a variation in temperature, humidity, external pressure or air velocity. Such changes inevitably result in the material losing or gaining moisture to re-establish equilibrium with its environment. These transitioning mechanisms are usually named after drying for fluid removal and imbibition and adsorption for fluid sorption; these phenomena have been extensively studied over the past century.

Familiar to anyone who ever filled a sponge with water and left it to dry, these transitions can affect the aspect, the integrity and the durability of the material. Sometimes, they may also fundamentally change the material's nature; this particular property is probably the main reason why drying and imbibition are found widely used in industrial processes. In fact, drying applies to a plethora of industry sectors where products are first prepared wet, as this liquid or pasty state enables easy formulation, mixing, and transport, then dried to transition into their final aspect. For the reasons mentioned just above industrial drying may convey technological or productivity issues depending on the nature and purpose of the material, here are a couple examples:

In the building industry, materials such as concretes, plasters or paints etc. are required to dry rapidly to keep up with productivity deadlines on site but also to maintain their integrity to keep their structural or aesthetic properties. Currently, the most effective way to eliminate drying induced defects in these materials, such as cracks, remains to apply extremely slow drying rates; a slow process leaves time to the material to re-equilibrate and dissipate the incremental stresses that builds up during desiccation. However, slowing down evaporation is time consuming and incompatible with a fast material production.

In the pharmaceutical and health industries, traces of solvent residues in pills may cause health problems to patients. Removing these traces of solvents to an acceptable level is difficult, oftentimes because of water retention in the smallest pores.

Recently in the state of art microfluidic manufacturing industry, the need for synthesis of amorphous nanoparticles triggered the use of supersonic air flow to dry droplets fast enough to prevent crystal nuclei formation; such flow rates are difficult to achieve and accurately control.

Surprisingly, despite drying applying to advanced applications, in many instances it remains a step empirically controlled which results in industrial drying being energy intensive and to represent 9% of the global energy consumption. Specifically, a significant amount of this energy is used to remove moisture in particulate materials with strongly hydrophilic surfaces or sub-micron pores.

Similarly, imbibition is found involved in a variety of industrial processes, in the previous applications, it may be used in the pre-processing phase to formulate wet mixture. Additionally, this mechanism is seen particularly employed in desalination, functioning of nano-porous batteries

electrodes, electrophoresis, oil recovery, food processing, impregnation, chromatography, agriculture and more. Imbibition is a faster process than drying, its driving mechanism being highly dependent on the structure of the porous network and less affected by the atmospheric conditions. Therefore, the physics of imbibition are rather well documented and the phenomenon considered as model to study liquid flow through capillary forces, especially in sub-micron pores where a great scientific challenge still stands.

The reasons behind the little knowledge in the field of liquid flow in sub-microporous media may stem from the existing challenge in building a model material representative for the physics in the great variety of the real systems; but also the difficulty to observe and measure the dynamics of the confined fluid with microscopy technics. Due to the high impact of this particular field on energy consumption in scattered industrial applications, it is crucial to gain greater understanding over the physics of drying and imbibition in confined porous media.

This manuscript aims at contributing to the understanding of the physics behind the kinetics and the flow of water in sub-micron porous media, with a strong focus on the transition from micron sized to nano sized pores; it also opens up new research perspectives in this field. This research is based on the study of drying and imbibition in model porous materials we specifically engineered to cover the need of a generalist approach. The model aspect of these materials stem from the homogeneity of their internal pore structure, the ability to tune their average pore size and to make them responsive to drying stresses, allowing a variety of deformations such as shrinkage, cracking, delamination etc. to develop and therefore to study. Note other materials are also studied. All materials are examined under a series of MRI imaging technics and may benefit from Electron Microscopy imaging (EM). Finally, this research was driven by two main purposes: gaining greater understanding in the phenomenon observed and quench a personal curiosity.

This manuscript develops along the following lines:

To clarify the scientific positioning of this study, the first chapter consists in reviewing the current understanding of the physics of drying in porous media initially saturated with water or a single phase of pure liquid and the physics of spontaneous imbibition in porous media.

The second chapter focuses on describing the materials synthesized and used, as well as the functionalities of the set-ups we built and the functioning of the measurement tools we used.

The third chapter of this thesis aims at bringing understanding to the kinetics of drying induced by sample deformations (cracking, shrinking etc). This section particularly features the analysis and modelling of the drying kinetics of homogeneous nano-porous gels, being highly responsive to drying stresses; as well as the a study of drying in sponges exhibiting various pore size distributions and special surface properties.

The fourth chapter consists in presenting the advance we achieved in the understanding of fluid transfers and vapor removal in submicron porous media during drying. We present a multiscale approach enabling to compare between the drying behavior of 10 model porous media each of them exhibiting a homogeneous structure with an equivalent pore size ranging from a few microns to a couple of nanometers.

Eventually, the fifth and last chapter of this manuscript reveals some new mechanisms for spontaneous imbibition in submicron materials, specifically probing the possible influence of liquid films or adsorption on the imbibition kinetics; this last piece of work opens up new perspectives for the study for the imbibition process in nanoporous media.

Summary

Introduction.....	2
Chapter 1 - State of the art	9
A - Basic concepts behind the physics of drying of pure solvents in model geometries	9
1 - Evaporation from an air-water interface	9
2 - The mechanisms of moisture transport in a dry region.	11
i. Case of a large cylindrical tube.....	11
3 - Effect of capillary forces and surface roughness on drying kinetics	12
i. Wettability	12
4 - Capillary pressure, Bond and Capillary Number.....	14
5 - Disjoining Pressure for thin liquid films	15
6 - Case of a square cross-sectional tube	16
B - Basic concepts behind the physics of drying for porous media	19
1 - Architecture of a porous media	19
2 - Darcy's law	19
3 - Models for Permeability	20
i. Permeability for a fully saturated porous media	20
ii. Permeability for a partially saturated porous media	21
4 - The mechanisms of moisture transport through coarse porous structures during drying	22
i. Historical understanding of the physics of drying in porous materials	22
5 - Drying regimes and water distribution for free water	23
i. Induction period and isotherm drying.....	23
ii. The constant rate period.....	23
iii. The Falling rate period	25
6 - Effect of pore size on drying regimes.....	27
7 - Effect of pore size distribution on water distribution within the sample.....	28
8 - Liquid films, surface forces and viscosity	29
9 - Drying stress and sample deformation for wetting porous media	30
10 - Shrinkage and wrapping	31
11 - Cracking.....	32
C - Basic concepts behind the physics of spontaneous imbibition of pure liquids in hydrophilic nanoporous media	33
1 - Description of the phenomenon.....	33
i. Capillary rise and Lucas-Washburn equation	33
2 - Spontaneous imbibition in Nano-pores	35
i. Validity of Lucas-Washburn equation in nano-pores	35
ii. Fluid flow in nanopores	36
iii. Front broadening.....	37
D - Positioning of this study	39

Chapter 2 - Materials and Methods.....	41
A - Measurement tools	41
1 - SEM and TEM Imaging	41
i. Technology	41
ii. SEM imaging in practise	42
iii. Sample preparation	44
2 - Nuclear Magnetic Resonance techniques	45
i. Principle of NMR measurements.....	45
ii. Free induction Decay	46
iii. The measurement of T2 : Spin Echo	47
iv. NMR Relaxometry, pore sizes and CPMG sequence	48
v. 1D profiling	50
vi. High resolution for 1D profiling	52
vii. Smoothing method for 1D profiling	53
B - Materials	55
1 - Synthesis of model nano-porous soft gels	55
i. Aggregation of colloidal particles.....	55
2 - Structure of gels.....	59
i. Evolution of the pore network during gel contraction	59
ii. Gels substrates	61
iii. Strain sensitive substrate	61
3 - Synthesizing model porous media	61
i. Viscous sintering, from gels to homogeneous porous media	61
ii. Protocol for large particles.....	63
iii. Pore size distribution in model porous media	63
4 - Sponges.....	66
i. Surface properties	66
ii. NMR analysis	66
iii. Macroscopic pore size distribution	67
iv. SEM Imaging of the porous structure.....	69
v. Sponges structures and relaxivity	70
C - Set-ups.....	71
1 - Drying set-ups for gels and sponges.....	71
i. Regular drying	71
ii. Drying set up in the MRI	71
iii. Imaging strain during drying	72
2 - Critical point dryer.....	72
3 - Imbibition set-ups	73
i. Regular imbibition	73
ii. Imbibition within the MRI.....	73

Chapter 3 - Drying kinetics of deformable nano-porous gels and sponges	74
A - Drying kinetics of deformable model nano-porous gels	74
1 - Drying rate for deformable nano-gels	74
i. Drying protocol specific to this study	74
ii. Drying curves.....	74
2 - Macroscopic phenomenology	77
i. The different phases of drying of shrinking and/or fracturing gels	78
3 - Evolution of the water content within the gels during drying	80
i. Measurement of the water distribution	80
ii. Scheme for gel saturation	81
i. Deformations and drying regimes.....	83
4 - Measurement of the material deformation during drying	83
i. Delamination	83
ii. Shrinkage and first crack regime	85
iii. Second crack regime	87
iv. Spiral cracks.....	87
5 - Origin for sample deformation	88
i. Delamination	88
ii. Suggested origin for cracks in the different cracking regimes	89
6 - Deformations influencing the drying rate.....	91
7 - Numerical simulation and modeling of the influence of the first crack regime on the drying rate.....	92
i. Distribution of the airflow velocity	92
ii. Modelling.....	93
iii. Model predictions	95
8 - Influence of the second crack regime on the drying rate.....	99
i. Crack density on drying kinetics	99
9 - Conclusion on the section.....	101
B - Study of Sponges during drying, a model deformable porous media with a wide pore-size distribution	102
1 - Drying curves	102
i. Reproducibility of the measurement.....	102
ii. Influence of airflow velocity on the drying mechanism	103
i. Influence of surface affinity on drying kinetics of the blue sponge	104
2 - Macroscopic deformations	104
3 - Drying Scheme	105
4 - MRI study of the water distribution within the sample during desiccation.....	106
i. MRI sequence	106
ii. Distribution of water in the green sponge.....	106
iii. Distribution of water in the blue sponge	108
5 - Scheme for the drying kinetics	109
6 - Study of the drying mechanism through pore emptying dynamics	110
i. Evolution of the T2 spectrum during drying	110
7 - Analysis of pore emptying dynamics	111
i. Global T2	111
ii. 1D profiles and Local dynamics	111
iii. Macroscopic measurement, optical microscopy	113
iv. Capillary equilibration process	114
8 - Wet imaging for the blue sponge.....	115
9 - Conclusion of the section	116

C - Conclusion	117
Chapter 4 - Drying regimes in homogeneous porous media from macro to nano-scale.....	118
1 - Experimental details	118
i. Protocol	118
ii. Physical framework	118
2 - Observation of the water distribution with varying pore size	118
i. Scheme for water distribution during drying varying bead sizes	122
3 - Drying rate	122
4 - Analysis of drying regimes	123
i. From water distribution to drying regimes	123
ii. Measurement of the apparent dry region	124
iii. Quantitative considerations for drying regimes.....	125
iv. Knudsen diffusion for vapor transport through the porous network	126
v. Kelvin Effect in nano-pores to explain the drying kinetics	127
5 - Analysis for water distribution	129
6 - Conclusion	129
Chapter 5 - Spontaneous imbibition in submicron porous media	131
1 - Macroscopic study	131
i. Phenomenology	131
ii. Imbibition curves and reproducibility	133
2 - Analysis of the imbibition curves	134
3 - MRI evidence of the evolution of water content during imbibition	136
4 - Analysis of the MRI data.....	138
i. Front dynamics	138
ii. Shape of the partially saturated front.....	140
iii. Opalescence	142
5 - Analysis at low moisture content.....	143
i. Evidence of precursor films	143
ii. Influence of initial liquid films on the imbibition dynamics	144
iii. Scheme for the influence of precursors films on imbibition dynamics	145
6 - Conclusion and perspectives	146
Conclusion and suggestion	147
References:	150
Annexes	157
1 - Pore size analysis software	157
2 - Image and mass acquisition software	157
3 - NMR measurement parameters Chapter 2 sponges.....	159
4 - NMR 1D profiling measurement parameters Chapter 4.....	160
5 - Dimensions of the samples presented in Chapter 5, Fig5-2	161
6 - NMR 1D profiling measurement parameters Chapter 5.....	161

Chapter 1 - State of the art

This first chapter aims at probing the scientific advance in the different fields we decided to investigate and explain the theoretical knowledge currently reached through the study of applied systems.

A - Basic concepts behind the physics of drying of pure solvents in model geometries

In the present section we describe the existing knowledge of the physics of water drying in atmospheric conditions within tubes with various geometries and a porous media.

1 - Evaporation from an air-water interface

Evaporation is a vaporization phenomenon and is the driving mechanism for water removal during spontaneous drying porous media filled with water. It occurs from the surface of water into the air, when the latter is not saturated with the evaporating substance. As a matter of fact, air can carry a certain amount of water molecules, this quantity is usually measured in terms of vapor density and denoted ρ_{vap} .

Evaporation from a liquid surface will proceed until thermodynamic equilibrium between the liquid and the gaseous phases is reached, i.e. until the air becomes completely saturated with water molecules; in this case, the equilibrium vapor density is reached and $\rho_{vap} = \rho_{sat}$. The equilibrium vapor density increases non-linearly with temperature according to Clausius-Clapeyron relation and takes the following values: $7\text{g}\cdot\text{m}^{-3}$. at $5\text{ }^\circ\text{C}$, $23.4\text{ g}\cdot\text{m}^{-3}$ at $25\text{ }^\circ\text{C}$ and $150\text{ g}\cdot\text{m}^{-3}$ at $60\text{ }^\circ\text{C}$.

From the ratio between the current to maximum vapor density can be inferred a familiar variable, the relative humidity of the air:

$$n = \frac{\rho_{vap}}{\rho_{sat}} (\%) \quad (1.1)$$

Therefore, when $n < 100\%$, the system is out of equilibrium and water molecules diffuse from the surface of the liquid to the air, leading to a mass transport phenomenon toward the dryer region described by Fick's Law as:

$$\vec{J}_F = -D_0 \cdot \nabla \vec{\rho} \quad (1.2)$$

where D_0 is the diffusion coefficient of vapor water through the air; at $25\text{ }^\circ\text{C}$, $D_0 = 2.7 \cdot 10^{-5} \text{ m}^2 \cdot \text{s}^{-1}$. Desiccation can be a very slow process therefore its study often requires to accelerate the rate of evaporation of the liquid; for this purpose, air is often blown at the sample surface; this is called convective drying (see Fig1-1).

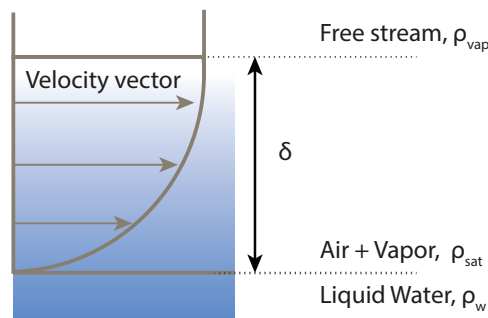


Figure 1-1 : Scheme of evaporation for convective drying of a water, air is blown parallel to the air-water interface.

When an air flux is blown over a wet surface S , water molecules are removed rapidly from this wet surface resulting in an acceleration of the evaporation process. Seen from a fluid dynamic perspective, blowing air alongside a wet interface in a laminar regime leads to the formation of a gradient in air velocity, perpendicular to this surface [7]. If the vapor density of the air blown $\rho_{vap} = \rho_0$ is inferior to ρ_{sat} , a gradient in vapor density appears within this boundary layer, [8], see Figure 1-1. For drying considerations a rough approximation [9, 10], consists in considering that this vapor gradient is constant in a region of thickness δ of the order of this boundary layer while the vapor density (ρ_0) is maintained constant in the region of nearly uniform velocity (see Fig1-1). In that case, from (Eq1.1 and Eq1.2), we obtain the following expression for the rate of evaporation V_e (in $\text{m} \cdot \text{s}^{-1}$):

$$V_e = \frac{j}{\rho_w} = D_0 \cdot \frac{\rho_{sat}}{\rho_w} \cdot \frac{(n - 1)}{\delta} \quad (1.3)$$

Where $\rho_w = 1000 \text{ kg} \cdot \text{m}^{-3}$ is the liquid water density and n the relative humidity of the convective air (see Eq1.1). This approximation well describes the drying rate recorded for any type of wet material put to dry when their surface exposed to the airflow remains covered by a significant layer of liquid water, but not only. In fact, Suzuki and Maeda [10], showed that the drying rate of a uniform liquid sheet and its counterpart presenting dry patches at its surface, can be identical if the

spacing between dry patches remains greatly inferior to δ . Therefore, (1.3) is verified as long as δ remains greatly superior to the characteristic length of the surface roughness or heterogeneities.

2 - The mechanisms of moisture transport in a dry region.

Although a porous medium with its hierarchy of pore diameters and junction structures is clearly much more complex than a cylindrical tube, the consideration of an individual channel as a model system to understand basic transport phenomena has often proven to be a useful and relevant model, [11]. In this section, we first describe the mechanism of transport in a circular tube during drying; we further consider a polygonal tube and probe the effect of the corner of the geometry on the drying process. This step by step approach enables to study individually crucial phenomena playing roles in the drying kinetics of porous materials.

i. Case of a large cylindrical tube

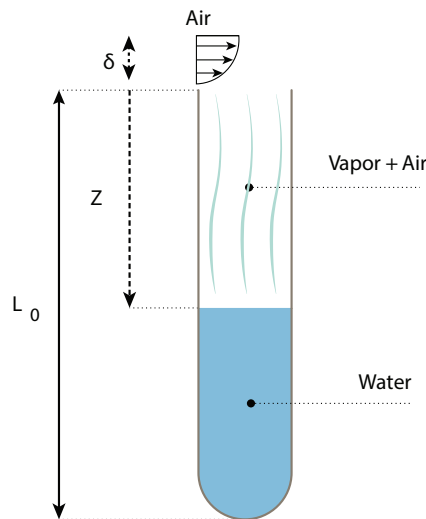


Figure 1-2 : Scheme of convective drying from a cylindrical tube. A boundary layer of thickness δ forms at the tube entrance where air is blown

The system is a circular tube of length L_0 and cross section S_0 as sketched in Fig1-2, the tube diameter is large enough so that the liquid-gas interface can be considered flat at all time, i.e. presenting no curvature. Z is the height of the air-water interface measured positively from the top to the bottom of the tube. Low vapor density air, ρ_0 , is blown perpendicularly to the tube at its open end giving rise to the formation of a boundary layer of thickness δ at this location. In these conditions, drying is seen to drive the air-water interface to recede within the tube; therefore, the distance a molecule of vapor water needs to travel to exit the system is $\delta + Z$. From the previous section we can express the drying rate of the tube and the evolution of the interface height with time:

$$V_e = \frac{1}{S_0} \cdot \frac{dm}{dt} = D_0 \cdot \frac{\rho_{sat}}{\rho_w} \cdot \frac{(n-1)}{\delta + Z} \quad (1.4)$$

with $m = \rho_w \cdot S_0 \cdot (L_0 - Z)$ being the mass of liquid water remaining in the tube. We therefore deduce the following differential equation for Z :

$$\rho_w^2 \cdot \frac{dZ}{dt} \cdot (\delta + Z) = D_0 \cdot \rho_{sat} \cdot (n-1) \quad (1.5)$$

and the solution is:

$$Z(t) = \sqrt{\frac{2D_0\rho_{sat}}{\rho_w^2} (n-1) \cdot t + \delta^2} - \delta$$

Remark that as soon as the height of the dry region becomes greater than δ we can make the following approximation $Z + \delta \sim Z$, and the equation (1.5) becomes

$$\rho_w^2 \cdot \frac{dZ}{dt} \cdot Z = D_0 \cdot \rho_{sat} \cdot (n-1)$$

Finally, the solution is:

$$Z(t) = \sqrt{\frac{2D_0\rho_{sat}}{\rho_w^2} (n-1) \cdot t}$$

We observe $Z \propto \sqrt{t}$, which shows that a diffusion process takes place for the development of the dry region; note that the drying rate evolves inversely proportional to the square root of time : $\frac{dm}{dt} \propto \frac{1}{\sqrt{t}}$.

3 - Effect of capillary forces and surface roughness on drying kinetics

When the diameter of a tube is decreased to a couple of micrometers or the geometry of the tube presents angle, a substantial curvature of the air-water interface is observed. This curvature originates from the affinity between each component of this liquid-solid-gas system and defines the wetting property of a solid surface by the liquid. Wettability is a crucial parameter that governs moisture flow in porous media; it is oftentimes studied through the shape a droplet adopts when put in contact with this surface.

i. Wettability

As articulated by Young, when a small liquid droplet is put in contact with a flat solid surface at given temperature and pressure, two different equilibrium situations may be found depending on the value of the contact angle θ_w observed (see Fig1.3). Specifically: partial wetting with $\theta_w \neq 0$ (see Fig1.3a and b) or complete wetting when $\theta_w = 0$ (see Fig1.3c).

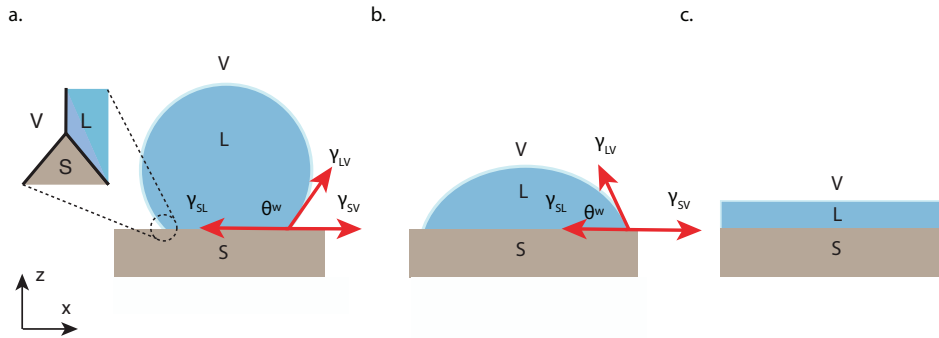


Figure 1-3 Schematic showing a sessile droplet on a flat solid substrate exhibiting (a) and (b) partial wetting, (b) stronger wetting than (a); (c) complete wetting. On the right side of each droplet is the conventional force balance used to derive Young's equation.

If partial wetting is encountered, a three-phase contact-line forms between the solid, liquid and the equilibrium vapor phase. The corresponding equilibrium angle is determined by a balance of solid-vapor, γ_{SV} , solid-liquid, γ_{SL} , and liquid-vapor, γ_{LV} , surface tensions (thermodynamically defined as the respective free energy per unit area for each interface, [12]). This equilibrium can be written, as a projection on the x axis (see Fig1.3), as follow:

$$\gamma_{SV} - \gamma_{SL} - \gamma_{LV} \cdot \cos(\theta_w) = 0 \quad (1.6)$$

At 25°C and atmospheric pressure, the surface tension for water is $\gamma_{LG} = 71.97 \text{ mN} \cdot \text{m}^{-1}$, this value decreases with increasing temperature. For water, a wettable surface, also termed hydrophilic, corresponds to $\theta_w > 90^\circ$ whereas a non-wettable surface, hydrophobic, corresponds to $\theta_w < 90^\circ$. In the following array we present examples for contact angles on rough surfaces for a water droplet on well-known materials:

Phases (L-S)	Contact Angle θ .
Water - Teflon	~110°
Water - Glass	~110°
Water - Silica	~180°

Table 1-1 : Values for the contact angle observed for water on well-known materials, [13].

As described by Wenzel, [96], the contact angle observed for a liquid on a flat solid surface greatly depends on the roughness of this surface, for instance a polished Teflon exhibits a 180° contact angle with water in air [13].

4 - Capillary pressure, Bond and Capillary Number

When water wets the walls of a sufficiently narrow circular tube (of radius r), the interface between air and water presents a curvature define by r_c the radius of the corresponding sphere: a meniscus is formed (see Fig1.4).

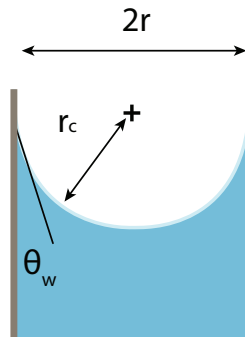


Figure 1-4 : Shape of the air-water interface in a capillary tube filled with water and made of hydrophilic walls.

The pressure drop across this interface verifies the Young-Laplace relation:

$$\Delta P = \frac{2\gamma_{LV}}{r_c} = \frac{2\gamma_{LV} \cos(\theta_w)}{r} \quad (1.7)$$

Often, for systems presenting strong wetting, the effect of surface tension on the shape of an liquid/air interface is likely to dominate the effect of gravity, this trend is assessed from the dimensionless Bond Number, defined as [14]:

$$B_o = \Delta\rho \cdot g \cdot \frac{L^2}{\gamma_{LV}} \quad (1.8)$$

Where $\Delta\rho$ is the difference in density between the two phases at the interface, g is the gravitational acceleration and L the characteristic length of the system. A high value of the Bond number indicates that the system is relatively unaffected by surface tension effects whereas a low value (typically less than one) indicates that surface tension dominates.

Surface tension forces may also compete with viscous forces when liquid flows (at a velocity V); it is of particular importance when liquid draining occurs through tiny films, as seen in the following section. For this reason, the capillary number quantifies the relative effect of viscous forces versus surface tension acting across a liquid and gas interface.

$$Ca = \frac{\mu V}{\gamma_{LV}}$$

Where μ is the dynamic viscosity, physically pointing at the resistance of a fluid measured from its gradual deformation. This value is temperature dependent; for water $\mu_w = 8.90 \times 10^{-4} Pa$ at $25^\circ C$

5 - Disjoining Pressure for thin liquid films

Capillary pressure is not the only force one may encounter from wetting a surface. When a thin liquid layer ranging from fractions of a nanometer (monolayer), to several micrometers in thickness, wets and spreads on a surface, surface forces set up an additional pressure, the disjoining pressure, Π . It defines the force of molecular interaction (per unit area) of bodies that are separated by a thin plane parallel interlayer. A positive value of Π corresponds to repulsion and a negative value to a confinement. B.D.V and Kusakov measured the thickness of the equilibrium wetting aqueous film that forms when a gas bubble is pressed against a glass plate immersed in the liquid. In that case, Π is the difference between the pressure in the thin film of liquid adjacent to the glass surface and that in the air interface, [15, 16], and is expressed as:

$$\Pi = -\frac{A}{6\pi h e^3} \quad (1.9)$$

Where e is the film thickness, A is the Hamaker's constant, $A = \pi^2 C \rho_a \rho_b$ defining the Van der Waals interaction between water and the solid surface with ρ_a and ρ_b the number of atoms per unit volume in the two interacting bodies; finally, C is a coefficient depending on the pairing interaction between particles. For a glass-water interface $A \approx 1.7 \cdot 10^{-20} J$; for a silica-water interface $A \approx 0.85 \cdot 10^{-20} J$.

Previously, we studied evaporation in a large cylindrical tube where capillary effects can be neglected as the air-water interface simply slides at the tube walls. Let's look at how capillary forces influence on the liquid distribution in a slightly more complex geometry i.e. a square tube.

6 - Case of a square cross-sectional tube

In a porous media, pores are often considered as cylindrical tubes in analytical or computational studies but such simplification prevents the capture of the rich phenomenology associated to the roughness or corners of the solid matrix. Considering the pores geometry is crucial to realistically study capillary flow, accurately estimate liquid and vapor distribution and thus find the origin of the drying rate recorded. Drying a cylindrical and a polygonal tube leads to different results owing to the different liquid distribution along the tube walls (see figure1.6), [17, 18].

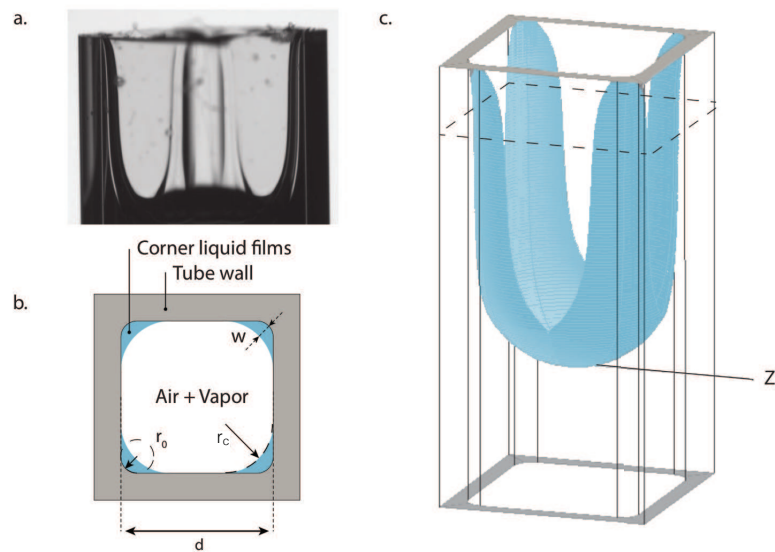


Figure 1-5: (a) Side view of the air-liquid interface in the square tube (c) between the dashed line and the top of the tube; (b) Scheme of tube cross section (dashed line) in (c); r_0 is the curvature radius of the tube's rounded corners, r_c is the in-plane curvature radius of corner menisci, and w is the thickness of the corner film, [9]. (b) 3D view of the air-liquid interface receding in the tube during drying.

Drying a solvent in a square tube results in the liquid interface pinning the corner walls while the bulk menisci recedes toward the bottom of the tube (see Fig1-5). An almost similar situation as the one encountered for a cylindrical cross section; however, in identical drying conditions, the total desiccation time for square geometries appears much shorter (see Fig1.6). This sharp difference stems from the development of corner films that, when thick enough [19], provide a pathway for transporting the liquid from the receding bulk meniscus up to the film tips. Prat and al. [18], followed the location of the film tips along desiccation and found the existence of 3 different dynamic regimes associated to the corner films thickness :

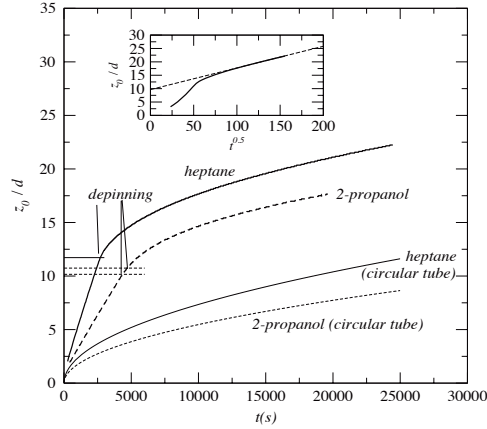


Figure 1-6: Comparison of the evolution of the menisci location during drying of circular (bottom curves, see graph) and square section capillary tubes, [18]. Here z_0 is the location of the bulk menisci and d the width of the tube.

Fig1-6 presents the evolution of the location of the bulk menisci with time and indicates crucial moments related to the evolution of the corner films. We observe that in a first regime (R1) the level of the bulk interface recedes into the tube linearly with time (see Fig1-6), in parallel, thick liquid films pinning the tube entrance develop in the corners of the geometry (as sketched in Fig1-5c) and are seen to progressively thin down with desiccation (see Fig1-7b, black curve in the main graph). For low Bond numbers, gravity effects on the interface curvature are neglected and its shape can be considered identical to its quasistatic counterpart, [20]. Accordingly, the interface's radius of curvature may be expressed as $r_c = d/3.77$, where d is the width of the tube (see Fig1-5b), and therefore the films thickness as $w = (\sqrt{2} - 1) \cdot (r_c - r_0)$, [18]. Further drying triggers the transition to a second regime (R2); in this regime, the main menisci slows down and the liquid films depin the entrance of the tube (see Fig1-6 at “depinning”). This regime essentially constitutes a transition phase to the third regime: (R3) where Z_0 (the location of the bulk menisci) simply recedes as the square root of time (see inset of Fig1-6), similarly to the situation of a cylindrical tube. Let's see how this 3 step process compares in terms of vapor removal and therefore drying rate.

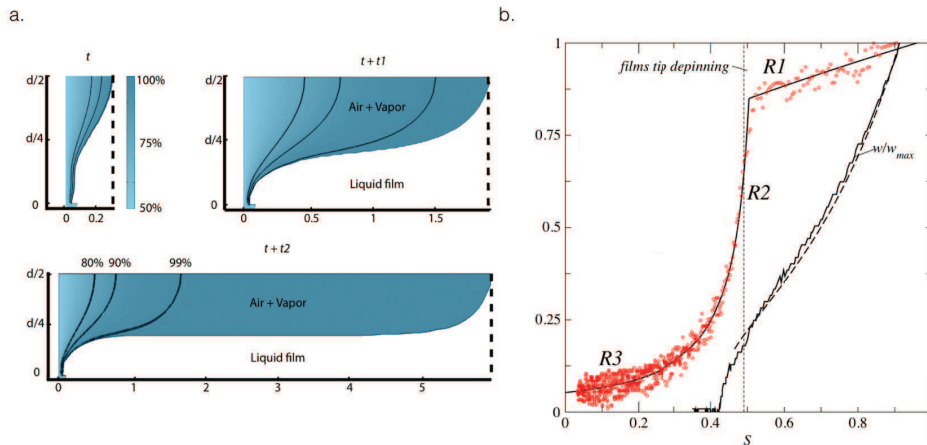


Figure 1-7: (a) Simulation of the distribution of vapor within a polygonal tube during the first regime (R1) identified in (b); the x axis represent the height of the tube in mm, black continuous lines represent the iso-surface for vapor density and dashed lines the location of the menisci; here $t_1 > t_2$, [21]. (b) Rescale drying rate (E/E_0 is the ratio of the current

to initial drying rate) as a function of the average liquid saturation of the tube (S) for a square tube, and evolution of the rescaled thickness of the corner films w (see text), [17].

As a first step toward greater understanding of the origins of variations in the drying rate recorded, it is necessary to look at how the vapor distribute in the system during the process. In Fig1.7a, we present the evolution of the vapor density field with time, calculated from 2D finite element modelling, [21]. This distribution shows that the gas phase within the tube, between the bulk menisci to the films tips is saturated with vapor except in a region very close to the tip of the liquid films (see Fig1-8a). Therefore, one can infer from (Eq.1.4) that the vapor transport by diffusion in the gas phase is only significant in the film tip region (where the gradient is the highest). Finally, the linear evolution of Z_0 (the location of the bulk menisci) with time in this regime (see Fig1-6a) indicates that, as long as liquid films are thick enough, water preferentially flows through the films rather than diffuse in the gaseous phase between the bulk menisci to the films tips; in this region evaporation can therefore be neglected and the drying kinetics observed on Fig1-7b may further be explained.

As a first drying regime (R1, see Fig1-7b) a period of slowly decreasing desaturation is maintained until the liquid films depin the entrance of the tube. This shows that as long as liquid films pin the tube entrance, liquid flows to the surface, evaporating from the film tips region. This slow decrease is likely due to the modification of the shape of the air-liquid interface [21], therefore to a modification of the contact angle (see Eq1.7) that entails a drop in capillary pressure at the pinned point, [22] and results in slower drainage. Further drying causes liquid films to become so thin that viscous forces dominate over capillary forces and therefore drainage is prevented, [12]. This latter situation gives rise to a falling drying rate (R2) and a slowdown in menisci recession (see inset on Fig1-7b). Eventually, thick films depin the entrance of the tube (see Fig1-6) and a diffusive regime (R3) identical to the one we encountered in a cylindrical tube takes over (see inset of Fig1-5).

Comparing between the drying kinetics of a cylindrical and square tube, we conclude that for a wetting liquid, the geometry of this tube can play a significant role in the drying kinetics observed; specifically, when a three phase contact line pins the entrance of the tube, liquid films can develop in the corners of the geometry and drain liquid toward it, resulting in a 3 phases drying process. While increasing the tube roughness ($r_0 \rightarrow 0$ in Fig1-6) have proven to extend of the period of regime R1, adding corners to the geometry have proven to increase the rate of drying in this regime, [53]; eventually both of these parameters are seen to reduce the total drying time. Considering a porous media as a simple bead packing made of holes and corners at the bead contact points (see Fig1-8), one may foresee that similarity in the mechanism of drying may exist and the importance for an averaging approach over the whole system.

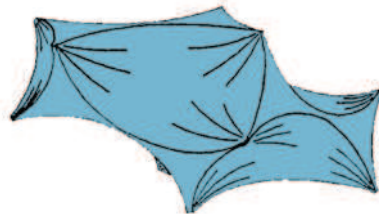


Figure 1-8: Scheme of the interface shape of the liquid wetting a couple of pores in porous media made of a spherical bead packing. Pinning points correspond to the corners of this geometry, [23].

B - Basic concepts behind the physics of drying for porous media

The physics behind drying of a porous media are ubiquitous, universal, and fairly simple. As evaporation proceeds, air progressively substitutes water within the porous structure. Evaporation drives the medium into a partially saturated state, which eventually empties. However, when scrutinized closely, this simple process exhibits rich phenomenology that arouse a plethora of intriguing wonders.

1 - Architecture of a porous media

A porous material is a three-dimensional structure presenting a solid matrix with asperities varying in size and distribution, these asperities are commonly named after: pores. Porous media are characterized by their porosity, denoted ε , defined as the ratio between their total pore volume to their overall volume; their pore size distribution (probability density function); their specific surface area and pore connectivity as pores may be inter-connected or isolated.

2 - Darcy's law

Liquid flows through a porous media is commonly described by Darcy's law, [26], highlighting a linear relation between flow velocity (v) and the pressure gradient (∇P) throughout the porous structure. For a directional pressure gradient along the z axis:

$$v = \frac{k}{\mu} \cdot \frac{\partial P}{\partial z} \quad (1.10)$$

where μ is the dynamic viscosity of the fluid. Note that v is the average velocity throughout a whole sample and v_i as $v = \varepsilon \cdot v_i$, the average velocity through the porosity.

3 - Models for Permeability

i. Permeability for a fully saturated porous media

The porous network of a material can be geometrically modelled to deduce the expression of its permeability:

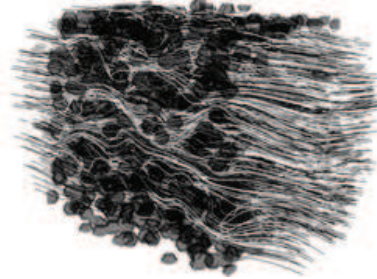


Figure 1-9: Schematic drawing representing the complexity of flow through a porous solid matrix (by Zbigniew Koza)

When a porous media contains solvent in its pore network, one can define the ratio of the total volume of the liquid to the total pore volume as the average saturation, ψ . Note that this value constitutes an average over the whole the porous body. If all the pores are filled, the material is said saturated and $\psi = 1$. For a saturated porous structure made of an homogenous pore size, the permeability is seen to scale proportionally to the square of the pore radius, [9]:

$$k = F(\varepsilon) \cdot r_p^2$$

The function $F(\varepsilon)$ takes different values depending on the geometric model adopted to describe the pore network:

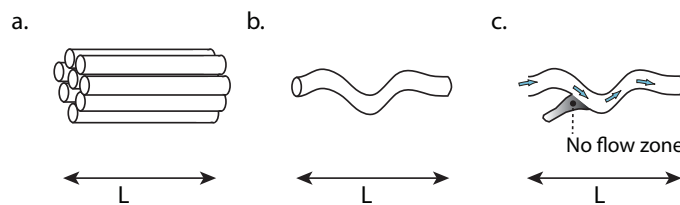


Figure 1-10: Scheme for a pore network of a porous media: (a) parallel ducts, (b) Tortuous duct, (c) connected tortuous ducts.

The simplest model consist in modelling a porous media by a series of parallel cylindrical tubes of radius r_p (see Fig1-10a). Under a pressure gradient the flow velocity may be calculated from the Poiseuille law, [27], and the pre-factor identified as $F_{pois}(\varepsilon) = \varepsilon/8$. However, this model remains very basic as it only describes unidirectional flow. Saffman model for porous media constitute a more realistic approach, starting from the previous model and implementing no restriction in canal orientation with space. In this case, $F_{saff}(\varepsilon) = \varepsilon/24 = F_{pois}/3$. The factor 1/3 stemming from the 3-dimensional direction in space, [116].

However, both these models fail to express the tortuous nature of the porous network, illustrated in Figure 1.6.1 by curved streamlines for solvent flow. In fact, for a porous sample of length L , the effective average length for a flow line through the sample is $L_e > L$ (see Fig1-8b), the ratio of those two values defines the dimensionless tortuosity, τ , of the porous media :

$$\tau = \frac{L_e}{L} > 1 \quad (1.11)$$

Note that by definition the tortuosity is always superior to 1. Now taking into account Saffman model and the tortuosity factor, one may compute the new factor F and find $F_\tau(\varepsilon) = \varepsilon/24\tau^2$. An more accurate geometric model would consist in adding the distribution of channel size, as of the porous media, for a distribution $\omega(r_p)$, the permeability is expressed as :

$$k = \frac{\varepsilon}{24\tau^2} \int r_p^2 \cdot \omega(r_p) dr_p$$

The limitation of this model falls into the knowledge of the material pore size and its distribution; these quantities being hard to measure accurately. The specific surface, A_s , of the porous matrix is however easily measureable, especially when the porous structure is made of a homogeneous bead packing. The Kozeny-Carman model for permeability takes this parameter into account and has shown to be very reliable in a laminar flow regime:

$$k = \frac{A_s r_p^2 \varepsilon^3}{180(1 - \varepsilon)^2} = \frac{\varepsilon^3 D^2 \varphi^2}{180(1 - \varepsilon)^2} \quad (1.12)$$

where D is the particle diameter and φ the sphericity of the particle in the packed bed ($\varphi = 1$ for a sphere).

ii. Permeability for a partially saturated porous media

When a porous medium becomes partially saturated with liquid its apparent permeability now depends on the permeability dictated from the structure of its solid matrix but also scales with a factor describing the hydraulic resistance of the liquid ($G(\psi)$). This parameter reflects the characteristic draining capability of the liquid network. Note that this implies this network being continuous throughout the whole sample. In this case and for a homogeneous distribution of liquid throughout the sample, k can be expressed as follow, [9]:

$$k = G(\psi) \cdot F(\varepsilon) \cdot r_p^2$$

4 - The mechanisms of moisture transport through coarse porous structures during drying

i. Historical understanding of the physics of drying in porous materials

The very first scientific exploration of the physics of drying started in the 1920s. First, Lewis, [28] in 1921, followed by Sherwood, [29] in 1929, proposed a description of the drying mechanism based on vapor evaporation from the free surface in soap slabs and vapor diffusion through porous clay bricks using Fick's Law. At that time a main hypothesis relied on the use of a constant diffusion coefficient for vapor appeared for both systems. This hypothesis was only proven wrong by Cunningham, [30] and Moyne, [31] in the 1980. However, already, in 1937, Ceaglske and Hougen, [23], demonstrated the limitation of the previous models highlighting the major role of capillary forces on water flow in granular packings. Twenty years later, in 1957 Philip and De Vries developed the theory for heat flux and thermal conductivity in partially saturated media. The most significant input was probably implemented in 1962 by Krishner, [32], who minutely described the different aspects of capillary transport, equilibrium, diffusion in the gas phase and for the first time highlighted a three step process for the drying kinetics under convective air flow through extensive experimental exploration of different material. In the following years, thermodynamic approaches were built to describe the three different regimes (Ludovik, 1966) and further knowledge was gained on the internal phenomenon (Marle, 1967; Slattery, 1967; Whitaker, 1967; Gray 1975). In the late 1980s Scherer provided extensive theoretical knowledge on drying induced deformation and material failure, [33-38]. Further industrial needs encouraged in 2000 the development of a general scaling approach by Coussot, [9]. And finally, thanks to the development of novel measurement technics and model analogous systems, as polygonal tube, recent research have proven the importance of liquid film flow during drying, Pratt and Yiotis, [18].

Most models describing moisture transport in real porous media (wood, clay, concrete etc.) during drying rely on the differentiation of two regions within the liquid: the bulk region, or non-hygroscopic region, where water is considered free from molecular or surface interaction with the porous matrix and a confined region (hygroscopic) consisting in a thin liquid layer around the pore walls where interactions exist between the liquid and the solid matrix. For water and glass this region was measured to 10nm, [39, 40]. While great understanding was achieved in the physics of drying for free water in large pores, very little understanding remains in the physics of drying at low moisture content, in nano-pores or even for adsorbed water layers.

5 - Drying regimes and water distribution for free water

Surprisingly the removal of free water during convective drying of a porous media is very similar to the one earlier encountered for a square tube; it is modeled with 3 main periods:

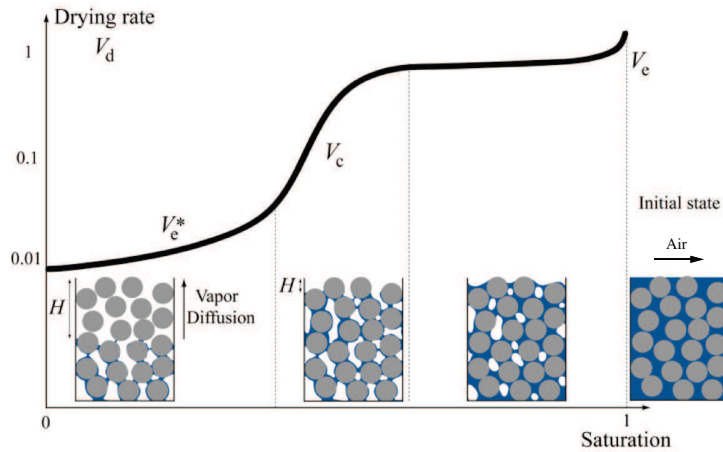


Figure 1-11: Evolution of the drying rate V_d matched with the evolution of the water distribution within the sample for a porous media. Air is blown parallel to the free surface of the sample at all time as pointed out on the far right scheme representing the initial state. H here represents the extent of the dry region forming from the sample free surface.

i. Induction period and isotherm drying

An induction period is observed until the heat and mass transfer processes between the material and the surrounding atmosphere approach an initial steady state (note the very small decrease in the drying rate at the very beginning of the test in Fig1-10) and the boundary layer of thickness δ (seen in section 1) has fully formed. The duration of the induction period is usually insignificant compared to the time of the other drying periods. During this short transient regime, the material is considered fully saturated. In this study, drying will be performed at room temperature in isothermal conditions.

ii. The constant rate period

Following the induction period, a constant drying rate is observed as long as the sample free surface is maintained effectively wet. Here the gas-phase mass transfer is determined by the thickness of the boundary layer δ and equation 1.1 applies. Evaporation only occurs from the free surface. Therefore, the extent of the constant rate period, depends on the material's ability to keep its surface wet enough, so to say to maintained a liquid network capable to drain enough water through the sample to the free surface for drying to remain boundary layer controlled (see Figure 1-12). For this reason, the water is also said to be in a “funicular” regime.

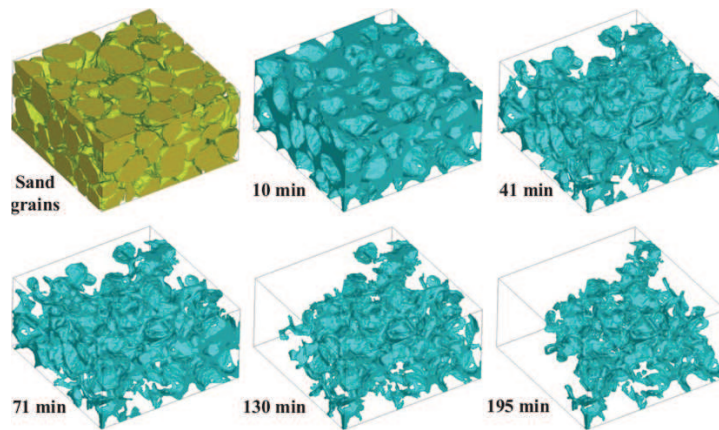


Figure 1-12: Liquid phase distribution during evaporation from a sand column obtained by synchrotron x-ray tomography. The arrangement of sand grains and liquid phase within the first scanned block ($3.3 \times 3.3 \times 1.7 \text{ mm}^3$) is shown for five time steps. Isolated liquid clusters were filtered out to highlight continuous liquid phase only. [117]. Note that this type of distribution is an example and is specific to the material studied, one can imagine other situations for water distribution, especially a more homogeneous distribution not including complete emptying of pores of network discontinuity, for instance in very hydrophilic porous media.

Liquid flow is triggered by a pressure gradient that develops over a short distance near the sample free surface (measured in the scope of 2.5 times the tube diameter in a polygonal tube system, [23]). In this region, water removal causes meniscus to progressively recede in the pores, increasing the local capillary pressure so that a pressure gradient develops in the sample. MRI profiling measurements presenting the concentration profile of water in the height of a bead packing during drying (see Fig1-12a) shows that during the constant rate period, the water remains homogeneously distributed throughout the whole sample. As a matter of fact, air substitutes water in an abrupt way, its dynamic being depicted by Haines jumps, [41], directing flow from area of higher depression (following depression gradients within the sample), see Fig1-12b. This overall mechanism of water redistribution is named after capillary equilibration process.

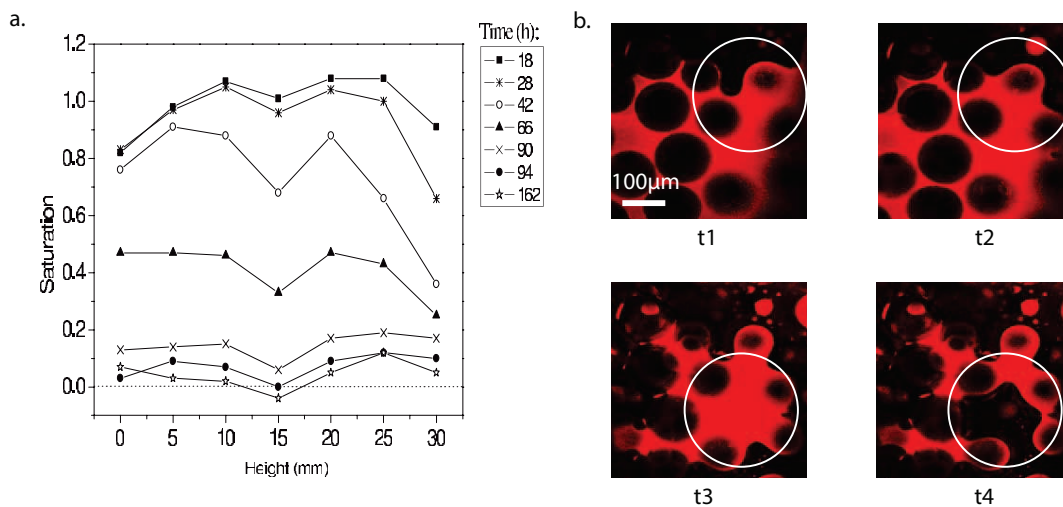


Figure 1-13: (a) Saturation profile, at different times during desiccation, within a homogeneous bead packing, [42], the flat profiles witness of an homogeneous distribution of water throughout the whole sample. (b) Confocal image of the capillary equilibration process during drying for an homogeneous bead packing, the fluid appears red because of a dye agent, beads appear in black, [43]; $t_1 < t_2 < t_3 < t_4$, from t_1 to t_2 , a first capillary equilibration step is observed in the circled area, from t_3 to t_4 a second one is observed in a different, but close area.

This constant rate period is therefore encountered in the case of hydrophilic solid matrix where meniscus can develop. However, when the contact angle between the liquid and the solid matrix is too high (close to 90°), drainage is prevented and similarly to the case of a large cylindrical tube, a dry region starts to develop from the free surface toward the inside of the porous matrix as presented on Fig1-14. This figure particularly shows the development of an apparent dry region from the free surface of the sample (at 30mm) from the beginning of the test.

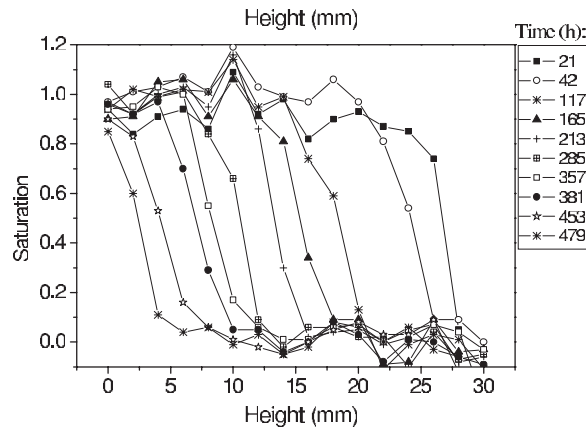


Figure 1-14: (a) Saturation profiles during desiccation for water within a hydrophobic porous media, [42]

Nevertheless, even for hydrophilic solid matrix, the constant rate period of drying is not always observed; typically, when drying system exhibiting very low permeability (as with extremely small pores for instance), this period may not be observed even if strong capillary forces exist (see Fig1-15 in the next section).

iii. The Falling rate period

The third stage of drying is the falling-rate period or periods (see Fig1-15). Essentially, this is the period when the removal of moisture from the solid is dictated by the material itself. The transition between the constant and falling rate drying periods appears at an average moisture content called the critical moisture content or saturation, ψ_c , which also corresponds to a critical capillary velocity, [9]. Note that past this point, the liquid network is assumed to become rapidly discontinuous [9]. Right before the regime transition, the flow of water within the sample remains dictated by Darcy's Law, Eq1.10. At the top free surface of the sample, the capillary pressure is α/r_p (α being a constant depending on wetting properties), at a distance L from the free surface,

the total pressure in the liquid considering the local saturation χ is $p(\chi) + \rho_w g L$ where $p(\chi)$ is the corresponding capillary pressure. Therefore, using Darcy's Law, the expression of the permeability for partially saturated system (Eq1.13), and providing that the driving pressure gradient is the difference of the former pressures divided by L ; one can find the expression of the capillary velocity:

$$v_{cap} = \frac{F(\varepsilon). G(\chi). r_p^2}{\mu L} \cdot \left(\frac{\alpha}{r_p} - p(\chi) - \rho_w g L \right)$$

At the free surface, the average meniscus curvature is higher than in the saturated area (located at L), therefore providing that $p(\chi) \ll \alpha/r_p$:

$$v_{cap} = \frac{\alpha. F(\varepsilon). G(\chi). r_p}{\mu L} - \frac{F(\varepsilon). G(\chi). \rho_w. g. r_p^2}{\mu} \quad (1.14)$$

Finally, in the case where gravitational effects on flow are negligible, the second term in Eq1.14 is neglected and the critical capillary velocity be expressed as:

$$v_c = \frac{\alpha. F(\varepsilon). G(\chi_c). r_p}{\mu. L} \quad (1.15)$$

where χ_c is the critical local saturation, at that point, the liquid is unable to flow and replace the evaporated liquid even along the liquid-limit of minimum curvature. Keyy (1972) followed by Coussot (2000) respectively proposed and scaled two distinct falling-rate periods in the drying of a porous medium: Initially, the moisture will recede to a position in the material where evaporation takes place with moisture supplied by capillary-driven flows. Usually this receded position remains close to the free surface, at distance H (see Figure 1-10), this first falling rate period is usually called after capillary regime. Inevitably, the drying time of this first falling-rate period depends on the size and distribution of the pores in the porous structure: macro pores extend this period of drying, [9].

Eventually, further drying will trigger a second falling-rate period, this transition known as the "percolation transition", triggers the propagation of a receding evaporative front and usually starts at low moisture content. In this regime specifically, the drying rate scales inversely proportional to the square root of the height of the dry region, H , as it was observed earlier in the case of a cylindrical tube (Eq1.4).

$$V = -D_p \frac{\rho_{sat} (n-1)}{\rho_w \bar{\delta} + H} \quad (1.16)$$

Where D_p is the diffusion coefficient of vapor through the partially saturated porous structure, $D_p = \varepsilon \tau D_0$ and $\bar{\delta} = D_p / D_0 \cdot \delta$ the relevant length to take into account considering drying conditions.

6 - Effect of pore size on drying regimes

Pore size is a crucial parameter that strongly influences the drying kinetics, [9]; for a porous media made of a close packing of spherical beads, the average pore radius can be approximated to 1/6 of the bead radius from geometrical considerations (space between 3 beads closely packed together in 3D). In this section, only porous media made of close packing of glass spherical beads are considered, note that the shape of the particle also plays a role in the drying kinetics one can observe [44], but this is beyond the scope of this study.

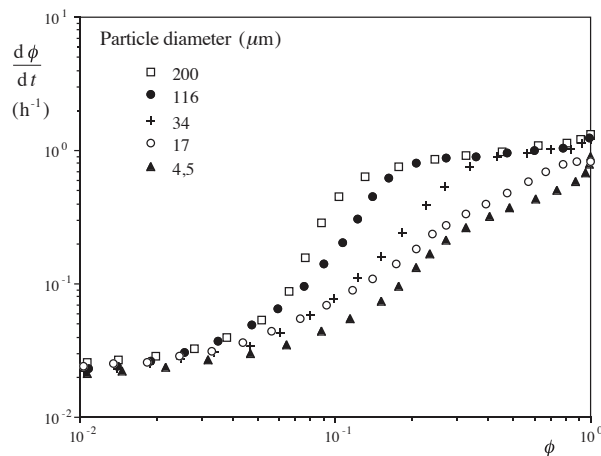


Figure 1-15 Normalized drying rate (in this graph the average saturation of the sample is noted ϕ) as a function of the average saturation in model bead packings filled with ethanol, [9].

Fig1-14 presents the evolution of the rate of drying during convective drying of homogeneous and compact ($\sim 60 - 63\%$) bead packings filled with ethanol and made with a different bead sizes. We observe that during the so called constant rate period, the drying rate is not exactly constant but slowly decreases, as already remarked by Van Brakel [45] and seen earlier on with the polygonal tube; additionally for porous media made with bead diameter ranging from 34-200 μm , in the drying conditions considered, we see that the same drying rate applies in this period regardless of bead size. In fact, in these drying conditions and this range of sizes, enough liquid can flow to the surface to cover the evaporation demand imposed by the airflow, regardless of the particle size. Going down to smaller pores, however, the data set shows that the drying rate of the materials decreases immediately from the beginning of the test and no CRP is observed. This trend is consistent with expectations from the Darcy's law and may be explained by the expression of the critical capillary velocity in Eq1.15: the later relation shows that the smaller the beads, therefore the pore size, the smaller the critical capillary velocity (v_c being directly proportional to the particles radii). Therefore, in systems where gravitational forces can be neglected to the capillary forces, the tinier the pores, the sooner the occurrence of the falling rate period, ultimately reached in the very beginning of the desiccation process.

The drying rate in the final stage is seen independent of the particle radius and tends towards an asymptotic value. This is in agreement with the theory corresponding to the receding regime which predicts that the drying rate simply decreases with the distance of the liquid-limit from the free

surface of the sample, considering that the tortuosity and the porosity of the porous structure remain similar (Eq1.16).

7 - Effect of pore size distribution on water distribution within the sample

Capillary equilibration is a process observed during the CRP, [Cousot et al.] that enables liquid transfers toward regions of higher depression, in other terms considering the capillary pressure only (Eq1.7), transfers occur from bigger to smaller pores. In Fig1-15a we present a scheme principle: big pore empty first and water is pulled by the Laplace pressure toward the smallest menisci (connection channels between pores are also called throat pores). In Fig1-16b NMR concentration profiles of water within a biphasic porous medium show the direction of liquid flow during drying. Specifically, this porous structure is made with 2 different compartments consisting of compact bead packings with different bead sizes (big beads at the bottom and small beads on top); we observe that drying triggers the bigger porosity to empty first and water to be sucked by the tiniest pores (consistently with Fig1-16a). Note that this system is a model system, a homogeneous pore structure is rarely found for a real porous media. As a matter of fact, the pore size distribution of actual materials is usually wide, (due to the heterogeneity in grain sizes or shapes etc.); In this case, numerical simulation with a three-dimensional invasion percolation model (see Fig1-16c) showed that depending on the width of this distribution different heterogeneous water distributions along the vertical axis of the sample could be expected. In fact, if a continuous liquid network remains within the sample: it suggests that big pores would empty first (probing higher equilibration velocities due to the lower permeability) even if they are located in the bottom of the sample (also seen on (b)) and water would be drained to the top surface in the partially saturated area by thick liquid films likely located in the smaller porosity. Note that this simulation suggests that the narrower the pore size distribution the smaller the vertical extend of liquid films during desiccation and therefore the earlier the formation of a dry region during the test.

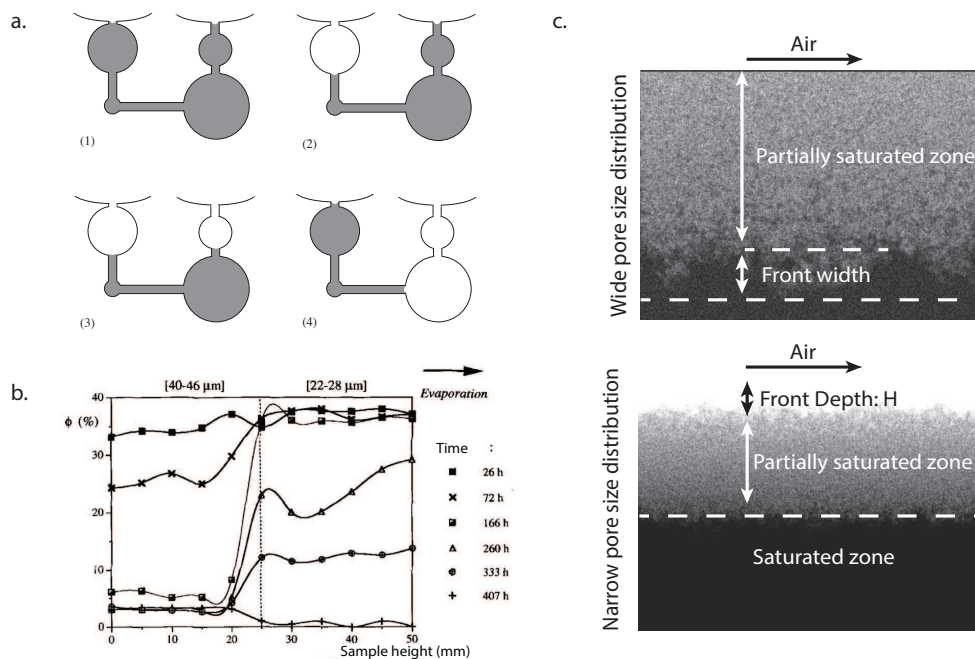


Figure 1-16: (a) Scheme for capillary equilibration in a porous structure presenting a wide pore size distribution. (b) 1D MRI profiles representing the water content in a porous media made of 2 homogeneous compartments each of them made of close bead packings with different sizes,[46]; (c) Numerical simulation suggesting the effect of the width of the pore size distribution of a porous media on its water content during drying, [47].

We conclude that heterogeneities in pore size may trigger different water distributions within the sample during drying and specifically possible liquid retention. Liquid retention may occur in the smallest porosity, or in the case of strongly hydrophilic surfaces, at the pore walls; in these cases, drainage through liquid films may be significant. Drawing a parallel with the previous study of a square capillary tube, one could expect a significant influence of draining films on the drying kinetics of the porous media considered. Let's further look at the current knowledge on liquid films.

8 - Liquid films, surface forces and viscosity

Two types of liquid films have been identified and distinguished in real porous media depending on their draining capacity [19, 48, 49]: The “thick” films that are trapped by capillarity in the corners of the porous geometry and are still considered as draining, i.e. typically corresponding to the films previously seen in the corners of a polygonal tube walls in the former section; and thin films, referring to physically adsorbed water in the form of multi-molecular layers on the walls of the solid matrix by disjoining pressure effects (Van der Waals and electrostatic contributions). The hydraulic conductivity of thin films is very small [50], and therefore their effect on the drying rate is assumed to be negligible compared to that of thick films. Recently, Yiotis et al [51] have presented a pore network model of drying, based on numerical simulation, including the effect of thick films. In accordance with previous works, their simulations qualitatively confirm the significant effects of thick films on the drying rates of coarse porous media. Their research specifically shows that drainage from thick liquid films enhances the overall drying rate of the material.

While drying free water, i.e. water retained in large pores by capillary forces, is well understood and gives rise to a 3 phase process, the physics behind drying of bounded water, referring to physically adsorbed water on the solid matrix remains unclear. The advance in the understanding we present therefore may remain rather qualitative.

The distinction of bounded and free water was specifically put to the fore through neutron scattering experiments during imbibition, [77, 78]. In fact, neutron scattering measurements being sensitive to liquid's viscosity, emphasized a partitioning of the diffusion dynamics of the molecules in the pores in two species: one component with a bulk-like self-diffusion dynamics and a second one which is immobile, sticky on the time scale of the experiment. While the rheology of the “sticky” water isn't clear, simple rheology consideration on pore bulk water during imbibition testified the absence of any non-Newtonian behavior for this part of the liquid, [76, 118, 119]. In fact, the disjoining pressure [15] as well as the structural peculiarities of the poly-molecular liquid layers are suspected to reduce mobility of liquid molecule, this is usually translated into an

increased viscosity for the wetting solvent. Additionally, recent computational investigation suggested that viscous flow may govern transport at the pore wall in adsorbed layers, [54]. Specific to our case, as we will be using silica surface and water in this study, we record studies performed with hydrophilic Vycor glass [76], that suggests the experimental existence of a sticky boundary layer of water at silica walls from macroscopic scaling. A conclusion which is supported by Molecular Dynamics studies on the structure of water boundary layers in silica pores [120-123], (see Fig1-19), or more generally the structure of water on hydrophilic surfaces [123-125]. In Fig1-18a, we illustrate these results showing the computed density of water molecules in a nanotube probing the existence of two different regions with distinct densities and finally a water density profile at the pore wall in Fig1-18b. These former simulations specifically emphasise that the thickness of these bounded liquid films may approximate to a couple of molecules of water (see Fig1-19b).

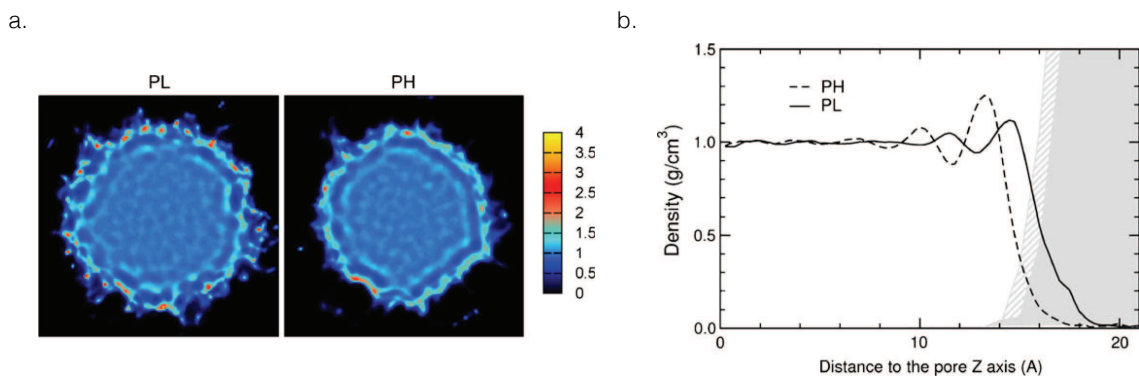


Figure 1-17: (a) Simulation of the average local densities of water in the horizontal plan (cross section of a tube) in 3nm diameter tubes simulated with silica walls with silanol groups concentration (chemical bounding of the water molecule to silica) of $PL=2PH$. The density scale is $0-4 \text{ g. cm}^{-3}$; (b) corresponding water density profiles $\rho(r)$ in pores (a) as a function of distance from the pore axis. The density profile of the silica matrix is also shown to locate the pore surface (partial and plain gray shadings for the PH and PL cases, respectively).

The physics behind flow of bounded water remains a very delicate topic that may add complexity to our study specifically when pores become a couple of nanometric and the saturation of the porous structure becomes very low.

9 - Drying stress and sample deformation for wetting porous media

Not only capillary forces play a role in the flow of water within the porous media, it is also responsible for its deformation. In fact, the mechanisms of pore fluid loss during drying of a deformable porous medium are seen to play a key role in the onset of drying shrinkage and cracks. The major drying stresses behind these mechanisms are commonly identified as the capillary pressure, the osmotic pressure, the disjoining pressure, [38]. This section focuses on describing the deformation generated by capillary forces during drying of deformable porous media. Along

desiccation menisci curvature increases giving rise to tension in the liquid phase. The maximum intensity of the capillary pressure is reached when the menisci curvature is small enough to fit into the pore i.e in the order of the pore radius. In certain cases, the latter pressure is so high that the sample is seen to shrink, warp or crack. In fact, shrinkage frequently occurs during drying and subsequently, in most cases, enhances the likelihood for the material to warp or crack.

10 - Shrinkage and wrapping

During the constant rate period, sufficient capillary tension may develop, depending on the pore size, at the sample free surface and provoke shrinkage of the solid matrix. The tension, ΔP , draws liquid from the bottom face of the sample in an effort to produce uniform hydrostatic pressure. The local contraction of the porous body, ϵ , may be expressed considering the young modulus, E , of the sample $\epsilon = \Delta P/E$, [38]. Introducing the latter expression in Darcy's law (Eq1.10), one can compute the characteristic length λ needed for the sample to equilibrate:

$$\lambda_{def} = \frac{k.E}{\mu.V_e}$$

Therefore, when $\lambda_{def} \gg \Delta z$ where Δz represents the extent of the pressure gradient inside the porous body along the vertical axis, the whole sample homogeneously contracts; whereas when $\lambda_{def} < \Delta z$ only the part subjected to the pressure gradient contracts. This situation gives rise to a heterogeneous contraction of the sample. If the sample delaminates (manage to unstick to its substrate), it will warp. Note that if the permeability is high, the flux of evaporation liquid is readily provided with a small pressure gradient if the permeability is low the tension becomes much greater on one face than the other, $\lambda_{def} < \Delta z$ and the sample will wrap.

11 - Cracking

Formation and morphology of desiccation cracks have been extensively studied over the past decades. A classical approach to crack nucleation in solid mechanics consists in comparing the intensity of the induced stress on the solid matrix from drying to the failure criterion of the material [56, 85]; if the intensity of the stress overcomes this criterion, a crack is nucleated. A plethora of mechanistic models have been formulated to explain crack nucleation, a brief physical explanation for the major theories is reviewed in the following array:

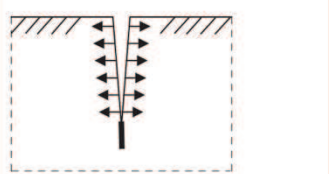
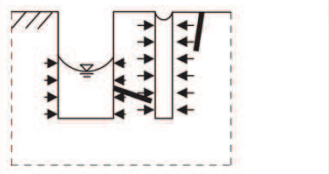
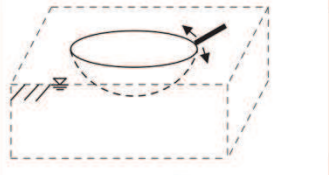
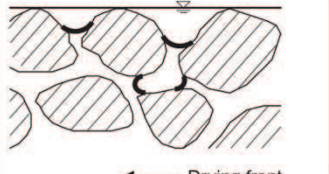
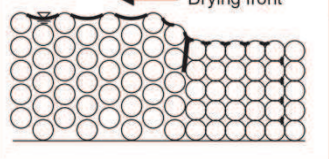
Theory		Mechanism (selected references)
Tensile failure		Tensile stress > material tensile strength. Most commonly assumed model (Lachenbruch, 1962; Allen, 1982; Morris <i>et al.</i> , 1992; Naser Abu-Hejleh & Znidarcic, 1995; Konrad & Ayad, 1997; Hallett & Newson, 2005)
Irregular drying front		Difference in capillary pressures and subsequent failure of pore walls Conceptual – no verification (Zarzycki <i>et al.</i> , 1982)
Circumferential tension		Growth of radial crack due to hoop tension Conceptual – no verification (Scherer, 1990)
Air entry		Menisci invasion due to increasing capillary tension Conceptual – no verification (Childs, 1969; Brinker & Scherer, 1990; Herrera <i>et al.</i> , 2007)
Packing collapse		Collapse of particle layers by capillary suction Concept used to explain desiccation cracks in a drying strip (Holmes <i>et al.</i> , 2006)

Figure 1-18: Mechanistic models for crack nucleation during drying, [56]

C -Basic concepts behind the physics of spontaneous imbibition of pure liquids in hydrophilic nanoporous media

1 - Description of the phenomenon

i. Capillary rise and Lucas-Washburn equation

To establish the physical framework for spontaneous imbibition in porous media, it is interesting to look at the phenomenon of capillary rise within a cylindrical tube first. Liquid flow driven by capillarity and resisted by viscous losses and gravitational forces, was first analyzed by Bell and Cameron (1906), who showed that the position of the imbibition front (h) advances as the square root of time (t). Heber Green and Ampt (1911) and Lucas (1918) and Washburn (1921) a few years later computed the proportionality constant for the case of a cylindrical tube of radius r immersed in a reservoir filled with a liquid wetting the capillary tube with a contact angle θ_w , see Fig1-20.

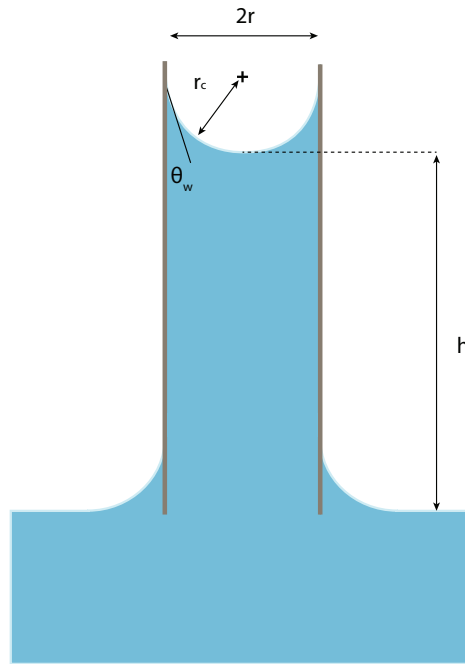


Figure 1-19: Capillary rise experiment performed in a cylindrical tubes. The base of the tube is dipped in an infinite water bath.

Under static conditions, the equilibrium height h_e of the liquid within a capillary is obtained by balancing the Laplace pressure $P_L = 2\gamma_{LV} \cos(\theta_w) / r$ by the hydrostatic pressure $P_g \sim \rho_w g h_e$ and finally the equilibrium height is found from the force balance equation:

$$h_e = \frac{2\gamma_{LV} \cos(\theta_w)}{\rho_w g r} \quad (1.17)$$

During capillary rise, the momentum balance equation of the liquid in the capillary can be written as :

$$\rho_w \pi R^2 \cdot \frac{\partial}{\partial t} \left(\frac{h(t) \partial h(t)}{\partial t} \right) = 2\pi R \gamma_{LV} \cos(\theta_w) - \rho_w \pi R^2 h(t) g - \frac{\pi \mu_w h(t)}{k} \cdot \frac{\partial h(t)}{\partial t}$$

In this last equation, each individual terms refer to, (from left to right): the inertia, the surface tension (capillary pressure), the gravity and the viscous loss (assuming Poiseuille flow to apply, $k = R^2/8$ being the permeability of the tube). If we assume that the liquid rises in the tube with a constant contact angle $\theta = \theta_w$, the latter equation can be written, inserting the equilibrium height h_e (see Eq1.17), as:

$$\frac{\partial}{\partial t} \left(\frac{h(t) \partial h(t)}{\partial t} \right) = gh_e - gh(t) - \frac{1}{\tau} \cdot h(t) \cdot \frac{\partial h(t)}{\partial t} \quad (1.18)$$

Where $\tau = \rho_w k / \mu_w$. This differential equation (Eq1.18) cannot be easily solved analytically as it, but numerical methods may be used. However, analytical solutions can be found for certain flow regimes where individual terms of Eq1.18 can be neglected (4 regimes can be identified depending on the predominance of each terms present in this equation). Here we only describe viscous dominated flow under capillary forces: if the influence of inertia and gravity can be neglected on liquid flow, Eq1.18 may be simplified as follow:

$$h(t) \frac{\partial h(t)}{\partial t} = \frac{2\gamma_{LV} R \cos(\theta_w) k}{\mu_w} \quad (1.19)$$

Eventually, solving this ordinary differential equation by means of separation of variables with the initial condition $h(0) = 0$ leads to the well-established Lucas-Washburn equation:

$$h(t) = 2 \cdot \sqrt{\frac{\gamma_{LV} \cos(\theta_w)}{R} \cdot \frac{k}{\mu} \cdot t} \quad (1.20)$$

Note that, $h(t)$ depends on the radius of the tube and the properties of the liquid: viscosity, surface tension, and contact angle and follows a \sqrt{t} -dynamic. Therefore, this model has limitations: at small times near zero the fluid velocity is approaching infinity, which is unrealistic, this discrepancy can be explained with the neglect of the inertia term.

Liquid flow in a homogeneous porous media is described by Darcy's law, which takes into account the influence of complexity of the porous network on flow properties through the permeability factor $k = k/\varepsilon$ in Eq1.18. Therefore, studying a porous media does not lead to modification of the previous equations and both physical scheme (capillary tube and porous media) are interchangeable with each other giving this permeability factor.

2 - Spontaneous imbibition in Nano-pores

Large pores, typically over a couple of micrometers, require to take gravity as a significant parameter to resist capillary rise. As seen in Eq1.18, gravitational effect introduces a resisting term proportional to $h(t)$ which introduces the existence of an equilibrium height for the liquid in the porous media (see Eq1.17). Nevertheless, this study is limited to spontaneous imbibition in nano-pores where gravitational effects do not interfere with imbibition kinetics. The study of the dynamic of water at the nanoscale is of particular interest as similarly to drying, it exhibits a particular phenomenology.

i. Validity of Lucas-Washburn equation in nano-pores

Pioneering experiments to probe transport behavior through pores a few nanometres across were performed by Nordberg and Debye, [70] and Cleland in the mid of the last century, [71]. As Abeles *et al*, [72] documented by an experimental study on toluene using nanoporous Vycor glass (thirsty glass), flow in nanoporous media can be driven by capillary forces (termed ‘spontaneous imbibition’) or by external hydraulic pressure (called ‘forced imbibition’); in this section we only focus on viscous flow driven by capillarity in nanoporous media.

Theoretical studies and simulations of nano flow in a single pore channel, [73] and collective array of interconnected channels [74] unlocked great understanding in flow across nanoporous media. Most importantly, Gelb and Hopkins [74], reporting a simulation study on the capillary rise of xenon into empty Nano-sized cylindrical silica pores, found classical Lucas–Washburn capillary rise dynamics to apply for a pure liquid (dynamics typically observed at the macro scale for spontaneous capillary imbibition after the initial, inertial capillary entering regime, [75]): the meniscus height increases as a \sqrt{t} (see Figure 1-26).

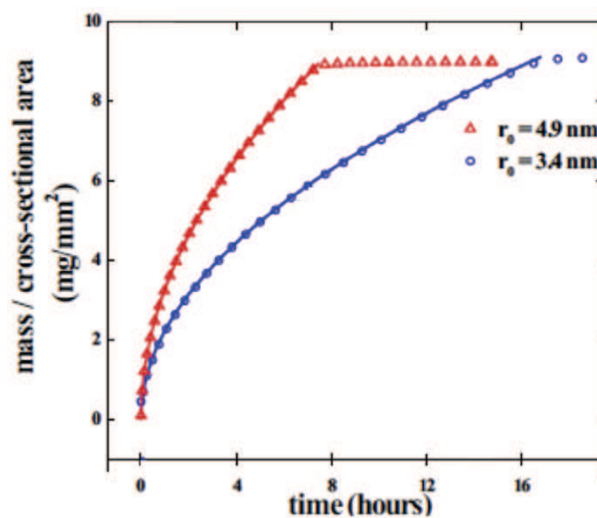


Figure 1-20: Normalized mass uptake $m(t)$ of Vycor with two different pore radii ($r_0 = 4.9$ nm: triangles, $r_0 = 3.4$ nm: circles) due to water imbibition as a function of time \sqrt{t} in comparison with Lucas–Washburn \sqrt{t} -fits (solid lines), [76].

ii. Fluid flow in nanopores

As seen earlier in the drying section, a thin layer of water can be adsorbed at the pore walls (see Fig1-17). In fact, among others, G. Whitesides and al. [126,131] demonstrated, recording imbibition of a rectangular silica capillary channel and tuning its wetting properties, that the shape of the imbibing liquid on a surface with high γ_{LV} shows precursor structures to precede macroscopic flow, whereas with low γ_{LV} , these precursor structures are absent. Specifically, possible shapes [127,130] of these precursor structures include slipping films (with or without shoulders, see Fig1-27a (a) and (b)) for high γ_{LV} and non-slipping films (wedge or mesa, see Fig1-27a (c) and (d)) or plug-flowing films (Fig1-279, (e)) for low γ_{LV} . For wetting fluids (our case of interest here), slipping films are characterized by “sliding” of the liquid layer along the surface, where the “support” liquid layer spreads freely (see Fig1-27b); From sliding, the advancing front moves with a new contact angle altered from its value at rest, the dynamic contact angle. For wetting fluids, the dynamic contact angle can substantially deviate from its static counterpart, especially at high flow velocity, therefore the rates of capillary imbibition can be greatly influenced (see Eq1.19). The extent of these precursor films is shown to a couple of pores ahead of the imbibition front, [128,129] (see Fig1.21b).

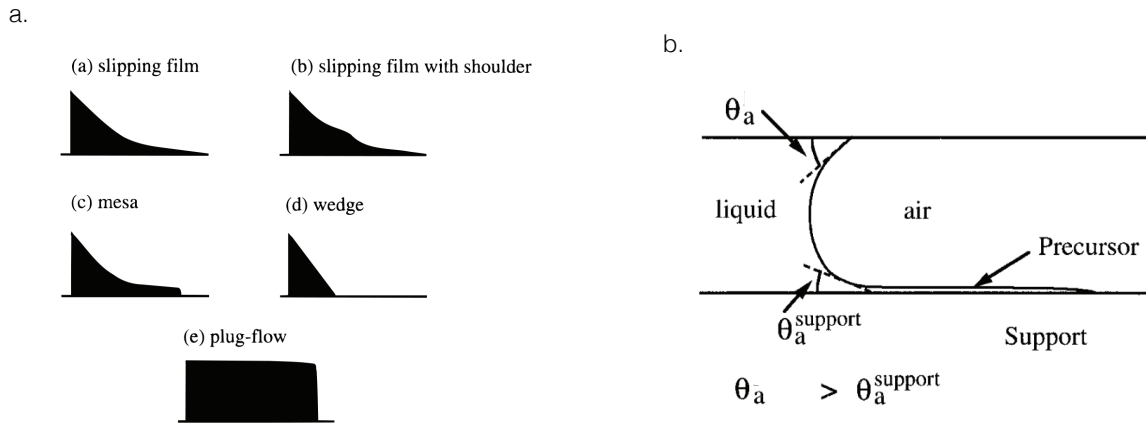


Figure 1-21 : (a) Diagrams representing different shapes of spreading liquids in a capillary channel; (b) profile depicting the shape of the imbibition front in a rectangular pore channel showing different advancing contact angles of the liquid on a wall free from precursor film (support) and with the precursor film (support) preceding the macroscopic flow, [126].

iii. Front broadening

During imbibition the liquid-gas interface advances and broadens due to local heterogeneities in pore sizes and shapes creating variations in the local bulk hydraulic permeability and in the capillary pressure. This broadening effect results in the coexistence of empty and filled pore segments at in the advancing front. For macro porous systems, this effect is well documented and its physics benefit universal scaling features on large length and time scales, [1,2,3]. In the past most imbibition front broadening studies focused on sand and paper. In these systems, pores being laterally highly interconnected, a flat, continuous liquid-gas interface rises up the porous structure; and front advancement is seen spatially correlated to the mass uptake, [79]. However, Gruener *et al* recently reported on the broadening of the imbibition front of water in nanoporous Vycor glass, [80]. For this porous medium imbibition front roughening manifests itself by a growing opalescence at the advancing front as seen on Figure 1-23a. The latter phenomenon supposedly originates for light scattering from the coexistence of dry regions (air) and liquid-filled pore segments on visible light length scales while the front broadens. However, it's detailed study is remains challenging since the liquid/vapor interface is buried inside the matrix, [81]. Neutron radiography, [82], nevertheless, allowed Gruener *et al* to image this process and to document on the interface width $w(t)$ evolution (see Figure 1-28b). The front width is to increase much faster than observed previously for imbibition front broadening in other porous materials such as sand and paper, here and scales as $w(t) \propto t^\beta$ with $\beta \approx 0.5$.

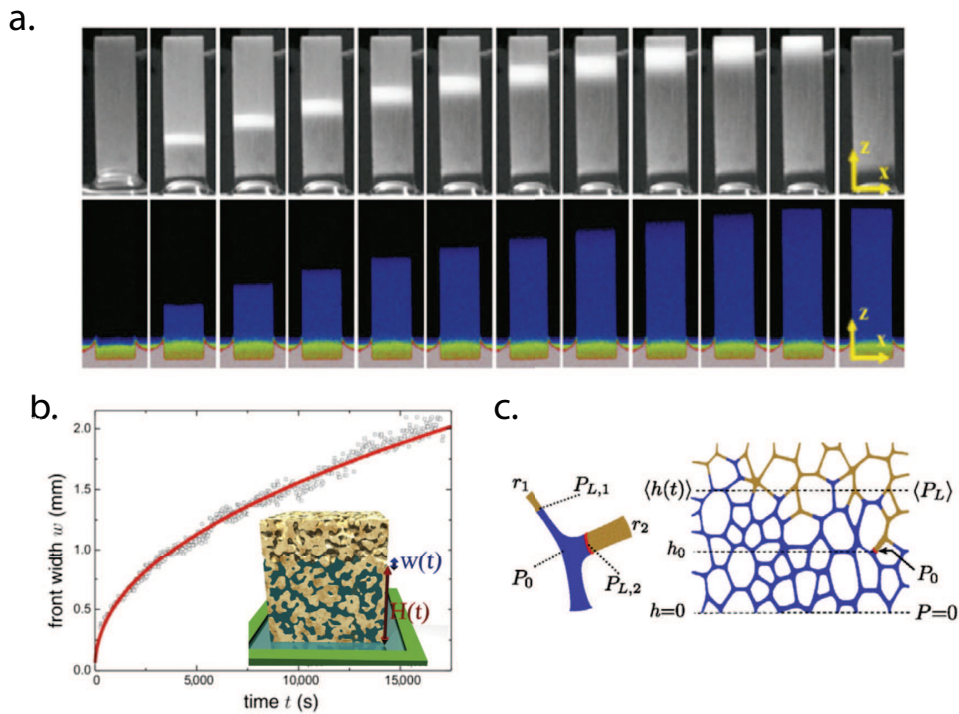


Figure 1-22: (a) Direct observation of spontaneous imbibition of water into nanoporous Vycor glass using visible light (top row) and neutrons radiography (lower row). The filling degree is shown in grayscale and pseudo colors, respectively. Snapshots are recorded for

0.1 s (light) and 30 s (neutrons) about every 15 min. The lateral direction x and the height z , i.e. the direction of capillary rise, are indicated. The width and height of the sample are 4.6 mm and 20 mm, respectively. (b) Evolution of the front width $w(t)$ and fit of $w \propto t^\beta$ (red line). : (c) Illustration of meniscus arrests during capillary rise in a network with elongated pores. r_i and $P_{L,i}$ denote the radius and Young–Laplace pressure, respectively, in pore i ; P_0 denotes the hydrostatic pressure. In the right panel, $\langle h(t) \rangle$ and $\langle P_L \rangle$ denote the average height at time t and the average Young–Laplace pressure, [6].

Additionally, Sadjadi and Rieger, [6], revealed through pore network simulations, that dynamics of the imbibition front in spontaneous imbibition, crucially depends on the pore aspect ratio $\vartheta = 2r_{av}/L_{av}$, where r_{av} is the average radius of the pores and L_{av} the average length between two interconnected nodes, (see Fig1-28c). Among other, they showed that for short pores (small ϑ), neighboring menisci merge leading to a continuous imbibition front; thus putting to the fore the smoothening effect of surface tension leading to slow broadening of the front. By contrast, for a large ϑ (like in Vycor) individual menisci form in pore space and the resulting strong broadening mechanism can be qualitatively understood this following way: at pore junctions, menisci with different Young–Laplace pressures compete, see Fig1-28c, the meniscus propagation in one or more branches can stop as soon as the negative Young–Laplace pressure of one of the menisci (here $P_{L,2}$) exceeds the hydrostatic pressure within the junction at height h_0 . These menisci arrests until the hydrostatic pressure in the junction, P_0 , becomes greater than the Young–Laplace pressure of the halted menisci. Because of the viscous-drag in the liquid column behind the advancing menisci, the junction pressure increases linearly with the distance of the moving menisci from the junction and this distance follows the Lucas–Washburn dynamics. Hence, the arrested menisci start to move, when the moving menisci have moved up from a distance, which is exactly proportional to \sqrt{t} . Identifying in this simple picture the width of the front with the maximal distance between arrested and moving menisci, the broadening of the front scales also as a \sqrt{t} -law.

It is important to stress that the strong imbibition front broadening found in the study on liquid imbibition in Vycor is not linked to the nanometer size of the pores. However, its experimental observation over large length and time scales significantly benefits from the dominance of capillary forces over gravitational forces, which results from the nano-sized pores. Therefore, strong broadening is a consequence of any spontaneous imbibition process in porous structures with interconnected elongated capillaries independent of their macroscopic extension and mean pore diameter.

D - Positioning of this study

This first chapter shows that a crucial parameter limits the current understanding in the physics of drying and imbibition: the knowledge of the evolution of the local state of saturation of the material during the whole processes. Therefore, we identify an opportunity to contribute to the understanding of these mechanisms by focusing on detailed observation of the water distribution and its evolution within homogeneous and heterogeneous (only during drying) porous medium, during both processes. To yield such information we use NMR and Electron microscopy technics, as described in the next section. Let's be more accurate about the directions of this study:

During drying, we saw that porous material may deform substantially under capillary forces. The variety of these deformation phenomena coupled with an undetermined water distribution in a sample that keeps evolving, give rise to poorly understood drying kinetics. For deformable and cracking medium, simple questions as to how these deformations could contribute to the drying rate of the material remain un-clear while studies on applied systems such as clay material [86] or cement pastes [87], bear empirical witness of a perturbation in the drying rate of cracking materials around their cracking events. These variations are usually assumed to be generated by the additional surface developed and thus newly available for evaporation. However, we saw [10, 88, 89] that the drying rate of a uniform liquid sheet (such as at the top of a saturated porous medium) can be the identical to its counterpart presenting dry patches at its surface; therefore, one can expect that a material that significantly crack would still dry at the same speed as their monolithic counterpart (associating cracks cavities to those dry patches). Since this assumption seems to be in contradiction with the above preliminary results and reasoning, as a first axis of the research, we investigate the kinetics of drying of material adopting a complex shape or conformation during drying. In detail, we carry out a full characterization of the deformation we encountered in contracting nano-porous media and build a model for the drying kinetics observed depending on the degree of deformation of the material.

Also, this first chapter emphasizes that during drying of a porous media, the exact conditions for which the FRP starts remains unclear as well as the evolution of the liquid distribution in the sample in that regime; it is generally considered that this regime is triggered when the evaporation rate from the free surface becomes larger than the critical capillary velocity but except in specific situations for which a receding dry front was imposed by external conditions (non-wetting liquid [133], accumulation of particles below the free surface [132]) the direct observations of the liquid distribution inside the medium during the FRP concerned particular materials and limited ranges of saturation [134, 136]. Therefore, in the second part of this manuscript we investigate the field through detailed MRI visualisation in homogeneous porous medium with pore sizes ranging from a couple of microns to a few nanometers, and down to full evaporation.

Lastly, if great understanding is brought to the field of capillary propelled flow at the sub-micron scale during imbibition, this knowledge mostly relies on results from the theory or molecular simulations. Experimental proofs of the physical mechanisms remain very slim and concern systems with pronounced structural peculiarities, such as thirty glass (Vycor glass) that usually exhibits a low porosity, close to 30%. A plain and ubiquitous questions as to what are the dynamics of capillary rise within a homogeneous and compact porous structure cannot find a clear answer.

To contribute to the understanding of this field, we follow imbibition with MRI, measuring concentration profiles of water in the homogeneous porous media we designed (pore sizes ranging from a couple of microns to a few nanometers) all along the process.

Chapter 2 - Materials and Methods

This section is dedicated to the description of the materials we used, the set ups we built and the measurements we performed. Let's first describe the functioning of at the measurement tool we use: electron microscopy and MRI, as we use them for material characterization.

A - Measurement tools

1 - SEM and TEM Imaging

i. Technology

In this study we use or synthesize materials with micrometric to nanometric structure details, to observe these details, we use electron microscopy (EM). An electron microscope uses a beam of accelerated electrons as a source of illumination; as the wavelength of an electron can be up to 100,000 times shorter than that of visible light photons, the electron microscope has a higher resolving power than a light microscope and can reveal smaller structure details of an object.

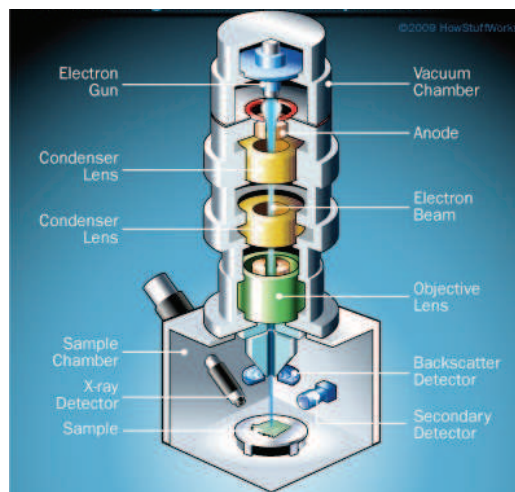


Figure 2-1: (a) Scheme for the architecture of an SEM (scanning electron microscope), microscope, by Johnatan Atterbery.

A Scanning Electron Microscope or SEM produces images by probing the specimen under vacuum with a focused electron beam generated by an electron gun (see Fig2-1). More specifically, this gun generates free electrons and accelerates them to energy levels in the range 1 to 40 keV; the resulting beam is then sent through a set of electron lenses (see Fig2-1) to create a small, focused (condensed) electron probe on the specimen. When the electron beam interacts with the specimen, the latter loses energy by a variety of mechanisms. This lost energy from the beam results in emission of a plethora of distinct radiations from the sample, among others we observe: heat, emission of low energy secondary electrons (SE, <50eV) and high-energy backscattered electrons (BSE, greater than 50eV). All these signals carry information about the properties of the specimen surface, therefore, collecting (detector in Fig2-1) the desired portion of this radiation (note that

only secondary (SE) or backscattered electrons (BSE) are used in this study), and amplifying it, an image can be reconstituted and displayed on a TV screen or computer monitor. The resulting image is generally straightforward to interpret, at least for topographic imaging of objects.

In this work we use 2 different types of SEM, the FESEM Supra55Vp (which functioning follows the above description) and the SEM EVO 55 both manufactured by Zeiss; the latter being an environmental SEM (ESEM) that among others, enables wet imaging (details on the instruments can be found at <http://cns.fas.harvard.edu/eSEM> for both microscopes). Even if the EVO SEM is a direct descendant of a conventional SEM it is necessary to specify how it operates.

The environmental scanning electron microscope (ESEM) permits wet and insulating samples to be imaged without prior specimen preparation (see next section), it does this by enabling a gas, here vapor water to be present in the sample chamber whilst retaining the rather high resolution of the standard SEM. A low pressure (up to 1500Pa) can be accommodated around the sample. When this gas contains vapor water, hydrated samples can be maintained in their native state. Also, as it is possible to dynamically tune the relative humidity of the air blown onto the sample as well as the temperature of the sample, cycles of imbibition (see Fig2-2a then b) and drying (see Fig2-2b then c) can be performed. To achieve sample saturation (in Fig2-2 a), we drop the sample temperature to just above freezing at 4°C (this is done by the use of a Peltier-chip controlled cooling stage), and increase the relative humidity of the air to 100%. On the other hand, drying (see Fig2-2b and c) is performed by dropping the relative humidity of the airflow to a couple of percent and heating up the stage to 50°C, in these conditions a pressure of 750Pa is necessary to obtain a workable image.

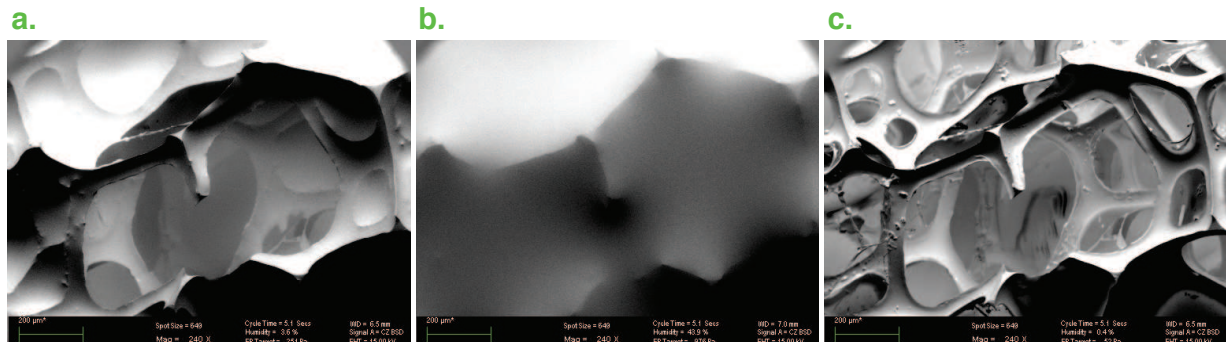


Figure 2-2 ESEM image of one of our sponge sample (see Chapter 3), from (a) to (b) once can see sample imbibition, from (b) to (c) sample drying (same sponge).

ii. SEM imaging in practise

Obtaining the perfect image with SEM is a trade-off between many factors. There are a number of problems we encountered while imaging. This section aims at giving guidance toward good imaging practise.

During EM imaging, one can encounter a lack of detail of surface structure. At high kV the electron beam penetration and diffusion within the sample become larger and result in signal (electrons

coming out of the sample) being generated from deeper within the specimen. One can think of it as a use to reveal thinner topographic details, however, it may as well obscure fine surface structures. In fact, high voltage increases BSE and so the image can potentially start to show changes in contrast based on composition. The solution therefore, for obtaining fine surface structure is to exclude these backscattered electrons by using lower kVs such as 3-10kV. Hence lower energy actually provides better detail of surface structure.

Edge effects may cause contrast issues. Edge effects are due to the enhanced emission of electrons from edges and peaks within the specimen. They are caused by the effects of topography on the generation of secondary electrons and are what gives form and outline to the images produced by the Secondary Electron detector. Electrons preferentially flow to and are emitted from edges and peaks. Poor signal intensity occurs in those regions shielded from the detector. Topographic contrast is also enhanced by Back Scattered electrons emitted from regions of the sample facing towards the detector. Lowering the beam kV can reduce edge effect.

Charging is produced by build-up of electrons in the sample and their uncontrolled discharge, and can produce unwanted artefacts, particularly in secondary electron images. When the number of incident electrons is greater than the number of electrons escaping from the specimen, then a negative charge builds up at the point where the beam hits the sample. This phenomenon is called charging and it causes a range of unusual effects such as abnormal contrast and image deformation and shift. Sometimes a sudden discharge of electrons from a charged area may cause a bright flash on the screen. These make it impossible to capture a uniform image of the specimen and may even be violent enough to cause small specimens to be dislodged from the mounting stub. The level of charge will relate to the energy of the electrons and the number of electrons. The energy of the electrons is related to the kV (i.e. high kV = high energy) so reducing kV can reduce charging. The number of electrons relates to a number of parameters including, beam current, the emission level of the gun, the spot size, and the apertures between the gun and the specimen. So reducing the number of electrons by adjusting these parameters can also reduce charging.

Charging is not as apparent in backscattered electron (BSE) imaging mode so that signal can be used or signals can be mixed (BSE and SE). A fast scan rate with frame averaging can be used to advantage in some circumstances too.

In the case of constant high charging, an SEM with low vacuum capability or an Environment Scanning Electron Microscope (ESEM) can be used to gain greater control over charging.

As seen previously, irradiating a specimen with an electron beam results in a loss of the beam energy to the sample in the form of heat and may cause specimen damage. A higher kV results in a higher temperature at the irradiated point and this can damage (e.g. melt) fragile specimens, such as polymers or very fine structures, eventually this can ruin a sample (see Fig2-3a and b). The solution is to lower the beam energy, sometimes down to a few kV. Increasing the working distance can also help since it produces a larger spot size on the sample for the same beam energy but this has the disadvantage of reducing resolution.

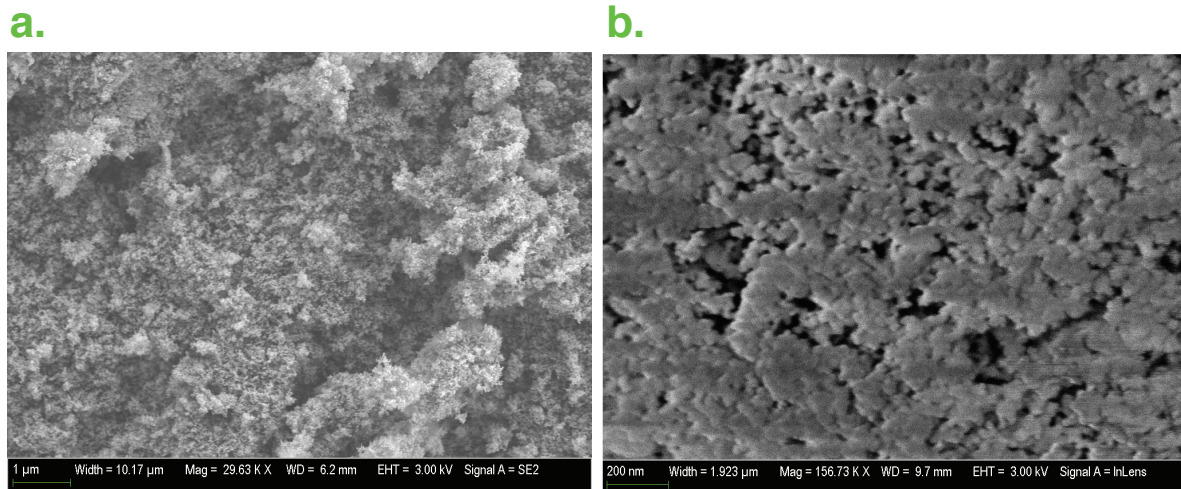


Figure 2-3: Example for sample (here silica) damage caused by high magnification (a) fine structure details can be observed, (b) the same sample melts.

iii. Sample preparation

Coating of samples is often required in the field of electron microscopy to enable or improve the imaging of samples. Thanks to a sputter coater, it is possible to spread a conductive layer of metal (here platinum, Pt) on the sample to inhibit charging, reduces thermal damage and improves the secondary electron signal required for topographic examination in the SEM (therefore increases the signal to noise ratio). Even if this technique would sensibly enhance resolution on our materials, as sputtered films for SEM typically have a thickness range of 2–20 nm, it would also cover the scale of the topographic details we are interested in or with wet imaging change the affinity between the sample surface and water; therefore, no coating was used in our SEM experiments.

2 - Nuclear Magnetic Resonance techniques

Magnetic Resonance Imaging or MRI is a non-destructive, non-invasive measurement technique that uses Nuclear Magnetic Resonance or NMR to locate a chemical species in space when the quantum mechanical magnetic properties of its nucleus allow it, [137]. In this study we use NMR spectroscopy to measure the quantity and relaxation behavior of H^+ protons in water in porous media (i.e. proton NMR). We perform two types of measurements: one consisting in averaging the NMR signal over the whole sample, for instance granting access to details of the porous structure (pore size distribution); the second, consisting in measuring the NMR signal along small and successive cross sectional portions of the sample in a unique direction of space; this last technique enables to measure 1D concentration profile along the axis considered.

The spectrometers we used are manufactured by the company Bruker, namely the minispec MQ20 series equipped with a 0.5T permanent magnetic field and a proton probe of 20 MHz (we use this particular apparatus to measure pore size distribution) and the Avance 24/80 DBX MRI spectrometer delivering a homogeneous permanent magnetic field of intensity of 0.5T over 20cm along the vertical axis with field gradients of 0.05 T/m and equipped with a proton probe of 20MHz. We use this last apparatus to yield 1D concentration profiles of water.

i. Principle of NMR measurements

Nuclear Magnetic Resonance allows one to probe the nuclear dipole moments within a material. Nuclei of certain atoms have an intrinsic spin with angular momentum that gives rise to a magnetic dipole moment and can be considered to be like a small spinning magnet. At rest, the average magnetization over a whole sample is zero, however when these nuclei are placed in permanent magnetic field \vec{B}_0 oriented along the Z axis, the magnetic dipole of each atom experiences a torque that causes them to align with this field and this value changes. Let's be more precise about the motion and orientation of those dipoles:

The motion of the magnetic dipoles describes a precessional motion around the direction of \vec{B}_0 analogous to the motion of a spinning top in the Earth's gravitational field. The frequency of this precession is known as the resonant or Larmor frequency (ω_0) and depends on the type of nuclei used and the intensity of the field \vec{B}_0 . The equation for this relationship is

$$\omega_0 = \gamma B_0$$

where γ is known as the gyromagnetic ratio, a nucleus-dependent variable, for protons, $\gamma = 2.675 \cdot 10^8 s^{-1} T^{-1}$. The direction of this alignment needs to be further detailed, in our case, the quantum number of the hydrogen nucleus being $I=1/2$, its magnetic quantum number (which defines the possible orbital orientations in space) can take either values $\pm 1/2$. In sum, this result in two possible orientations for the Z component of the magnetic moment of each individual dipole: aligned or anti-aligned to the field direction \vec{B}_0 . At room temperatures there is a slightly greater number of aligned nuclei than anti-aligned so the sum of all the nuclear magnetic moments

results in a small ‘net’ magnetization $\overrightarrow{M_0}$ proportional to and in the direction of the permanent applied field $\overrightarrow{B_0}$.

It is possible to measure this magnetization M_0 by firstly causing it to rotate in the XY plane and then detecting its precession using a pick-up coil (antenna). To rotate the magnetization a torque needs to be applied and this is done by applying another magnetic field perpendicular to $\overrightarrow{B_0}$. The problem is that it would normally require a static field significantly larger than B_0 to do this. The way around it is to move into the reference frame rotating at the Larmor frequency so that in this frame $\omega_0 = 0$ and B_0 disappears. In this rotating referential, we can apply a torque to the apparent magnetization that now appears as stationary, this is made possible by applying a sinusoidal radio frequency (RF) signal perpendicular to $\overrightarrow{B_0}$ (this new signal will be called $\overrightarrow{B_1}$). The result of all this is that only a small magnetic field is required to interact with the spin system as long as it is synchronized: at resonance. The $\overrightarrow{B_1}$ field pulse used to achieve this is known as a 90-degree pulse as it tips the magnetization by 90° into the xy plane. Once the magnetization has moved in this plane, the B_1 coil switches from emitter to receptor and the signal within this plane only, is recorded. The amplitude of the signal recorded with the latter coil progressively vanishes with time as the magnetization de-phases and returns to its equilibrium position along $\overrightarrow{B_0}$. This is called the relaxation processes and specifically, this simple experiment is called the Free Induction Decay (detailed later on).

Because of the complex movement of the magnetic dipole (precession), two uncorrelated process of relaxation exist, characterized by distinct relaxation times: to the longitudinal spin-lattice relaxation corresponds a characteristic time parameter, T_1 , that quantifies the rate for magnetization to recover along $\overrightarrow{B_0}$; the spin-spin relaxation or transverse relaxation, quantified with T_2 , is a characteristic time parameter for signal decay rate on the transverse axis. Typically, for pure water $T_1 = 4.5\text{sec}$ and $T_2 = 2.5\text{sec}$ depending on the level of dissolved oxygen. Note that so called ‘ T_1 ’ and ‘ T_2 ’ relaxation processes appear as uncorrelated. As a physical constraint $T_1 \geq T_2$. Also both magnetization rates (decay or recovery) follow an exponential dynamic (seen later on). It exists a plethora of measurement protocols (sequences) to yield both the relaxation dynamics and the amplitude of a species, all of them consist in an interplay of pulses and delays, the main goal being to flip magnetization into the XY plane for measurement. NMR is frequently used in the field of porous media to study characteristics of their structures such as their porosity and pore size distribution; but also to follow dynamic processes such as its water saturation with time. In this study, we chose to work with T_2 measurement over T_1 for porous media. The reason behind this choice is that we are here measuring dynamic processes (imbibition and drying); NMR offering a trade-off between measurement time and measurement quality, because T_2 can be measured faster than T_1 , studying relaxation through T_2 gives us an initial advantage.

ii. Free induction Decay

The simplest pulse sequence is already mentioned above. It consists of one 90° RF pulse at the Larmor frequency. The resulting magnetization is called a Free Induction Decay (FID). Once the pulse is applied, as mentioned earlier, the coil switches from emitter to receiver, and the precessing magnetization, inducing a voltage in the same coil, is measured (see Fig2-4). In a perfectly

homogeneous B_0 field, the decay of the envelope of the FID (dotted line in Fig2-4) occurs because the transverse relaxation mechanism gradually destroys the transverse (visible) magnetic contribution.

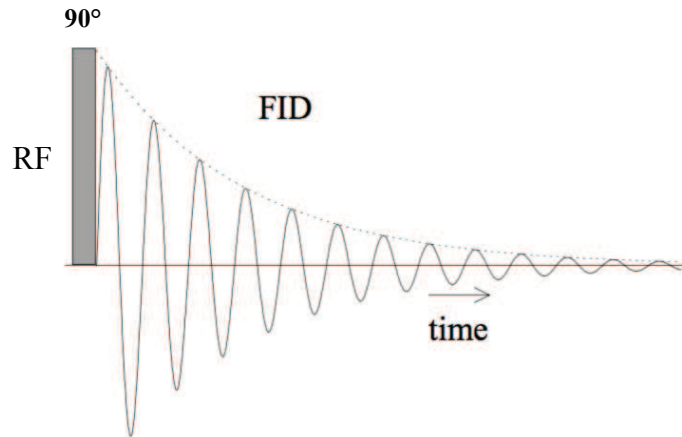


Figure 2-4: Free Induction Decay (FID) measurement, signal oscillates at the Larmor frequency; the dotted line corresponds to the envelope of the FID, its decay is exponential. Scheme inspired from [137].

Because the magnetic field can never be made perfectly homogeneous, not all spins in the sample precess at exactly the same resonance frequency. This gives rise to a dephasing mechanism, now if an ensemble of spins is considered, this leads to a loss of coherence. FID signal then decays faster than T_2 (described by the Bloch Equations, [138]).

iii. The measurement of T_2 : Spin Echo

In porous materials, the inhomogeneous broadening effect reduces the duration of the FID to typical times of 1ms. When the magnetic field heterogeneities are large, it can even be impossible to detect the induced voltage. If this is the case, the Hahn (June 9, 1921 – September 20, 2016) spin-echo pulse sequence, [139], may be employed to help recording a clear signal. This pulse sequence starts with a 90° pulse and a resulting FID (see Fig2-5). In practice, when the FID has decayed significantly, a 180° pulse is applied. This pulse will flip the phase of all individual spins. Because it does not change the phase accumulation itself, it will result in a rephasing effect and at this precise point, the signal echoes. Looking at Fig2-5, consider a spin which had accumulated a net phase shift of φ during the time τ between the 90° pulse and the 180° pulse. The 180° pulse will invert this phase into $-\varphi$. After this pulse, the spin starts to accumulate phase at the same rate as before the 180° pulse therefore after a time 2τ the net phase shift is zero. This holds for every spin in the sample. Therefore, at Echo time $t_E = 2\tau$ the transverse components of all individual spins are aligned and give a maximum signal intensity in the RF coil. The signal is called spin echo and will have a shape like the continuous line described in Fig2-5 at 2τ . If the translational motion of the nuclei of interest can be neglected in the sample, the height of the spin echo is only influenced by the transverse relaxation mechanism, which will give a decay of $\exp(-t/T_2)$ (follow dashed line on Fig2-5), not affected by magnetic field inhomogeneities.

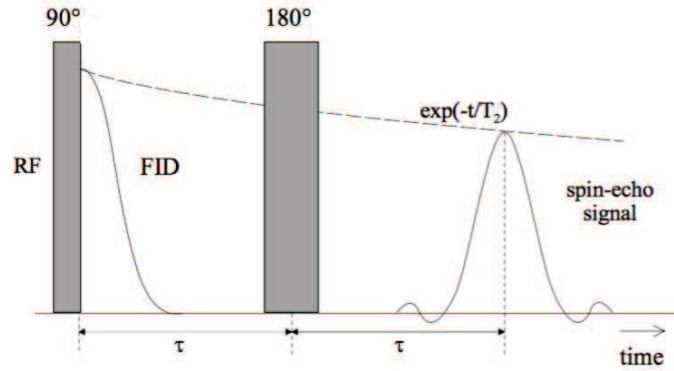


Figure 2-5: Scheme for the Spin-Echo sequence; as a signal (continuous line, see Fig2-4), the envelop of the FID is represented first, followed by the resulting spin-echo signal, [137].

iv. NMR Relaxometry, pore sizes and CPMG sequence

It is necessary to understand the relationship between the relaxation time of water and pore geometry (surface and volume) to further understand the reasons behind the design of our sequences and the need to adjust our measurement parameters during our experiments. Consider an arbitrary isolated pore with volume V and surface S filled with water. During an NMR experiment, the water molecules in the pore diffuse due to Brownian motion. If the transverse relaxation time for bulk water ($T_{2, bulk}$) is on the order of seconds, it can largely decrease for molecules near the pore wall to a value on the order of microseconds. Brownstein and Tarr, [140,141] calculated the resulting relaxation time $T_{2, meas}$ for such a model pore filled with a liquid:

$$\frac{1}{T_{2, meas}} = \frac{1}{T_{2, bulk}} + \frac{S}{V} \cdot \eta_{2, surf} \quad (2.1)$$

where S is the wet surface of the filled pore, V the liquid volume, $\eta_{2, surf}$ is the surface relaxivity which reflects the capacity of the solid matrix to relax H protons from the liquid phase. When water content varies within a material (be it during imbibition or drying), the relaxation time, $T_{2, meas}$, of the sample varies according to Eq2.1. When water strongly relaxes on the solid matrix and all the more when the sample consider exhibits a large specific surface S , $T_{2, meas}$ may become way smaller than $T_{2, bulk}$ (for water $T_{2, bulk} \sim 2.5$ sec) and the first term in equation 2.1 becomes negligible compared to the second. This probes that water molecules preferentially relax at the pore walls rather than in the bulk liquid. In this particular framework, one T_2 linearly depends on the ratio S/V in Eq2.1 and this equation may reveal some characteristic features of the porous network.

When surface relaxation dominates bulk relaxation, in the a single spherical pore system filled with water, the absolute pore size ($S/V = 3/r_p$) can be directly inferred from the value of $T_{2,meas}$ as:

$$T_{2,meas} = \frac{r_p}{3\eta_{2,surf}} \quad (2.2)$$

The model of a single pore may be extended to a system of multiple pores under specific pore network connectivity conditions, [137, 142]. Particularly, in the limiting case of isolated pores or porous structures with small throat pore size (the pores being weakly couple), the total magnetization can be written as the sum of the magnetization of all individual pores, each with their own relaxation time $T_{2,i}$ and volume V_i , as $\sum_i V_i \exp(-t/T_{2,i})$. Finally for a continuous pore-size distribution this sum may be converted to an integral over the whole range of T_2 within the sample and the relaxation function for the nuclear magnetization is then the Laplace transform of the probability distribution of relaxation rates $V(T_2)$ (which gives the volume fraction of pores with their relaxation time T_2). Hence in this situation every pore contributes to the total magnetization with an amount proportional to its volume. This case is however very specific and usually applies to sedimentary rocks; in this study, we measure the spin-spin relaxation in porous media made with close packings of beads; in this case, the ratio S/V constitutes a complex averaging of the underlying heterogeneities in the pore domain (throat pores and pores) and masks the true distribution of pore-scale properties. However, the volume fraction of particle may be expressed as $\phi = \Omega_p/\Omega$ (where Ω is the apparent volume of the sample and Ω_p the volume of particles), therefore $S/V = S/\Omega_p \cdot \phi/(1 - \phi)$. Therefore, for monodisperse spherical beads of radius R , similarly to Eq2.2, in the framework of surface relaxation Eq2.1 may be written:

$$T_{2,meas} = \frac{R}{3\eta_{2,surf}} \cdot \frac{1 - \phi}{\phi} \quad (2.3)$$

And the mean distance between particles may be probed trough ϕ . We use a CPMG (Carr-Purcell-Meiboom-Gill, [143, 144]) sequence over the whole sample (volume of $\sim 1cm^3$) to measure $T_{2,meas}$. Specifically to this sequence, the dephasing of the spins after the spin echo is not different from the dephasing of the spins directly after the 90° pulse, except that the magnetization has decreased by an amount of $\exp(-t/T_2)$ as seen on Fig2-5, the same rephasing action as done with the first 180° pulse can be done again. If a second 180° pulse is applied at a time 3τ , a second spin echo will appear at a time 4τ . Again, for an ensemble of static spins, the spin-echo intensity is not influenced by magnetic field inhomogeneities, but only by the transverse relaxation mechanism. Typical numbers of 180° pulses and spin echoes are between 64 and 1024. This way of measuring T_2 is much faster and accurate than the repetitive Spin echo with increasing interpulse time. However, a simple-echo sequence with variable echo time may be of better practice if very short relaxation times need to be recorded, as time sampling provided at short times by CPMG sequence is very crude.

v. 1D profiling

Unidimensional profiles of proton density within a sample may be obtained through the various sequencing techniques earlier described when coupled with a spatial encoding method. In our case, because short relaxation times need to be recorded, we use a dual Spin-Echo profiling sequence; its architecture is illustrated on Fig2-6. To measure the local proton density $\rho_0(z)$ with a resolution δ_z within a field of view Δz along the vertical axis z , one technique consists in applying a constant field gradient (G) to the whole sample in the desired direction during the collection of the NMR signal during time intervals centred on Echo times (see Gradient 2 and 3 in Fig2-6). Note Gradient 1 in Fig2-6 represents half of gradients 2 and 3, and is made necessary to produce gradient echoes at desired times. Along the z axis, the magnetic field then becomes $B_z = B_0 + G \cdot z$ and $B_z = G \cdot z$ in the rotating frame. This results in a linear variation of potential resonance frequencies in that direction and in this rotating referential: $\omega_{0z} = \gamma B_z$. This gradient in magnetisation acts to setup a one-to-one correspondence between the resonance frequency and spatial position (this is known as frequency encoding). Finally, the recording of a NMR spectrum during gradient application provides a 1D picture of the sample (concentration profile), simply converting the frequency axis into space coordinates.

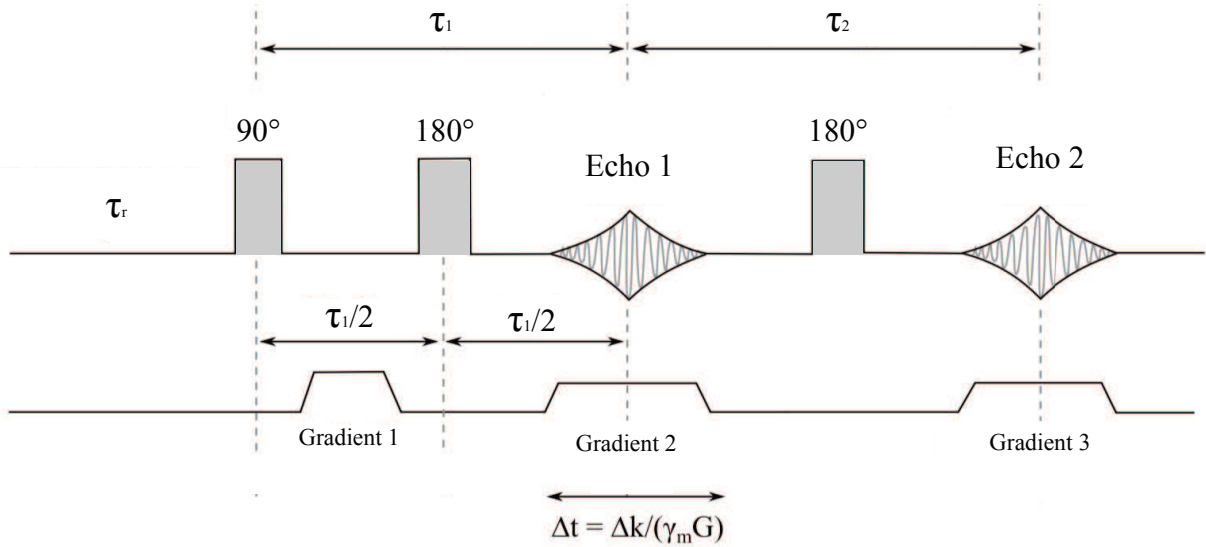


Figure 2-6: Architecture of the dual Spin-Echo sequence providing unidimensional proton concentration profiles on the vertical or horizontal axis of our samples; all parameters are described in the text.

Going into details, when the NMR signal is recorded, it fills up a mathematical space called the Fourier space or K-space, over a zero-centered domain Δk with a sampling step δk . During acquisition, the current position in k-space is related to measuring time through this space through $k(t) = \gamma G(t - t_{echo})$. The K-space is not directly readable but contains all the different information necessary to form the image of the sample. The K-space links to the acquisition space (real space); specifically, the spatial resolution (δ_z) and field of view of acquisition (Δz) are linked to their counterpart within the K-space by the Nyquist relations as:

$$\Delta k = \frac{2\pi}{\delta_z} \text{ and } \delta k = \frac{2\pi}{\Delta z}$$

Recorded signal in the rotating frame at a given echo time may be written:

$$\tilde{s}(k) = \int \rho(z) \exp(ikz)$$

Where $\rho(z)$ is the 1D proton density at echo time, possibly diminished by relaxation effects. Note that $\tilde{s}(k)$ constitutes the Fourier transform of $\rho(z)$ and the latter can then be obtained through an inverse Fourier transform (IFT) and taking the norm of the result.

In order to compensate signal loss due to relaxation, the dual echo sequence in Fig2-6, measures two echoes at τ_1 and $\tau_1 + \tau_2$, thus yielding two profiles $\rho_1(z)$ and $\rho_2(z)$ corresponding to the signal of protons that has relaxed over these periods of times respectively.

In this study, the correctness of the (quasi-) exponential assumption for signal decay in each single pixel was verified experimentally. Using a sequence with a larger number of echoes, the evolution of NMR signal intensity for relevant echo times was followed for a few pixels, in the case of a partially desaturated sample which seems to us the most critical case. It was seen that for any given pixel, recorded data can be accurately fitted by a decreasing exponential function, within the noise level. Therefore, for a mono-exponential relaxation in each layer, we obtain:

$$\begin{aligned} \rho_1(z) &= \rho_0(z) \exp\left(-\frac{\tau_1}{T_2}\right) \\ \rho_2(z) &= \rho_0(z) \exp\left(-\frac{\tau_1 + \tau_2}{T_2}\right) \end{aligned}$$

Where $\rho_0(z)$ is the unbiased proton density to be determined. In order to remove the contribution of spin-spin relaxation, the proton density is extrapolated using the following formula:

$$\rho_0(z) = \frac{\rho_1^2(z)}{\rho_2(z)} = \frac{\rho_1(z)^{\frac{\tau_1 + \tau_2}{\tau_1}}}{\rho_2(z)^{\frac{\tau_1}{\tau_2}}} \quad (2.4)$$

Note that this formula still provides a fair quantitative correction if T2 exhibits slight fluctuations inside each sample slice. Precisely, the extrapolation formula (Eq2.4) is not adequate when each slice in the sample exhibits a large distribution of various T2 values. However, provided echo times are short regarding the shortest relaxation time in the sample, it can be shown that Eq2.4 still performs close to a linear interpolation:

$$\rho_0(z) \approx \frac{\tau_1 + \tau_2}{\tau_2} \rho_1(z) - \frac{\tau_1}{\tau_2} \rho_2(z) \quad (2.5)$$

It is then still able to provide reliable estimates of $\rho_0(z)$. In our work, all extrapolations were made with Eq2.4. An Scheme for the resulting measurement is presented in Fig2-7.

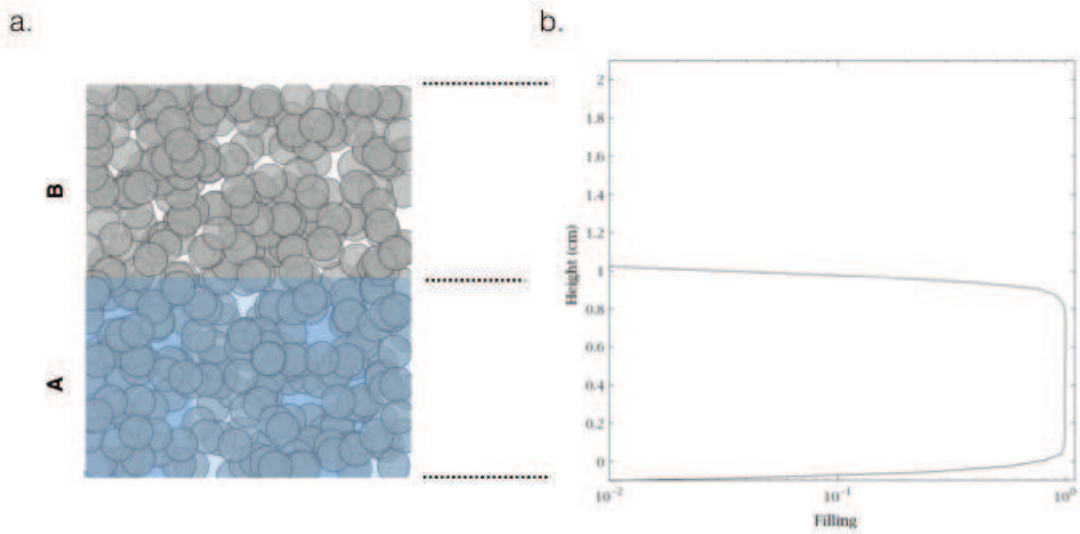


Figure 2-7: (a) Scheme for a porous media half filled with water, part (A) is filled, (B) is dry. (b) corresponding 1D NMR profile spotting the water concentration along the z Axis of sample (a). A dual Spin Echo sequence is used for the measurement (see text above). Filling is complete when the saturation is equal to 1.

vi. High resolution for 1D profiling

In this study, great attention is spent to measure 1D profiles at the highest resolution achievable for all samples. In this section we describe our approach toward this goal, note that the resolution is limited by the intrinsic relaxation properties of the sample and therefore varies from one sample to the other. Here we present the most critical case (highest resolution reached overall) but the same scheme was followed to determine the experimental parameters in all measurements performed. The experiments are performed at the magnetic center of our gradient coil (a BGA26 by Bruker, 26 cm inner diameter), which guarantees minimal profile distortion due to possible gradient nonlinearity (at least well under our space resolution). The gradient strength used for highly resolute experiments is $G=40\text{mT/m}$ which is actually close to the maximum gradient strength available on our hardware. We used $500\mu\text{s}$ stabilizing time on the horizontal axis and $300\mu\text{s}$ on the vertical axis and freshly tuned preemphasis which removes eddy effects at the end of this stabilizing time. Our echo time (which also more or less corresponds to the time length of each echo recording) reached a minimum of $\sim 8.4\text{ms}$, which according to the Shannon rules provides the theoretical space resolution:

$$\delta_{th} = \frac{2\pi}{T_E \gamma G_z} \approx 70\mu\text{m}$$

This estimate is however theoretical only, and may be impeded by field inhomogeneities through the sample due to magnetic susceptibility contrasts between the sample, air, and the setup. Prior to the experiment, our magnetic field was shimmed to get a $\Delta f = 50\text{Hz}$ large spectral line for our sample. The blurring to be expected on our NMR profiles due to field inhomogeneities is then:

$$\delta_{blur} = \frac{2\pi\Delta f}{\gamma G_z} \approx 30\mu m$$

Therefore, the maximum effective space resolution on our data may be estimated as:

$$\delta_{eff} = \sqrt{\delta_{th}^2 + \delta_{blur}^2} \approx 76\mu m$$

Our measurements were not subjected to any T_1 weighting, because the recycling delay between sequences (τ_r , see Fig2-6) was always set to 5 times the spin-lattice relaxation time in our sample at the beginning of the experiment (and this time was not prone to increase during sample drying).

vii. Smoothing method for 1D profiling

If great care was taken to use appropriate echo times with regard to the T_2 values of our samples, the limitation of the Dual Echo measurement is inevitably reached due to the couple effects of the process dynamics (offering a limited time to perform the measurement) and the reduction in proton content per layer within the material (water) during drying. In fact, the joint action of these phenomena gives rise to delicate measurements, where a minute trade-off between sequencing parameters (resolution, accumulation, sequencing time ect.) is needed to conserve a proper Signal to Noise ratio (SNR) on the profiles. Indeed, the need to tune parameters from one profile to the other may appear at very low moisture content. Therefore, when needed, it is useful to smooth the profiles to enhance the SNR to interpret the shape of the profiles. We smooth our profiles taking great care for them to conserve the closest shape to their original's i.e the result of this smoothing is presented in Fig2-8 and one can observe that the red line (smoothed profile) closely describes the shape of the raw profile (black line), in a log-log representation.

In practise, this filter corresponds to convolution by means of a Gaussian distribution ($g(z) = \exp(-z^2/2\sigma^2)$, where σ , the standard deviation of the Gaussian, is empirically set to 1 to 1.75 pixels in this study). Since the amplitude of measured profiles may suffer base-line overestimation at very low SNR, this filter is applied to the complex signal of each echoes before their amplitude is treated and prior extrapolation. Note that when this filter is applied, the resolution of the profile can be considered blurred and the new resolution is $\delta_{G-blur} \sim 2\sigma\delta_z$.

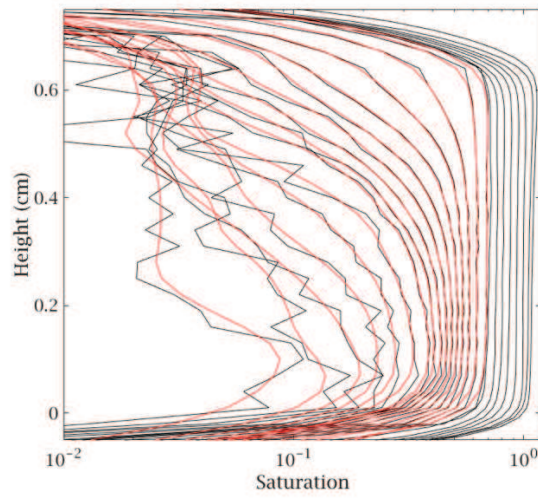


Figure 2-8: 1D profiling experiment performed on a sample made with 80nm particles during desiccation (black) raw profiles we (red) profiles smoothed with the Gaussian filter earlier described. On the last profiles the $\sigma = 1.75$. Time between profiles for ~ 35 min initial spatial resolution $\delta_z \sim 275\mu\text{m}$.

B - Materials

In this study we synthesize model porous media aggregating spherical colloidal silica particles together and sintering them. We also work with cellulose sponges. In all cases water is used as the liquid phase, protocols and measurement set-ups are described below.

1 - Synthesis of model nano-porous soft gels

i. Aggregation of colloidal particles

Colloidal gels were prepared by adding a solution of sodium chloride (0.5mol/L) into a suspension of Ludox SM-30, HS-40 or TM-40 (initial particle volume fraction $\phi \sim 15\%-23\%-23\%$ respectively) made with monodispersed silica beads of 6-12 or 40nm diameter respectively, in water.

When embedded in water silica particles become submitted to 2 dominant forces: the attractive Van Der Waals forces due to their sub-micron size and, because they become negatively charged in water (due to the dissociation of silanol groups at their surface), the repulsive electrostatic interactions that enable particles to repel each other (see Fig2-9). According to the DLVO (Derjaguin, Landau, Verwey, and Overbeek) theory, [144], the ions adsorbed at the surface of colloidal particles suspended in water tend to diffuse slightly and counter ions tend to approach the particles, thus forming a so-called electrical double-layer (see Fig2-9) which more or less represents the distance of interaction between two neighbouring particles. The double layer thickness (κ^{-1}) is expressed as:

$$\kappa^{-1} \sim \sqrt{\frac{\epsilon_r \epsilon_0 k_B T}{2 N_A e^2 I}} \quad (2.4)$$

where I is the ionic strength of the electrolyte (mol/m^3), ϵ_r the permittivity of free space, ϵ_0 the dielectric constant, k_B the Boltzmann constant, N_A the Avogadro number, e the elementary charge and T the temperature of the electrolyte. This double-layer prevents the particles from a further approach which would lead to strong aggregation through van der Waals attractions. When salt is added in the suspension of charged particles, more counter-ions become available therefore the ionic strength (I , see Eq2.4) of the solution increases which reduces the double-layer thickness (κ^{-1}) and thus screens electrostatic interactions between particles; the particles can therefore start to aggregate. The higher the salt concentration in this electrolyte, the higher rate of aggregation and the formation of the gel phase [145]; up to a point where a thixotropic behaviour is observed (over 0.7mol/L).

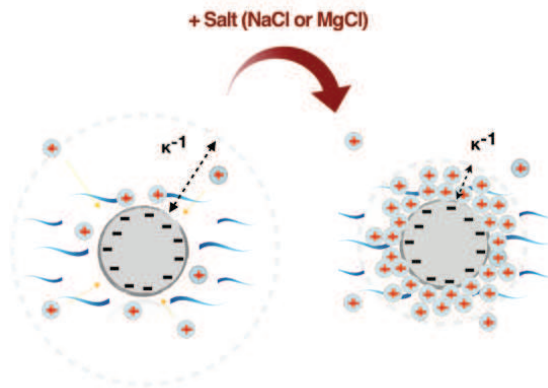


Figure 2-9: Scheme for the evolution of the electrical double layer thickness κ^{-1} (outer diameter in dashed grey line) with ion concentration within an aqueous suspension.

Therefore, to obtain a fairly homogeneous final gel structure i.e. avoiding structural heterogeneity possibly caused by local gradients of rate of aggregation (sedimentation not applying here), we dissolved the desired quantity of salt into a volume of water resulting in particle volume fractions ranging from 5% to 20% after mixing the two homogeneous phases together. After preparation, the mixtures were poured as 5 mm layers in glass Petri dishes (10 cm diameter) and left at rest for their respective gelation time. The gelation time (T_g) is determined following the behavior of G' and G'' respectively the elastic modulus (stress to deformation ratio) and the loss modulus (the viscous stress component in oscillations at low deformations), of the samples with time through steady rheology oscillation experiments ($\gamma=0,0003$, $f=1\text{Hz}$) on an Anton Paar rheometer with a 20mm plate-plate geometry and a 0.5mm gap. These measurements enabled to record the phase transition within the sample, specifically the moment at which a network of aggregated particles starts to span the sample and an elastic behavior of the material builds up, since this corresponds to a transition from a simple liquid behavior (with large G''/G' ratio) to a solid behavior (with large G'/G'' ratio). We define T_g as the time required for G' to exhibit a clear steady state evolution. This definition means that beyond T_g the gel structure negligibly evolves spontaneously. The typical values for G' reached in this regime are $10^3 - 10^6 \text{ Pa}$ depending on the initial particle volume fraction of the gel. On Fig2-10, is presented the typical aggregation we record for such an experiment. One can observe a first phase during which G'' is superior to G' , meaning that likely particles start pairing together but do not form a solid network throughout the sample yet (the length of this phase is seen dependent on the initial particle volume fraction, the higher, the shorter); later on a G' overshoot is recorded, G' crosses G'' , a solid network is formed and spans the whole sample. This structure further consolidate with time (G' increases) until a plateau appears for both parameters and T_g is reached. Note that the increase of G' is not linear with time, this is supposedly due to aggregation of bigger and bigger clusters together, [145].

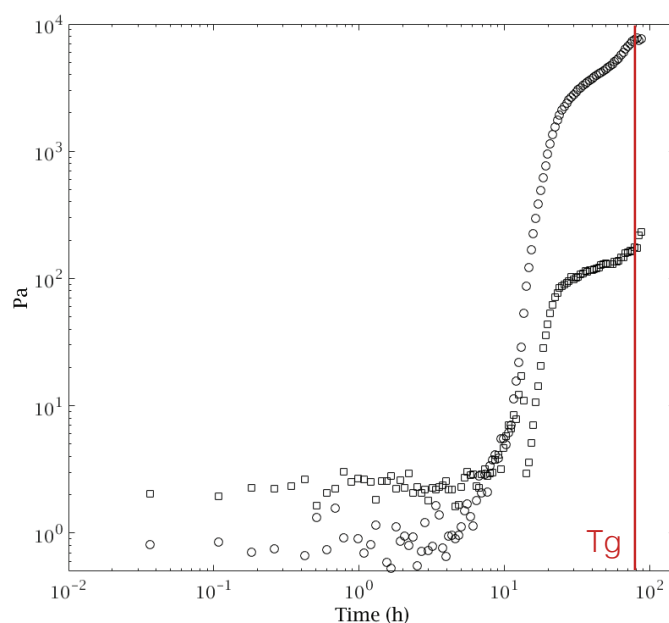
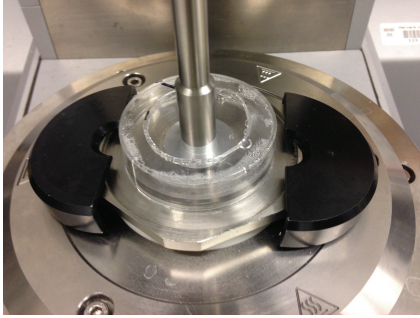


Figure 2-10: Evolution of the (circle) storage and (square) loss modulus with time during aggregation of 12nm silica particles with initial volume fraction of 5%; T_g is indicated by a red continuous line. Steady rheology oscillation experiments $\gamma=0,0003$, frequency $f=1\text{Hz}$, plate-plate geometry 20mm, gap 0.5mm.

Once T_g is reached we dialyze the gels prior to drying, extracting 97% of the salt initially incorporated and thereby avoiding phenomena generated by the presence of sodium chloride in the electrolyte during drying (crystallization, advection etc.). To dialyze a gel, we cyclically added deionized water on top of the formed colloidal gel, waiting the necessary time for the concentration of sodium chloride to homogenize throughout this new biphasic system, and then carefully removed the fluid on top; the dialysis usually needs a few days of time to be completed and 10 cycles. Each dialysis enabled us to remove roughly half of the quantity previously contained in the gel. The amount of NaCl extracted during each dialyze was evaluated by performing conductivity measurements on the dialysate; the mass calculated steadily corresponding to the 1/10 of grams to the mass measured further drying this same extract; the conductivity generated by the silica particles in water being negligible in our case.

We also managed to dialyze the sample on the rheometer during the measurements thanks to a special set up allowing a water bath of the geometry (see Fig2-11 a): a plastic dish is designed and sealed to the geometry with epoxy; water can be added and removed with a pipette. As seen in Fig2-11b, we recorded a drop of about 25% of the G' value when water is incorporated in the curve, likely due to a structure modification of the gel generated by the osmotic pressure of deionized water in the bath, but afterwards no further evolution of G' . This proves that we were able to keep a structural strength of the same order of magnitude as the un-dialyzed sample; this dialysis process does not significantly alter the sample.

a.



b.

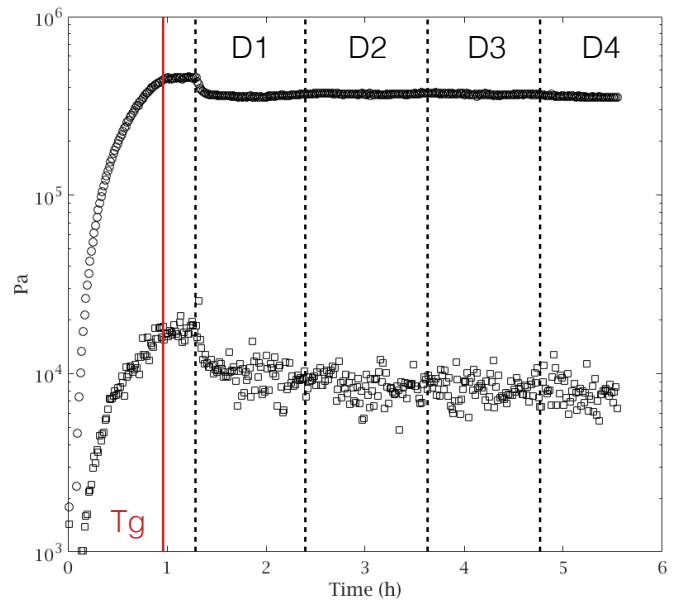


Figure 2-11: (a) Dialysis set-up on the rheometer, (d) Evolution of the (circle) storage and (square) modulus with time during aggregation first (up to T_g , the gelation time) and during the dialysis protocol, for a 12nm silica particles with initial volume fraction of 20%. Four successive dialysis are performed and indicated by dashed lines (D_i). Steady rheology oscillation experiments $\gamma=0,0003$, frequency $f=1\text{Hz}$, plate-plate geometry 20mm, gap 0.5mm.

2 - Structure of gels

To further characterize our gels, we look at the relaxation properties of their porous network with NMR relaxometry. In this section, the CPMG sequence we use features a shortest echo time at $75\mu s$ and a logarithmic distribution of Echo times up to $\sim 3sec$; 64 to 128 scans were performed for signal accumulation. Specifically, during desiccation, the gels we study shrink and end up reaching a close packing fraction (seen later on in Chap.2), we first start by characterising the evolution of the porous network during contraction.

i. Evolution of the pore network during gel contraction

Drying a gel made with 12nm particles at $\phi_0 = 19.84\%$ in the NMR tube and using the bulk NMR CPMG technique earlier described (see Chapter 2 -A -2 - iv.), we follow the evolution of the pore structure during contraction. Note that during this phase the sample remains entirely saturated (result demonstrated in the Chapter 3) and spin-spin relaxation mainly occurs at the pore-wall $T_{2,meas} \ll 2.5sec$ (as seen in Fig2-12). Therefore, the framework of Eq2.3 applies and the T_2 value we measure linearly relates to the ratio V/S.

Since our gel may be considered as a loose (initial state) or compact (final state) cohesive and saturated bead packing, its liquid and pore network may be considered as highly connected, [146], therefore, the T_2 distribution observed in Fig2-12 constitutes a complex average of the heterogeneities in the pore network (throat pores and pores) which masks the true distribution of individual pores to the global magnetisation (see Chap.2-A -2 - iv. therefore, V/S corresponds to an average in the whole domain explored by water molecules within the sample, within the time frame of the experiment. This measurement may however be useful to characterize gel contraction, estimate the volume fraction of particles within the sample when contraction stops and obtain an equivalent pore size.

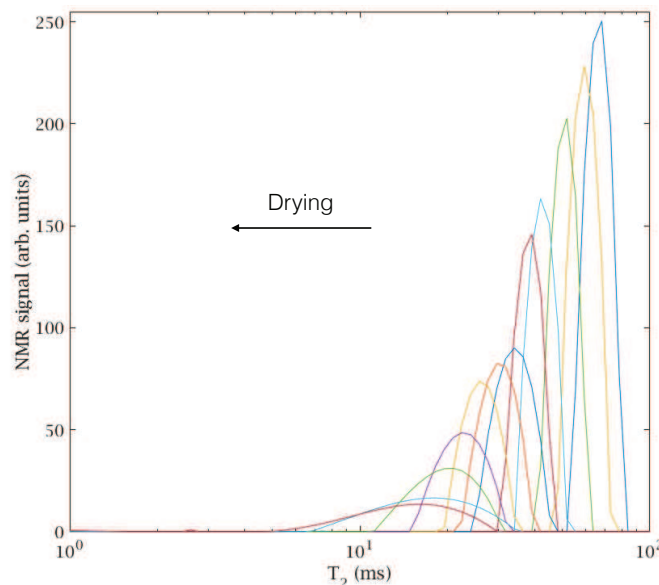


Figure 2-12: (a) Evolution of the T_2 spectrum of a gel made with 12nm particles and $\phi_0 = 20\%$ during drying. Only the phase of contraction (shrinkage) is shown, the measurement step is 0.5ms, between every measurement 22min is elapsed.

Fig2-12 shows the T_2 distribution with regards to the NRM signal (arbitrary) within the gel sample at different stages during the shrinkage process of the material. Note that details on the numerical Inverse Laplace transformation performed is given in [147].

On this main graph, we observe a single NMR peak on the whole T_2 spectrum measured at each stage of the drying process (note that Fig2-12 only presents the first 100ms of the spectrum as water does not relax slower in the system). Also, the amplitude of this peak decreases with the advance in desiccation which is relevant to liquid water evaporating thus protons leaving the system with time. Furthermore, this peak (see its center) displaces to lower T_2 values with drying. At last, we observe that the width of each peak remains rather narrow (smaller than half a decade) with regards to the T_2 distribution regardless of the stage of desiccation.

In fact, the width of NMR peak could be related to heterogeneities in pore sizes within the gel as well as a degradation of the SNR (typically encountered when loosing moisture content). In standard measuring conditions (about 100 measured echoes in raw relaxation data, with about 100 signal to noise ratio on the first data point), the contribution of measurement noise to the width of the NMR peak is about one third of a decade [148]. Since our peaks are no wider than this, our data suggest a very narrow level of heterogeneities on our sample, although this cannot be precisely quantified.

Before drawing any conclusion on the sample structure, it is useful to probe the length scale (L) considered for this experiment. The sequencing time being close to T_2 , the equivalent diameter of the volume explored by a molecule of water within this timeframe may be approximated to $L \sim \sqrt{(6D_w T_2 / \tau)} \sim 10 \mu m$. Therefore, we conclude that at any stage of the drying process, the presence of a single narrow NMR peak probes the homogeneity of the porous structure over a length scale of $10 \mu m$ and finally the contraction of the porous media can be considered homogeneous at higher length scales. Let's now look at the additional structural information one can yield from this measurement.

The surface relaxivity is assumed to be constant during drying (as seen later on in Chapter 4, the gel remains saturated) and controlled by the surface properties of the pore walls only, supposedly unchanged during the process. Therefore we may compute the relaxivity parameter from Fig2-12 and Eq2.3 (as $T_{2,meas} = 67ms$ and $\phi_0 = 19.84\%$), and find $\eta_{2,surf} = 1.19 \times 10^{-7} m \cdot s^{-1}$. Eventually this measurement grant us with the final volume fraction (ϕ_{final}) when contraction stops (as $T_{2,meas} \sim 10.9ms$, and from Eq2.3, $\phi = R / (3\eta_{2,surf} T_{2,meas} + R)$): $\phi_{final} = 60.85\%$.

Note that the gel is very compact in its final stage as ϕ_{final} is very close to 64% (the maximum packing fraction for spheres in 3D); therefore the equivalent pore size may be approximated to the dimension of the gap between 4 spheres closely packed in 3D (geometrical considerations), i.e. $r_p = R\phi_{final} / 6(1 - \phi_{final})$, so to say $r_p \sim 2nm$.

We conclude that drying of those gels results in a homogeneous contraction leading to a compact homogeneous final structure.

ii. Gels substrates

In this study we used gels made with 12nm particles (in Chapter 3) to measure and model deformation in porous media during drying. To influence on these deformations, one way is to tune the friction between the gel and its substrate (see Chapter 3). To do so we chemically treat or coat the walls of the petri dishes that contain the samples when it is needed. Gels are prepared in glass petri dishes of 10cm outer diameter; without any treatment the glass walls of the dish constituted a highly adhesive substrate; a very low friction substrate (later called non-adhesive substrate) was designed by coating the dish with a fluorinated grease (KRYTOX 205 from Dupont); lastly a chemical treatment of the dish walls with trichlorododecyl silane gave a highly hydrophobic substrate (later called semi-adhesive) seen to exhibit adhesive properties intermediate between the two previous substrates. To sum it up, 3 different substrates are designed to study the influence of the gel-substrate adhesion on the deformation of the gels during drying.

iii. Strain sensitive substrate

To yield qualitative information about the distribution of the local strains between the gel and the substrate and help us suggest an origin to the deformation of the gels we observe during drying, we designed a strain sensitive substrate. We do so by pouring a soft crosslinked gel (PDMS) into a glass petri dish, further gluing a thin (2mm thick) birefringent polymer sheet placed on top of it. Special care is taken to reduce the pre-constrain on the birefringent sheet. This new substrate sticks to the colloidal gels and is seen to exhibit adhesive properties intermediate between the semi-adhesive and adhesive substrates previously designed (see just above). As neither the colloidal gel nor glass is birefringent, if polarised light is projected through the system and strain is applied to the substrate, the polymer sheet will dipphase light and the strain intensity can be visualised thanks to a polarizer lens and a camera (set up described in detail in C -1 - iii. Here we only use black and white imaging, so the main result we yield is the location of the strain.



Figure 2-13: Picture of the petri dish (glass, 10cm outer diameter), containing the PDMS gel at the bottom and the birefringent polymer sheet on top (yellow color).

3 - Synthesizing model porous media

i. Viscous sintering, from gels to homogeneous porous media

We remarked that once our gels are completely dry, cohesion remains between the particles of the solid matrix, the latter is not friable. What is more, the smaller the particles, the higher the final cohesion in the material. This cohesion most likely stems from sintering (formation of a cohesive solid material from fragmented portions of this same material) occurring during evaporation. In fact, viscous sintering was seen to occur during evaporation of aqueous suspensions of sub-micron silica particles, [149-151]. Due to densification (shrinkage) through capillary forces the particles are pushed closely against each other triggering diffusion of the solid boundary onto the neighbouring particle. This process is called “necking”, it is characterised by the ratio of the radius of the neck disk (x) to the radius of particle (R) and creates a solid bond between the particles (see Fig2-14a). The higher this ratio the higher the cohesion. Specifically, for a system of 2 silica particles embedded in water and drying, sintering follows the kinetics described by Kuczynski, [150]:

$$\left(\frac{x}{R}\right)^3 \propto \frac{Bt}{2R^2}$$

Where B is a constant specific to the mechanism of mass transport, [149,150] and depends on parameters such as the absolute temperature, the grain boundary diffusivity, the vapor pressure, the density of the liquid and its molecular weight etc. Note that for a system of the same chemical nature and considering a similar time scale, this equation points out that the bigger the particles the lower the sintering which confirms our experimental observation on cohesion of materials made with different bead sizes. Let’s look at the surface of our sample made with 40nm particles under the SEM (see Fig2-14b).

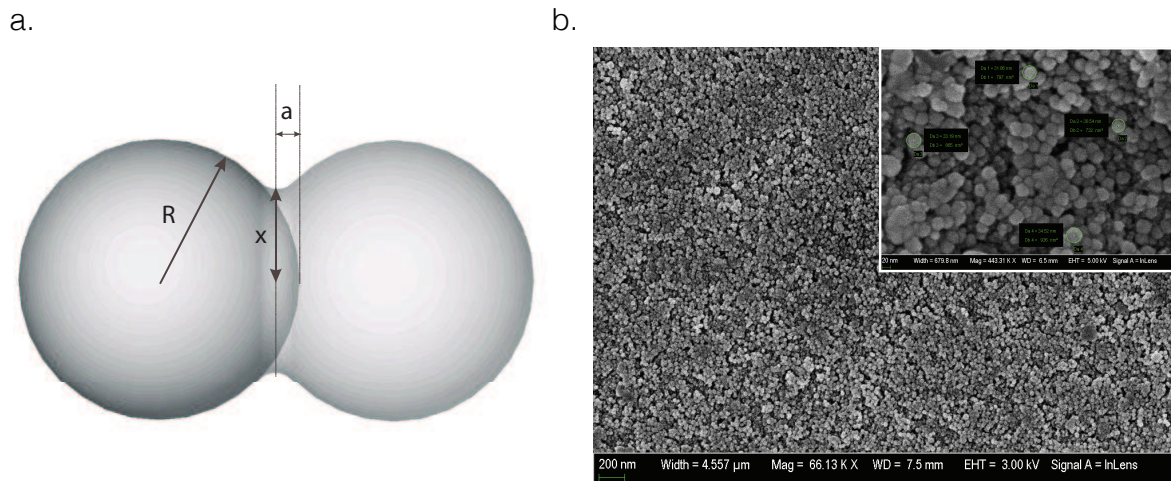


Figure 2-14: (a) Scheme for the formation of a neck during viscous sintering between 2 silica particles, [149]. (b) SEM image of the surface of our gels made with 40nm particles, inset zooms in a cavity of the main picture.

Fig2-14b presents a SEM observation of the surface of a 40nm silica gel when fully dried. We observe that particle packing is very dense (Figure2-14b). The distribution of particle sizes seen in the inset is measured narrow, oscillating around 34nm+/-7% (particle size can be measured on the microscope directly, green circles in the inset show 4 of these measurements). Moreover, looking

closer, at the particle level, we distinguish the existence of bridges between particles, corresponding to the “necks” classically formed during viscous sintering. In this study, we use this technique to synthesise model porous medium with silica particles ranging from 1500nm to 6nm diameter. To avoid surface defect potentially occurring from advection of particles during drying of suspension (compaction front, [133] and interface buckling, [68,91]), we first consolidate the particle network as a gel (see B-1 - i.) and further dry these gels on a non-adhesive substrate (B-2 - ii.).

ii. Protocol for large particles

As mentioned above, we synthesise homogeneous and compact porous medium by drying aqueous colloidal silica gels, as during this process particles sinter (see previous section). When particles diameter $D < 40\text{nm}$, the protocol seen in B-1 - i. applies, however, when particles are bigger than 40nm, a different protocol is employed to obtain the gel phase; specifically because all particles larger than 40nm in diameter are provided anhydrous (by Fiber Optics Center). Therefore, we first disperse these particles in water and stir the suspension during 24h to obtain a homogeneous suspension. We then centrifuge the suspension at 5000rpm for 25min and yield a concentrated and wet packing from the induced sedimentation. Subsequently, we dilute this extract with an aqueous solution of magnesium chloride at 0.05mol/L to trigger aggregation (due to the high ionic strength of this salt, very low quantity is necessary $\sim 0.07\text{g}$ on average for a 60ml sample). The amount of solution added is computed so that the initial volume fraction of the mixture reaches $\phi_0 \sim 50\%$. Eventually, the mixture is placed in the same glass petri dishes (10cm outer diameter) treated with non-adhesive walls and rested until gelation is complete. Then samples are put to dry.

Note that, in this second protocol we do not dialyse our samples prior to drying and there are several reasons for this: as very little salt is incorporated ($\sim 0.07\text{g}$ on average) neither crystallisation nor advection of the salt (the Peclet number in our experiment is so low) should disturb the process; last but not least, as the samples are quite soft taking the salt out could alter their mechanical properties and trigger surface defects (see in Fig2-11b).

iii. Pore size distribution in model porous media

We study the T_2 distribution within the compact porous structures synthesized as it may reveal important information on their porous structures. We measure spin-spin relaxation for samples made with 6nm, 12nm, 40nm, 80nm and 750nm particles with the CPMG measurement earlier described, when samples are saturated with water. Fig2-15 presents the T_2 distributions obtain from this measurement for: samples made with particles $D < 40\text{nm}$ (see Fig2-15a) and particles $D > 40\text{nm}$ (see Fig2-15b). For the sake of clarity the NRM signal (S) is rescaled on its peak value (S_{max}). Note that we differentiate between these two sets of samples as the relaxation kinetics are seen to slightly differ from one set to the other; let's be more accurate:

First, one can notice that all peaks of Fig2-15 appear for T_2 values situated decades away from free water ($\sim 2.5\text{sec}$) therefore the process of relaxation mainly occurs at the pore walls in all samples (see Chap.2-A -2 - iv. and the framework of Eq2.3 applies. Since a single peak is observed, similarly to Chapter 2 - i. the porous structures of the samples can be considered homogeneous over a scale of 10microns (the tortuosity of the porous matrix and echo times being in the same

order of magnitude than previously). However, note that the values for the peak in T_2 for $D > 40\text{nm}$ are very close or smaller than the values measured for samples with smaller beads, which is unrealistic considering the similar compaction of the sample (computed macroscopically) measured in Table2-1 and the size of the beads. This slight discrepancy witnesses of a variation in the relaxivity of the silica particles, likely due to the different manufacturing process involved for their synthesis (different providers) and therefore slightly different surface properties.

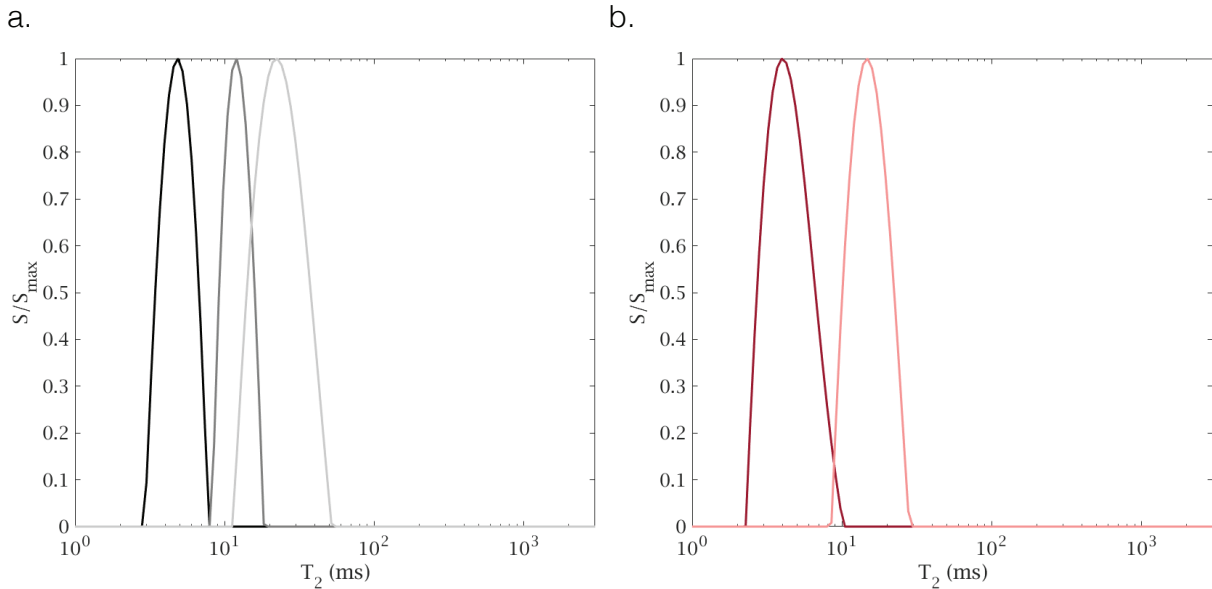


Figure 2-15: T_2 distribution in model porous media made with (a), (black) 6nm, (dark grey) 12nm, (light grey) 40nm; (b), (red) 80nm, (pink) 750nm particles.

Looking at the NMR peak in the initial state (not presented here) of the gels presented in Fig2-15a, similarly to Chap. 2 - i. one can deduce the final volume fraction of those gels in their compact state (results are presented in Table2-2). For the samples presented in Fig2-15b, the initial state of the gels was not measured with NMR, therefore the only information on compaction we yield is macroscopic. Finally, the compaction of the porous media we synthesized are gathered in the following table:

D/Compaction	Macro	NMR		Macro	NMR
6nm	57.0%	62.48%	300nm	53.0%	X
12nm	55.1%	60.9%	750nm	55.6%	X
40nm	55.1%	61.2%	1000nm	56.2%	X
80nm	55.3%	X	1500nm	56.3%	X

Table 2-1: Final compaction for each porous structure synthesized sintering them during drying depending on their particle diameter; these values are an average on at least tests (macro) computed from the dry mass and the apparent sample volume (NMR) computed from Eq2.3.

Note that we observe a slight discrepancy between the Macroscopic and NMR results but the compaction of all samples remains very high: $> 55\%$. We conclude that using the phenomenon of viscous sintering through densification during drying shrinkage, we are able to form homogeneous and highly compact porous media of the same nature.

4 - Sponges

In this work we also study cellulose sponges being soft materials responsive to drying stresses. Specifically, we study two different sponges, a green and a blue one; here we review their wetting properties, their pore size distribution while saturated and finally we image their dry solid matrix at the pore level.

i. Surface properties

When a $1\mu\text{L}$ water droplet is placed at the sponge surface, the green sponge absorbs it instantaneously (therefore clearly hydrophilic) whereas on the blue sponge the drop stays still with a high contact angle, measured to $65^\circ \pm 6.3^\circ$ (see Fig2-16a).

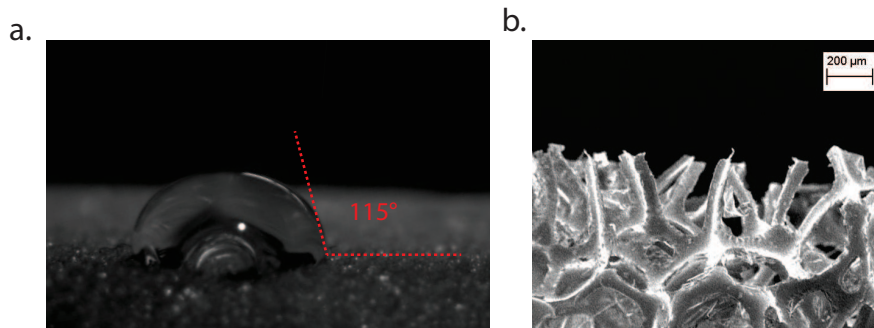


Figure 2-16: (a) contact angle between the blue sponge and a drop of water (25mg). (b) SEM (ultra 55) image of the surface blue sponge rugoses.

Fig2.16 shows the shape a water droplet adopts when it is put in contact with the blue sponge (a) and a side view of the surface of this sponge (b). In fact, surface roughness can play a significant role in the value of the contact angle we measured in Fig2-16a: as expressed by Wenzel, [96], the actual contact angle of a drop on a rough surface can be expressed as : $\theta_w = \cos^{-1}(\varpi \cdot \cos(\theta_m))$ where ϖ is the roughness parameter defined as $\varpi = 1 + L/100$ and L the characteristic length associated to the surface roughness. From the SEM picture in Fig2-16b showing a representative portion of the solid matrix of the blue sponge, one can measure $L \sim 520\mu\text{m}$ as an average on the height and spacing of the roughness details. Therefore we can compute that the actual contact angle is $\theta_w = 65^\circ$. Eventually we conclude that the blue sponge is also hydrophilic, but to a lower extent than the green sponge.

ii. NMR analysis

Similarly to Chapter 2 – 2 - one can decide to look at the pore size distribution within the sponges measuring their T_2 once fully saturated (see Fig2-17).

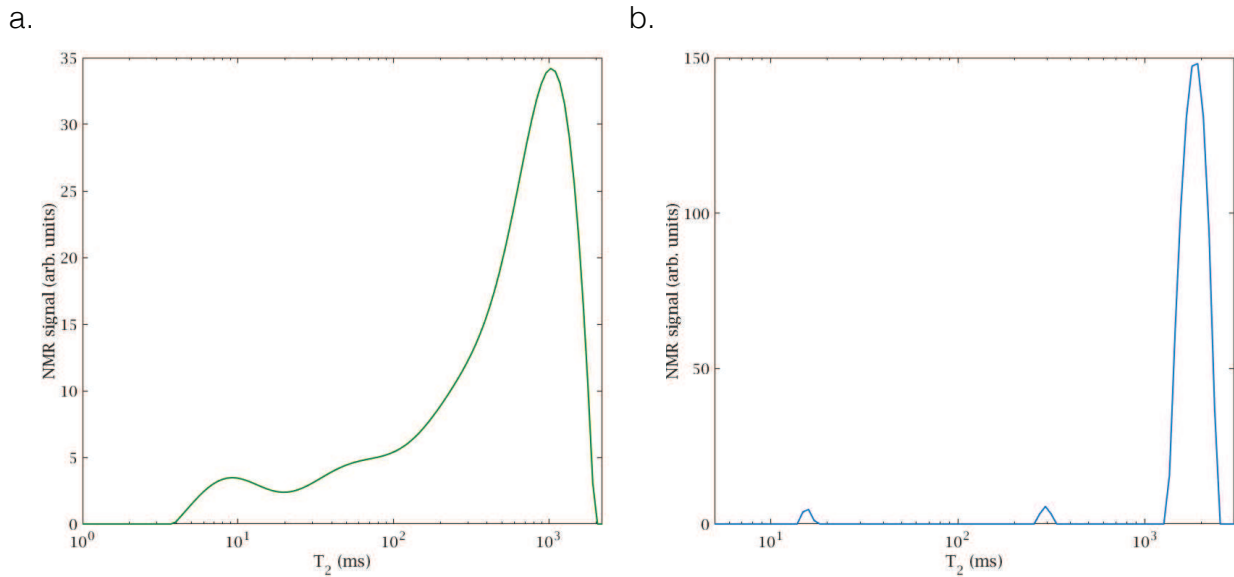


Figure 2-17: T_2 spectrum for (a) the green sponge, (b) the blue sponge, both fully saturated with water.

Fig2-17 shows the T_2 spectrum we measure from both samples with the CPMG sequence seen in A -2 - iv. (note that in Fig2-17, the amplitude of the NMR signal is arbitrary and therefore cannot be compared between the 2 graphs). For the green sponge, the framework of surface relaxation applies $T_2 < 2.5\text{sec}$ and therefore Eq2.3 applies. Due to the strong broadening of the peak, we can affirm that this material exhibits a large pore size distribution. However, looking at the blue sponge, the main NMR peak being located at T_2 values close to 2.5seconds, it seems like water does not relax at the pore wall. It is necessary to obtain additional information on pore sizes to further characterise both materials. Let's look at the sample macroscopically and measure pore sizes thanks to an image analysis software.

iii. Macroscopic pore size distribution

For the sake of simplicity (relevant to this analysis), we assume that the pores in both sponges are cylindrical. Following this hypothesis, we measure the size of the holes spotted at the sponge free surface (considered as a representative cross section over the whole sample) and compute the equivalent diameter of holes (considered as pores). Specifically, we use an image analysis software developed on MATLAB (see in Pore size analysis software in Annexes) to obtain the equivalent circular radius of the pore measured. This program uses the Least-Squares criterion for estimation of the best fit to an ellipse from a given set of points in the same plane. An adaptive thresholding algorithm helps to separate the foreground from the background with non-uniform illumination and outputs a binary file. Independent holes in the image, considered as pores, are then filled in white (see Fig2-18b). Eventually, the coordinates of the independent white surfaces are extracted and fit to the closest ellipsoid (see colourful ellipses on Fig2-18b). we convert the ellipses dimensions to an equivalent circular radius and we yield the equivalent circular pore size. Counting pores over the whole sample, we establish the pore size distribution of the material (see Fig2-18).

Note that heterogeneous illumination of the sample as well as change in the color of the surface (brightening) may introduce an error in the measurement.

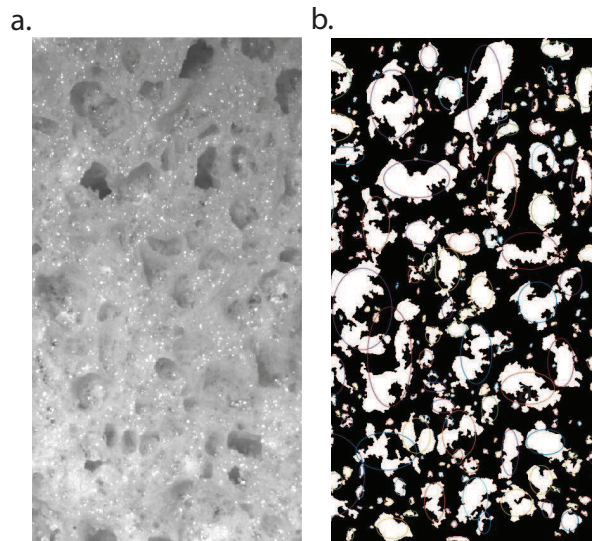


Figure 2-18: Example of pore detection and pore fitting from the software (a) represents the portion of the sponge analyzed (5.2cm x 3cm – photo cropped for size purposes) (b) detection and fitting results from the software.

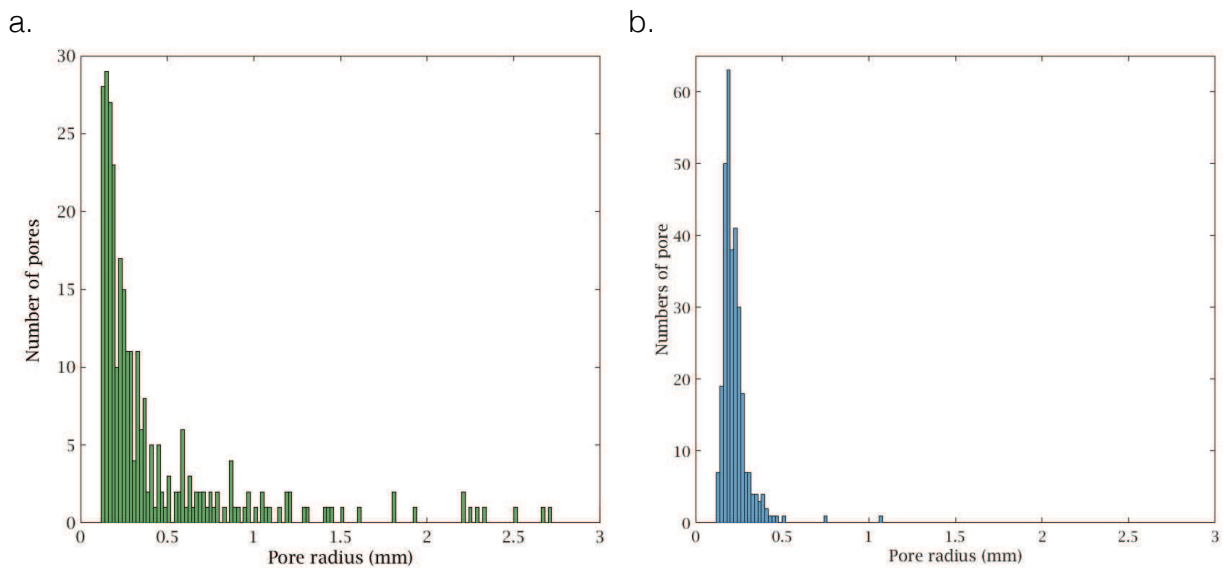


Figure 2-19: Histograms of the pore size distribution for the two samples in their initial state (sponges fully saturated), for the (a) green sponge, (b) blue sponge. The bandwidth for the histograms is $50\mu\text{m}$, a pixel size being approximately $5\mu\text{m}$.

Fig2-19 presents the number of pores spotted at each sponges' free surface depending on their radius in a histogram representation with a bandwidth of $20\mu\text{m}$; note that a pixel is $5\mu\text{m}$ wide and this measurement is performed when sponges are saturated. This figure shows the existence of a wide pore size distribution for the green sponge (see Fig2-19a) with pore diameter ranging from

6mm down to $100\mu\text{m}$; and a narrower pore size distribution for blue sponge (see Fig2-19) as we observe a large majority of pores at $500\mu\text{m}$ diameter.

If this measurement already yield great information on the pore structure, its resolution is limited due the set-up we used (detailed below in Chapter 2 -C -1 - i. that prevents to observe the finest details of the structure. To complement this study, we image the structure with an SEM.

iv. SEM Imaging of the porous structure

Here we use the FESEM Supra55VP earlier described (see A -1 - this measurement enables to look at surface details once samples are dried. If the green sponge contracts up to 20% during drying, the contraction of the blue sponge is insignificant and lies under a couple of percent (seen later in Chapter 3). In the following figures we present images of sample in their final stage (dry), therefore contracted. Dry imaging is performed under vacuum ($\sim 100\text{Pa}$) and grants access to tiny surface details for both samples.

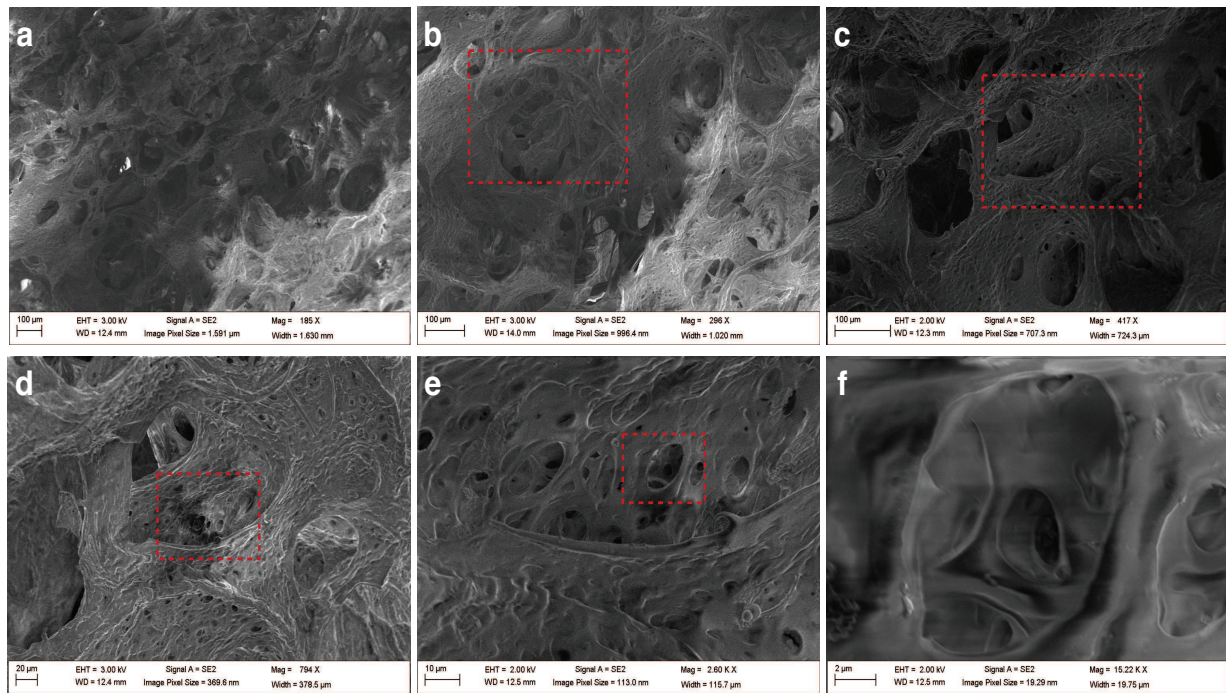


Figure 2-20: SEM images of the solid matrix of the green sponge once the sample is dry. Dashed rectangles indicated the areas we have zoomed in on the next picture. (a) is just a broader field of view from (b) in another area.

Figure2-20 shows the porous structure of the green sponge is a dense network of pores of a wide range of sizes (Fig2-20a and b); In Fig2-20a to d particularly, we observed that a lot of pores are in the range of $100\mu\text{m}$ and above. Now looking closer at the structure within the branches forming these pores we observe a very high density of tiny asperities (see Fig2-20e and d) of approximately $10\mu\text{m}$ diameter.

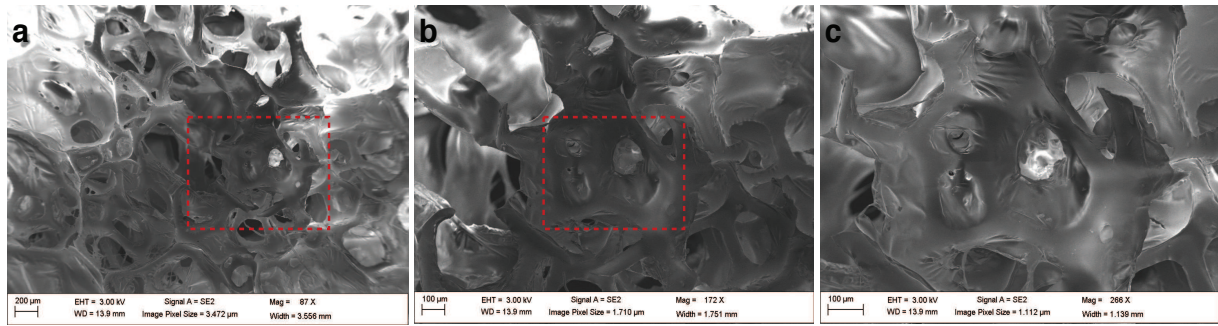


Figure 2-21: SEM images of the solid matrix of the dry blue sponge. Dashed rectangles indicate the area zoomed in the next picture.

Fig2-21 presents pictures of the structure of the blue sponge and shows that the pore size distribution seems quite narrow and to range between $500\mu\text{m}$ to $100\mu\text{m}$. Note these are consistent with the image analysis presented in Fig2-21.

Let's sum up our finding on the sponges' structures in the next section.

v. Sponges structures and relaxivity

We carried out a multi-scale study of the structure of both sponges with different measuring tools that gave consistent results. Image analysis of the surface of the samples showed that the green sponge exhibits a wide pore size distribution with pores ranging from 5mm to tenth of microns, specifically, a very high density of finest porosity is observed; whereas the blue sponge shows a narrower distribution mostly comprise between $500\mu\text{m}$ to $100\mu\text{m}$.

On one hand, the analysis of the NMR spectrum of the green sponge correlates to the macroscopic observations showing a continuous distribution of T_2 ranging from a couple of seconds (likely corresponding to the water within the big pores of the structure) to lower T_2 , precisely a thousand times smaller. Note that this range matches our optical observations and therefore this measurement shows that the relaxation in this sample is governed by surface effects. This is of particular interest as it may give the opportunity to look at the evolution of the water content within the different pore sizes during drying later on.

On the other hand, the analysis of the T_2 distribution within the blue sponge shows a dominating narrow peak situated right at the point of relaxation of free water, even if two very tiny peaks can be distinguish at lower T_2 , the location of this main peak put in relation to the pore sizes observed macroscopically tend to indicate that the spin-spin relaxation in the blue sponge mainly occurs in bulk and not at the pore wall. Note that the sponge has a low affinity with water and water does not relax at its surface, but these phenomena are not correlated. For the rest of the study, we assume that water does not relax at the blue sponge surface.

C - Set-ups

1 - Drying set-ups for gels and sponges

i. Regular drying

Convective drying is performed by blowing a controlled airflow (velocity and relative humidity) at the sample free surface. This is made possible by the following set up:

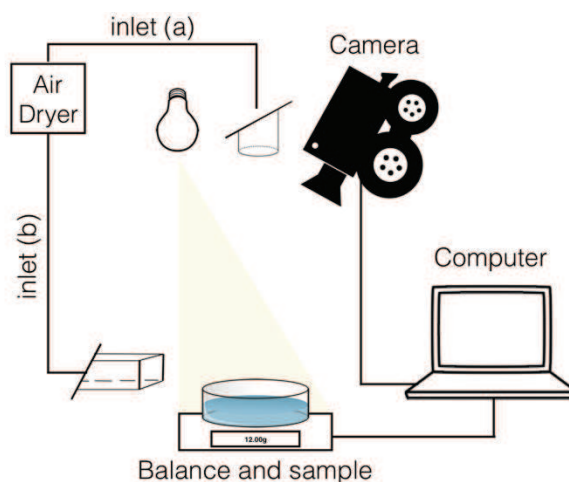


Figure 2-22: Drying set-up, the sample is lightened, weighted thanks to the balance; pictures are taken by the camera and air is blown either (a) perpendicular (b) parallel to the sample free surface.

The sample is put under a fiber optic light (not heating the sample); weight and pictures are acquired thanks to a high resolution (black and white) CMOS camera USB2.0 for Thorlabs and a precision scale both linked to a computer interface running a MATLAB acquisition code (see Image and mass acquisition software). In this study, the air can be blown in two different directions (this parameter is always mentioned), either perpendicular (turbulent flow) or parallel (laminar flow) to the sample free surface. When the airflow is blown vertically on the sample the air induces an additional force on the scale that induce a maximum mass data uncertainty of 0.07g in the range of airflow velocity studied. The relative humidity of the air is controlled by an air dryer and the flow velocity by a flowmeter.

ii. Drying set up in the MRI

Drying in the MRI is performed using the geometry of the tool. The latter is composed of a long tubular (1m long, 20cm diameter) sample holder going through the spectrometer magnet. We therefore designed a piece of acrylic material (no metal being allowed near the tool) enabling to hold our air inlet and guide the air on the sample (the air arrives perpendicular to the sample surface). Similarly, an air dryer was used, here placed outside the MRI room, not to perturb the measurement. This set up was used for all in situ drying experiment.

If NMR enables to spot the location of the wet interface within a sample in space, a critical information is the location of the free surface of this sample and how the two compare; this is of particular interest to measure sample thickness. We therefore place upon the central point of the sample a sealed tripod pot (3cm diameter) containing a solution with a similar NMR behavior; the sample to pot size ratio and the distance (3cm) between the pot and the sample are sufficiently large to negligibly affect the drying characteristics. Imaging the position of this pot provides the exact position of the sample free surface in time.

iii. Imaging strain during drying

As seen earlier on in 2.iii, we designed a dish equipped with a birefringent substrate to be able to image and locate strains at the gel-substrate interface. Birefringence polymer are strain sensitive polymers that diphase polarised light when they deform. One may simply use a polariser to recover the dephasing light and observe the regions where the gels pull on the substrate.

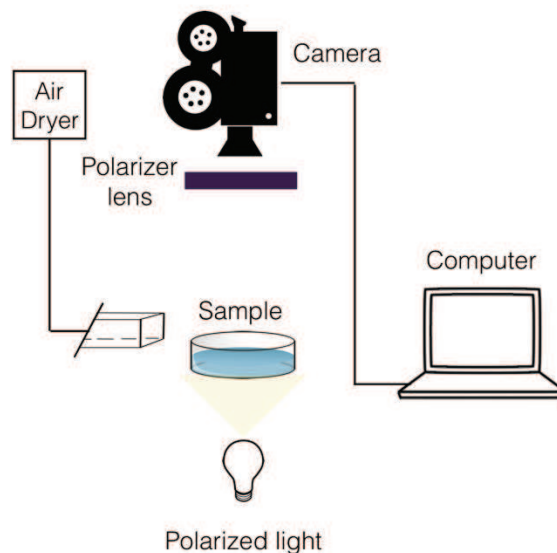


Figure 2-23: Set-up built to image strain at the gel-substrate interface thanks to a polarized light and lens

2 - Critical point dryer

We use this particular drying technique to eliminate all residue of water within our sample prior starting an imbibition test. Compounds which are in the critical point can be converted into the liquid or gaseous phase without crossing the interfaces between liquid and gaseous avoiding the damaging effects (due to surface tension mainly). The dehydration of the samples using the critical point of water is not easy since it lies at 374 °C and 229 bar and damages our samples (we observed that heat drying samples enhances the development of cracks in the porous matrix). To overcome this problem, water is replaced with liquid carbon dioxide (CO_2), which critical point lies at 31 °C and 74 bar which are easy conditions to maintain at the laboratory scale. However, CO_2 is not miscible with water; therefore, water has to be replaced by an exchange fluid, here ethanol, which is miscible in both water and liquid CO_2 , (Ethanol cannot be used for critical point drying due to

its critical point temperatures: 241 °C). This is made possible by performing imbibition cycles of ethanol on our samples. After water is replaced with the Ethanol and in turn replacing this exchange fluid with liquid CO_2 , the liquid CO_2 is brought to its critical point and converted to the gaseous phase by decreasing the pressure at constant critical point temperature. We eventually obtain a sample fully dry, ready for the imbibition experiment.

3 - Imbibition set-ups

i. Regular imbibition

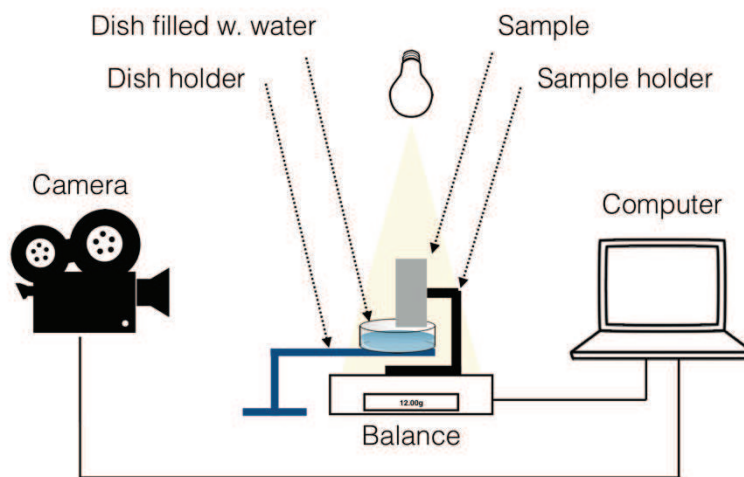


Figure 2-24: Imbibition set-up, the sample is lightened and filmed, carried out by a holder sitting on the scale, its tip dips in a dish filled with water carried to the sample by an holder which does not touch the scale. Mass and picture are taken thanks to a computer interface.

Similar to drying, the imbibition process is followed by weighting the sample with a scale and taking picture of it with a camera. As seen in Fig2-24, the sample is carried by a holder sitting on top of a balance and put in contact with a water bath hold by a different holder not interacting with the scale.

ii. Imbibition within the MRI

In the MRI spectrometer, the sample, suspended by a holder made of acrylic, is simply put in contact with water.

Chapter 3 - Drying kinetics of deformable nano-porous gels and sponges

In this chapter we study deformation during drying of soft materials such as sponges, with different surface properties and pore size distributions, and colloidal gels, varying their initial particle volume fraction. Drying of these materials with various boundary conditions is seen to trigger a plethora of deformations to develop such as shrinking, bending and different types of cracks.

A -Drying kinetics of deformable model nano-porous gels

1 - Drying rate for deformable nano-gels

i. Drying protocol specific to this study

Drying was performed on the set-up described in Chapter 2 -C -1 - at $20^{\circ}\text{C} \pm 2^{\circ}\text{C}$ in a controlled environment where the relative humidity was set to $45\% \pm 5\%$ and airflow guided vertically toward the sample at a mean velocity of 6 m/s at a distance of approximately 20cm from the sample free surface. Gel sample are contained in glass petri dishes of 9cm inner diameter.

The initial water mass $m(t = 0)$ is measured from the difference between the initial weight and the weight after the end of the test and after two days in an oven at 115°C to remove possible residual water.

ii. Drying curves

Let us first look at the evolution of water mass contained in the gels with time, the drying curves, for different samples with different substrates. Since samples at different initial concentrations ($\phi(t = 0) = \phi_0$) have different initial water masses, in order to be able to compare the different curves obtained, the current water mass $m(t)$ and is rescaled by the initial water mass $m(t = 0)$. Moreover, since for the different tests we observe slight fluctuations of the initial drying rate (see Fig3-2) as a result of slightly different boundary conditions (sample roughness or exact free surface shape, exact position of the air flux with regards to sample free surface) we further rescale the time multiplying it by the ratio of the initial rate of evaporation (in g/s) to the initial mass of water contained in the sample. In such a representation two samples of different sizes or different initial concentrations, or subjected to slightly different air flows, but both undergoing a first constant drying rate period would exhibit similar drying curves along this regime.

The drying characteristics of a non-shrinking model porous medium (glass bead packing) are independent of the substrate. As expected it shows first a constant drying rate period (CRP) followed by a falling rate period (FRP) during which the drying rate progressively decreases (see Fig3-1a). This period starts approximately from $m(t)/m(t = 0) = 0.10$.

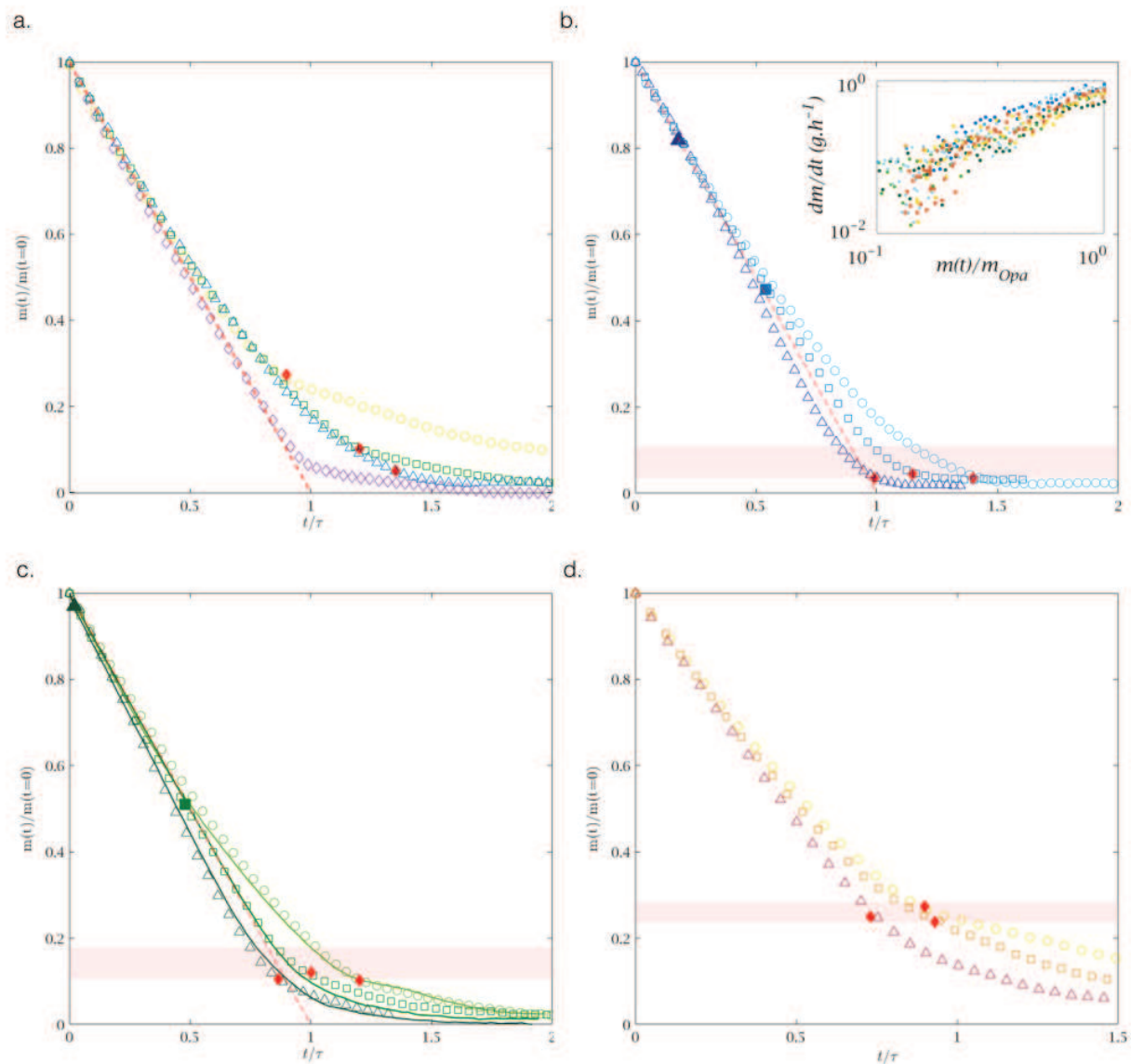


Figure 3-1: Rescaled drying curves (see text) for different materials: (a) model porous media (sintered glass beads) (purple, diamond) and gels on non-adhesive substrates at $\phi_0=5\%$ (light blue, triangles), $\phi_0=10\%$ (light green, squares) and $\phi_0=20\%$ (light yellow, circles); (b) $\phi_0=5\%$, (c) $\phi_0=10\%$ and (d) $\phi_0=20\%$ on either adhesive substrate (dark, triangles), semi-adhesive substrate (medium, squares) or non-adhesive substrates (light, circles). Larger filled symbols spot the occurrence of the first crack event respectively to its drying curve. The red area shows the period during which opalescence is observed and red diamonds indicate the time at which the opalescence has spread over the whole sample surface. Inset b', shows the evolution of the drying date of all gels right after the opalescence has spread over the sample surface (corresponding to $m(t)=m_{Opa}$); the black discontinuous line is a guide for the eyes.

In Figure 3-1 we present the evolution of the mass of water contained in the samples with time for the different samples studied. For all samples, we find first a period of drying at a high rate (regime A), followed by a rapidly decreasing drying rate period (regime B), i.e., we have a behaviour typical of that of porous medium. However, we also find perturbations in the rate of evaporation in the first period, the mass curves do not align to the red dotted line modelling a constant drying rate, as well as clear differences between the results for the different systems in this first period. For a given substrate (e.g. non-adhesive, see Fig3-1a) the initial solid fraction has an impact on the time at which the transition between the two regimes occurs: it occurs earlier for more concentrated systems. We also remark that for a fixed concentration the higher the adherence between the sample and the substrate, the faster the drying (up to 35% faster for our systems, see Fig. 3-1b, c, d.). Indeed, we notice that the drying rate in the second regime (starting from the red diamond in the drying curves, corresponding to the moment where $m(t) = m_{opa}$) seems identical for all samples and follows master-curve independent of the substrate considered (see Inset Fig3-1b'). Good reproducibility of these results is observed (see Fig3-1c): the maximum relative difference on measurements for identical tests is about 6% both on time and mass.

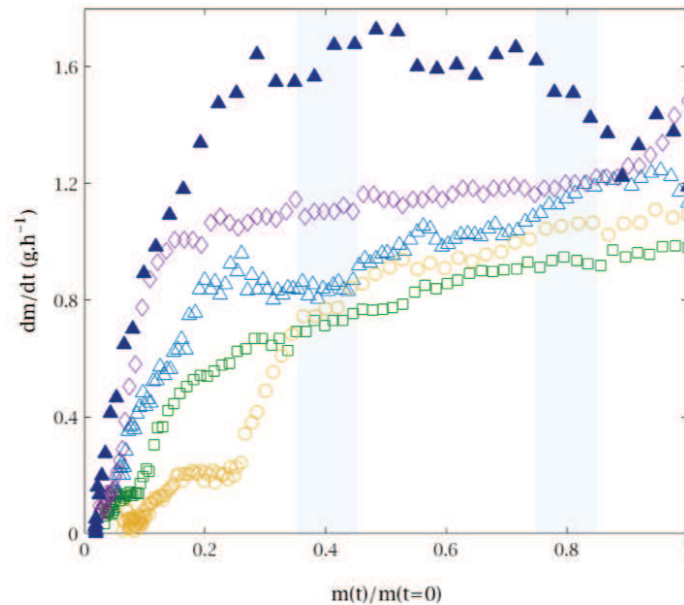


Figure 3-2: Drying rate (dm/dt) for different samples: the model porous media (sintered glass beads) (purple, diamond); gels on non-adhesive substrates at $\phi_0=5\%$ (light blue, triangles), $\phi_0=10\%$ (green, squares) and $\phi_0=20\%$ (yellow, circles) and $\phi_0=5\%$, (dark blue, filled triangles), on adhesive substrate. The shaded area represents the major crack events occurring for the latter sample.

Let us examine data presented in terms of the drying rate as a function of the saturation (see Fig3-2). This representation makes it possible to identify and quantify variations in the drying rate over short period of times (or associated saturation). For one sample to another, the initial value of the drying rate (after the possible fast initial decrease) may differ slightly depending on the exact surface conditions. Eventually, the main trends that can be extracted from such data, leaving apart the noise on data due to the short time fluctuations of mass measurements, are similar to those observed in our mass vs time curves: a constant drying rate that collapse at a low saturation for the simple bead packing and a slowly decreasing drying rate, for the gels, that collapses sooner for

higher initial particle volume fraction. On the other hand, looking closer into the localization of the crack events in relation with the drying rate variations of the 5% sample drying on an adhesive substrate, one could argue that major cracking events seem to trigger a local increase in the drying rate but actually the noise on data does not allow to be clear about that. Therefore, considering the significant measurement noise on such representation of data, it is difficult to be relevantly quantitative on the impact of the phenomena analysed in this paper. As a consequence, we will instead base our analysis on long time variations encountered on the drying curves such as those observed in the representation of mass vs time measurements as shown in Figure 2-1.

2 - Macroscopic phenomenology

The observation of the sample upper surface, in contact with the air flux, makes it possible to identify different stages in the shrinking and cracking processes along desiccation. Note that dimensionless time (denoted at the bottom right of Fig3-3 pictures) is computed by dividing the current time by the time for full drying by air flow, macroscopically at that time the sample appears fully translucent and a plateau is reached in the drying curves (as seen Fig3-1). We observe that gels drying on a non-adhesive substrate shrink as shown in Fig3-3A and Fig3-1A'. This shrinkage eventually stops and the samples become opalescent (see Fig3-3A and Fig3-3A'). Afterwards cracks nucleate and eventually the samples turn translucent again as seen on A Fig3-3A' at 1.00. This overall behaviour is found to be independent of the initial volume fraction of particles in the gel.

From samples drying on an adhesive substrate, we observe a first cracking event occurring in the early stage of the desiccation process as spotted on Fig3-3C and Fig3-3C'. Further shrinkage leads the gel to separate into additional pieces as may be seen at Fig3-3C at 0.29 or Fig3-3C' at 0.61. Then shrinkage stops and an opalescence "invades" the sample as seen on Fig3-3A at 0.75 and Fig3-3A' at 0.67. Eventually, in the very last stage of drying another cracking regime takes place before the sample turns translucent again as seen on C and Fig3-3C' at 1.00.

A very similar but intermediate behaviour is found for samples drying on semi-adhesive substrates. The gel first dries as it would on a non-adhesive substrate, i.e. it contracts smoothly without cracking therefore detaching itself from the sidewalls of the Petri dish as may be seen in Fig3-3B. from 0.00 to 0.25; only then the sample starts to fracture (see Fig3-3B at 0.33 and Fig3-3B' at 0.59). Further drying enables the sample to shrink additionally and crack until the opalescence invades the gel surface (see Fig3-3B at 0.68 and Fig3-3B' at 0.69). A second regime of crack finally takes place before eventually the sample turns translucent again as seen on Fig3-3B and B' at 1.00.

From this first set of observations we are able to distinguish two cracking regimes that will be referred to as first (pointed as 1 on Fig3-3C), appearing when the sample shrinks on an adhering substrate, and the second (pointed as 2) cracking regimes, appearing after the sample turned white, in reference to their chronological order in the desiccation process when both types occur with the same sample.

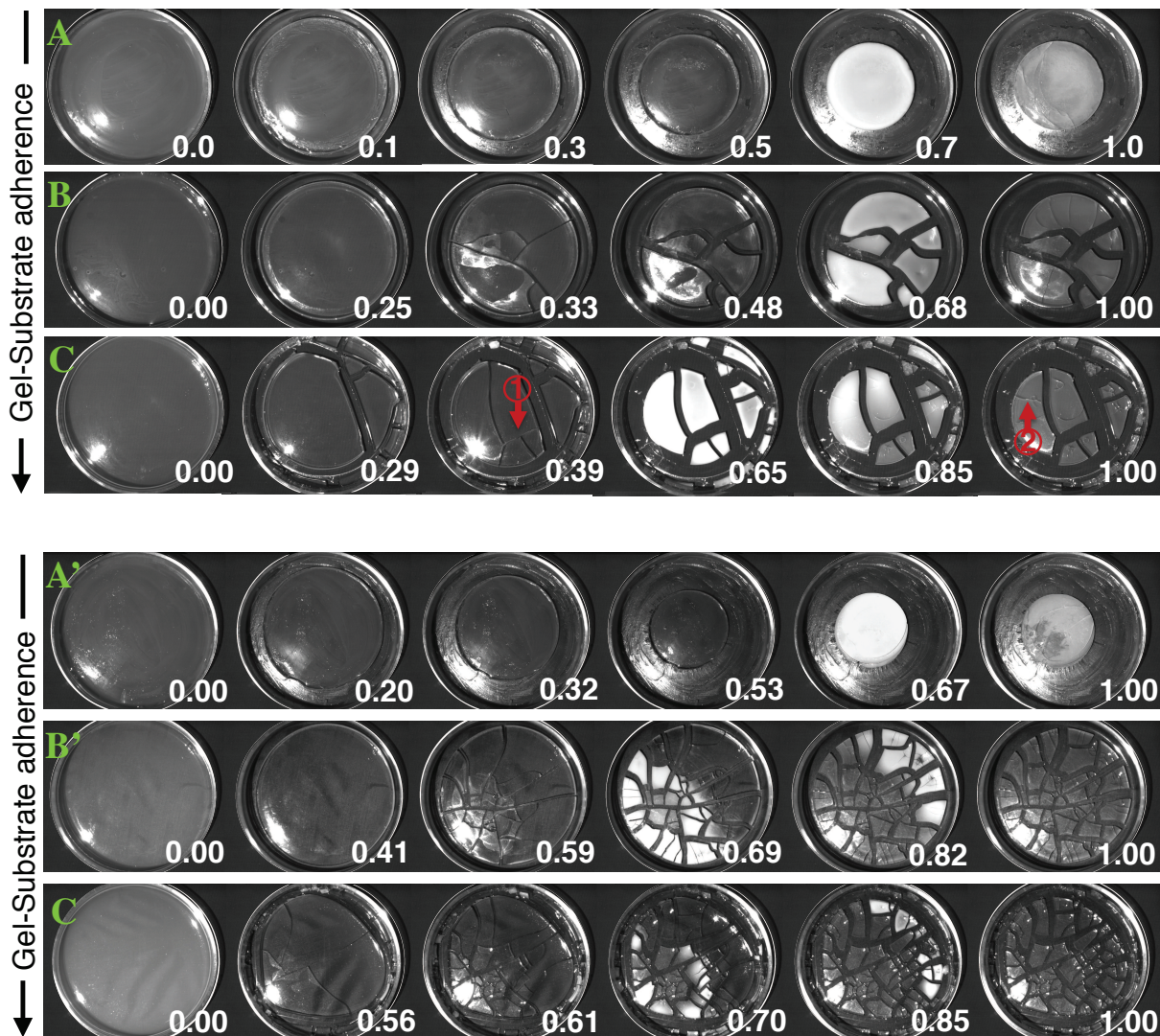


Figure 3-3: Aspect of the upper face (submitted to air flux) for gels on different substrates at different stages of drying: (A) $\phi_0=10\%$ on the non-adhering substrate, (B) $\phi_0=10\%$ on the intermediate-adhering substrate, (C) $\phi_0=10\%$ on the adhering substrate, (A') $\phi_0=5\%$ on non-adhering substrate, (B') $\phi_0=5\%$ on the intermediate-adhering substrate (C') $\phi_0=5\%$ on the adhering substrate. The white numbers indicate the current to total drying time ratio. The red arrow (1) shows a crack from regime 1, (2) from regime 2.

i. The different phases of drying of shrinking and/or fracturing gels

Along the desiccation process several different phenomena are successively observed, including a change of shape when contracting or cracking or changes in the sample colour. The latter may then be usefully put in relation to the drying rate and their role and influence can be identified.

Regardless of the substrate they dry on and whether the sample cracks during drying, samples are seen to shrink whether they crack or not while undertaking during their high drying rate period

(regime A). Specifically, to this period, it is noticeable that, the rate of drying does not necessarily remain constant for all samples. While a sample exhibiting no crack and simply contracting in regime A is seen to dry slower and slower as the sample desiccates, by contrast, fracturing samples are seen either to keep the same drying rate (see Fig.1 Graph-b sample $\phi_0=5\%$ and Graph-b sample $\phi_0=10\%$ on semi-adhesive substrates) or dry faster (see Fig.1 Graph-b sample $\phi_0=5\%$ and Graph-b sample $\phi_0=10\%$ on adhesive substrates) until the opalescence occurs. In particular, the appearance of a large number of cracks during this fast drying period (comparing adhering and semi-adhesive substrates for samples $\phi_0=5\%$ et $\phi_0=10\%$ on Fig.3) seems to correlate with a higher rate of drying. This therefore suggests that cracking could be the relevant parameter that explains the variation in drying rates. Moreover, we observe that the drying rate of samples that slide on their substrate and shrink, seems to drop slower and slower with contraction. This suggests that there may be an antagonist effect from drying and cracking in the during the first drying regime.

Commonly, drying of those gels leads to the appearance of opalescence on the sample surface, which matches the start of a decreasing rate regime (regime B) observable on the drying curves. This latter phenomenon takes place in the last stages of drying when the material stops contracting. From Fig.1, we also notice that it appears at a specific range of values of $m(t)/m(t=0)$ depending on the initial concentration of particles which actually corresponds to a common maximal particle volume fraction ϕ_{max} ranging from 55-60% for all gels. Finally, the red windows drawn on the drying curves of Fig2-1 covers the period during which the opalescence spreads over the sample surface; this diffraction within the network or near the surface is consistent with the idea of a modification in the gel content, the penetration of air and therefore a drying regime transition.

To gain further understanding in the role of these deformations on the drying rate and find the origin of these variations and deformation, it is crucial to look at the evolution of the water content within the sample during desiccation.

3 - Evolution of the water content within the gels during drying

i. Measurement of the water distribution

It is interesting to look at the water distribution within our samples to further correlate the rich phenomenology previously observed on Fig2-3 to the local saturation of the sample and further better understand the drying curves in Fig2-1. In the next figure we present the evolution of the water distribution with time, additionally we follow the location of the sample free surface by placing a pot of water, mounted on a tripod on the top of the sample (see Chapter 2 -C -1 - ii.).

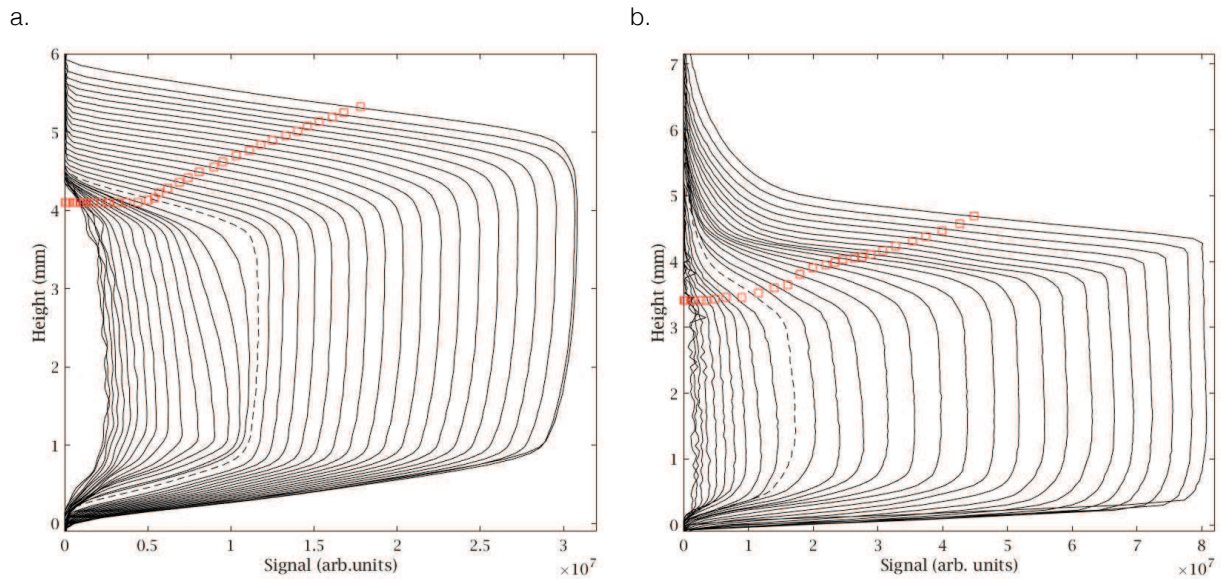


Figure 3-4: Distribution of water content in time inside a non-adhesive (a) and adhesive (b) gel ($\phi_0 = 20\%$) during drying. The continuous curves from the top to the bottom correspond to successive times (every 30min for (a) and every 55min for (b)) from the beginning of the test. The red symbols are the corresponding position of the sample free surface as measured (by NMR from the position of the water pot (see Chapter 2 -C -1 - ii.). The dashed line corresponds to the transition between the two regimes (see text).

Fig2-4 illustrates that the water content for adhesive and non-adhesive samples continuously decreases in time as shown by the decrease of the profile level. On Fig2-4a During a first period both the profile level and extent decrease, indicating a loss in water content in the radial and axial directions; furthermore, we observe the profiles holding parallel to each other and the position of the sample free surface exactly following the position of the end of the plateau in the water profiles (see Fig2-4). In a second regime (profiles starting from the dashed line; see Fig2-4) the sample thickness remains approximately constant while the profile level goes on decreasing. Additionally, we notice that the measurement is highly reproducible with an uncertainty of less than 2.5%, as shown on Fig2-5.

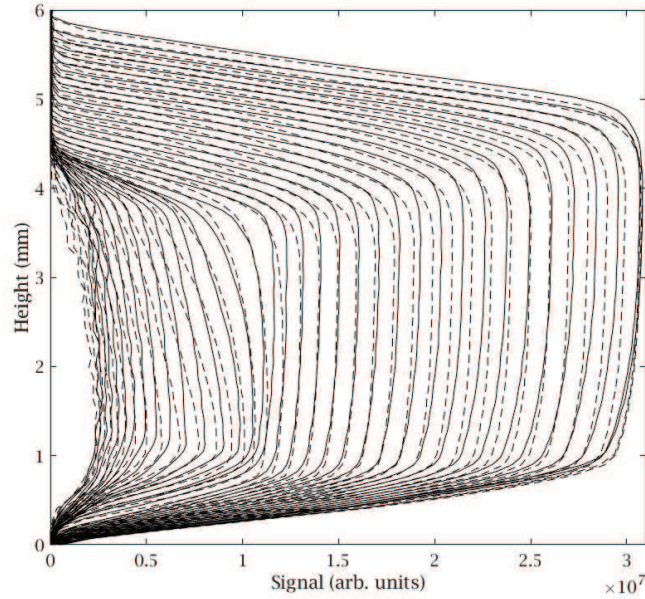


Figure 3-5: Measurement reproducibility, water content profiles in time for two identical tests under conditions of Figure 2-4a. Data of Figure 2-2a are in black, the second set of data is black dashed lines.

ii. Scheme for gel saturation

The comparison between the location of the sample free surface and the location of the wet interface during desiccation give us a crucial information on the drying mechanisms taking place. Before further analysis, it is important to clarify a point on the lecture of the MRI profiles above presented: note the linear ramp shape at the bottom and the top sides of profiles at the beginning of the experiment, and the nonzero water amount above the measured position of the free surface. Both are due to the bending (see Fig2-4) of the sample which becomes slightly concave (with an almost constant radius of curvature of about 1m) rapidly after the test beginning (so that squares in Fig2-4 only indicate some average position of the tripod's legs on the curved sample surface), this phenomenon is reviewed later on. For the adhesive samples the measurements correspond to the average water amount through different material pieces. This suggests that each of the pieces resulting from fractures behaves in a similar way, but here the analysis of the water content profiles is not straightforward since the different pieces formed with different sizes, shapes, and curvatures may evolve with somewhat different timings.

The critical question is whether the samples are saturated ($\psi = 1$) or not during desiccation. In order to clarify this we use our measure of the total water amount in the sample Ω_{water} (from the integral of each profile as the latter is directly proportional to the amount of water), the sample thickness (h) in time as measured from MRI profiles (distance between the bottom of the sample and the bottom pot on the trip minus the distance between the sample free surface and the bottom of the pot, the latter being fixed), and the horizontal apparent area (neglecting the impact of bending here) of the sample (S) measured from pictures taken from above during the test (see Fig2-1), which provide the apparent volume $\Omega = Sh$. We deduce the saturation:

$\psi = \Omega_w / (\Omega - \Omega_p)$ in which $\Omega_p = \phi_0 \Omega(t = 0)$ is the volume of particles and the solid fraction $\phi = \Omega_p / \Omega$. Since the reproducibility on the MRI data is excellent (see Fig2-5), the main uncertainties on the present data result from slight variations of sample shape and the uncertainty on the estimation of its section area, which explains some saturation values larger than 1 through our above computations.

From the evolution of ψ as a function of ϕ two regimes clearly appear (see Fig2-6). In the first regime ψ remains equal to 1, indicating that a negligible amount of air penetrates the gel therefore the latter remains saturated. The material finally reaches a solid concentration which is not exactly the maximum packing fraction in a disordered configuration for non-colloidal particles ($\approx 55\%$ - 60%), but here the initial loose system was already an aggregated network. In the second regime ϕ first slightly increases [38], the contraction of the solid matrix in this stage being in the order of a couple of percent, then remains constant while the saturation drops to zero. This regime transition particularly corresponds on Fig2-3 to the opalescence spreading on the sample surface. Therefore, one can conclude that the latter phenomenon macroscopically indicates the beginning of the sample desaturation. Since the opalescence appears from a partially saturated volume, we here bring an evident proof that it corresponds to light scattering from the coexistence of dry regions (air) and liquid-filled pore segments on visible light length scales, as suggested in earlier studies, [80].

The results are the same for a sample fracturing in Regime A. This means that we would get the same overall characteristics (shape and water content) for a non-adhesive and an adhesive sample by gathering the pieces formed in the latter case.

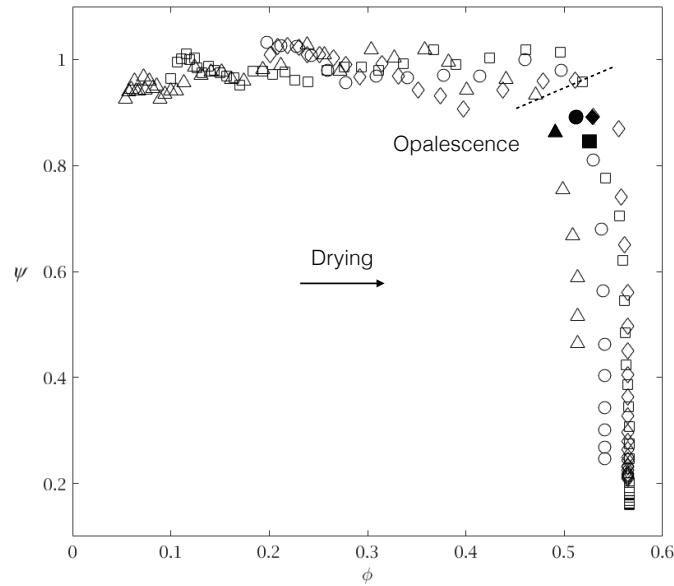


Figure 3-6: Saturation as a function of particle concentration for different ϕ_0 , h_0 and V_e . Non-adhesive: (circles) 20%, 5 mm, 0.33mmh^{-1} , (squares) 10%, 10 mm, 0.23mmh^{-1} ; (triangles) 5%, 5 mm, $0.13\text{mm}\cdot\text{h}^{-1}$; Adhesive: (diamond) 20%, 5 mm, 0.21mmh^{-1} . Black filled symbols show the time of appearance of the second type of fracture. The arrows show the drying progression. On each test the uncertainty on ψ and ϕ is 10%.

i. Deformations and drying regimes

From the previous results, since the gels remain fully saturated in regime A, i.e. before they turn white, crack in regime 1, i.e. when shrinkage occurs could potentially play a role in the drying kinetics observed. Our hypothesis is as followed: the variations in the drying rate recorded in regime A stem from the increase in the surface area of the sample exposed to airflow when cracking as drying now occurs from several of the sample faces. In this case a natural conjecture it that the gel would experience an increase in drying rate proportional to its total external surface area. However, this hypothesis raises a question about the absence of a drying rate overshoot upon cracking in this regime, since this phenomenon occurs rather abruptly and can increase the total surface area of the sample up to 35%. Thus, it is useful to look at the evolution of the geometry of the sample in time in deeper details. Note that the regime 2 for cracks, taking place in regime B for the drying kinetics (corresponding to a falling rate period) does not seem to significantly influence the drying rate (see inset of Fig2-1b’).

4 - Measurement of the material deformation during drying

In this section, we follow the evolution of the sample geometry during drying by measuring bending, shrinkage and the moments of crack nucleation to better understand the impact of the sample shape on the drying kinetics.

i. Delamination

As established previously, nano-sized gels remain fully saturated in their first drying stage (regime A). Therefore, in this stage, the water distribution within the sample reflects directly the sample geometry. From the MRI profiles presented in Fig2-4a and b, one can follow the deformation of the solid matrix during drying; varying drying conditions (the velocity of the airflow), this deformation can accentuate see Fig2-7.

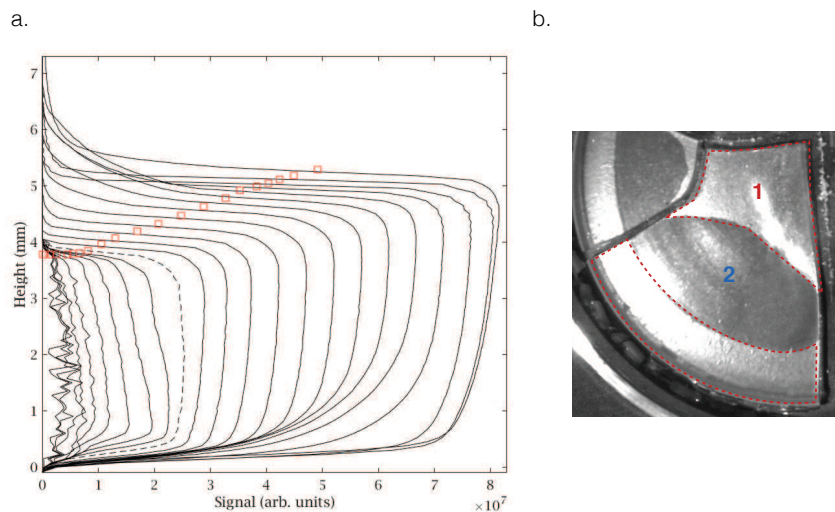


Figure 3-7: Water content profiles in time for a test under the same conditions as in Fig2-2 but a lower air flow velocity. The curves correspond to successive times (every 55 min)

and the squared symbols correspond to the sample free surface similarly as in Fig2-2The red symbols are the corresponding position of the sample free surface as measured (by NMR from the position of the water pot (see Chapter 2 -C -1 - ii.). Dashed line profile indicates the appearance of the opalescence thus the end of the contraction. (b) Photography zooming on a piece of the free surface of a sample made with 12nm particles and 10% initial volume fraction during its contraction phase when drying on a semi-adhesive substrate; the red contoured area (1) shows the area that free from contact to the glass substrate; (2), the darker area still sticks to the substrate.

On this last figure, we observe that the location of the free surface perfectly matches the location of the wet interface, probing once again the sample is fully saturated during its contraction. Second, we notice that along desiccation, the original shape of the sample progressively transforms and, as mention earlier, the sample starts to bend. This is also visible in Fig2-2 but all the more in Fig2-7 where we clearly spot that after a couple of profiles the top of these profiles overcomes the location of the free surface seen in the initial state (see 1st profile in Fig2-6); also, the sample highly bends on the bottom. Looking closer we observe that the part of the sample situated between amplitude between 0 and 3×10^7 arb. units, do not actually deforms. Having a look at the sample from above in this particular stage of the drying process may enhance understanding.

To yield additional information on this bending mechanism at play, we chose to look at a portion of the free surface of samples drying on a semi-adhesive substrate (see Fig2-8a). On this latter sample one can clearly see a part of the sample sticks to the substrate (part 2) and another part that is free from any contact with it (part 1). When drying proceeds, the area in contact with the substrate progressively reduces and the whole piece contracts (see Fig3-1).

ii. Shrinkage and first crack regime

In this section, we quantitatively follow the evolution shrinkage and crack nucleation in the first drying regime, in order to better understand the impact of the sample shape regarding drying kinetics.

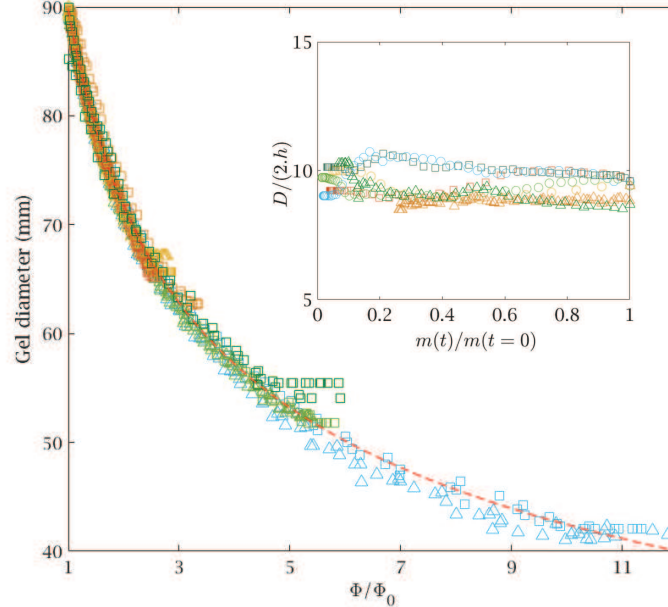


Figure 3-8: Equivalent diameter (see text) of the top area of shrinking samples as a function of the volume fraction of particles rescaled by the initial volume fraction for the materials and tests of Figure 1 (same symbols). Red dotted line is a fit to the data. The inset shows the sample aspect ratio along desiccation for all samples.

Direct observations of the sample from above allows for following the evolutions of its top free surface (defined as S_p) with time; here delamination only accounts for a very small error on the measurements, estimated to be less than 3%, giving the large radius of curvature of the gel. In order to quantify the evolution of S_p , we compute the equivalent diameter defined as $D = 2 \cdot \sqrt{(S_p(t) / \pi)}$. To compare shrinking behaviours between samples, we represent this diameter as a function of the ratio of the current to initial sample volume fraction of particles (ϕ/ϕ_0), where ϕ is computed from the mass data. From we observe that all gels from a same initial volume fraction, regardless to their substrates, tend to shrink in a similar manner during drying as their diameter evolves identically; indeed, all curves finally fall into master curve (red dotted line) which generalises the results and enables to say that all gels actually shrink the same way.

Specifically, as shown in the inset in Fig2-10, we observe that the aspect ratio of all samples remains constant along desiccation; the shrinkage therefore appears isotropic (here h , the sample height, is measured with a MRI profiling as seen earlier in this section). Each sample shrinkage stops when a volume fraction of 55% is reached; this concentration approximately corresponds to the maximum compaction that may be obtained from disordered bead packing. From this information we deduce that all samples shrink in an isotropic way. As a matter of fact, deriving the relation $R/H \approx 10$, translates to:

$$\frac{\Delta R}{R} = \frac{\Delta H}{H} \quad (3.1)$$

Which by definition witness of an isotropic transformation. The sample remaining fully saturated suggests that the origin of the differences observed on the drying rate, in particular for samples of similar initial solid concentration, are related to cracking since the only parameter that varies during this period is the number of pads, N , created.

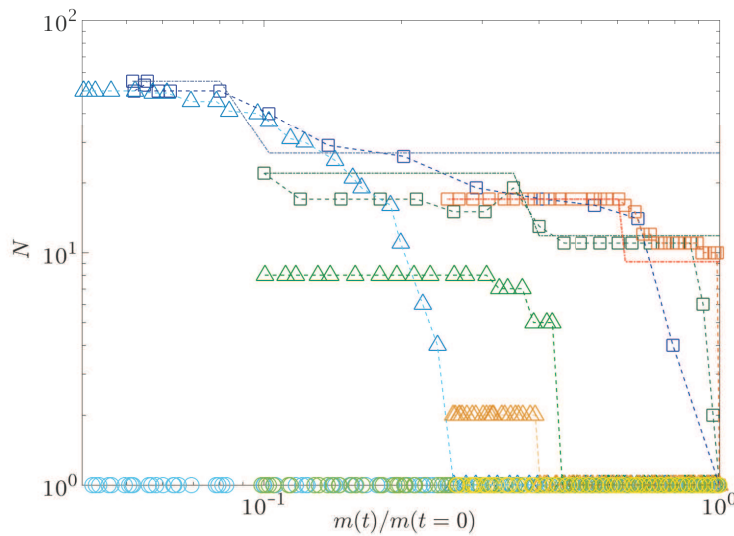


Figure 3-9: Evolution of the number of pads during shrinkage only for samples of initial particle volume fraction ranging from $\phi_0=5\%$ to $\phi_0=20\%$ drying on the 3 different types of substrates with drying for the materials and tests of Figure 1. Dashed lines are guides for the eyes, dotted dashed lines represents the results of the fitting model established later on.

Figure2-11 presents the evolution of the number of pads during drying while gels shrink. Consistently with previous observation samples on non-adhesive substrates present a single pad over the whole duration of the drying process. For other substrates an increasing number of cracks develop in time, with a step-like dynamic. We observe an alternation of short crack nucleation phase, followed by a long period of shrinkage of the existing pads. Fewer pads are obtained for highly initially concentrated gels and lower adhering substrates but they form more rapidly. Since these differences between samples seem correlated with the trends of drying curves for the different situations this tends to favour the hypothesis stipulating the appearance and development of pads could play a role on the drying rate.

iii. Second crack regime

As mentioned earlier, and pointed out on Fig2-6, the second cracking regime appears during desaturation when approximately 80% saturation is reached. Let's characterize these cracks:

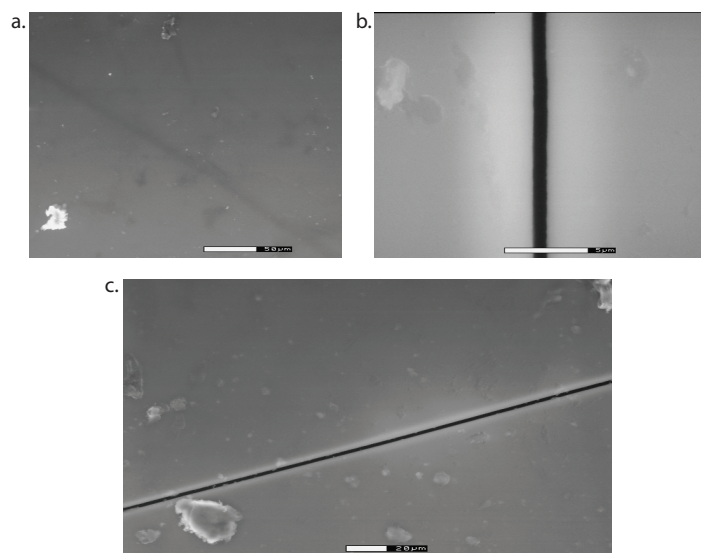


Figure 3-10: SEM observation of cracks in regime 2, (a) crack underneath the free surface, (b) zoom on crack, (c) Extent of a crack. 2keV as the energy for the electron beam.

As seen on Fig2-11a, regime 2 cracks do not necessarily span the gels nor reach the free surface. These cracks can extend over a significant length, typically a few centimetres and are not necessarily vertical nor straight. They develop instantaneously to human eye and their average width is measured to approximately 2 microns (see Figure 3-10b). Their density is rather low on all samples.

iv. Spiral cracks

Finally, Fig3-12 shows a type of crack we often encounter in our samples a little time before the opalescence appears; its shape is one of a spiral here but is also seen to describe a circle sometimes. Its centre locates at the last attachment point visible of the gel on its substrate; this type of cracks do not span the gel entirely.



Figure 3-11: Photography of spiral cracks observed at the end of the drying process for samples drying on adhesive substrates.

5 - Origin for sample deformation

i. Delamination

The impact of sample curvature on the MRI profiles is illustrated in the bottom scheme of Fig2-9 in the case of a spherical shape of the sample, with a large radius of curvature. In that case a simple mathematical integration of the total water volume in each cross section shows that the resulting gradient in water content observed at the top and bottom of the sample is a constant, giving a straight inclined line at the beginning and end of the profile. However, note that the profiles shape for the sample do not exactly match the mathematical spherical model, notice the difference with regards to a straight line (see Figure 2-4). One may also notice the initial profile shape, different from a pure rectangle, relating to surface effect tension and affinity between the suspension and the dish walls prior to gelation (see Figure 2-4).

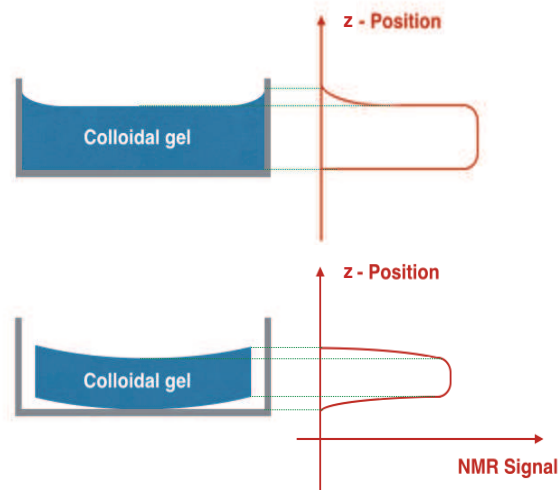


Figure 3-12: Scheme of sample shape in a radial cross section and corresponding MRI profiles of the water content for a fully saturated sample at the beginning (upper view) or after some contraction (lower view)

Having a closer look at the sample geometry (Fig2-4a and b), we observe that the edges of the sample are lifted which generates concave surface and therefore produce this profile shape: samples actually follow a well-known process of delamination, , [91, 92]. Furthermore, it is interesting to note that during the CRP, a first stage during which the sample significantly bends is observed and followed by a second stage where its curvature tends to cancel.

Indeed, the effective sample shape in this first stage can depend on the rate of drying, as shown for the test of Fig2-7 which corresponds to the same conditions as in except that the air flow velocity was much lower, this previous trend was previously observed, [38] however, the dependency of the curvature on the drying rate does not constitute a focus for this study. Note that despite these differences, the evolution of the water content profiles is similar to those observed for a larger air flow velocity: the same two regimes and a transition at almost the same solid volume fraction are observed from Fig2-4 to Fig2-7. This process of delamination also plays a role in the appearance of cracks as it helps building up stress in the solid matrix.

ii. Suggested origin for cracks in the different cracking regimes

To enhance our understanding on the origin for crack nucleation in the different regimes or crack morphology, it is useful to look at how the substrate deforms under the action of the gel during drying to complement our observations on the water distribution within the samples. To do so we perform a strain imaging experiment, detailed in Chap.2 (Strain sensitive substrate), which enables to locate the strain generated by the sample to its substrate. The adhesion between the 2 components seem relatively high and comparable if not higher than our previous semi-adhesive substrate (comparing the number of fragments in the final stage). If the next experiment does not show the exact total strain generated by the gel on its substrate because of imperfect binding between the two components, we believe it still reflects enough of this behavior to constitute an interesting system to approach qualitatively.

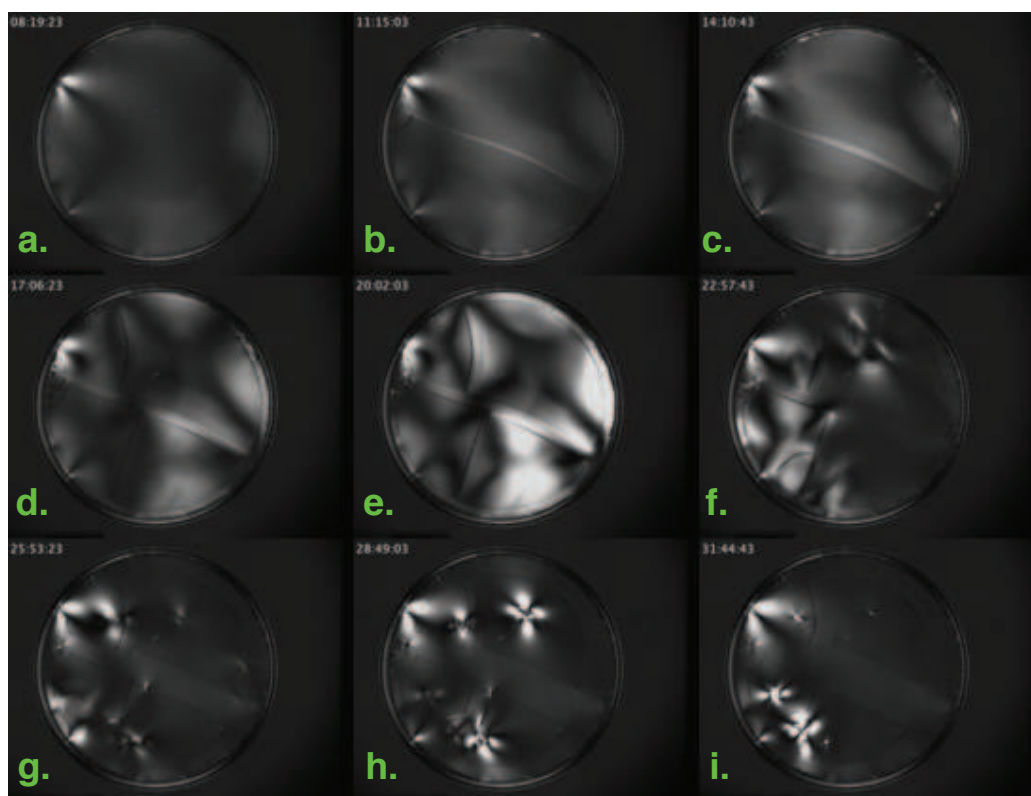


Figure 3-13: Image of the strain induced by the gel on its substrate during drying. The whiter and brighter the area, the higher the strain generated by the gels on the substrate. Dark areas translate to the absence of strain. The total time of the experiment is 39h, the time elapsed since the beginning of the test is written at the top left of each picture in the following format: hh:mm:ss.

The typical phenomenology seen in Fig3-2 can as well be observed on Fig3-13 but now with further indications on the substrate deformation. In the initial state, the gel wants to contract (Fig3-13a), and pulls on its substrate preferentially at its periphery, near the dish walls where the boundary conditions are the toughest. Further drying triggers the apparition of a crack (Fig3-13b), and strain

progressively builds up on the substrate (the brightness increases on the whole picture, see Fig3-13b, c). Finally, some strain patterns arise underneath the gel fragments (see Fig3-13d) meaning that these fragment pull on the substrate (see Fig3-13e). On Fig3-13e to f, one can observe a very high strain developing underneath the bottom right piece that further dissipates, this constitutes the nicest example we yield of strain release from cracking. Additional drying triggers concentration of the strain in very focuses areas (see Fig3-13g, h); eventually the sample completely unstick to the substrate and turns opaque (the opalescence spreads at the sample surface), no more strain is generated from adhesion (see Fig3-13i). Now let's analyse the situation gathering our previous results assuming that the location of strain on the substrate relates to le location of strain within the sample.

In regime 1, gels remain fully saturated therefore capillary stresses are very unlikely to play a role in the nucleation of these type of cracks. In fact, we observe that these crack nucleate only when gels dry and shrink over an adhesive substrate (see Fig3-1). Additionally, these cracks are seen to relieve stress that build up from the adhesion of the substrate (Fig3-13e, f). Because the mechanism of shrinkage puts the gel in tension when it adhesion to the substrate exist, we conclude that the origin for these cracks is associated to the tensile failure of the material. And the classic approach of fracture mechanics may apply, it is likely that cracks nucleate when the intensity of the stress exerted on the solid matrix becomes greater than the material strength.

The spirals and circular cracks observed when gel fragments gradually fold up and detach from the substrate, (see Fig3-11) are typically observed right before the sample turns opalescent. This correspond to the timing seen in Fig3-13g and h. On these images, we can see that very high stress is generated in the solid matrix on very targeted points corresponding to the last attach of the gel on the substrate. In fact, the origin for this type of cracks are well documented, they are supposed to result from large tensile stresses in the radial direction at and normal to the front of detachment. When the stress at the front exceeds the material strength, a crack is nucleated. The crack tends to propagate along the front only in one direction where more stresses can be released. By the time the crack growth completes a cycle, the front has already advanced, leading eventually to an inward spiral crack. Since the stresses are concentrated at the layer-substrate interface, the spiral is confined there, with a typical penetration of 20-60% of the thickness. These cracks will not constitute a focus of this study.

Finally, regime 2 cracks, are seen to appear when the global saturation of the sample drops to $\psi \sim 0.80$ (see Fig3-6). Because water is still rather homogeneously distributed throughout the sample in this regime, one can assume liquid films to cover the solid matrix. We can compute the thickness (e) of these films:

$$e = \frac{\text{liquid volume}}{\text{solid area}} = \frac{1}{3} \cdot \left(\frac{\varepsilon}{1 - \varepsilon} \right) \cdot R_{part} \psi \approx 8.6 \text{ \AA}$$

When thin liquid films cover the solid matrix (here approximatively 3 water molecules thick), high local stresses likely induced by disjoining pressure effects (see Chap.1 – Disjoining pressure), or capillary stresses, when air fingers enter the thin liquid films, can push close particles against each other, and tend to further concentrate the system which is already well packed. Only some slight

rearrangements extending over large distances are possible, leading to failures then allowing slight further concentrations in separate regions.

6 - Deformations influencing the drying rate

Drying of nano-gels gives rise to a large library of deformations, it is useful to put them in relation with the variations of the drying rate we observed in the frame of the different drying regimes and the state of saturation of the sample, before further analysis. During the first drying regime, the gels are fully saturated hence their drying rate is high; during this first period we observed shrinkage and delamination to occur simultaneously as well as cracks to nucleate and fragment the gel in several pieces (pads) if the gel adheres on its substrate. During the second drying regime, the sample desaturates and its drying rate drops progressively. The thinning of the liquid layers covering the particles generates high mechanical stresses on the solid matrix that eventually trigger several regimes of cracks with various cracks morphology such as straight, spiral or circular cracks; none of these cracks span the gels.

Even if cracking is clearly seen to make the drying rate of materials vary in the first drying regime, a minute analysis of the drying curves in Fig3-1 suggests that these variations are not directly proportional to the vertical surface created: indeed, these variations are smooth whereas the total external interface area varies as successive steps (see Fig.5). Therefore, we foresee that the drying rate of a deformable material can be more complex than strictly proportional to the external area of the sample certainly because of the distribution the air velocity in the vicinity of the sample crack cavity. It is therefore interesting to get some ideas about the way the evaporation process is affected in such a situation, so we performed basic numerical simulations as described in the next Section.

Furthermore, if inset in Fig3-1 shows that regime 2 cracks do not seem to play a role in the drying kinetics observed in regime B (during desaturation), one may think it is because there is only very few. Later on, we study the influence of cracks in regime B on the drying kinetics of the gels.

Note that due to the high radius of curvature of our sample in the drying conditions we study (1m), this phenomenon will be neglected especially as it does not play a significant role in the airflow profile we present in the next section.

7 - Numerical simulation and modeling of the influence of the first crack regime on the drying rate

i. Distribution of the airflow velocity

Here aim to identify airflow characteristics around samples that exhibit multiple cracks in the first regime and their effects on evaporation. In this section, the effect of the curvature of the gels on the airflow properties is neglected; our simulations have shown that it negligibly affects, in the range of the deformation observed experimentally, the distribution and intensity of the airflow. In this frame we will consider a 2D airflow along a box (see Fig3-14) which represents a cavity between two cracks. Such a tangential flow is assumed to reflect qualitatively the radial flow, which occurs along the sample free surface as a result of the vertical airflow turning abruptly at a 90° angle when reaching the sample.

Airflow simulations were performed on COMSOL Multiphysics software using the interface for single-phase flow enabling velocity and pressure fields calculations in turbulent and stationary regime. The equations solved by this interface are the Reynolds averaged Navier-Stokes equations for conservation of momentum and the continuity equation for conservation of mass. Turbulence effects are included using an enhanced viscosity model based on the local wall distance. The physics interface therefore includes a wall distance equation. The boundary conditions are shown in Figure 5: no slip conditions were applied to the bottom and top walls of the box; the entire left face is set as an inlet for the airflow and the right face is set as the outlet (the pressure on this face is set to zero). The cavity of width “e” and height “h” is located at a large distance (1000mm) from the inlet face so that the air flow inlet is not affected by the cavity for all simulations. The sample upper surface corresponds to the bottom wall of the box which is set to $y=0$; we define the aspect ratio of the crack cavity as e/h (Fig3-15).

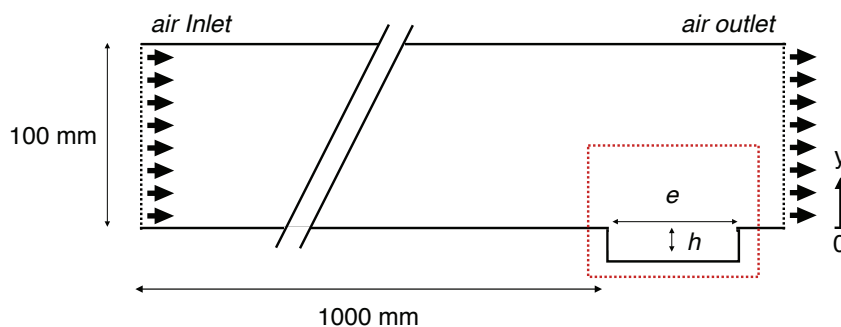


Figure 3-14: Scheme of the simulated geometry. The red dotted square represents the area observed in Figure 6.

We carried out simulations in the range of inlet velocities [0.1-30m/s]. In this range the trends described below are similar, which ensures that the conclusions are sufficiently general. For all aspect ratios (see Figure 3-15) we can distinguish two regions of the velocity field: above the envelope of the sample surface ($y>0$) the velocity is relatively high and close to the upstream velocity; in the cavity the velocity is significantly lower. Obviously there is a transition zone between the two regions with a velocity gradient. Looking at the details of the velocity field in the cavity we observe a vortex, which more clearly appears in Figure 3-15E showing the velocity field. This vortex originates from the top right hand corner of the wall of the cavity, i.e. in front of the

flow direction. The tangential velocity of the vortex is approximately equal to 0.15 times the inlet velocity for all aspect ratios tested here. However, the size of the vortex significantly evolves with the geometry of the cavity: when $e/h=1$ (Figure 3-15), the vortex completely fills the cavity; when $e/h<1$ (Figure 3-15D) it only covers the upper portion of the cavity, and when $e/h>1$ (Figure 3-15A and B) it fills the right part of the cavity. Finally, the vortex diameter corresponds to the smallest dimension of the cavity.

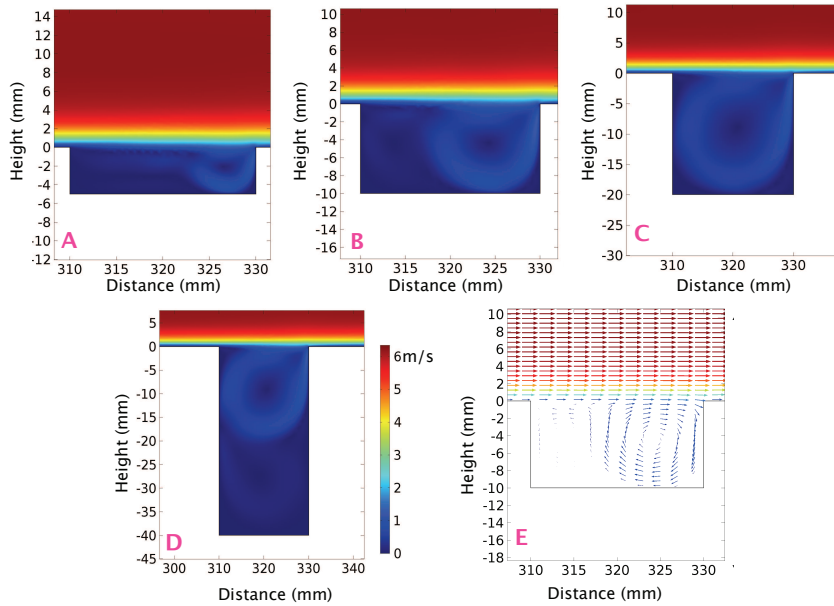


Figure 3-15: Results of numerical simulations showing the magnitude of the airflow (from left to right) velocity for any point of the 2D plan along the cavity squared in red on (Fi3-14) for different aspect ratios e/h (A) 4, (B) and (E) 2, (C) 1, (D) 0.5. The colour scale is the same for all simulations. the arrow length indicates the velocity amplitude in a logarithmic scale

Experiments showed that cracks span the gels vertically and the resulting pads significantly bend, reaching curvature radius up to 40 cm. We carried out additional simulations with curved boundaries which showed that bending of gel fragments negligibly affects the magnitude (up to 12%) and distribution of the airflow velocity in the crack vicinity. Therefore, this effect will be neglected.

ii. Modelling

On the basis of the qualitative observations above and with further simplifications for describing the evaporation process we can propose a simple model for the drying of a set of pads lying on a surface and exposed to a tangential air flux.

With the help of the above results from simulations, we can adapt the scaling approach from Chapter 1 -A -1 - to the more complex present situation where evaporation can occur from the different free surfaces of the pads. In the initial situation, the gel embraces the shape of the petri dish so that the only surface exposed to the airflow is the horizontal surface; therefore we can then determine the value of δ leading to a total vapor flux $V_e S$ equal to the rate of decrease of the water

volume during the first constant rate period of drying when the sample is saturated and the surface is still homogeneous. The value associated with the data presented here (see Fig3-1) is $\delta = 4\text{mm} \pm 8\%$.

During drying we observe a variation (decrease) of the total area of the upper free surface of the sample; neglecting possible deformations of the pads (see above) this area is assumed to be submitted to the same airflow throughout the experiment. Moreover, we may have cracks, which provide new areas along which evaporation may occur. Here considering only, the period during which the sample is saturated, so that water layers remain relatively close to free surface of the sample, and the above approach for the estimation of the evaporation rate remains valid. In particular the process of drying, boundary controlled, applies for the crack cavity walls, with now specific values for the boundary layers δ_i depending on the face “i” of the sample considered.

In any case we assume that the evaporative flux from the upper surface of the sample, i.e. parallel to the airflow, is $V_e S_p$. This approach is relevant since we have seen that the air flow characteristics over the horizontal surface are rather weakly perturbed by the presence of openings (see previous Section). Additionally, there is some vapor flux coming from the interior of the cracks (see Figure 7). Inside the crack cavity we have seen that the airflow is complex; it in particular includes a vortex. A rough approximation to assess the evaporative flux along the crack walls consists in assuming that most evaporation occurs along the wall area in contact with the vortex, whereas evaporation along the other walls is negligible. This is justified by the observation that the air velocity around the latter regions approaches zero while it is much larger around the former regions. Then we assume that all occurs as if such a wall was simply at a distance larger than the upper surface from the air flow. This additional distance is d , where d is the vortex diameter, so that the rate of evaporation along the vertical walls in contact with the vortex is $Ve \cdot \delta / (\delta + \alpha d)$, with α being a geometrical coefficient. Considering the mean total path of water molecules (see Figure 3-16) we can expect $\alpha = 2$. Under these conditions we distinguish two different regimes according to the configuration of the vortex in the cavity:

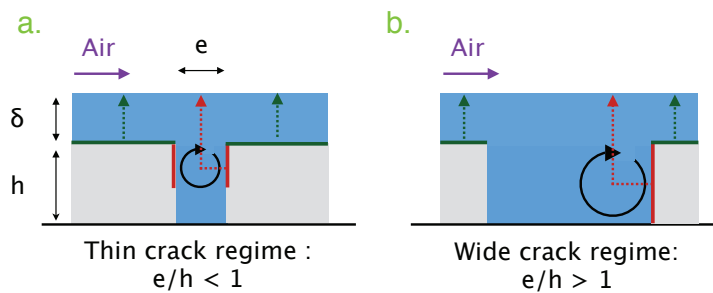


Figure 3-16: Scheme of the regimes of evaporation during drying of a shrinking and cracking gel layer depending on the aspect ratio e/h of the crack cavity. The surfaces along which most evaporation occurs are shown in green (horizontal) or red (vertical). Dotted lines (colors corresponding to each surface type) indicate the average pathway a molecule of vapor water follows during desiccation in order to reach the ambient air. The circular black arrow represents the air vortex.

(1) Regime 1 (see Figure 3-16a): $e/h < 1$ “Thin cracks”. In this case the size of the vortex is e and only the fraction e/h of the total area (S_v) of the internal crack air-sample interface provides

evaporation (at the rate indicated above) from the crack. Finally, the total water flux of evaporation is:

$$\Phi = V_e \cdot \left(S_p + S_v \cdot \frac{\delta}{\delta + e} \cdot \frac{e}{h} \right) \quad (3.2)$$

And (2) Regime 2 (see Figure 3-16b): $e/h > 1$ “Wide cracks”. In this case the size of the vortex is h and since it is in contact with only one of the walls of the crack; only the area of the internal crack air-sample interface provides evaporation. Therefore, the total water flux of evaporation:

$$\Phi = V_e \cdot \left(S_p + \frac{S_v}{2} \cdot \frac{\delta}{\delta + h} \right) \quad (3.3)$$

In (3) in particular, we neglected the evaporation along the vertical crack wall opposite to the vortex. A rough estimation of the corresponding rate of evaporation can be obtained by considering that the additional length is now e , which yields an additional term in (3) equal to $V_e(S_v/2)(\delta/(\delta + e))$. (3). This makes it possible to get a continuity of the expressions (2) and (3) for $e = h$. However, in this context of description we ignore processes associated with this term which rapidly becomes negligible.

iii. Model predictions

The predictions of the above model are then computed thanks to the information obtained through the different measurement methods: the set of pictures taken during drying yields $S_p(t)$ and $e(t)$ (the average crack spacing) and $P(t)$ the perimeter of the gel and MRI profiles provide the average height $h(t)$ of the sample. From this information, we finally deduce $S_v(t) = P(t) \cdot h(t)$. Now being able to follow the ratio e/h with time, we simply apply the different regimes established in (2) and (3) depending on this later value, to deduce the evolution of the drying rate as a function of time (see Figure 8). Note that in the case of the gel contracting without cracking, seen on non-adhering and intermediate substrates, the cavity created between gel and the dish walls is taken into account as a crack and the different regimes apply. Crucially, it is worth emphasizing that this description explains the reason for the absence of abrupt variation (increase) of the drying rate when cracks appear: as soon as a crack forms there is a new additional term in the drying rate (2) but it is proportional to e/h which implies that it is initially negligible and will become significant only when the crack thickness is sufficiently large.

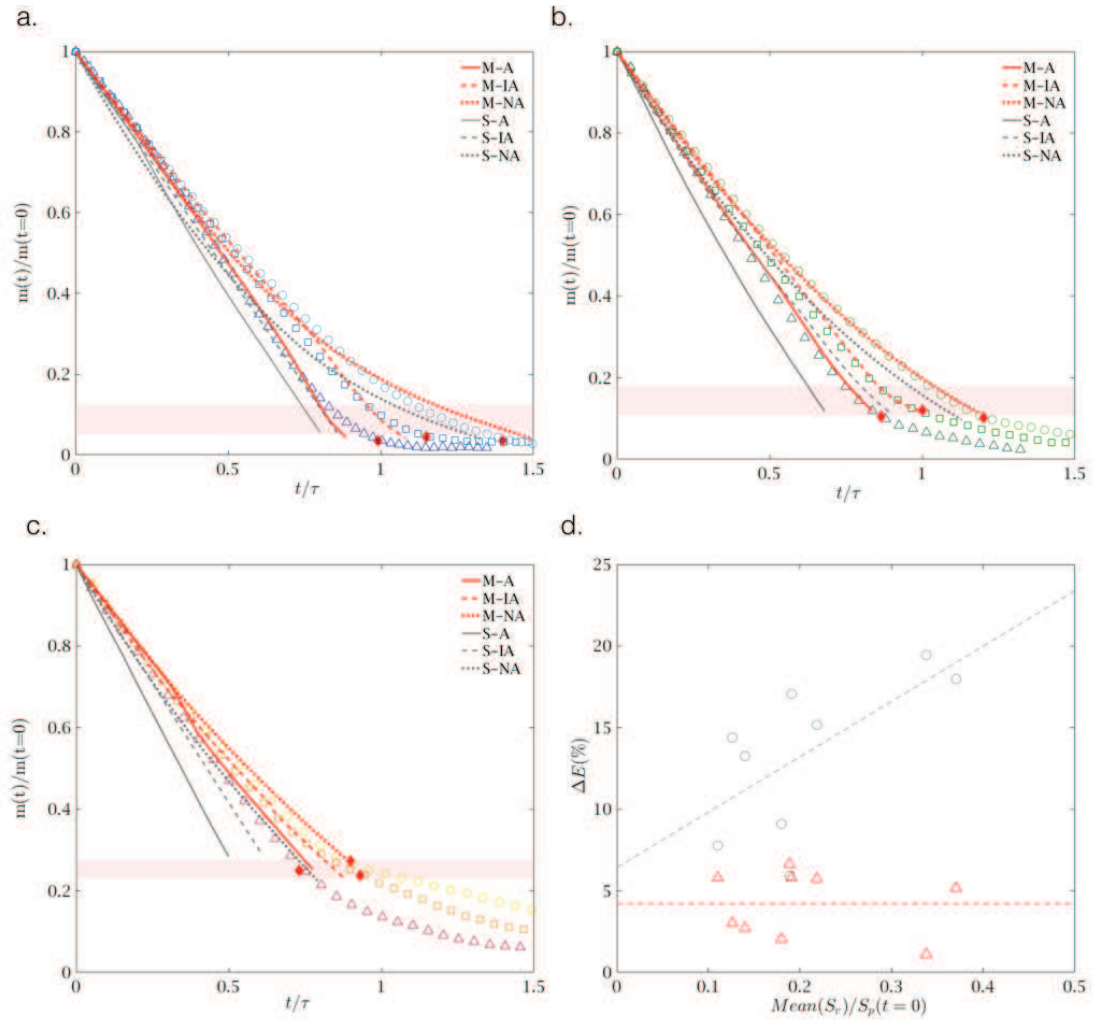


Figure 3-17: Comparison between the experimental data (same as in Fig3-1) and the scaling model (2) and (3) (red lines), for graph (a) $\phi_0 = 5\%$, (b) $\phi_0 = 10\%$ and (c) $\phi_0 = 20\%$, (M-A) Adhesive (M-IA) Intermediate Adhesive, (M-NA) Non-Adhesive substrates. The predictions assuming a constant rate of evaporation over the total generated surface (see text) are also shown (grey lines) for (S-A) Adhesive (S-IA) Intermediate Adhesive, (S-NA) Non-Adhesive substrates. (d) Relative error (ΔE) to the experimental data (triangles) for our model, (circles) if a unitary surface flux is considered, as a function of the mean vertical surface generated during drying.

From Figure 3-17, we see that the computed mass of water, integrated from the drying rate presented in the previous model, appears to be in good agreement with the experimental data. We observe that every red curve closely follows the experimental data before the sample turns opalescent (red diamond) i.e. during the first period of drying; be it in graph a, b or c. Indeed, as shown on Figure 3-17.d, the relative error to the experimental data remains very low ($\sim 4\%$) for a wide variation of the average vertical surface generated during drying, which is related to the number of pads, meaning that the model is robust.

In order to explain the variations in the drying rate recorded when a material cracks, studies often assume the existence of a simple proportionality law between the drying rate and the total surface

generated while cracking, [87]. In Figure 3-17 we show that assuming a constant rate of evaporation per unit surface over the whole sample surface, fails to explain the actual measurements and introduces a relative error to the data that increases linearly with the amount of vertical surface (see Figure 3-17d); thus pointing out that the drying rate tend to be significantly overestimated. This tends to confirm the relevance our model shows for the prediction of the drying kinetics observed.

Now taking our model as a reference we bring the analysis and understanding of the drying kinetics further. Our aim is to determine the drying rate evolution on the basis of the geometrical evolution of the sample. Considering the above experimental results, we can describe this geometry through the number of pads only. We now express each variable as a function of S_p and N : the mass of water contained by the sample can be written $m = \rho S_p h$; the sample equivalent radius $R = \sqrt{S_p/\pi}$; we deduce from the inset of Fig.3-8: $10h \sim \sqrt{S_p/\pi}$. Finally, the evaporation flux $\Phi = 1/\rho \cdot dm/dt$ may be expressed as:

$$\Phi(t) \sim \frac{3 \cdot \sqrt{S_p}}{20\sqrt{\pi}} \cdot \frac{dS_p}{dt} \quad (3.4)$$

Since in addition we may write the vertical surface as $S_v \sim P/10 \cdot \sqrt{S_p/\pi}$, where P, the perimeter of the pads can be approximated to $P = \sqrt{N \cdot S_p/\pi}$, where N is the number of pads (overall relative error of to the experimental data <15%), and we therefore:

$$e \sim \frac{S_p(t=0) - S_p}{\sqrt{\frac{S_p}{\pi}} \cdot N} \quad (3.5)$$

the equations (3.2), (3.3) and (3.4) provide differential equations from which one can find $S_p(t)$, and thus the water mass in time, as a function of $N(t)$. For non-adhering surface we do not get new information from this approach since the sample shrinks as a monolithic disk without cracking.

As the cracking regimes recorded in samples drying on intermediate adhering substrates are identical to the one for adhering substrates (simply delayed) but with a smaller overall number of pads, we will here focus our analysis on samples drying on adhering substrates. The results we yield are however valid for any sample cracking while being saturated. In the case of adhering substrates, the number of pads strongly varies during drying. Looking at data in Figure 3-9 and the relevance of the fit obtained for gels adhering to their substrates, it seems possible to approximate the evolution of the number of pads for samples drying on adhering substrates in the form of a two-steps process:

$$N\left(\frac{\phi}{\phi_0}\right) = \begin{cases} \frac{N_{max}}{1.86} & \text{if } 1 < \frac{\phi}{\phi_0} < \frac{\phi_{max}}{2.5\phi_0} \\ N_{max} & \text{if } \frac{\phi}{\phi_0} > \frac{\phi_{max}}{2.5\phi_0} \end{cases} \quad (3.6)$$

where N_{max} is the final number of pads and $\phi_{max} \sim 61\%$ the final volume fraction reached before desaturation starts and the factors 1.86 and 2.5 being calculated from the experimental data. Subsequently, from the integration of (2)-(5) we can deduce the variation of the water mass in time as a function of N_{max} and ϕ_{max} . Note that here the material is assumed to be split in pads of equal dimensions, consistent with the experiments.

Through this new approach, let's see how cracking plays a role in the duration of the first drying regime (defined as t_{R1}) and how transitions in cracking regimes trigger the drying rate variations. This theoretical approach not only enables to simulate the impact of the total number of pads on drying, but also makes it possible to quantify the impact of the different cracking regimes on the drying kinetics, by following the ratio e/h and minutely observing the drying rates. In that aim we consider the case $\phi_0 = 10\%$ drying on an adhering and non-adhering substrates as a case of reference.

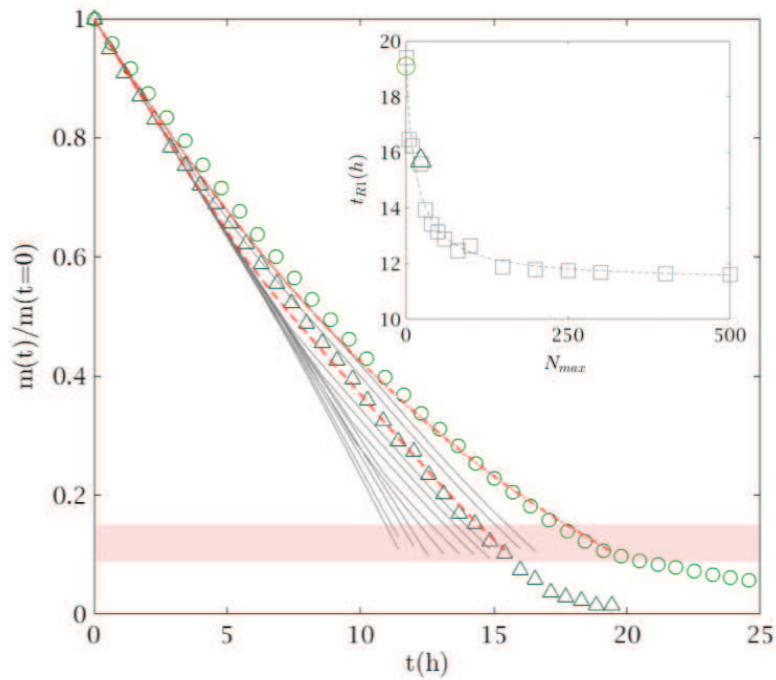


Figure 3-18: Normalized drying curve for the experimental data on adhering substrate (green triangles), non adhering substrate (green circles), the prediction of the model established with the measured $N_{max} = 23$ (red line on triangles), for one pad and a single crack regime transition during drying (red line on circles), (grey lines) model prediction with different N_{max} ranging from 1 to 500 (1-10-40-50-60-80-100-200-500-1000-3000) featuring two crack regime transitions during drying. Arrow indicates the increase in the number of pads. The full green triangle spots the first cracking event. The red shaded area represents the transition in the second drying regime (i.e opalescence). Inset presents the

evolution of the simulated t_{R1} with N_{max} (grey squares); experimental data for t_{R1} for adhering substrate (green triangles), non-adhering substrate (green circles). Grey dashed line is a first order rational law fit.

Figure 3-18 shows that this simple model succeeds in describing the kinetics of drying for samples which dry saturated and cracks, (the red line on the green triangle curve), and samples that exhibit pure shrinkage (the red line on the circle pointer curve). The relative error to the experimental data, for a sample drying on an adhering substrate, when introducing the measured $N_{max} = 23$ in the model equation, remains inferior to 5%. Note that this model constitutes a prediction of the drying kinetics if the final number of pads is known.

Furthermore, by observing the different simulated drying curves, representing distinct N_{max} values, we see that the higher N_{max} , the shorter the t_{R1} . This trend is consistent with the trends observed comparing and Figure 3-9 and finds here a quantitative support. In fact, from the inset of Figure 9, we observe that t_{R1} decreases progressively as N_{max} increases and this trends follows a first order rational law. This for example means (in the case $N_{max} = 23$) that a sample showing twice as much pads would dry ~6% faster in this first drying regime and ~15% faster with four times more pads. However t_{R1} tends to a finite value (around 12 hr) when $N_{max} \rightarrow \infty$. Indeed, the initial area of the sample being fixed, as the number of pads increases their thickness tends to zero which tends to decrease the additional term (due to crack) in the drying rate expression and thus balances the tendency of this rate to increase due to the crack density. As a consequence, for a given material and air flux, this asymptotic value likely depends on the initial sample area.

8 - Influence of the second crack regime on the drying rate

i. Crack density on drying kinetics

At first sight, cracks nucleating in the second drying regime are seen not to influence the drying kinetics in regime B (see Fig3-1 in inset b') but very few of these cracks are actually observed on or within the samples (see Fig3-2). Cracks can potentially drain water in their vicinity and therefore significantly enhance the drying rate, [25]. In this section we investigate the influence of the second regime of cracks on the drying rate of gels drying on a non-adhesive substrate; to do so, we measure the drying curves and the water distribution for the gels. Two different gels are studied (see Fig3-19a and b) exhibiting a crack density of 0.7 (see Fig3-19a and typically seen in Fig3-2C and C') and 14 (see Fig3-19b) in regime 2. We define and measure the crack density as the average number of times a crack crosses a radius drawn at gel surface in the final stage of desiccation, the centre of the gel defines the departure of the radius (image analysis). We look at 20 radii evenly spaced (every 13°).

Tuning crack density in regime 2 is made possible by adjusting the pH of water within the gels as it modifies the surface charge of the silica particles and therefore the intensity of the interactions between silica and water molecules. Since liquid films of a couple molecules thick have been measured on the solid matrix when this types of crack nucleate, changing the intensity of the molecular integrations (ionisation of silanol groups at the silica surface, see Fig1-18) likely makes

the intensity of the disjoining pressure (electrostatic contribution) vary and we observe a change in the crack density. The extent of these variation is not known; further study is needed. What we observed is that a lower pH enhances crack density (see Fig3-19).

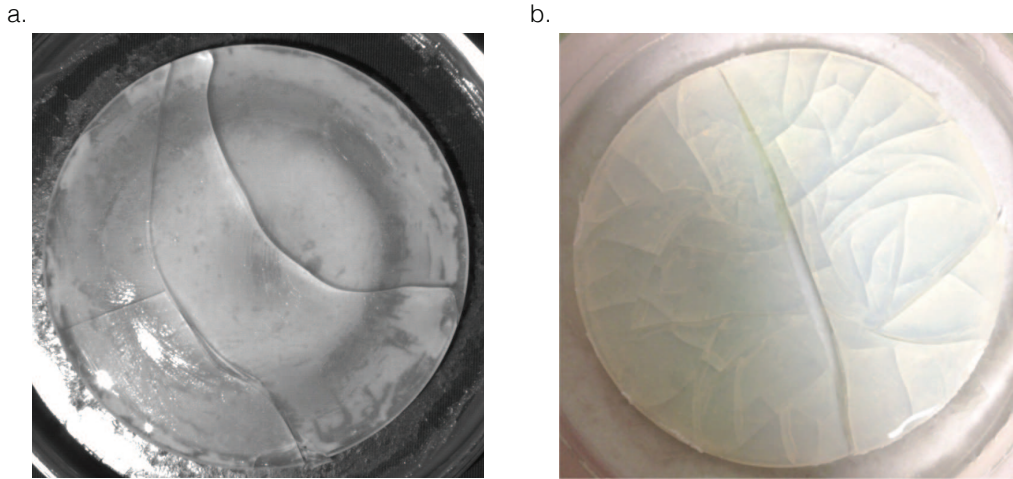


Figure 3-19: Picture of the free surface of sample made with 12nm particles at $\phi_0 = 20\%$ exhibiting a crack density in regime 2 of (a) 0.7, (b) 14.

From Fig3-19a, χ being the local saturation, one can observe that whether the sample crack a little or to a large extent in the second regime for cracks, no variations are observed on the drying curves. Additionally, Fig3-19b shows that the water distribution within the sample in regime B remains identical regardless of the number of cracks. Therefore, we conclude that there is no influence of the cracks in regime 2 on the drying kinetics.

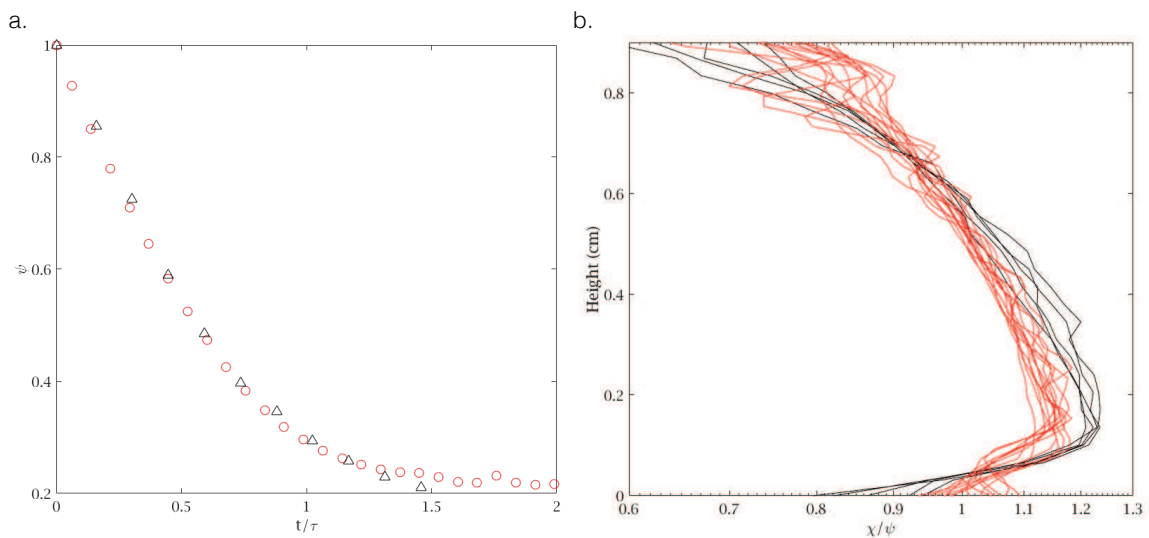


Figure 3-20 Drying curves (a) and rescaled (local to average) saturation profiles (b) in regime B for gel exhibiting a crack density of (black) 0.7, (red) 14

9 - Conclusion on the section

We have shown that under convective drying, a nano-porous gel undertakes two drying stages associated with two cracking regimes. During the first stage, the sample delaminates and shrinks isotropically while remaining fully saturated, this enables a high rate of evaporation for the material; whereas the second drying period, macroscopically occurring as the sample turns opalescent, features the desaturation process associated with a decreasing drying rate, apparently common to every sample. Specifically, a homogeneous water distribution throughout the whole sample is observed.

A variable number of pads can develop during the first stage, in the form of a step like evolution for crack nucleation. This phenomenon may induce significant variations of the drying rate, as evaporation can also occur along the new vertical sides of the sample. On the contrary the number of cracks nucleating during desaturation do not drain water, and therefore do not influence on the drying rate.

Eventually, taking into account the shape of the airflow velocity field around and inside a crack cavity during the first drying regime, we were able to establish a simple model that makes it possible to well predict the observed variations in the drying rate of the material depending on the number of pads formed. We showed that the duration of the initial stage of drying decreases when the number of pads increases and tends to an asymptotic value. As a consequence, the use of strongly adhering substrates, leading to a large crack density, will tend to reduce the drying duration. Moreover, using larger intensity of the air flux blown on the sample should result in an increase of the crack density as it is commonly stated to increases the drying stress generated in the material. This implies that the drying duration could further be decreased strictly from the air flux increase.

B - Study of Sponges during drying, a model deformable porous media with a wide pore-size distribution

Through this study of convective drying of cellulose sponges with different pore size distributions we aim at bringing further understanding in the mechanism of drying and of deformations at play. To identify the mechanisms responsible for the drying kinetics observed in these sponges, we first put their drying regimes in relation with their macroscopic deformation; we then look at the evolution of their water content along those lines. Afterwards, to gain greater understanding in the role of capillary equilibration in both samples, we measure local pore deformation at the sample free surface in time. Eventually, we qualitatively conclude on the dynamics observed. Drying of sponges is performed using the set-up described in - Chapter 2 -C -1 - .

1 - Drying curves

We recall the main characteristics of the two samples earlier studied in Chapter 2 -B -4 - : water perfectly wets the green sponge, presenting a wide pore size distribution, and partially wets the blue sponge ($\theta_w = 65^\circ$), which distribution is narrower.

i. Reproducibility of the measurement

In this section we measure the evolution of the mass of water within the samples with time or their derivative. Our measurements of the mass data with time are highly reproducible as on average there is a 6% variability between two identical tests. To prevent evaporation from the side walls of the sponge, samples are placed in plastic petri dishes of their dimensions once filled with the appropriate solvent (6cm diameter). From Fig Fig3-21b, representing the drying curves of two identical samples placed in a hydrophobic and hydrophilic petri dish; as both curves super-impose, we conclude that neither the nature of the dish walls nor the contact between the sponge and the dish affect the drying kinetics we observe. The error between the two curves remains inferior to 6%.

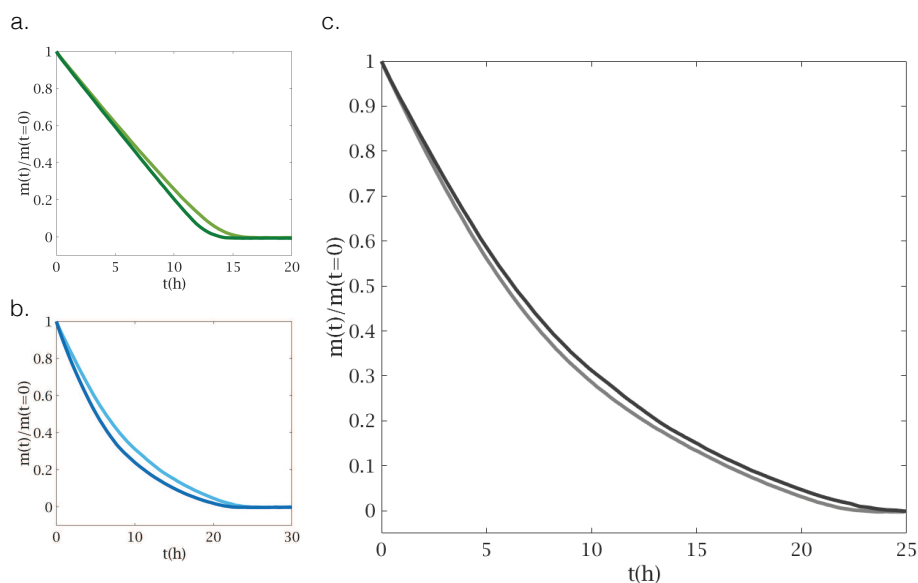


Figure 3-21: Drying curves showing the reproducibility for the measurement of (a) the green sponge, (b) the blue sponge; (c) shows the drying curves obtained for blue sponge in a (grey) hydrophobic, (black) hydrophilic petri dish.

ii. Influence of airflow velocity on the drying mechanism

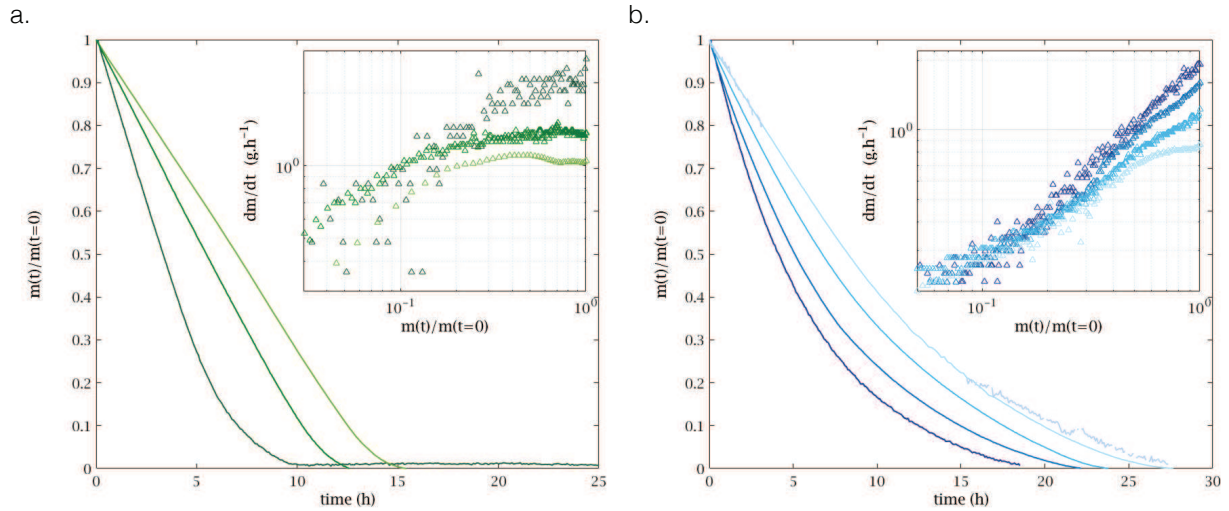


Figure 3-22: Drying curve for (a) The green sponge, for an air flux velocity of (dark green) 3m/s, (lighter green) 0.8m/s, (lighter green), 0.6m/s; (b) The blue sponge for air flux velocity of (dark blue) 3m/s, (lighter blue) 0.6m/s, (lighter blue) 0.3m/s, (lighter blue) 0.2m/s, (lighter blue) 0.01m/s. Insets present the corresponding drying rate for each color matching drying curve.

Figure 3-21a depicts the drying curves and the drying rate of both sponges. From the drying curves of the green sponge, 2 main drying regimes are observed: at first a constant loss of mass is observed and lasts until low sample saturation ($m(t)/m(t=0) \sim 0.1$), then drying progressively slows down. This is particularly visible in the inset graph. From this latter graph, we may also observe that the drying rate of the green sponge, in the first regime, depends on the velocity of the convective air flux applied at its surface (see the different values for the plateaus in Insert a); this is however not verified in the second regime as all curve super-impose.

On Figure 3-21b, one observes that drying progressively slows down with time and the distinction of two different drying regimes becomes less evident. This tendency is confirmed by the study of the drying rate in inset b which shows the rates follow a constant decrease in a log-log representation. Now varying the velocity of the external air flux, if we hardly differentiate between two periods in this same graph, similarly to the case of the green sponge, it seems like a first period exists where the rate of evaporation is sensitive to the airflow velocity; this period is followed by a second period where this is not verified anymore and all curves super-impose. Note that no precise value of the transition saturation can be identified from this set of data.

Therefore, the major difference between the drying kinetics of the two sponges lies in the existence or absence of a constant rate period.

i. Influence of surface affinity on drying kinetics of the blue sponge

As seen in Chapter 2 -B -4 - water has less affinity with the blue sponge ($\theta_w = 65^\circ$) than the green sponge (perfect wetting). We however found that ethanol ($\mu_{eth} = 0.6 \text{ mPa} \cdot \text{s}^{-1}$) perfectly wets the blue sponge, as a drop of this liquid is directly absorbed in the porous media, similarly to water with the green sponge. Now let's look at the drying kinetics of the blue sponge filled with ethanol and compare them to the case of water.

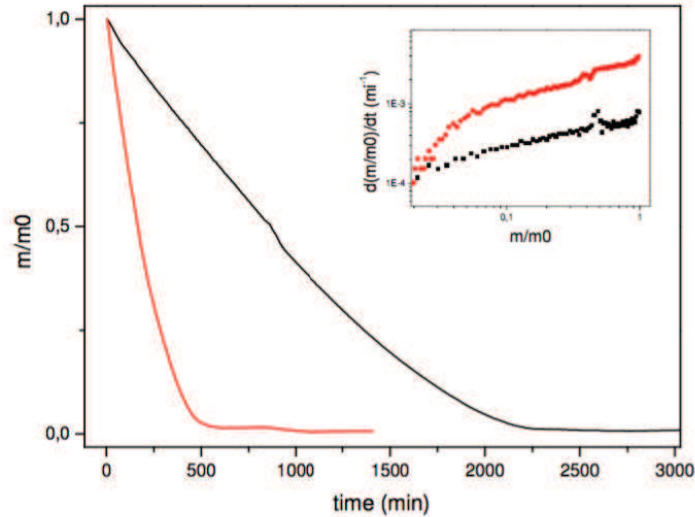


Figure 3-23: (a) Drying curve for the blue sponge filled with (black) water, (red) Ethanol for an external airflow velocity of 0.6m/s. Insets present the corresponding drying rate for each color matching curve.

Fig3-22 presents the drying curves and drying rates for the blue sponge filled with water then methanol. Interestingly, despite the difference in wetting properties for the two liquids, the drying curves for ethanol and water appear very similar in their shape. Inset a confirms this saying as in a log-log plot the drying rates for the two sponges are parallel to each other at all time, meaning that these curves are roughly shifted from a factor 4.5. we observed that the blue sponge filled with ethanol approximately dries 4.5 times faster than its counterpart filled with water. Note that this matches the volatility ratio between methanol and water (~ 4). Let's now observe the evolution of shape of each samples during the process.

2 - Macroscopic deformations

Looking at sponges' free surface during drying one can follow their radial deformation. On one hand, the green sponge substantially dries before its matrix macroscopically contract (contraction starting at Fig3-24A, picture 3). On the corresponding movie the contraction of this sponge is relatively sudden. On the other hand, the blue sponge does not seem to contract at all during the process (see Fig3-24B).

Note that the radial contraction of the green sponge (in the order of 20%) occurs during evaporation of the last 6-7% of water content. Additionally, the vertical contraction of both sponges appears negligible from measurement of the sample height before and after the test.

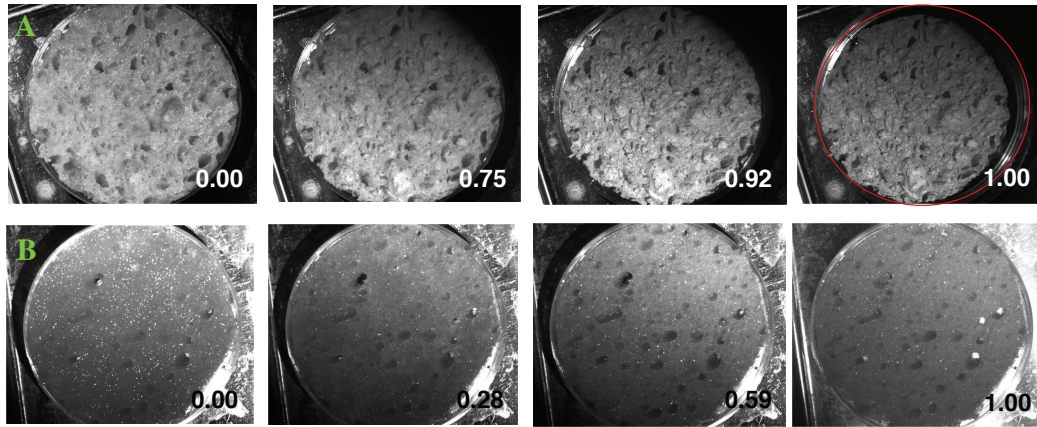


Figure 3-24 observation of the free surface of (row A) the green sponge (row B) the blue sponge during drying. The numbers in white or black at the bottom refers to the current time to the total drying time (time needed for the drying curve to reach a plateau). The red circle on the last picture of Row A shows the initial size of the green sponge. The dish has a diameter of 6cm.

3 - Drying Scheme

The green sponge apparently exhibits the typical drying rate evolution expected from a coarse porous media filled with a wetting fluid during desiccation: a first CRP followed by a FRP (see Fig3-21a). Also note that this sample contracts radially at the end of the process (see Fig3-22A); therefore one can conclude that unlike the situation encountered with nano-gels, contraction here does not play a role in the extend of the CRP for the green sponge.

The blue sponge shows the absence of a CRP (see Fig3-21b) and macroscopic shrinkage (see Fig3-22B); rather a FRP takes place from the very beginning of test (see Fig3-21). Additionally, we remark that whether the fluid within the sponge strongly or poorly wets the solid matrix, the drying rates measured remains parallel, in a log-log representation and over the whole test (see inset in Fig3-23); this piece of information shows that the evolution of the rate of drying is independent of the wetting properties of the inner fluid, be it water or ethanol.

From this first analysis, we conclude that if the green sponge follows the classical scheme for drying of a wetted porous media while slightly contracting at the end of the process, this is not the case of the blue sponge that shows a FRP starting from the beginning of the test. This behavior is surprising as it is usually encountered during drying of non-wetting fluids within porous structures or porous medium presenting very low permeability, which does not seem to be the case here as the sponge is hydrophilic and the pore size distribution centred around 500microns. Let's look at the water distribution within the sample to gain better understanding.

4 - MRI study of the water distribution within the sample during desiccation

i. MRI sequence

In this section, we use a dual spin echo sequence on the horizontal and vertical axis (detailed in the Chapter 2 -A -2 - Water is the only solvent used during drying. Drying is performed within the MRI spectrometer (see Chapter 2 -C -1 - ii.). Note that all profiles presented are extrapolated with Eq2.4; specifically, since the green sponge shows a large pore size distribution and relaxation occurs at its surface, there may be a slight uncertainty on the measurement. For clarity, we study the two sponges individually, starting with the green sponge.

ii. Distribution of water in the green sponge

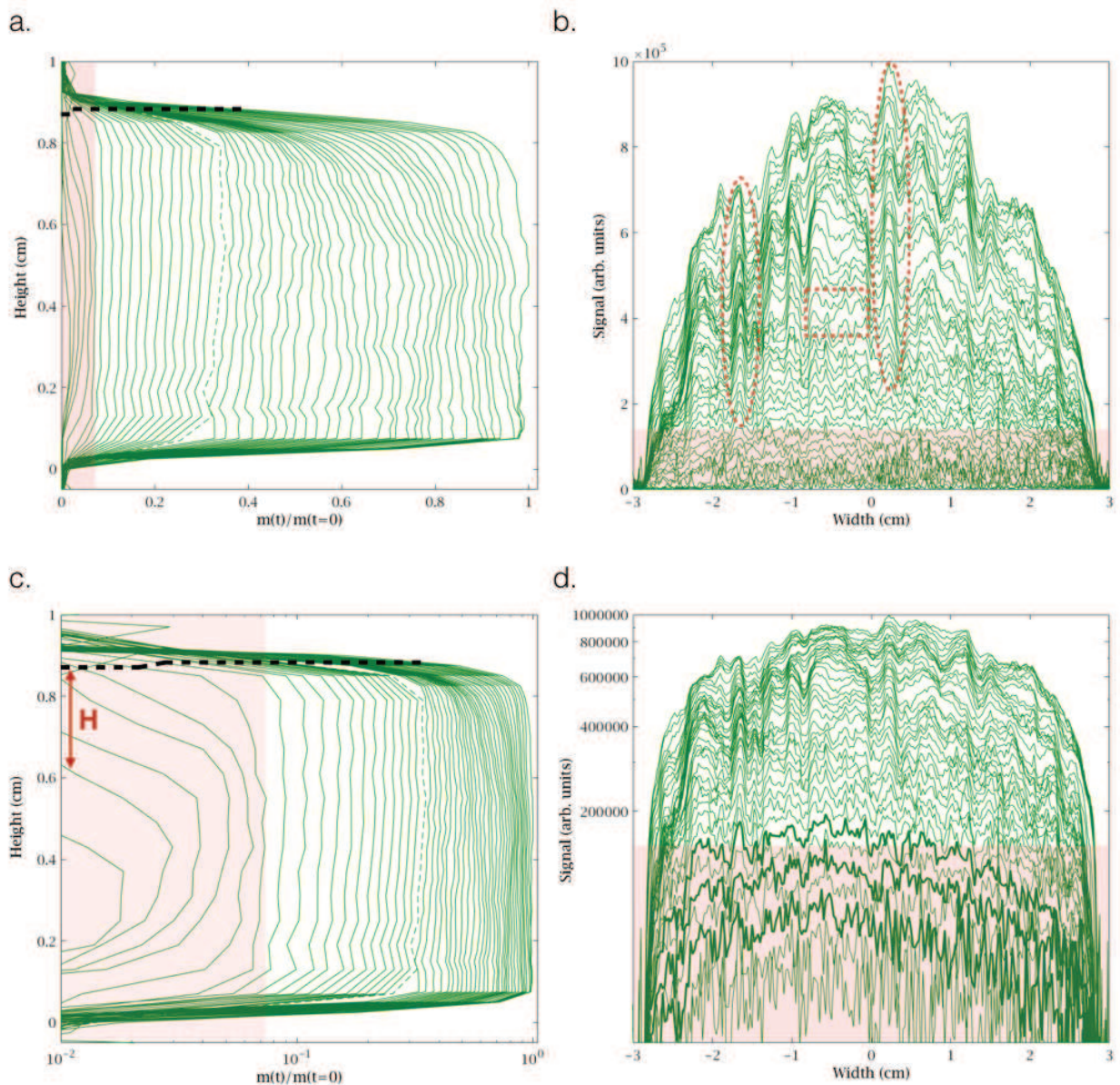


Figure 3-25: The continuous curves from top to bottom correspond to profiles of the water content within the green sponge every 1h, (a) and (c) along the vertical axis, (b) and (d) along an horizontal axis. (c) and (d) are logarithmic representations of (a) and (b) respectively. The black dashed line on (a) and (c) correspond to the location of the sample free surface (see Chapter 2 -C -1 - ii.). The red shaded area indicates the second drying regime. The Dashed squares and ellipses are indicators used later in the analysis (see text). Measurement parameters are changed on the vertical axis at the dashed line profile. The first set of profiles on the z axis shows a spatial resolution of 250 μ m per pixel, the second set 600 μ m; on the horizontal axis, the whole measurement shows a spatial resolution 250 μ m. Note the red shaded areas may not correspond to the same signal amplitude on the x and z axis as measurement parameters are different, they however correspond to the same saturation state. In (d) bold profiles are an indicator for the following analysis (see text). Details for measurement parameter at the end of the section.

Figure3-25a and c, presents measurements of water content along the vertical axis for the green sponge as well as the evolution of the sample height. We observe a first period where the height of the sample remains unchanged and water, homogeneously distributed throughout the sample (profiles are straight and vertical in the sample thickness), evaporates; therefore, in this phase the sample desaturates homogeneously. This proceeds until a saturation of ~ 6 to 7% is reached (see the red area) and suddenly a vertical contraction of the matrix occurs, the final height of the sample is reached, and a dry region of height (H) starts to develop from the free surface of the sponge (see Fig3-25c)

Graph b and d, presents the measurement of water along a horizontal axis for the same sample. Particularly, before the red shaded area is reached, one can observe a substantial deviations of the profile shapes from the water profile expected from the measurement of a cylindrical container (semi-circle). However, once we enter the red shaded area, the profile shape become closer to this shape (see Fig3-25).

Looking at the variations of the amplitude on the horizontal profiles in Fig3-25b in deeper details. These variations are seen to conserve their location on the x axis of the graphic from a profile to the other and their amplitude to decrease during drying (see red dashed ellipses on Fig3-25 for example). Note that this Scheme is particularly visible until the red area is reached, afterward, even if being quite noisy, profiles seem to evolve quite parallel to each other's (see Fig3-25d). As these variations do not constitute noise fluctuations of the measurement, they likely reflect local average on the quantity of water in pore clusters.

iii. Distribution of water in the blue sponge

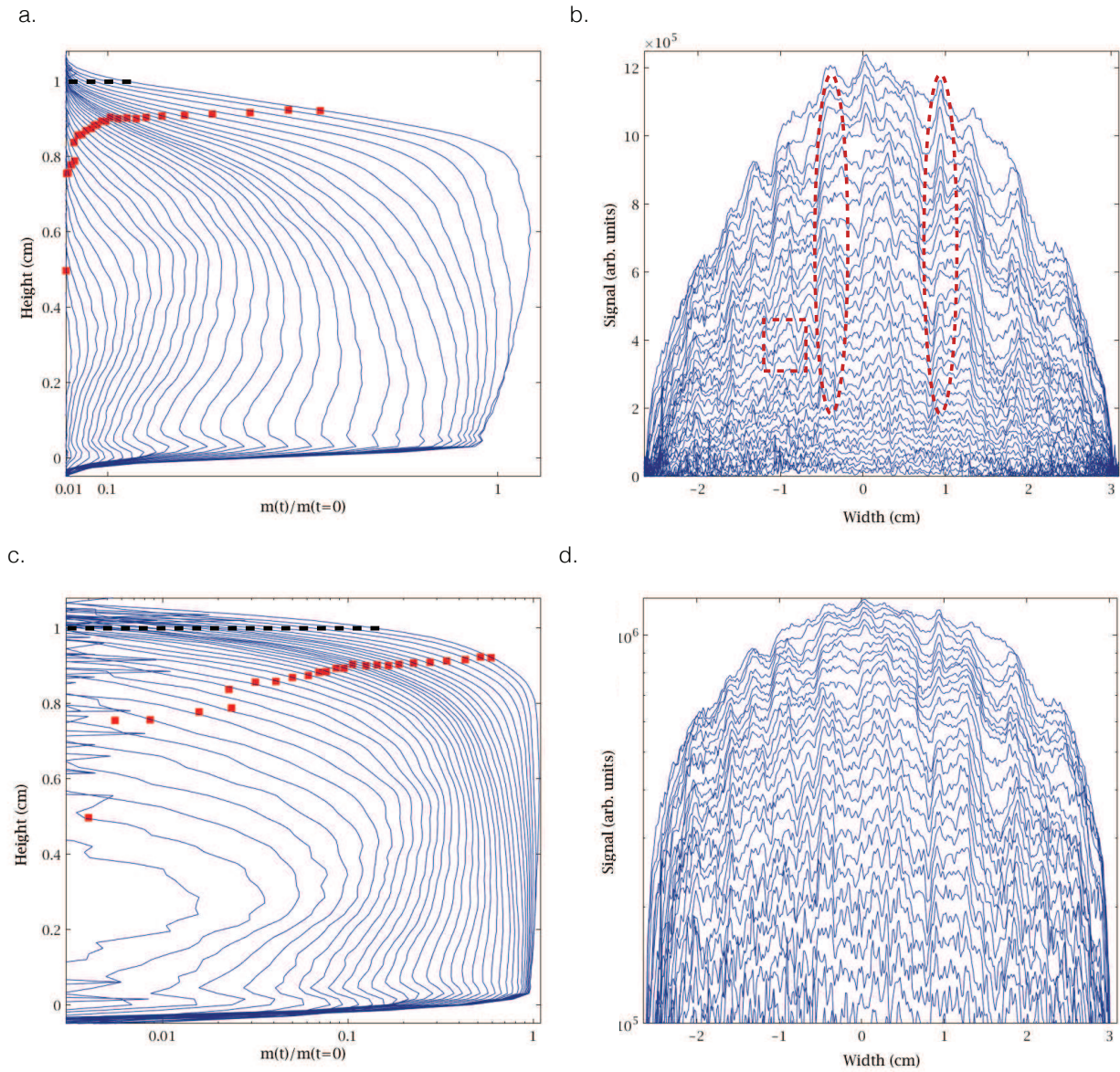


Figure 3-26: The continuous curves from top to bottom correspond to profiles of the water content within the blue sponge every 2h30min, (a) and (c) along the vertical axis, (b) and (d) along an horizontal axis. (c) and (d) are logarithmic representations of (a) and (d) respectively. The black dashed line on (a) and (c) correspond to the location of the sample free surface (see Chapter 2 -C -1 - ii.). The resolution of the measurements is (z axis) $200\mu\text{m}$ (x axis) $250\mu\text{m}$. The Dashed squares and circles are indicators used in the analysis (see text). The dashed squares and ellipses are indicators used later in the analysis (see text). The red squares show the position of the wet interface within the sample one can expect modelling the drying kinetics by the development of dry region (see text). Details for measurement parameter at the end of the section.

In Fig3-26, graph a and c show the water distribution along the vertical axis quite different from the one observed in the blue sponge. Note that the sample height is seen to remain constant throughout the test. We observe a first regime where a continuous water distribution is spotted from bottom to the top of the sample (first 7 profiles on Fig26-c); the regime is quickly followed by a regime where a dry region develops. Interestingly, all along desiccation, the profiles indicate the presence of areas of significant gradients in saturation: the profiles are relatively flat toward the bottom and significantly bending approaching the free surface. Note that at the very bottom of the sample, the saturation drops quite fast with desiccation, as no drying is expected from the bottom of the sample (this face not being exposed to the airflow) we attribute this decrease to the emptying of a very large pore spanning the sample.

Similarly, to the green sponge, Graph b and d in Fig3-26 presents profiles with shape that deviate from the shape of a semi-circle. If the location of these deviations remains fixed with drying (same abscise) their amplitude decreases with drying.

5 - Scheme for the drying kinetics

The previous results on the green sponge show that the regime of homogeneous distribution of water within the sample is associated to a constant drying rate period (see Fig3-21a and Fig3-26a). This could also be seen directly on Fig3-26a as profiles appear evenly spaced in saturation with time. For the same sponge, further drying triggers a falling rate period (Fig3-21a) that originates from the development of a dry region (red shaded area in Fig3-26a and c). While the total radial contraction of the sponge is in the order of 20%, its vertical contraction is negligible and we observe that the sample follows the classic scheme for drying of wetted porous media. However, the vertical 1D profiles reveal a unexpected phenomenon: during the falling rate period, the saturation in the wet region is not supposed to vary, according to the theory (Chapter 1), and looking at Fig3-25c, a clear variation of the saturation is seen in this period. As no drying is expected from the sides of the sample considering the little contraction (see Fig3-24A), this progressive desaturation within the wet region suggests that capillary equilibration takes place and therefore a continuous liquid network still exist in the wet region despite the very low moisture content.

The drying kinetics for the blue sponge remains hard to describe. Particularly, we learn from Fig3-26c that a dry region starts to develop quite early in the sample (~ 0.9 in saturation) as expected from the drying curve. Also, the height of the measured dry region does not explain the FRP observed; in fact, we plotted (spotted with red squares) the height where the wet interface should locate to match the drying kinetics of the sample with the model of vapor diffusion through a dry region. One can clearly see that the two locations do not match (see Fig3-26c), instead, gradients in water content exist in the sample. Note that simulations of flow in porous media presenting a narrow pore size distribution suggested such distribution in Chapter 1 -B -7 - .

If the kinetics of drying for both sponges are clearer now, still we do not find a satisfying answer to the origin of the dry front in the blue sponge. Specifically, because the water distribution in this sponge seems to be related to the pore size distribution, it is interesting to look at how the solid

matrix deforms at the pore-scale level and how this distribution evolves during drying. We may yield additional information about the mechanism or structural aspect governing the distribution of water within this blue sponge.

6 - Study of the drying mechanism through pore emptying dynamics

Let's start by looking at the information we yield measuring the global T_2 distribution during drying as it may reflect the global scheme for pore emptying. We then look at our MRI profiles in deeper details to yield local information on the drying of pore clusters and eventually we follow the evolution of the distribution of pores sizes at the free surface in time.

i. Evolution of the T_2 spectrum during drying

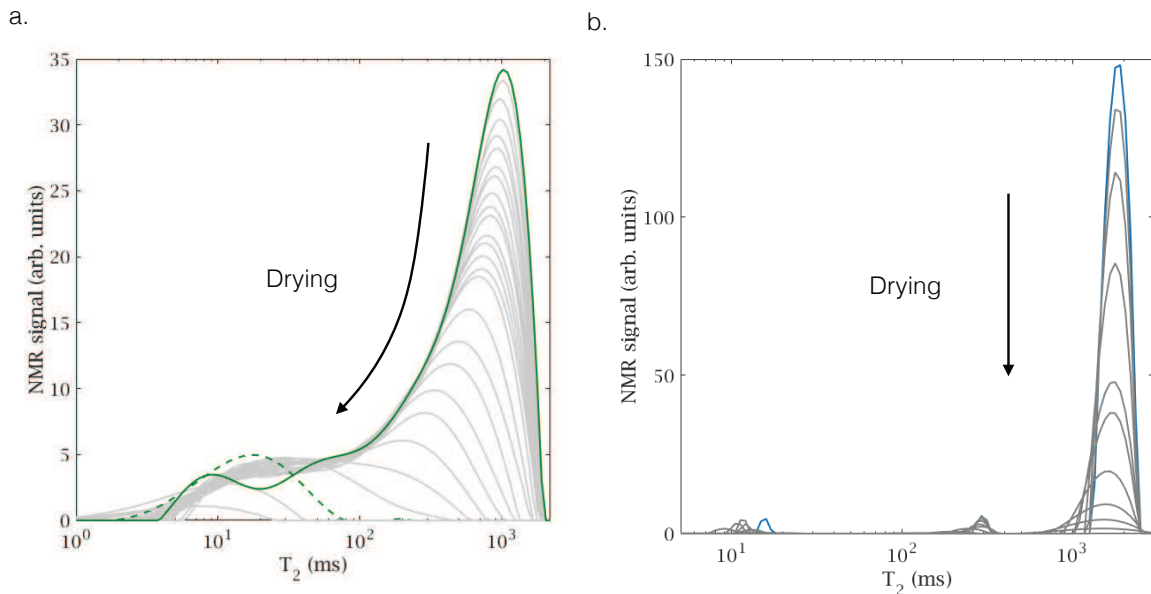


Figure 3-27: Evolution of the T_2 distribution within (a) the green sponge, (b) the blue sponge during drying. The continuous distribution profile is the initial profile, in (a) the dashed green distribution profile in corresponds to the last profile before contraction of the solid matrix occurs.

Fig3-28 presents the evolution of the global T_2 time distribution within both sponges during drying. Note that, the amplitude of the signal is proportional to the overall water content and the T_2 value is proportional to an absolute pore size (if the relaxation mainly occurs at the pore walls, see Chapter 2 -A -2 - iv.). Therefore studying T_2 with its associated amplitude translates into studying the water content in the different pores sizes during drying.

In Fig3-27a we observe a wide initial T_2 distribution for the green sponge that progressively narrows down to lower T_2 values and lower global amplitude with drying (follow the arrow in Fig3-27a). Before contraction (dashed green peak), the peak measured is very slim and spreads between a low range of T_2 values (30 to 50ms). Additionally, we remark the amplitude of the peak at this precise stage is very close to the initial one for the same T_2 range (compare dashed

profiles to the first few profiles in green or grey). Eventually, the peak loses amplitude and disappears.

Similarly, on Fig3-27b, we observe a single peak at $T_2 \sim 2.5 \text{sec}$ therefore indicating that the relaxation of water on the sponge surface is very low (as expected from Chapter 2 -B -4 - ii.) and equal to the typical spin-spin relaxation for bulk water. Likely, water does not relax at the blue sponge surface at all, we therefore cannot exploit this measurement in terms of pore sizes. However, this graph constitutes a good reference point as it reflects drying of bulk water.

7 - Analysis of pore emptying dynamics

i. Global T_2

From the progressive T_2 distribution decreasing to lower amplitude and to the lower values in to Fig3-27a, one can conclude that in this sample pores empty by order of size: the bigger pores emptying first. Additionally, right before the sample starts to contract (Fig3-27a, dashed profile) the narrow peak observed presenting the same amplitude than initially, suggests that until contraction, the smallest porosity remains saturated throughout the whole sample. In fact, the homogeneous water distribution spotted on the 1D profiles in Fig3-25a and b at this precise moment (dashed profiles), tend to confirm this statement. Finally, by observing in Fig2-18 we note that the smallest porosity covers the whole solid matrix, therefore we conclude that only the smallest porosity corresponding to a pore size in the range of $30 \text{ms} < T_2 < 50 \text{ms}$ triggers contraction in the green sponge.

No additional information can be yield on the blue sponge at this stage. However, we have an idea of the general scheme for pore emptying for the green sponge, let's carry out a comparative analysis between the MRI profiles of the 2 sponges seen earlier on in Fig3-25 et Fig3-26.

ii. 1D profiles and Local dynamics

In the horizontal profiles in water content presented in Fig3-25c and d and Fig3-26c and d, we observed the existence of a substantial deviation of the profiles shape from a semi-circle. In fact, these deviations do not constitute measurement noise, the sample saturation being high and therefore the signal to noise ratio as well ($S/N > 10$ at 0.05 saturation). Additionally, for both samples, these deviations keep their locations from one profile to the other and their amplitude decreases. These deviations therefore likely correspond to water located in pore clusters including large and medium sized pores within the sample as they tend to disappear slowly with desiccation. Following the variations of the signal in these clusters therefore reflects the equilibration process at play, let's look at these variations in detail.

Following the evolution of the profile shape in the red dashed ellipses on Fig3-25b and Fig3-26b, we remark that the decrease in the amplitude of the deviations is non-constant with time (from one profile to the other. Let's be quantitative on this last point: we measure the rate of variations in the amplitude of these deviations with time: $d(S/S_0)/dt$ for the 2 sponges at 2 different locations (pixels) on the x axis: for a same pixel, S is the signal amplitude measured time t and S_0 the initial

signal (at $t=0$). We compare the evolution of these rates to the rate of the overall signal. This measurement therefore consists in looking at the drying rate of local pore clusters and compare it to the overall drying rate of the sponge.

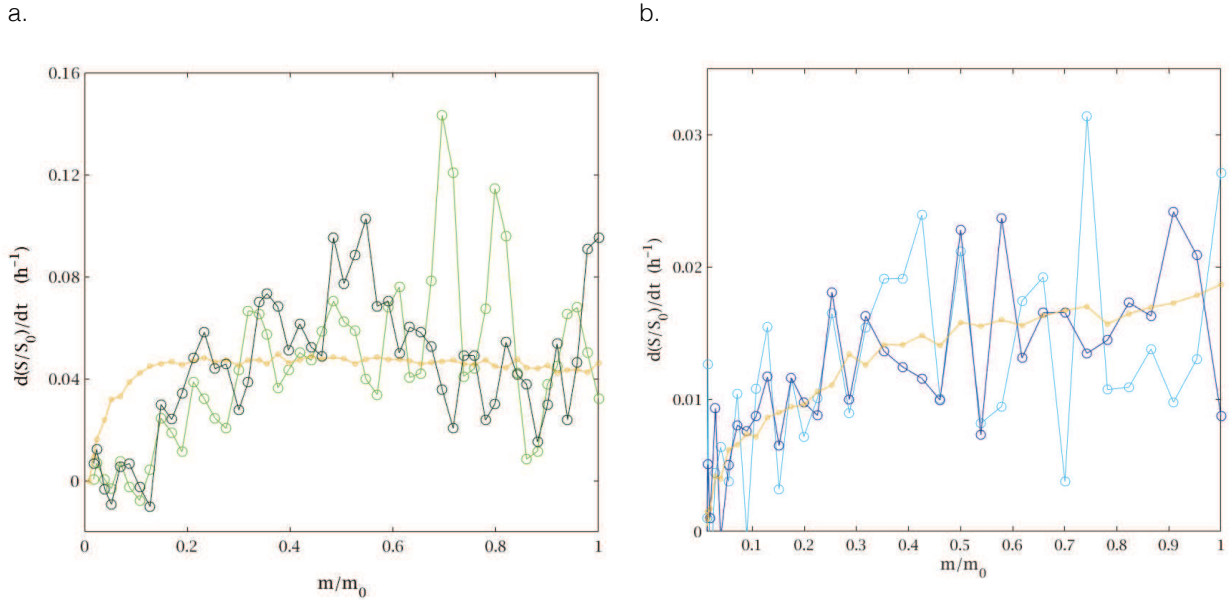


Figure 3-28: Drying rate variations in (a) the green sponge: (yellow) globally computed as the time derivative of the integral of the 1D profiles in Fig3-26b, (light green) pixel at 0.2cm and (dark green) pixel at -1.8cm on Fig3-26b; (b) in the blue sponge (yellow) globally computed as the time derivative of the integral of the 1D profiles in Fig3-27b, (light blue) pixel 0.945cm and (dark blue) pixel at -0.87cm on Fig3-27b.

Fig3-28 presents a comparison between the local drying rate in selected pixels and global drying rate for both samples. One can observe the drying rate of these clusters is not steady with time but rather shows successive bumps for both sponges. These local fluctuations in the drying rates are typically expected from capillary equilibration. Specifically, we observe that despite the large distance separating the two pixels these bumps show strong correlation, either acting in opposite phase to the global drying rate (see Fig3-28a for m/m_0 between 0.6 -0.5 and Fig3-28b for m/m_0 between 0.45-0.35) or in phase (see Fig3-28a for m/m_0 between 0.9-0.8 and Fig3-28b for m/m_0 between 1-0.9). This might suggest a continuous liquid network within the wet region of the sample at all time and the exchange of liquid between different regions within the sample, however additional study is needed to model this mechanism.

This analysis fails to explain the development of a dry region; however, it shows that the same pore emptying mechanism takes place in two samples, therefore that even if an apparent dry region develops capillary equilibration still occurs. Let's look at the evolution of the structure down to the pore level from the sample free surface; additional pieces of information may be found.

iii. Macroscopic measurement, optical microscopy

As shown in Chapter 2 -B -4 - , we can measure the individual pore sizes present at the free surface of the samples. Let's now look at the evolution of the distribution of pore size during drying.

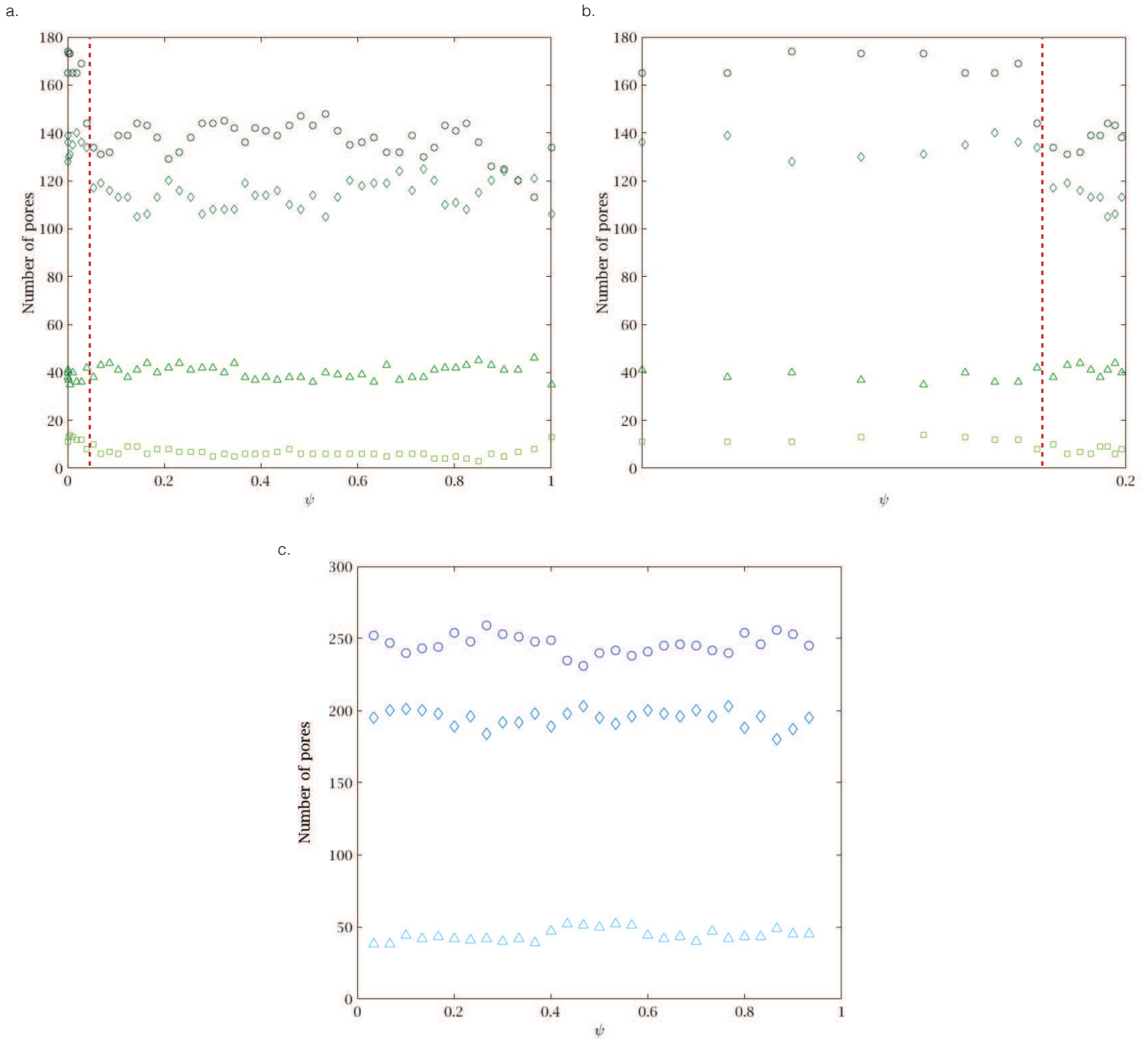


Figure 3-29: Evolution of the number of pores spotted in various size groups by the image analysis software (detailed in Annexes 1) during drying of (a) and (b) the green (c) the blue sponge. (b) is a zoom on the regime of low moisture content from (a). For (a) and (b), 4 pore size groups are followed (green circles) 50-250µm, (green diamonds) 300-700µm, (green triangles) 750-2000µm, (light squares) 2050-6000µm. The red dashed line announces the macroscopic contraction of the sponge. For (b) only 3 ranges of sizes are

followed (blue circles) 0-250 μm , (blue diamond's) 300-450 μm , (blue triangles) 500-6000 μm .

Fig3-29 illustrates the evolution of the number of pores we spot in groups encompassing different pore sizes during drying of both sponges. Note that the bandwidth of the groups are chosen arbitrarily from the initial pore size distribution (see Chapter 2 -B -4 - iii.) and supposedly correspond to the small, medium and larger fractions of the porosity. On Fig3-29a, observing the green sponge, we distinguish 2 regimes in this evolution of the number of pores: before contraction occurs (red dashed line), we measure a steady average quantity of pores in each groups and after contraction a sudden increase of the number of pores in the groups containing the smallest pores ($\sim 30\%$ increase in the number of pores under 250microns, see Fig3-29b). As for the blue sponge, the number of pores spotted in each groups remains steady during the test.

Looking at the variations in these curves in detail, we observe the presence of oscillations in the number of pores detected in each groups and for both samples (specifically visible in the smallest fraction of the porosity for both samples) and these oscillations last until full evaporation has proceed ($\psi = 0$). Additionally, we can see that the groups representing smallest pores evolve in opposite phasing. Finally, it seems like a higher number of oscillations is observed in the green sponge.

iv. Capillary equilibration process

Both Fig3-28 and Fig3-29 constitute measurement of the dynamics of the capillary equilibration process; It is useful to recall that Fig3-28 shows a measurement based on the quantity of water within pore clusters and Fig3-29 reflects the deformation of the free surface of solid matrix thanks to the measurement of individual pore sizes, therefore these measurements are independent of each other. However, both measurements showed that capillary equilibration is a fluctuating process taking place all along desiccation. If fluctuations are expected, the extent of the mechanism to low moisture content is not and especially during the FRP when dry region develops within the sample. In fact, it is assumed (Chapter 2 ; The Falling rate period) that when a dry region develops from the sample free surface, its saturation remains constant and the liquid network becomes discontinuous [9] and no capillary equilibration is expected to take place. In fact, none of the two situations are observed, even the saturation of the wet region varies for both sponges during the FRP (see the saturation level in Fig3-26a and Fig3-26b). We will not analyse further this phenomenon on these samples.

Note that this pore emptying analysis fails to give us additional information on the reason for the dry front to develop in the blue sponge. Lastly, we observe drying of at the pore scale thanks to SEM wet imaging.

8 - Wet imaging for the blue sponge

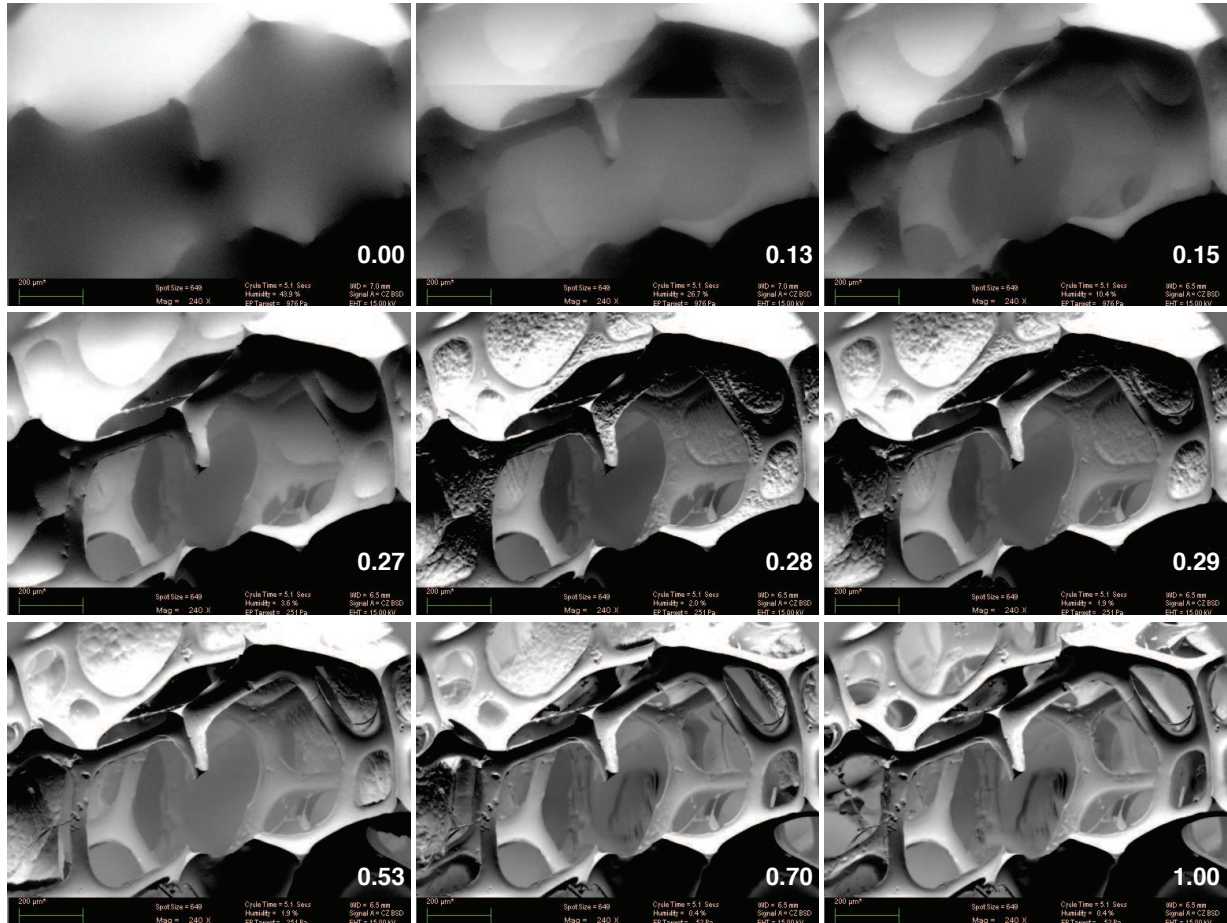


Figure 3-30: Drying of the blue sponge within the environmental SEM, drying is performed at $RH \sim 5\%$, and $50^\circ C$. Numbers in the lower right corner indicate the current to total drying time.

Fig3-30 presents drying of the blue sponge at the pore scale, picture are taken from above. In the initial state (Fig3-30 at 0.00) the sponge is completely saturated. Very quickly, we observe that the biggest pores empty with priority (at 0.15 saturation the biggest pore at the centre of the image has already emptied), while at its periphery tinier pores (holes at the pore walls) are still saturated. Additionally, following the aspect of the surface of the solid matrix (looking at the pore branches), one can observe the evolution of its wetting with time: we observe a bumpy texture appearing at 0.28 that further slides toward the bottom of the sample at 0.29. Likely this witnesses de-wetting of the solid matrix and the recession of water film toward the bottom of the sample. On these images, no contraction is visible, but when playing the corresponding movie, a tiny bit of contraction is observed (2-3%).

9 - Conclusion of the section

We have shown that under convective, on one hand, the green sponge, showing a wide pore size distribution and perfect wetting with water exhibits the typical drying kinetics reviewed in Chapter 1 a CRP from which it starts to desaturate, followed by a FRP. This sample is seen to contract when the FRP is triggered. Interestingly, the study on the dynamics of the capillary equilibration process shows that during the FRP, this process keeps taking place and the saturation of the wet region decreases with further advance of the desiccation process.

On the other hand, the blue sponge showing a narrower pore size distribution than the green sponge and partial wetting with water, exhibits a decreasing drying rate from the beginning of the test. If the water distribution within the sample seems to match predictions from numerical simulations (see Chapter 1 -B -7 -) we are unsure of the reasons leading to the development of this region. Note that this study constitutes the first NMR study of capillary equilibration.

C -Conclusion

In this chapter we studied the convective drying of deformable materials such as nano-gels and sponges. More precisely, we observed how the degree of deformation (number of cracks, shrinkage), the affinity of the solvent with the pore walls or the pore size distribution of the solid matrix, may influence on the drying rate and the water distribution of the samples considered

We saw that under similar airflow conditions (velocity and vapor density), the same type of deformation can be triggered at different saturation state of the porous media: be it cracking or shrinking; ultimately, these phenomena do not necessarily impact on the drying kinetics of the material. However, in the particular case of a material cracking, shrinking and negligibly bending while remaining saturated, we are able to predict the drying curve of a material by looking at the velocity field of the airflow. Note that our drying rate predictions may be limited to systems where the hypothesis of a tangential flow at the sample free surface can be considered.

Following the water content within such materials during drying revealed interesting situations one may encounter varying the pore size distribution of the structure or the wetting properties of the fluid; Typically looking at the water distribution in sponges during the FRP probed the existence of a continuous liquid network and capillary equilibration to take place at very low moisture content. Last but not least, if we systematically end up observing development of a dry region for coarse porous structures during desiccation, in nano-gels a homogeneous desaturation occurs.

Chapter 4 - Drying regimes in homogeneous porous media from macro to nano-scale

In this chapter, through detailed MRI visualizations only, we look at the drying kinetics and the water distribution in homogeneous and compact porous medium with pore sizes ranging from a couple of microns to a few nanometers.

1 - Experimental details

i. Protocol

In this study, we follow drying of 9 homogeneous porous media made with particles diameter of $45\mu\text{m}$, $1.5\mu\text{m}$, $1\mu\text{m}$, 750nm , 300nm , 80nm , 40nm , 12nm and 6nm . Note that the largest sample is made with $45\mu\text{m}$ diameter glass beads sintered by heating but all the others one are made with silica beads sintered through viscous sintering (as described in Chapter 2 -B -3 -). Drying is performed within the MRI spectrometer (set-up detailed in Chapter 2 -C -1 - ii.). A dry air ($\rho_0 = 0$) is blown vertically in a turbulent regime to the sample free surface, the velocity of the airflow is $0.02\text{m}\cdot\text{s}^{-1}$.

This study is entirely based on the measurement of concentration profiles of water along the vertical axis of the samples here mentioned; for this purpose a Dual Spin-Echo NMR profiling technique is used (see Chapter 2 -A -2 - iii. for additional details). Details of the measurement for each sample are presented Chapter 6. As seen in the previous chapter, this technique offers great reproducibility (see Chapter 3 -A -3 - i. .

ii. Physical framework

As we are carrying out a multiscale approach (micron to nano scale), it is necessary to assess the impact of gravity on the shape of the water profile we present. For each sample, we compute the corresponding Bond Number (see Chapter 1 -A -4 -) its value being extremely low and greatly inferior to 1 in any case, we conclude that gravity negligibly impacts the menisci curvature in our porous media and therefore the shape of the profiles we present; eventually, liquid flow can be considered capillary driven only.

2 - Observation of the water distribution with varying pore size

Figure 4-1 presents the 1D profiles we yield drying the previous samples until full evaporation has proceeded. Note that we provide profiles reaching 0% saturation. In fact, there is a limit to the amount of water one can realistically measure thanks to the NMR profiling technique we employ. This limit is typically reached when the characteristic relaxation time of water within the sample becomes of the order of magnitude of the echo times set as experimental parameters, (see Chapter 2 -A -2 - iii. Therefore, in Fig4-1 regions where the saturation is null (corresponding NMR signal

is null) do not necessarily correspond to an actual dry region but an apparent dry region where likely thin films of water may still cover the particles. Additionally, we must mention that for clarify reasons, low saturation profiles were smoothed with a Gaussian filter (see Chapter 2 -A -2 - vii.) for samples made with 80nm, 300nm and 750nm. Note that this smoothing enables to keep the initial shape of the profile. Let's first describe this Figure.

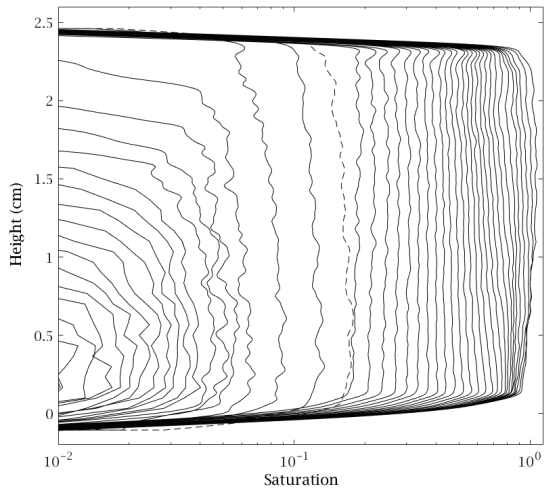
In Fig4-1, for bead sizes down to $1.5\mu\text{m}$, we observe a first period where saturation decreases while the profiles remain perfectly parallel to each other in a logarithmic scale. Further drying triggers profile tips to bend (typically profiles with lower saturation than the dashed profile) and an apparent dry region to develop from the sample's free surface. The wet front progressively recedes toward the bottom of the sample until it completely dries out; at the meantime, one may notice that the water distribution in the wet region remains homogeneous and its saturation progressively decreases.

For bead sizes ranging from 1000nm to 80nm diameter (see Fig4-1c, d, e and f), the same scheme seems to apply, i.e. we observe a first period featuring parallel profiles and profiles to further recede within the sample at lower saturation. However, one can notice that in this second period (typically after the dashed profile) the front of the wet region is not flat anymore (as seen on fig4-1a) but rather takes the shape of a slight gradient in water content. additionally, in samples made with 300nm and 80nm particles (see Fig4-1e and f), a residual saturation (in the order of a couple of percent) remains in the height previously identified as a dry region.

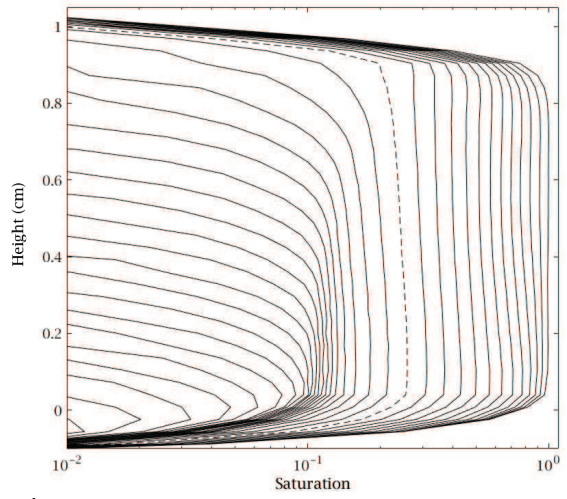
In 40nm samples (see Fig4-1g) an ambiguous situation is observed for the water distribution. In fact, similarly to bigger beads, we notice a short period during which water profiles remain parallel; afterwards, profiles start to bend close to the free surface and finally a tiny dry region develops while a gradient in water content progressively spans the whole sample.

Further, decreasing pore sizes, going down to 12nm particles and under, the water distribution clearly differs from what is observed at a larger scale (see Fig4-1h and i). It is possible to see that water initially homogeneously distributed throughout the whole porous structure (see first profile), first slightly depletes in the closest volume to the free surface giving rise to a gradient water which progressively extends from the top to the bottom of the sample with lower saturation. We notice the whole sample stays wet at all time and at the very end of the drying process, a high saturation remains (roughly 20%). Therefore, we observe an almost homogeneous desaturation for both samples.

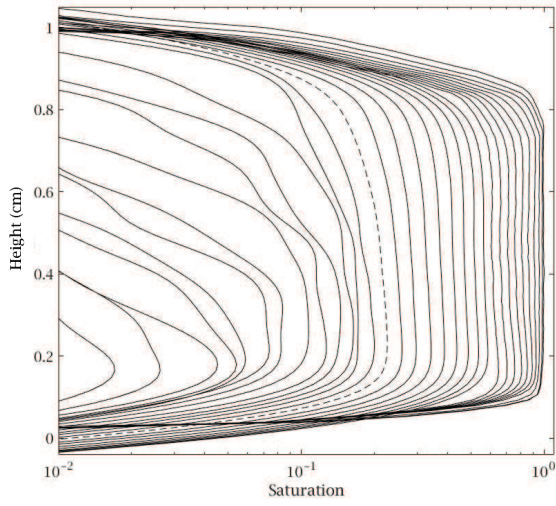
a.



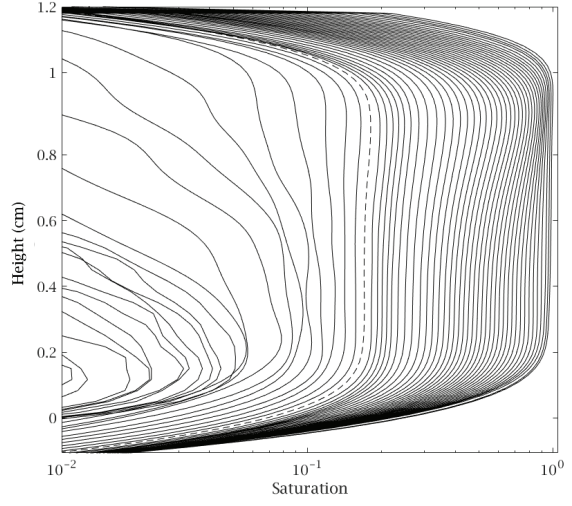
b.



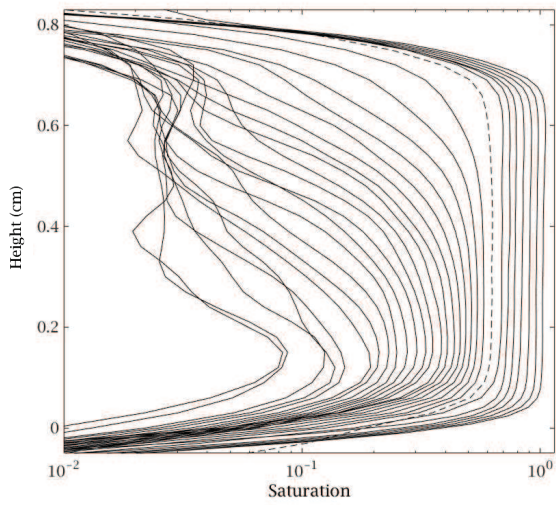
c.



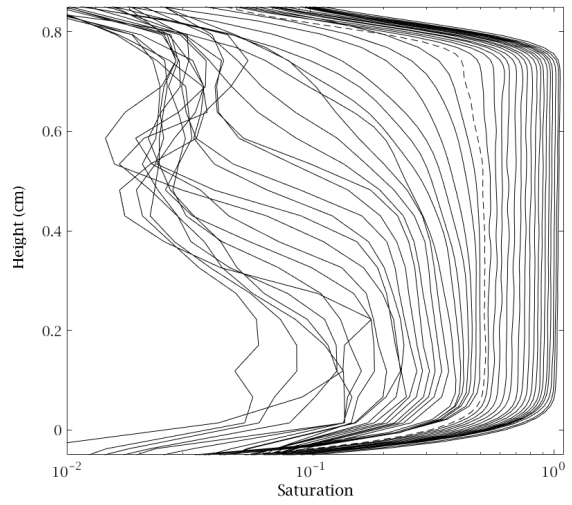
d.



e.



f.



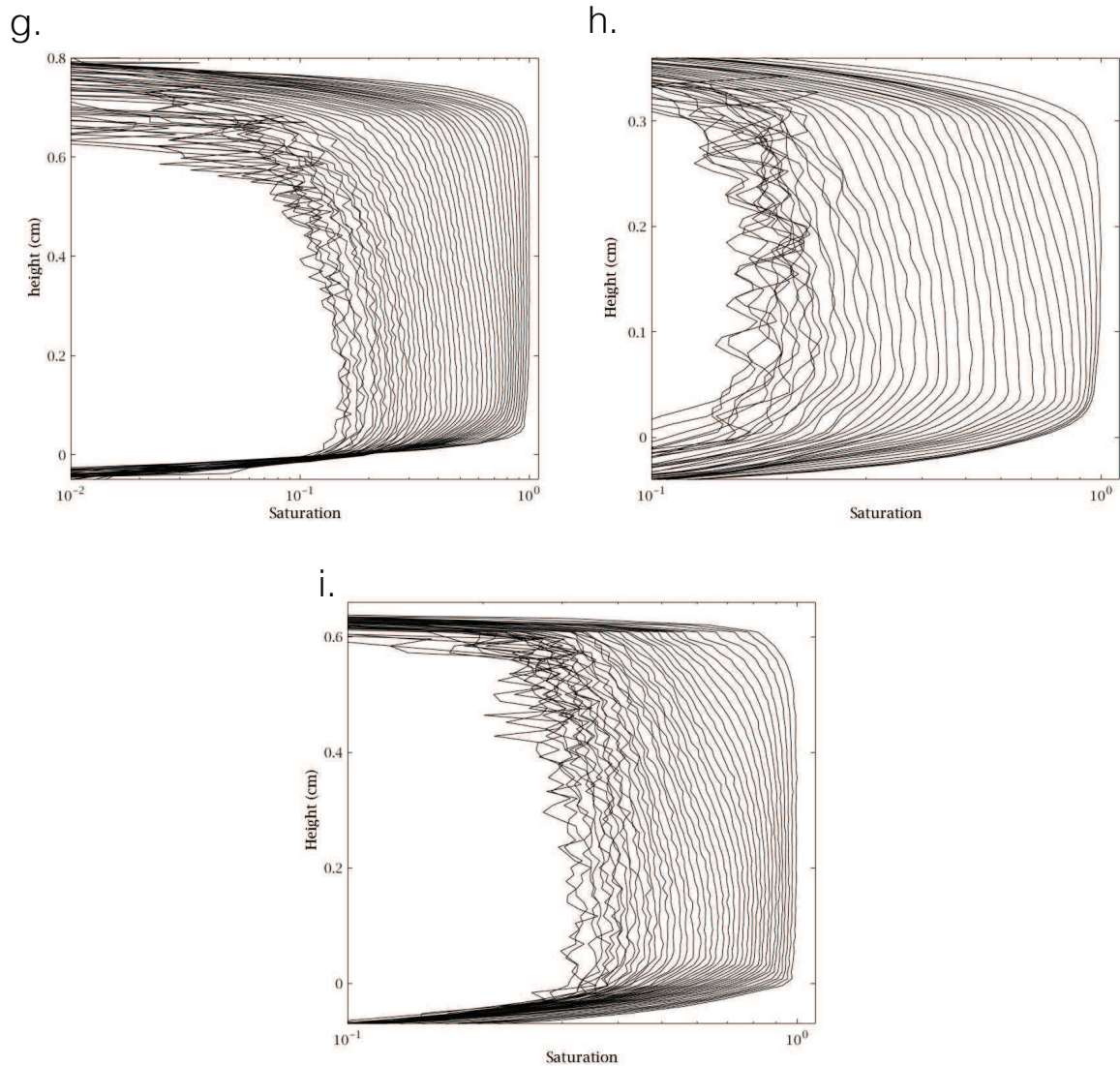


Figure 4-1: NMR profiling measurements along the vertical axis showing the distribution of water with time within samples made with particle diameter: (a) $45\mu\text{m}$, (b) $1.5\mu\text{m}$, (c) $1\mu\text{m}$, (d) 750nm , (e) 300nm , (f) 80nm , (g) 40nm , (h) 12nm , (i) 6nm . Profiles in (c), (d), (e), (f) have been smoothed for clarity. On average, time intervals between profiles are (a) 40min , (b) 38min , (c) 37min , (d) 27min (e) 33min , (f) 30min , (g) 28min , (h) 15min , (i) 35min and the average resolution (a) $120\mu\text{m}$, (b) $150\mu\text{m}$, (c) $120\mu\text{m}$, (d) $200\mu\text{m}$, (e) $200\mu\text{m}$, (f) $275\mu\text{m}$, (g) $160\mu\text{m}$, (h) $310\mu\text{m}$, (i) $250\mu\text{m}$. All samples are approximately 1cm thick except (h) which is 5mm . Full details about the measurement can be found in Chapter 5. Dashed profile is an indicator that spots a change in the shape of the profiles and the critical saturation ψ_c (see text).

i. Scheme for water distribution during drying varying bead sizes

Fig4-1 highlights a clear difference between the water distribution during drying of porous media made with small particles ($D < 40\text{nm}$) and porous media made with larger particles ($D > 40\text{nm}$). For small pores ($D < 40\text{nm}$), we saw that during desaturation the medium stays wet from top to bottom and desaturates rather homogeneously during the process, particularly we observed the apparition of a growing gradients in liquid content starting from the free surface. For bigger pores ($D > 40\text{nm}$), if desaturation starts with a series of parallel profiles witnessing of an homogeneous distribution of liquid throughout the sample, at lower saturation we notice a discontinued distribution of water featuring the development of an apparent dry region, the wet interface receding toward the bottom of the sample. The critical bead diameter at which this change appears is 40nm (see Fig4-1g).

Comparing samples all together, we observe the progressive changes leading to this radical transition in water distribution in the smallest pores. Particularly, we can see that the smaller the size of the particles, the higher the final saturation of the sample (from $\sim 0\%$ to $\sim 25\%$ between $45\mu\text{m}$ to 6nm , see Fig4-1a and i). Also, we observe that the smaller the beads diameter the higher the critical saturation (ψ_c) for which the profiles start to bend (at their very tip) and the wet front to recede within the sample if a wet front develops (as an indicator, profiles start to bend from the profile represented with dashed lines for each samples); specifically ψ_c increases from 0.16 to almost 0.5 saturation between samples with $45\mu\text{m}$ to 80nm bead diameter respectively. Additionally, we remark that the silhouette of the profiles tends to refine from a straight vertical line (homogeneously distributed water, see Fig4-1a and b) toward the shape of a gradient with smaller beads. Eventually, we notice that gradients profiles look very parallel to each other in a logarithmic scale. Note that if a dry region develops, the saturation in this remaining wet keeps decreasing with drying.

This homogeneous water distribution when $D < 40\text{nm}$ is unexpected from the theory reviewed in the first chapter of this manuscript; in fact, if the permeability of the medium is low a dry region would be expected to form from the beginning of the test. As the water distribution usually strongly influences the drying kinetics, it is interesting to look at the drying curves and the evolution of the drying rate with time.

3 - Drying rate

All data we present in Fig4-2 are extracted from the profiles presented from Fig4-1: the liquid volume is computed from the integral of the saturation profiles presented and the time elapsed between points corresponds to the spacing between each profiles. Note that many more points than profiles presented in Fig4-1 may appear in Fig4-2 as for the sake of clarity many intermediate profiles were not showed on this former Figure. The imposed air flux induces different initial drying velocities (V), decreasing from 0.125 to $0.05 \pm 0.01\text{cm. h}^{-1}$ for bead diameter (D) ranging from 45microns to 6nm . In Chapter 1 -B -6 - drying homogeneous porous medium with varying bead sizes when filled with Ethanol, we observed that the smaller the beads the sooner the apparition of the FRP due to the linear decrease of the critical velocity with pore size (see Eq1.15). Let's look at the trends we observe for our samples Fig4-2.

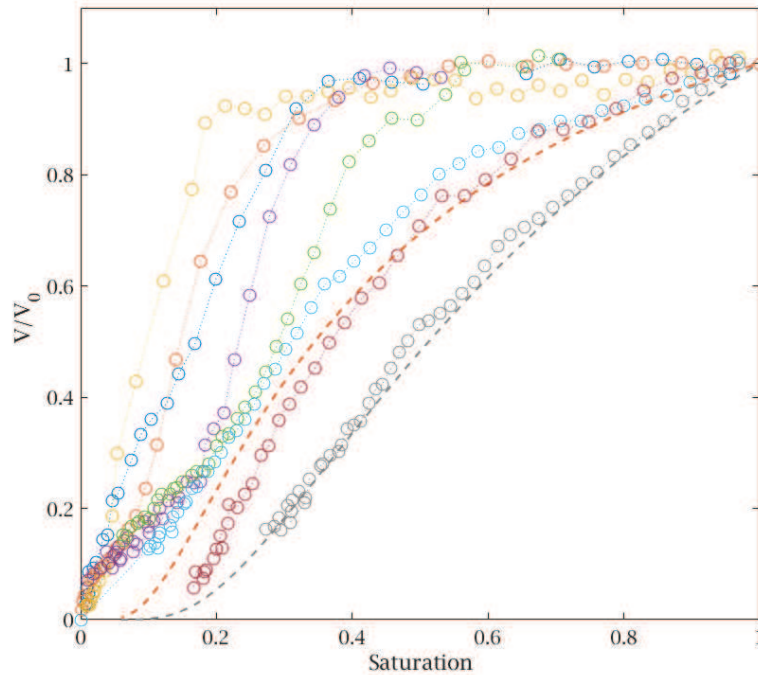


Figure 4-2: Drying velocity (rescaled by the initial one) as a function of the saturation for bead packings with different bead diameters: 45000 nm (cross-squares), 1500 nm (filled squares), 1000 nm (circles), 300 nm (triangles), 80 nm (stars), 40 nm (diamonds), 20 nm (crosses), 6 nm (cross-circles). Red diamond symbols correspond to the first NMR profile with a visible gradient (corresponding to a global saturation ψ_c).

Fig4-2 presents the evolution of the rescaled drying rate (current to initial velocity) as a function of the overall sample saturation. We observe the following trends: for big beads ($D > 40\text{nm}$) two main regimes are spotted, i.e. a first regime where the rescaled drying rate remains constant or slowly decreasing followed by a second regime where this rate progressively collapses to zero. On this graph we also observe that the bigger the beads the longer the duration of this constant rate period. Looking now at smaller beads ($D < 40\text{nm}$), we see that the drying rate seems to start to decrease from the very beginning of the test.

4 - Analysis of drying regimes

i. From water distribution to drying regimes

Comparing the water distribution observed on Fig4-1 to the drying kinetics on Fig4-2, we are able to draw the following conclusions on the drying mechanisms at play: for bead sizes down to about 80 nm we have observed (see Fig4-1) a first period during which, while decreasing, the saturation remains almost perfectly homogeneous: in a logarithmic scale the saturation profiles remain strictly parallel to each other (see Figure 4-1 a,b,c,d,e and f). This means that although water is withdrawn in the form of vapor from the top surface of the sample a balance of capillary effects is maintained throughout the sample whatever the value of the average saturation in this regime. Thus at each time the Laplace pressure is uniform in the liquid network and is not directly at the

origin of the liquid flow towards the sample free surface. Instead the liquid motion is induced by a series of successive bursts of capillary re-equilibration throughout the medium as a result of the increasing withdrawing of liquid in the top layers of the sample [9, 46, 101].

Now comparing Fig4-1 and Fig4-2, we observe that the extent in saturation for the period of parallel profiles in Fig4-1 well correlates to the length of the constant rate period on Fig4-2; therefore, within some uncertainty on the exact moment of onset of this regime, we can state that it is essentially associated with a constant drying rate. The end of this regime corresponds to the beginning of a significant decrease of the drying rate (see the diamond symbols Fig.4-2), found at the critical saturation ψ_c corresponding to the dashed profiles in Fig4-1.

Below ψ_c , a slight saturation gradient appears underneath the sample free surface, profiles tips starts to bend (see Fig4-1). Around the same time the drying rate starts to decrease (see Fig4-1). This occurs sooner (i.e. at higher ψ_c) for smaller bead radius, consistently to observations in Chapter 1 -B -6 - For the largest beads ($D \geq 40\text{nm}$) we observe the development of an apparent dry region, just below the free surface, where the saturation profiles drop to very small values (see Figure 4-1 a to f).

In fact, for 80 and 300nm samples, a residual saturation is observed in the height of the sample, above the wet region. This saturation is seen to remain after the sample has completely dried and can only be removed using high temperature. Our hypothesis is that this residual saturation likely correspond to the thin films (previously seen in Chapter 1 -B -8 -) i.e. adsorbed liquid layers at the pore walls that do not drain water and therefore are assumed to poorly influence on the drying rate. We conclude that this residual saturation can simply be consider to an apparent dry region, i.e. from which no more liquid can be extracted. To be further quantitative regarding the drying kinetics, it is necessary to look at the thickness of the apparent dry region; Let's clarify this measurement.

ii. Measurement of the apparent dry region

We measure the thickness of this region (H) from the MRI saturation profiles. This perform this measurement looking at the profiles in a log-log representation and drawing a straight vertical line spanning sample thickness at very low sample saturation (typically corresponding to an attenuation of 2 decades of the raw NMR signal) as shown on Fig4-3. Eventually, we measure H as the vertical distance between the intersection of the saturation profile with this line and the free sample surface. Note that the sample free surface is spotted using the protocol described in Chapter 2 -C -1 - ii. The growing dynamics of this apparent dry region can now be measured for all samples, let's establish the analysis framework.

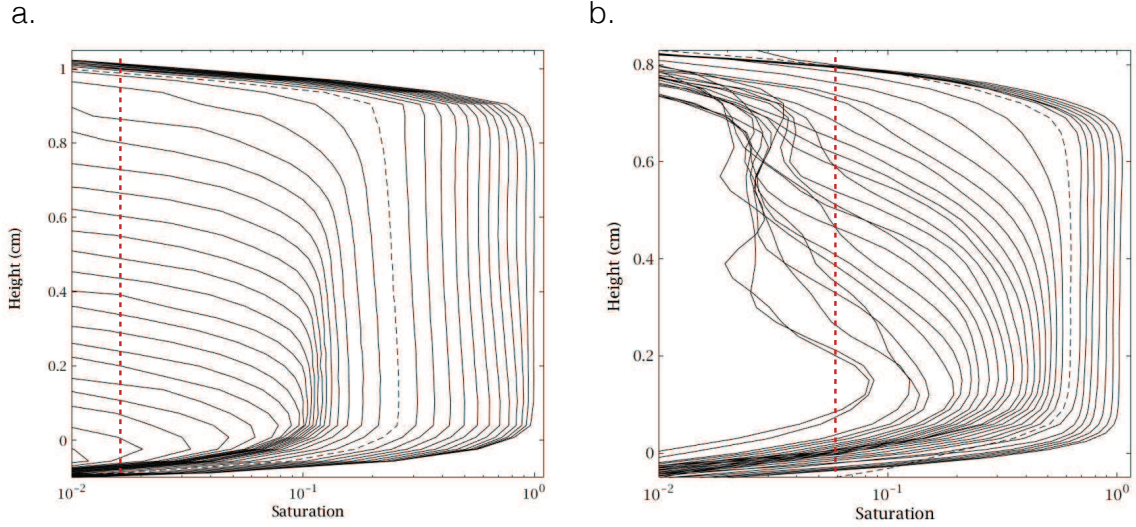


Figure 4-3: Measurement of the apparent dry region in sample made with (a) 1500nm, (b) 80nm particle diameter. Dashed line shows the measurement line.

iii. Quantitative considerations for drying regimes

Let us quantify the evolution of the drying rate according to these observations. Initially the relative humidity n is equal to 1 at the sample free surface and the drying rate may be described through Eq1.3. When a dry region (H) has developed inside the sample from its free surface, the vapor density gradient along the dry region induces a vapor flux which may be expressed in steady state as in Eq1.4 with n_1 the relative humidity of the air at the free surface of the sample. Equating Eq1.3 and Eq 1.4 for the vapor flux we deduce, the expression of the relative humidity at the sample free surface during the FRP regime $n_1 = 1/(1 + D_0H/D_p\delta)$. Finally, injecting the expression of n_1 in Eq1.3, one can compute the equivalent quantity: $(V_0/V - 1) = (\rho_{sat}/\rho_w D_p)V_0H$, where $V_0 = D_0\rho_{sat}/\rho_w\delta$ and finally:

$$\beta \left(\frac{V_0}{V} - 1 \right) = V_0H \quad (4.1)$$

where $\beta = \rho_{sat}/\rho_0 D_p$. Measuring H , as described just above, we present in the main graph of Fig4-4, the evolution of these quantities during the whole evaporation process (until the last profile presented in Fig4-1). We observe that for bead size $D \geq 40nm$, 2 regimes are observed during the development of the apparent dry region (from left to right): a first regime where data points, regardless of bead size, seem to closely gather around a master curve of slope 1 (see red dashed line in the main graph) and a second regime where a deviation is observed. We also observe that the bigger the beads the longer the duration of this first regime.

From the straight line fitted from the dataset for $R \geq 40nm$, we can extract the value for D_p (see Eq4.1); we show that it corresponds to a tortuosity $\tau = 1.5 \pm 0.2$, which is very close to the ratio of the length of the effective path of a molecule to skirt the grain to its diameter, i.e. $\pi/2 \approx 1.57$.

This confirms the consistency of the theoretical description of the drying process during the FRP for porous media in a wide range of pore sizes (see Chapter 1 -B -5 - iii. This agreement tends to indicate that in this regime, there is no significant impact of the bead diameter below 1 μm on the process of evaporation. This is all the more surprising as when the pore radius become of the order of magnitude of the mean free path of the water molecules (i.e. $l \approx 80 \text{ nm}$ under a pressure of 1 atm) Knudsen effects for vapor diffusion should play a role. Let's further look into the description of the Knudsen effect to comment on this figure.

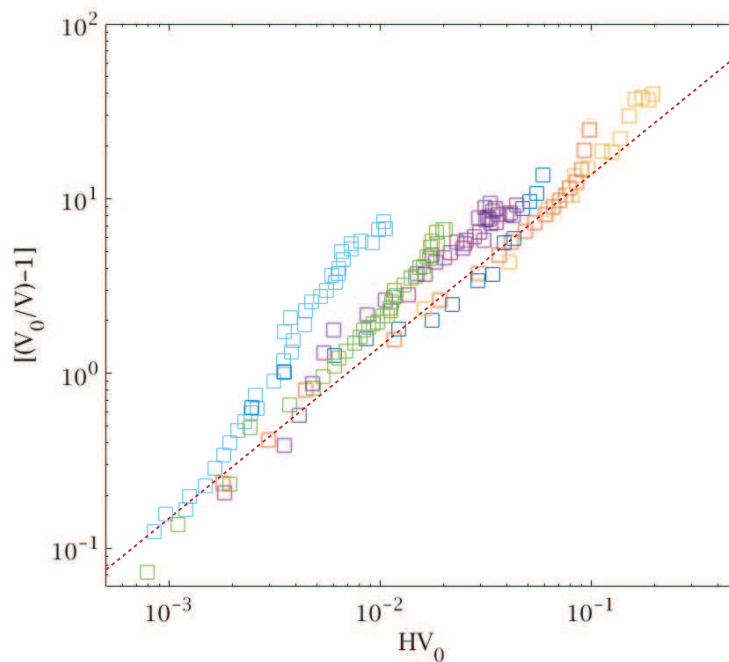


Figure 4-4: Evolution of a function of the rescaled velocity as a function of the thickness of the apparent dry region (see Eq4.1) times the initial velocity for the different bead sizes (same colors as in Fig.4-2). Red dotted line has a slope 1.

iv. Knudsen diffusion for vapor transport through the porous network

Knudsen diffusion is a mean of diffusion expected to take place when the length scale of a system (L) is comparable to or smaller than the mean free path of the particles studied (l), see Fig4-5. The ratio of these length scales defines the dimensionless Knudsen number ($K = L/l$); therefore, if $K \leq 1$, Knudsen effects are expected to slow down diffusion (case typically expected here during the FRP when particles diameter drops below $1\mu\text{m}$). In these conditions, the gas molecules collide with the pore walls on a more frequent basis than in the case of a wider channel, resulting in a slower diffusion process. If $K \leq 1$, Knudsen suggests that the diffusion coefficient of the gas in the air within the channel becomes linearly dependent of the channel diameter (L).

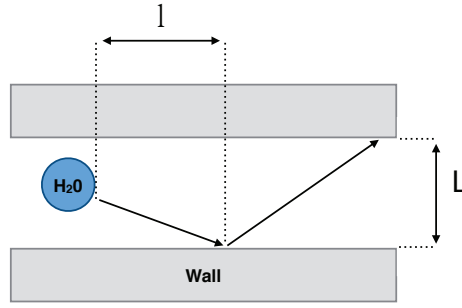


Figure 4-5: Scheme for Knudsen effect for diffusion of vapor through a tiny channel of diameter L ; l the mean free path of the water molecule.

As a first approximation, [154], we can describe this effect in our porous medium over the whole range of pore sizes by considering that the diffusion coefficient of vapor through the porous structure is in fact $D_k = \xi D_p$, with $\xi = (1 + l/L)^{-1}$; and therefore (Eq1.16) may be re-written as $V = \xi \rho_{sat} D_p / \rho_w (H + \xi \bar{\delta})$ and particularly Eq4.1 as :

$$\xi \beta \left(\frac{V_0}{V} - 1 \right) = V_0 H \quad (4.2)$$

We ignore the exact value of L for a porous medium (for a straight channel this is the channel diameter as seen on Fig4-5), but if L was of the order of the typical pore size the coefficient ξ would be significantly smaller than 1 for particles of diameter $R < 300nm$. However, this coefficient is independent of other characteristics (dry region thickness, saturation, etc.), it will thus tend to shift the data as a whole above the theoretical curve in Figure 4-4, but it cannot explain the change of slope which clearly appears for $D = 40nm$ and $D = 80nm$, which induces a discrepancy between the data and the current model; this discrepancy increasing with H . The result is a drying rate significantly smaller than expected from the diffusion model for the observed dry region thickness.

This effect induces a limited growth of the dry region for these two bead diameters over the duration of our test, especially for $R = 40nm$. For smaller beads, namely 6 and 12 nm diameter, no dry front at all can be observed while their drying rates decrease to zero (see Fig.4-2). This means that there is an additional effect which tend to slow down the drying rate and whose impact increases when the pore size decreases. The origin of this feature is likely that Kelvin effect [155-156] that starts to play a significant role when the pores are sufficiently small. Let's look into this phenomenon in detail.

v. Kelvin Effect in nano-pores to explain the drying kinetics

Assuming that water vapor behaves as a perfect gas, in a medium in contact with a curved liquid-air interface, the Kelvin effect predicts that the saturation vapor pressure is smaller than otherwise. As a matter of fact, if thermodynamic equilibrium exists, the equality between the chemical potentials for liquid (λ_L) and vapor (λ_V) water is verified; considering the local temperature

(supposedly uniform at the interface) and the pressures (P) different in the liquid (Laplace) and air phase, one may write $\lambda_V(T, P_V) = \lambda_L(T, P_L)$. Assuming that water vapor to behave as an ideal gas in these experimental conditions, one can then write:

$$RT \ln \left(\frac{P_V}{P_{sat}} \right) = V_M (P_L - P_{sat}) \quad (4.4)$$

Where V_M is the molar volume and P_{sat} is the saturation pressure. Further, a simple force balance at the menisci interface yields, neglecting gravity effects, assuming perfect wetting between water and silica:

$$P_V - P_L = \frac{2\gamma_{LV}}{r_c} \quad (4.7)$$

where r_c is the curvature radius of the interface and finally substituting Eq4.7 in Eq4.4 the approximate equation of Kelvin can be found and a numerical application to our experimental system specifically gives

$$n_r \approx \exp \left(- \frac{0.54}{r_c} \right) \quad (4.9)$$

We deduce that this effect becomes significant ($1 - n_r > 10\%$) i.e. for $r_c < 5nm$. If we now simply assume again that evaporation mainly occurs around the most external liquid-air interface for nanoporous media which apparently remains wet up to the free surface (see Fig4-1), we get a drying rate equal to:

$$V_r = \frac{n_r \rho_{sat} D_0}{\rho_w \delta} \quad (4.10)$$

In order to compare this prediction with our results, we have to determine r_c as a function of the current (mean) saturation. We simply assume that, in the range of saturations $[0.3-1]$, r_c varies like the thickness of the liquid films inside the sample, i.e. it is essentially proportional to R and ψ . Since we also know that it tends to infinity when $\psi \rightarrow 1$ and is of the order of the pore size (proportional to R) when $\psi \approx 0.5$, an expression which well reproduces all these trends is:

$$r_c = \frac{\zeta R \psi}{1 - \psi} \quad (4.11)$$

The factor ζ allows to express the exact pore size value to be taken into account around the most external liquid-air interfaces, i.e. resulting from the saturation gradient at the approach of the free surface of the sample. Using this expression for r_c in the above drying rate equation (Eq5.10) we can compute the evolution of the relative drying rate (V_r/V_0) as the saturation decreases. The results are presented in Fig4-2 by the dashed lines; remarkably with this model we are able to reproduce very well the data for 6 and 12 nm with a single factor $\zeta = 1/4$. The validation of this model confirms that for nanoparticles evaporation essentially occurs close to the top surface of the sample.

Eventually, even if the drying rate description with kelvin is apparently able to predict our observations it is likely that adsorption to the pore walls also play an important role at some time

during the drying process. We can expect that it will tend to damp evaporation when the apparent liquid layer is of the order of a few molecules.

5 - Analysis for water distribution

Since we now have a clearer view of the origin of the drying rate evolution as a function of the liquid distribution in time inside the sample it is interesting to see if we are able to predict this distribution. Let us consider the receding front regime. A usual assumption in that case [9] is that this recession corresponds to a situation for which the liquid is unable to flow through the porous medium because the liquid network is now discontinuous. Our data providing precise information at low saturation show that this is not the case (Fig4-1). Indeed even when the dry region occupies a significant fraction of the sample the saturation in the wet region goes on decreasing almost homogeneously, more or less as in the CRP regime (but now with a significant saturation gradient at the approach of the dry region) (see Fig4.1 a,b,c), and over a wide range of saturation (of the order of one decade). Since evaporation in the wet region is a priori negligible because the vapor density is at its maximum along most of this region, the homogeneous saturation decrease is still associated with some capillary re-equilibration processes and liquid flow towards the wet-dry frontier. If the velocity of capillary re-equilibration was larger than the drying rate associated with the current dry region we would get a homogeneous saturation decrease without change in the thickness of the dry region, as during the CRP. Since we observe a simultaneous desaturation of the dry region thickness this means that at any step we have some balance between the velocity of capillary re-equilibration and the drying rate.

6 - Conclusion

This unique study reveals new details of the dynamics for vapor removal and liquid flow during the FRP regime when transitioning from micron size to nano size pores. Specifically, we showed that drying of a compact and homogeneous porous media made with bead diameter $D >$

40nm gives rise to the classical scheme for drying, i.e. a heterogeneous desaturation that triggers an FRP; whereas when beads diameter drops to $D < 40nm$ and below a homogeneous desaturation process takes place, also featuring an FRP regime. Looking at the drying kinetics in detail, we showed that in the case where an apparent region develops and $D > 1\mu m$, the kinetics are well described by the second Fick's law. Surprisingly, when the system becomes smaller, Knudsen effects do not seem to apply but rather adsorption and the kelvin effect may act on the drying kinetics and reduce the drying speed. Particular to $D < 40nm$ since the free surface of the samples remains wet, Kelvin effect seem to predominate and a very good prediction of the drying kinetics is obtained with the scaling law we establish.

Eventually, we show that regardless of pore size, the liquid network remains continuous at all time within the wet region of the samples, even at very low moisture content or when a dry region develops. In the latter case, we find that liquid still flows as re-equilibration occurs since the water remains homogeneously distributed, similarly to the case with sponges seen in Chapter 2. Additional analysis would be needed to evaluate the condition of flow in this region.

Chapter 5 - Spontaneous imbibition in submicron porous media

In this chapter we look at the spontaneous imbibition of homogeneous porous medium with water, their pore size varying in size from the a few microns to a couple of nanometers. Firstly, We look at the aspect of the sample during the process macroscopically and compare the rising dynamics of the equivalent height of water (mass to cross sectional ratio) to the predictions of Lucas-Washburn equation. Second, we measure concentration profiles of water (MRI) along the vertical axis of our samples during imbibition; this study enables to gain understanding on the macroscopic phenomenology and the role of pore sizes on the imbibition kinetics. Eventually we look at the influence of the initial saturation on the imbibition kinetics.

1 - Macroscopic study

i. Phenomenology

The protocol for this study is explained in Chapter 2 -C -3 - and simply consists in dipping the bottom of the sample in a water bath. In this first sub-section, we present pictures for samples made of 6nm, 12nm, 40nm, 80nm and 750nm particles during imbibition. Dipping the bottom of a dry sample in a water bath exhibits rich phenomenology (See Fig5-1). First, looking at row A, B and C, one observes that in the initial state, the color of the sample on the picture is grey (see first picture in each of these rows), this color corresponds to a strong opaque white/grey color in reality; it is the color of the initial dry state for these samples. Rapidly, 3 areas can be distinguished (see the 3rd picture of each of these rows for more clarity); from the bottom to the top: a black area (actually translucent), a bright white area (opalescence) and a grey (actually opaque white/grey) area. After some time, one can notice that the black front climbs up and the opalescence widens (see Fig5-1 from 18min to 2h41min). Eventually, the opalescence reaches the top of the sample (see Fig5-1, row A at 3h17min for instance) and the whole porous media becomes dark (see Fig5-1 row A at 4h15min).

When particle diameter becomes greater than 40nm (see Fig5-1 rows D &E), samples appear white in their dry state (see Fig5-1 row D and E in the initial state), likely due to the particle size approaching the wavelength of light as they go bigger. When water is absorbed by the porous structure, a slight color change is observed: it becomes darker, however this trend is hardly seen on the picture presented. Therefore, to ease the analysis of these pictures we mark the level of this color change with a red dashed line in Fig5.1. Following these dashed lines now, one can observe for the samples concern that the apparent front simply progresses from the bottom to the top of the sample with time.

Additionally, as all samples present a similar volume, porosity (see Chapter 2 -B -2 - and surface area in contact with water (see legend of Fig5-1), we can qualitatively compare the time needed for the samples in Fig5-1 to complete imbibition (written on the final picture in each row of Fig5-1). We observe that the bigger the particles, the faster the imbibition process. Let's now be quantitative about the dynamics.

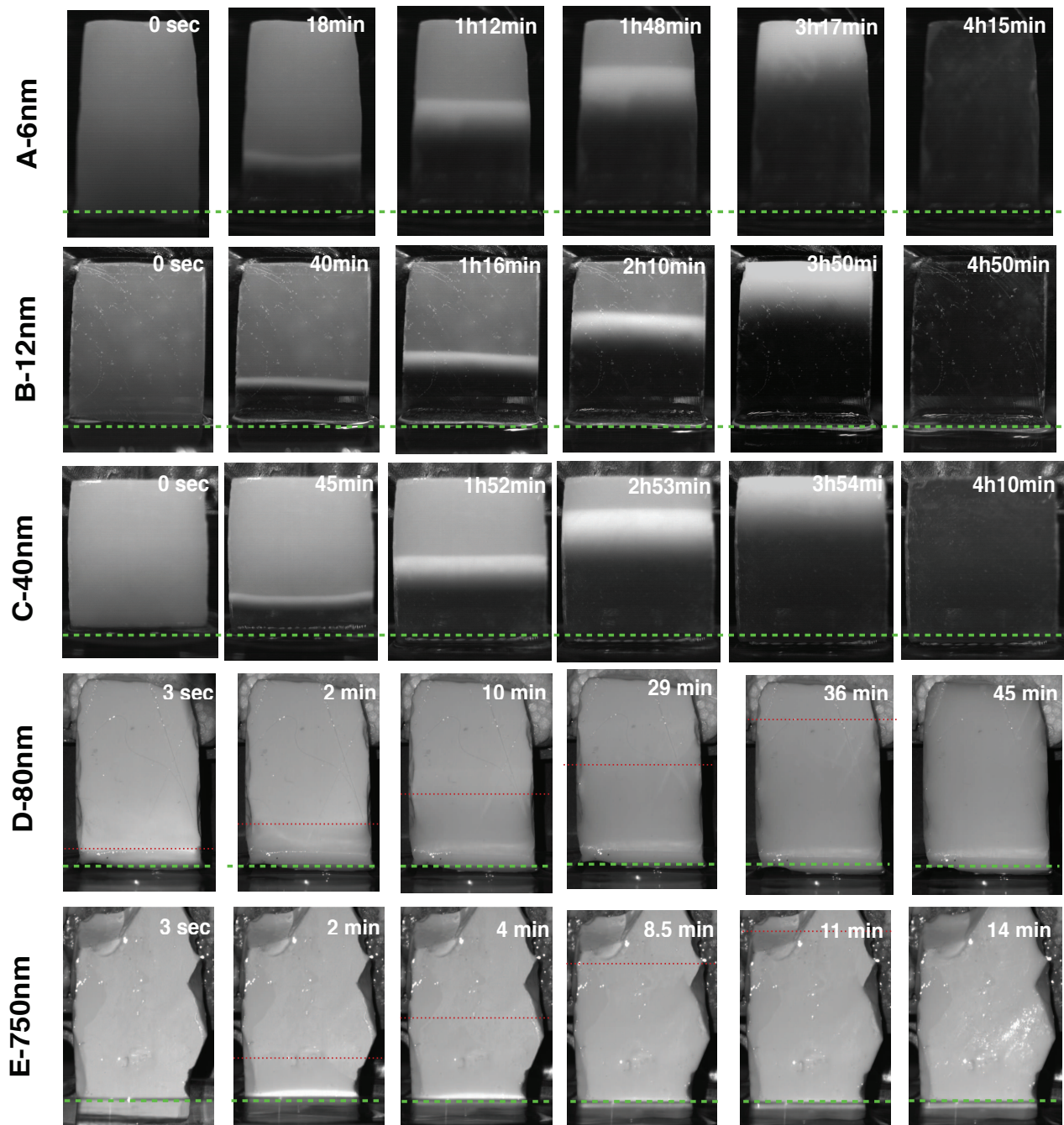


Figure 5-1: Evolution of spontaneous imbibition in porous media made with particles diameter (row A) 6nm, sample dimensions 32×17×6mm, (row B) 12nm, sample dimensions 32×30×6.5mm, (row C) 40nm, sample dimensions 30×29×6mm, (row D) 80nm, sample dimensions 32.5×23×8.5mm (row E) 750nm, sample dimensions

35×25×9mm. Sample in (row E) is shiny because its side walls were coated with epoxy in order to maintain the sample cohesion during the test. The time elapsed between the beginning of the test and the moment the picture is taken is written in white. The green dashed line represents the contact line of the sample with the water bath, the red dotted line is a guide for the eye and spots the location of the apparent imbibition front when needed.

ii. Imbibition curves and reproducibility

Measuring the mass of our samples during imbibition, we can quantitatively compare the imbibition dynamics between samples looking at the amount of water they absorbed per cross sectional area ($m(t)/\varepsilon\rho_w S_c$, where S_c is the cross sectional area) in time, i.e. the equivalent height of the water front, h_{eq} , within the porous samples. Additionally, since L-W equation suggests a linear dependence of the height of the water front with \sqrt{t} , it is useful to look at the evolution of h_{eq} with \sqrt{t} directly in Fig5-2.

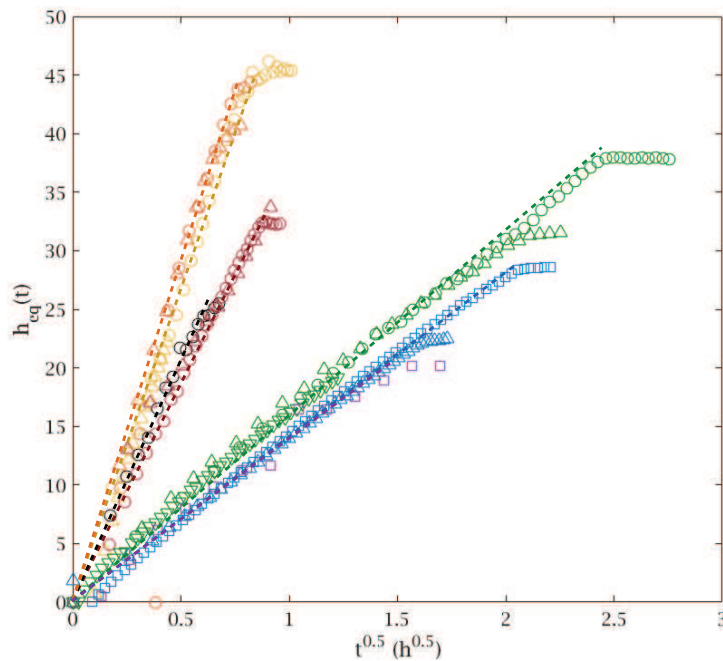


Figure 5-2: Imbibition curves presenting the mass of water absorbed within the porous structure divided by the cross sectional area of the sample with bead size (blue) 6nm, (purple) 12nm, (green) 40nm, (red) 80nm, (black) 300nm, (yellow) 750nm, (orange) 1500nm with time. Triangular symbols show the reproducibility of the measurement of matching color. Dashed lines shows the corresponding \sqrt{t} -fits.

Firstly, Fig5-2 shows that the triangular data points super-impose on the circular ones of their matching color. Triangular symbols on Fig5-2 correspond to the imbibition of another piece of the same material, from the same or different main piece. The identical behavior for this pair samples emphasize that our experiments are highly reproducible.

Furthermore, we observe a linear evolution of the ratio plotted with \sqrt{t} and the \sqrt{t} -fits, (dashed lines), to perfectly fit the experimental data. Finally, looking at the dynamics of imbibition (time

elapsed between the beginning of the test and the beginning of the plateau seen on the imbibition curves), we observe that the bigger the particles, the faster the process.

2 - Analysis of the imbibition curves

The \sqrt{t} -dynamic observed for the ratio plotted for all samples in Fig5-2 suggests that Lucas-Washburn (L-W) equation (see Eq1.20) could describe the dynamics of imbibition in our case. Beforehand, as most of the faces of our samples are not sealed, it is natural to think that evaporation of water from the wet faces of our samples could play a role in the dynamics observed. Let's consider this hypothesis: it is possible to take this assumption into account in Eq1.20: a natural way is to introduce an evaporation rate proportional to the area of the fluid exposed to the air (evaporation from the dry faces are assumed negligible, see Eq1.3): the total drying rate (V in $g \cdot s^{-1}$) can be expressed as: $V = -2V_s (h(t) \cdot (w + l))$ where w is the width of the sample at time t , l its thickness at time t , $h(t)$ the height of the wet region at time t and V_s the drying rate per unit area. With predominance of the viscous term for capillary driven flow (neglecting inertia and gravity), Eq1-19 becomes:

$$\frac{\partial h(t)}{\partial t} = \frac{k}{\mu_w} \cdot \frac{\gamma_{LV} r_p \cdot \cos(\theta_w)}{h(t)} - 2V_s(w + l) h(t) \quad (5.1)$$

Note that this form neglects the changes in concentration toward the interface as well as front roughness but still constitute a sufficient approach for this case. An immediate consequence of (5.1) is the existence of an equilibrium evaporation height that depends on the drying rate per unit area and the geometry of the sample as:

$$h_e = \frac{k \gamma_{LV} r_p \cdot \cos(\theta_w)}{2V_s(w + l)\mu_w} \quad (5.2)$$

Finally, to be complete, Eq5.1 can be solved analytically and $h(t)$ behaves as:

$$h(t) = \sqrt{h_e(1 - \exp(-4V_s(w + l)t))} \quad (5.3)$$

Therefore, if significant evaporation takes place we would observe an exponential relaxation in the front height dynamic in time. Note that when $h(t)$ is located well below h_e i.e. $\exp(-4V_s(w + l)t) \sim \mathcal{O}(1)$, thus $\exp(-4V_s(w + l)t) \sim -4V_s(w + l)$ and finally $h(t) \propto \sqrt{t}$. In fact, since Fig5-2 shows that $h(t)$ exhibits a \sqrt{t} -dynamic for each of the samples presented, therefore Eq5.3 suggests that evaporation should negligibly affect the imbibition process in our porous structures, and we can now assess if the dynamics observed are described by L-W equation.

To verify if the rising dynamics observed on Fig5-2 follow Eq1.20, we quantitatively look at the slopes (α_i for sample "i") of the \sqrt{t} -fits presented in this graph. From this data set we compute the equivalent capillary radius, $r_w = \beta D$ (where β is a coefficient we call after capillary coefficient) i.e the radius of interface curvature at the imbibition front needed to propel water within the

porosity of the sample (γ_{LW}/r_w). Using L-W equation and the Kozeny-Carman model for permeability (Eq1.12) we find: $\alpha_i = \sqrt{\gamma_{LW} \cdot \varepsilon^2 D / 90 \beta (1 - \varepsilon)^2 \mu_w}$ and β can be found numerically. Due to the high compaction of our samples (see Table2-1), in Chapter 2 -B -2 - , we have seen that it is possible to estimate the values of this parameter should take, as $\beta = \phi / 12(1 - \phi)$. Note that this latest expression depends on the particle volume fraction of the porous structure only; therefore, since $0.55 < \phi < 0.61$, β is expected to take the following values $0.10 < \beta < 0.15$ for all samples. The numerical values we find for β from the slopes of the \sqrt{t} -fits presented in Fig5-2 are presented in Fig5-3 as a function of the particle diameter.

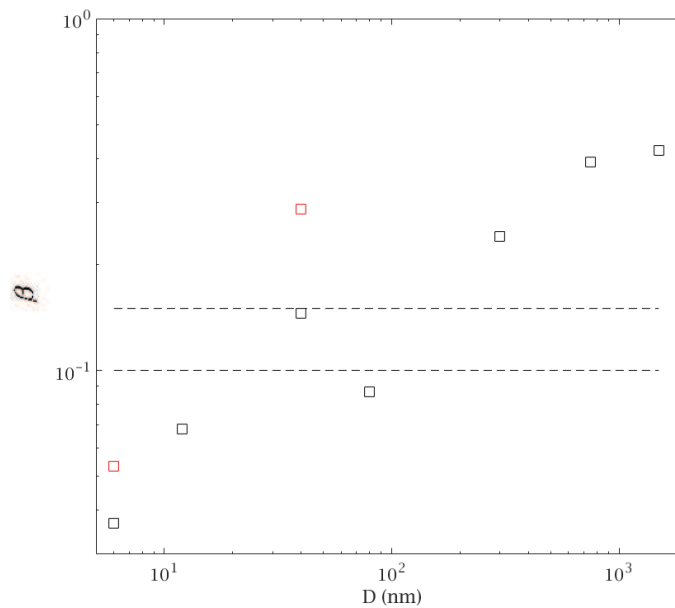


Figure 5-3: Comparison between the values of the capillary coefficient β computed from (black square) the slopes of the \sqrt{t} -fits presented in Fig5-2 (between black dotted lines) the expectation from sample compaction (see Table2.1). The red square corresponds to the value of this coefficient for the 6nm and 40nm samples CPD treated (see later in the text).

On Fig5-3, we observe that the values of the capillary coefficient for samples made of particles $40nm \leq D \leq 300nm$ approximately falls into our range of expectations (between the 2 black dotted lines). For $D \geq 750nm$ and $D \leq 12nm$ this coefficient substantially deviates from our expectations, probing a faster imbibition process than expected in tiny pores and slower kinetics at bigger sizes. Note that $D = 1500nm$, β may suffer from the sample shape as to maintain cohesion during the process it was shaped with slight bevelled edges and tightly wrapped in a film. Eventually these discrepancies seem to increase with decreasing and increasing particle diameter on both scales respectively.

If large heterogeneities within the pore network seems unlikely due to the very high compaction of the samples, some uncertainties remain in the permeability of our porous structures and the value of the dynamic contact angle at play. This study also suggests the need for a reference experiment to compare these kinetics with. We conclude that when $D < 80nm$, due to the rich phenomenology observed in Fig5-1, , the classical consideration of Lucas-Washburn may not

apply. To gain better understanding in the physics at play, let's look at the MRI profiling data probing how water distributes within the samples during the process.

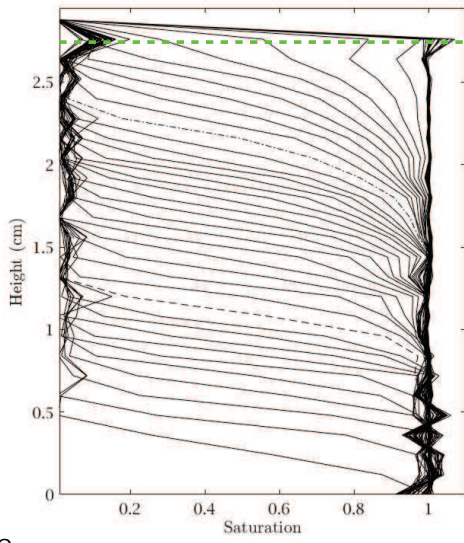
3 - MRI evidence of the evolution of water content during imbibition

A Dual Spin Echo sequence (see Chapter 2 -A -2 - v. is used to measure the water content along the vertical axis of the samples during imbibition (see Fig5-4); the protocol used for this measurement is detailed in Chapter 2 -C -3 - ii. This measurement discloses a plethora of information:

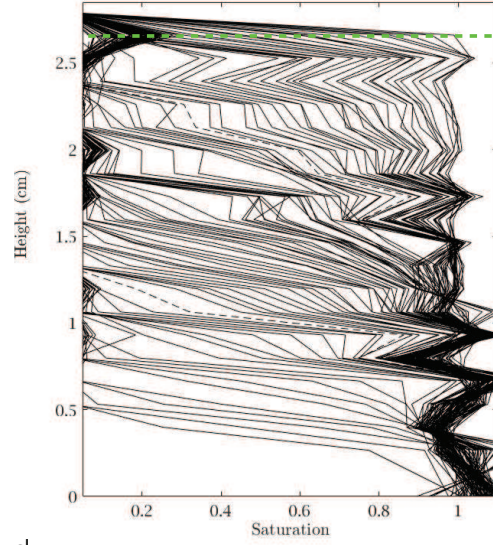
During the test, water progressively invades the porous medium, starting from the bottom of the graphs. From the shape of all water profiles in Fig5-4, we identify 3 different regions: a first region where the profile is straight vertical and shows a saturation equal to 1, followed vertically with a region where a gradient in water content is observed, this region therefore being a partially saturated region, and finally a region apparently dry (saturation close to zero). This type of distribution is seen until the samples become fully saturated. Moreover, we notice that the dimensions of the different regions evolve dynamically with the sorption fluid: the saturated region climbs up the height of the porous structure and the gradient in water content substantially widens.

One may also remark that all water gradients within a same sample seem to remain parallel to each other until the tip of the gradient reaches the top of the sample. What's more, it seems like all gradients of all samples could be parallel regardless of sample particle size. Last but not least, we observe that the saturation in the area situated above the water gradient is actually slightly greater than zero at all time.

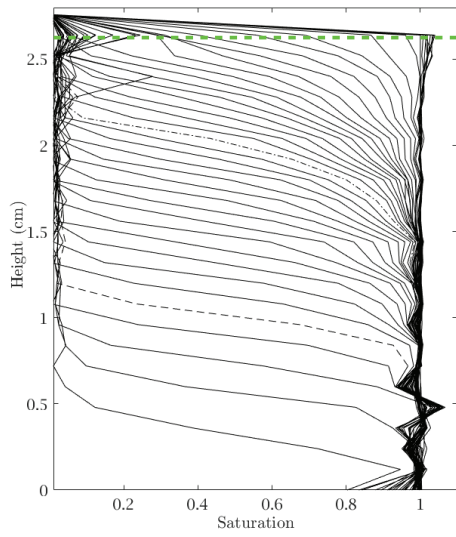
a.



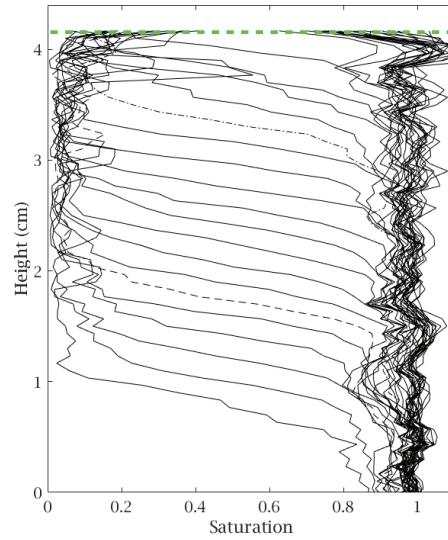
b.



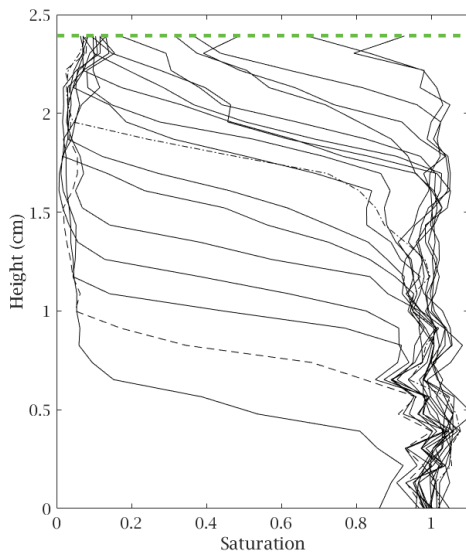
c.



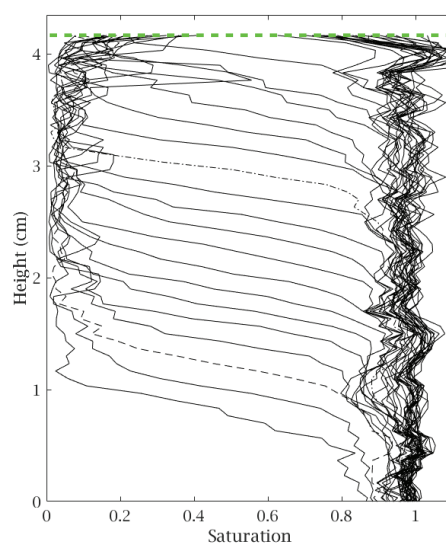
d.



e.



f.



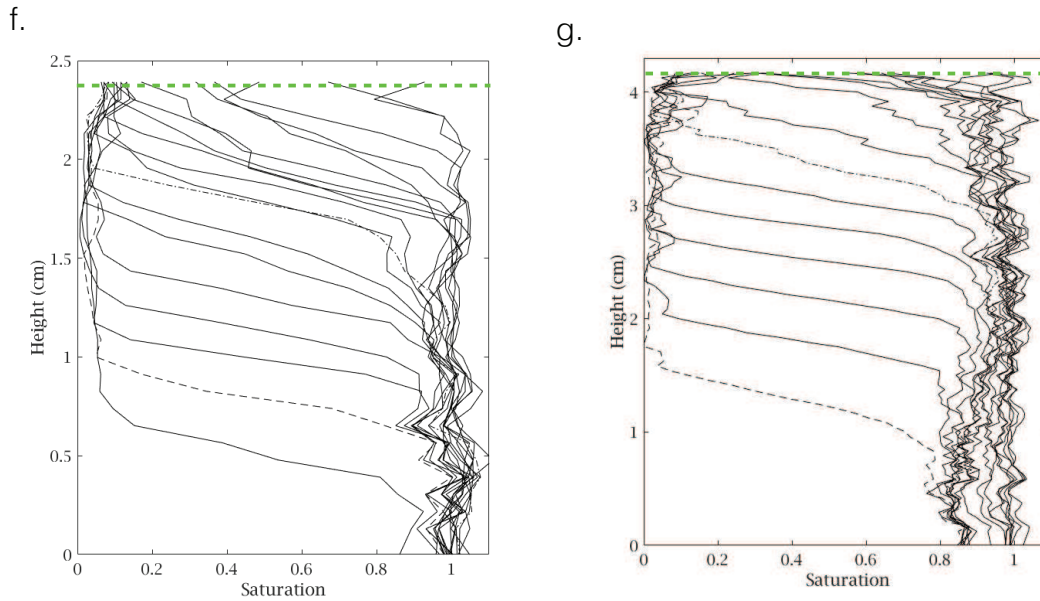


Figure 5-4: 1D profiling measurement along the vertical axis presenting the evolution of the water content during the imbibition process within samples made with (a) 6nm, (b) 12 nm, (c) 40nm, (d) 80nm, (e) 300nm, (f) 750nm, (g) 1500nm particles. The temporal resolution (time between each profiles) is on average (a) 11min, (b) 8min, (c) 10min, (d) 3.5min, (e) 2.0min, (f) 2.0min, (g) 1.39min; the spatial resolution is on average (a) 660 μ m, (b) 800 μ m, (c) 660 μ m (d) 870 μ m, (e) 600 μ m, (f) 410 μ m; additional details on the measurement parameters and the sample sizes can be found in Annexes 6 - The saturation is determined as the current to final amplitude of the NMR signal. The dashed profiles indicate the profiles used later on in Fig5-5 (see text). The green dashed lines indicate the top of the sample.

4 - Analysis of the MRI data

i. Front dynamics

In Fig5-4 we observe a similitude in the way the water distributes along the vertical axis during the process of imbibition from one sample to the other. Specifically, we saw that the shape of the profiles suggests the existence of 3 different regions; let's quantitatively compare between the growing dynamics of the two wet regions observed; beforehand, we clarify the delimitation of these regions on Fig5-5.

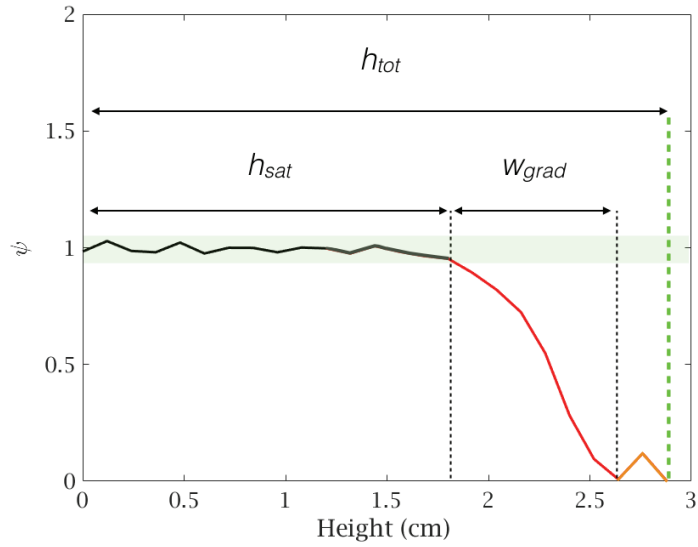


Figure 5-5: Scheme for the different regions observable on the MRI profiles, quantitative considerations. In black is the saturated region, in red the gradient region, from bottom to the top, the total height of the sample.

Figure 5-5 presents a water profile (corresponding to $\psi = 0.83$) of Fig5-4a as an example to define the dimensions of the different regions. We distinguish the height of the saturated region (h_{sat}) and the width of the gradient in water observed (w_{grad}). We measure h_{sat} as the height from the bottom of the sample to the point where the saturation drops below 95% for the 6nm and 40nm samples (see green shaded area in Fig5-5) and 90% for the other bead sizes (the noise of the measurement being higher on these data); w_{grad} is measured as the distance between the end of the saturated area and the tip of the gradient; h_{tot} defines the height of the porous media.

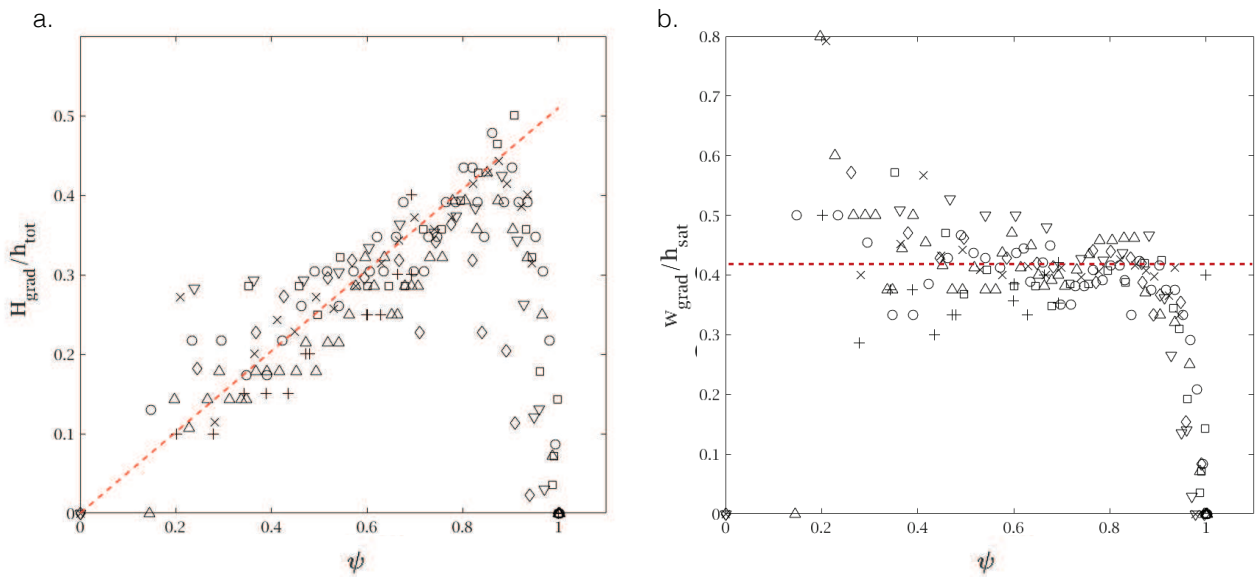


Figure 5-6: Evolution of (a) the rescaled width of the gradient part of the profiles (b) the ratio of the current dimension of the wet regions, with the average saturation, for samples

with particles diameter (upward triangle) 6nm, (straight cross) 12nm, (circle) 40nm, (square) 80nm, (diamond) 300nm, (tilted cross) 750nm, (downward triangle) 1500nm. The red lines are fits. The saturation ψ is defined as the current to last integral of the NMR profiles in Fig5-4.

Fig5-6 gathers the representations of the evolution of the rescaled width of the partially saturated region with ψ (see Fig5-6-5a) and the evolution of the ratio of the current dimension of the wet regions: w_{grad}/h_{sat} with ψ (see Fig5-6b), for all samples.

In Fig5-6a, we observe that all data points gather very close to describe a single curve, indicating that the ratio w_{grad}/h_{tot} evolves the same way with ψ regardless of particle size. What is more, as pointed out by the red dashed line, we find a linear evolution of this ratio with the average saturation of the samples until 0.9 saturation is reached (average saturation at which the gradient in water content is seen to reach the top of the porous media in Fig5-4) afterwards, as the gradient in water content progressively disappears due of complete filling (see Fig5-4), $w_{grad} \rightarrow 0$ and $w_{grad}/h_{tot} \rightarrow 0$.

Similarly, Fig5-6b shows that all data points in this graph distribute along the same line, suggesting that the evolution of the ratio plotted with ψ is independent of particle size. Specifically, w_{grad}/h_{sat} is seen constant until the average saturation reaches 0.9 (see Fig5-6b, dashed line) and then drops to zero for the same reason. Note that between 0 and 0.9 saturation, $w_{grad}/h_{sat} \approx 0.42$.

From this first set of results, we deduce that if $\psi < 0.9$ therefore during the majority of the imbibition process, $w_{grad}(t) \propto \psi(t)$ (see Fig5-6a) and $h_{sat}(t) \propto \psi(t)$ (see Fig5-6b). Furthermore, since $h_{eq}(t) = m(t)/\varepsilon\rho_w S_c \propto \sqrt{t}$ (seen in Fig5-2) and as the definition of average saturation is $\psi(t) = m(t)/m(t_{final})$, t_{final} being the time needed for the sample to complete imbibition, we deduce that for all samples in Fig5-6a and b: $w_{grad}(t) \propto h_{sat}(t) \propto \sqrt{t}$.

Now that the rising and growing dynamics of the wet fronts are clearer, let's look at the shape of the partially saturated region and how it evolves with time and particle size.

ii. Shape of the partially saturated front

In Fig5-4 we observed a strong resemblance between the shape of the water profiles regardless of the state of saturation or the particle size of the samples. Let's be quantitative on this observation. To compare the evolution of the shape of the water gradient with particle size during the imbibition process, we present in Fig5-7 the rescaled evolution of the gradient part of profiles seen in Fig5-4. Specifically, in this graph, h describes the vertical length of this gradient, therefore to $h = 0$ corresponds the beginning of the partially saturated region. Since we just saw that $w_{grad} \propto \psi(t)$, to relevantly carry this study, it is necessary to plot $h(t)/w_{grad}(t)$. Note that for clarity reasons, we only represent 2 profiles for each samples in Fig5-4, spotted as dashed ($\psi \sim 0.4$) and dotted ($\psi \sim 0.8$) in Fig5-4, this is relevant as all profiles from a single sample are seen to super-impose on each other with this representation as seen in the inset of Fig5-7 showing this rescaling for all gradients for sample made with 6nm particles (see Fig5-4a).

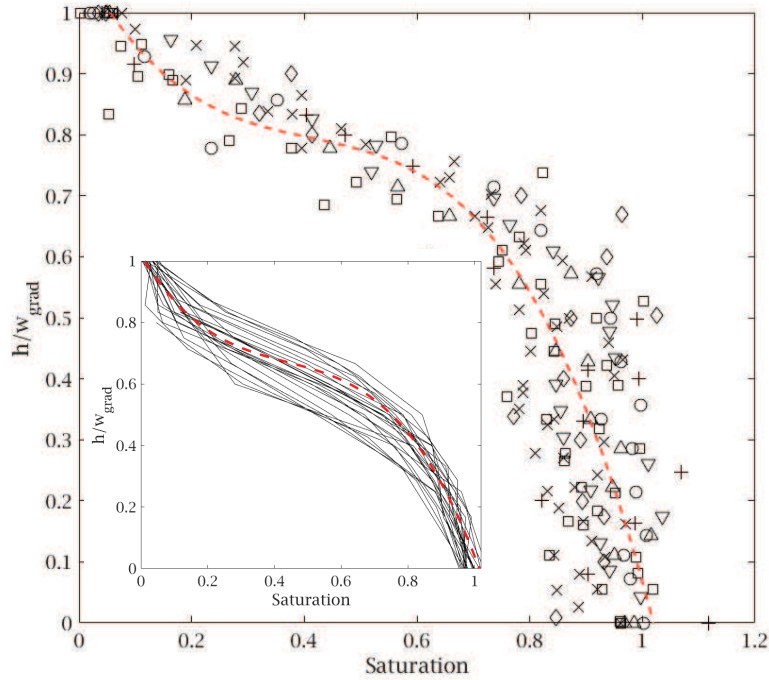


Figure 5-7: Rescaled gradients width for all bead sizes: h is the vertical coordinate starting at the bottom of the gradient and w_{grad} the width of the sample (see Fig5-5): (upward triangle) 6nm, (straight cross) 12nm, (circle) 40nm, (square) 80nm, (diamond) 300nm, (tilted cross) 750nm, (downward triangle) 1500nm. For clarity reasons, only 2 gradients per samples are presented in the main graph, corresponding to a global saturation of $\psi = 0.4$ and $\psi = 0.8$ respectively represented as the dashed and dotted profiles in Fig5-4. Inset shows the evolution of the same quantity in the sample made with 6nm particles only, in this graph all profiles ranging from $\psi = 0 - 0.9$ are plotted. Dashed lines in inset and in the main graph represent the same 3rd power polynomial fit for the 6nm data (see text). Note that on the x axis of both graphs is represented the local saturation ($\tilde{\psi}$).

In the inset graph, we see that all gradients of the 6nm sample super-impose with this rescaling (in fact this is the case for all samples). What is more, the evolution of the local saturation $\tilde{\psi}$ (x axis) in this gradient is seen to follow a master curve with this representation (see the red dashed line). This same red dashed line is presented in the main graph of Fig5-7, and we observe that all data points in this graph closely gather around it. Therefore this rescaling suggests that the evolution of the local saturation $\tilde{\psi}$ in the gradient is independent of the particle size. Thus the evolution of the gradient, $G(h, \tilde{\psi})$, can be described by the product of two independent functions: $G(h, \tilde{\psi}) = f(t)k(\tilde{\psi})$, where $f(t) = A\sqrt{t}$, A being a constant depending on the porous structure and $k(\tilde{\psi})$ the polynomial function of the local saturation describing the evolution of the red dashed line. Note that the shape of this gradient is independent of the intensity of the capillary pressure that governs drainage here, we therefore suggest this shape could be strongly related to the affinity between the liquid and the solid matrix.

From the previous data, we conclude that the imbibition front is not flat but spreads over the height of the sample in the form of a gradient in water content in all samples, thus, front broadening is

observed for all samples regardless of the bead size. Let's see how this understanding helps to explain the macroscopic phenomenology observed in Fig5-1.

iii. Opalescence

We saw that 2 fronts propagate with a \sqrt{t} -dynamic during imbibition of our samples. Specifically, these fronts differentiated by their water content, one is fully saturated whereas the other one is only partially saturated (gradient). Fig5-1 shows that in samples made with particles diameter inferior to 80nm, a growing opalescence appears at the sample surface as the mass uptake increases. This whitening effect was previously observed [80] and supposedly correspond to light scattering from the coexistence of dry regions (air) and liquid-filled pore segments on visible light length scales; suggesting the opalescence to constitute a partially saturated volume. In order to verify if the opalescence corresponds to the gradient in water observed on the MRI data, we carry out an additional experiment involving the couple study of the sample aspect and its water distribution via MRI profiling.

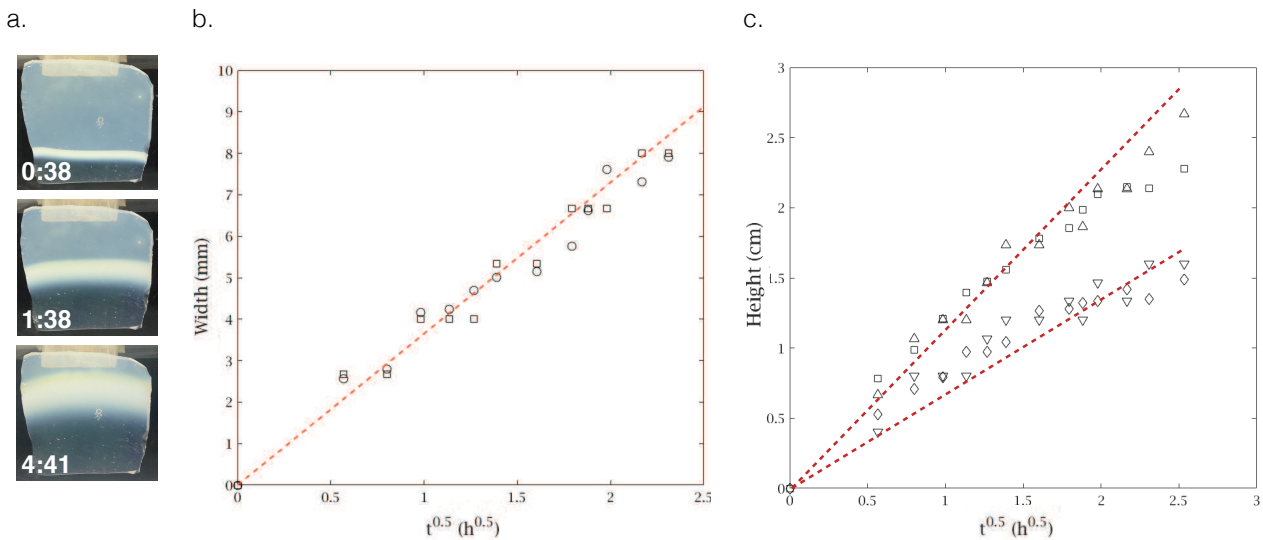


Figure 5-8 (a) Photography of sample (dimensions 28×24×3mm) made of 6nm particles; pictures are taken between successive MRI profiling measurements, time is indicated in white in the following format: hh:mm. (b) evolution of (black square) the width of the opalescence, measured from the picture, and (black circle) the width of the gradient, measured from the MRI profiles. In (c) are presented, measured from the picture, (triangle) the height of the opalescence and (downward triangle) the height of the translucent area; measured on the MRI profiles (circle) the height of the tip of the gradient, (diamond) the height of the saturated area. Red dashed lines are \sqrt{t} -fits in both graphs.

Fig 5-8 presents this comparative measurement, in detail, we firstly compare the width of the opalescence seen in Fig5-8a to the width of the gradients measured from the corresponding 1D profiles (see Fig5-8b) with \sqrt{t} ; we finally look at the \sqrt{t} -dynamics of both wet fronts with MRI and compare them to those of the different fronts measured on Fig5-8a.

On Fig5-8b, we observe that both the macroscopic and profiling measurement describe the same curve, this suggest that the growing dynamics of the gradient in water and the opalescence match with time. Similarly, Fig 5-7c shows a superposition of the MRI and macroscopic data for each set

of data, this suggests that both the tip of the gradient and the top of the opalescence match in their location and dynamics, as well as that the tip of the translucent front and the top of the saturated area.

This study highlights that the opalescence and the gradient share the same location (see Fig5-8c), and the same growing dynamics (see Fig5-8b), which enable us to identify one to the other. Therefore, we conclude that the opalescence constitutes a partially saturated spread front that widens and rises in the porous media as \sqrt{t} . If this study confirms the likelihood of the origins of the opalescence i.e. light scattering due to the coexistence of dry and wet regions on visible light length scales it does not tell yet, how water distributes at the solid surface; Specifically, we have seen that in such systems (see 0 precursor films can possibly spread on the solid matrix and strongly influence the kinetics observed. Let's look at the information we can yield on the precursor films from our data.

5 - Analysis at low moisture content

i. Evidence of precursor films

An important information we yield from the water distribution presented in Fig5-4 is that the region located above the water gradient, expected to be dry, is actually not. In fact, even if the measurement is noisy (the signal to noise ratio being very low due to low moisture content) one can easily see that the average saturation in this region (ψ_{top}) is different from zero for all samples presented in this figure. Remarkably, accumulated 1D profiling experiments showed that the initial saturation within the samples (before they touch the water bath) is not zero and comparable to ψ_{top} for the first profiles once imbibition has started. We measure ψ_{top} , taking great care not to include the tip of the opalescence nor the very top of the sample (where border effects may apply), we obtain the following results for the different samples.

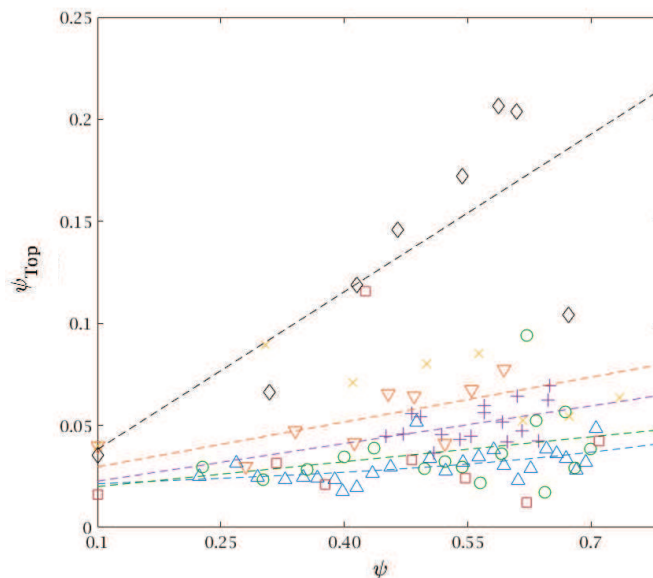


Figure 5-9: Evolution of ψ_{top} for samples made with beads of diameter: (blue upward triangle) 6nm, (purple straight cross) 12nm, (green circle) 40nm, (red square) 80nm,

(black diamond) 300nm, (yellow tilted cross) 750nm, (orange downward triangle) 1500nm. Colored dashed lines are fits of the data of the matching color, only a few fits are plotted for clarity reasons. The measurement was performed from the initial state until the global saturation has reached 0.70, as afterwards, the measurement is seen strongly influenced by edge effects and the opalescence rising.

Fig5-9 shows that ψ_{top} increases as the global saturation increases. What is more, this saturation roughly doubles between the initial state and 70% average saturation is reached. The presence of water in this region is unexpected and suggests that the initial saturation of the sample (before the test) is different from zero, meaning the protocol seen in Chapter 2 -C -3 - i. fails to completely dry the samples. If the hypothesis of liquid films covering the solid surface can be considered, these results suggests that due to the increase of ψ_{top} , water is slowly drained up the sample ahead of the imbibition front, therefore pointing out the capacity of adsorbed liquid films to drain water. If the relatively high level of the saturation in this region casts a doubt on the efficiency of the protocol seen in Chapter 2 -C -3 - i. in the next section, to guaranty our samples are dryer in their initial state, we use a protocol of critical point drying (technique detailed in Chapter 2 -C -2 - Let's look at how the initial saturation acts on the drying kinetics.

ii. Influence of initial liquid films on the imbibition dynamics

In this section we use a special protocol (protocol 2) called critical point drying on our porous structures, this protocol (see Chapter 2 -C -2 - supposedly eliminates all traces of water within the sample, with a higher efficiency that the first protocol (protocol 1) we used (see .Chapter 2 -C -3 - i. In this study, two samples are analysed (made with 6nm and 40nm beads), each of these samples undertake two imbibition cycles. Prior to the first imbibition samples undertake Protocol 1, afterwards, a second imbibition is performed prior to which they are dried with protocol 2. We measure the imbibition curves of these four tests with the same set up as before (see Chapter 2 -C -3 - i. The results are presented in Fig5-10. Note that only 2 samples were studied due to time and experimental constrains.

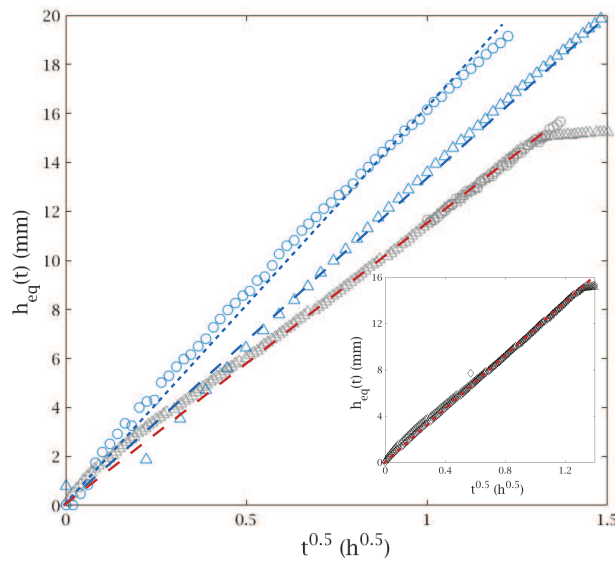


Figure 5-10: Evolution of the equivalent height (h_{eq}) with \sqrt{t} for samples made of (blue upward triangle) 6nm and (blue circle) 40nm previously dried protocol 1, (grey upward triangle) 6nm (grey circle) 40nm dried with protocol 2. Dashed lines are \sqrt{t} -fits. Reproducibility is shown in inset for the 6nm sample dried with protocol 2 twice in a row.

Fig5-10 shows the comparative study of imbibition curves for sample prepared with the different protocols highlighted earlier on. From the identical evolution of the imbibition curves of the 2 measurements in inset, we show the good reproducibility of the data we present but also the linear evolution of h_{eq} with \sqrt{t} . From the main graph in Fig5-10 we observe that samples initially dried with protocol 2 present a slower imbibition process than their counterpart initially dried with protocol 1. Moreover, we observe that the imbibition curves for the two different pore sizes superimpose.

iii. Scheme for the influence of precursors films on imbibition dynamics

Fig5-9 suggests the presence of water in our porous structures in their initial state and Fig5-10 probes its effect on the imbibition kinetics. In Fig5-3, (red squares) we can look at the intensity of the equivalent capillary forces (through the capillary coefficient) at play within these samples from the slopes for the CPD treated samples presented in Fig5-10 (similarly to Chapter 5 – 0 We find that the capillary coefficient for these samples increases. This tends to indicate that pre-wetting could play a role on the kinetics observed. let's assess this assumption. It is possible to attempt an interpretation of these results assuming that the water spreads over the solid matrix in the form of liquid films. This hypothesis is proved reasonable from Fig5-9 as it would entail liquid films to be a couple of water molecules thick at the pore walls (computing the thickness of the liquid layer at the bead surface considering the average value of ψ_{top} measured in Fig5-9). To simplify the problem, we consider that the only difference standing between the samples in Fig5-10 is the presence of liquid films on the solid surface when samples are dried with protocol 1; one may therefore think about the effect of the dynamic contact angle (θ_D) to explain the different kinetics observed on this figure (see 0). As a matter of fact, we saw that a contact line advancing on a dry solid makes with this solid a contact angle which depends on the line velocity, because of the viscous dissipation in the liquid wedge [113, 114]. However, the value of the contact angle during the dynamic process in the case of a pre-wetted surface is higher than on a dry solid matrix (see Chapter 1 -C -2 - This conjecture would place the capillary forces at play in the pre-wetted structure to be less efficient in than in the case of a dry matrix and therefore results in a slower imbibition process which contradicts the above observations.

6 - Conclusion and perspectives

Spontaneous imbibition of water in a series of compact and homogenous sub-micron porous media showed that the dynamics of capillary rise follow a Washburn type of imbibition even in nano sized pores. Regardless of the pore size studied, we found the existence of a strong front broadening effect. This imbibition front appeared to rise and widen in the sample with a \sqrt{t} -dynamic and to constitute a partially saturated region; eventually, in nano-sized pores, this front gave rise to strong light scattering likely due to the coexistence of dry regions (air) and liquid-filled pore segments on visible light length scales. In similar experimental conditions, we observed a water distribution pattern common to every samples in this front. Additionally, we saw that this pattern depends on the geometry of the material and its state of saturation but is independent of pore size. Note that the role of this partially saturated region in the imbibition kinetics remains unknown specifically its action on the advancing of the saturated region situated just below.

Looking at the evolution of the equivalent capillary coefficient, we observed a significant acceleration of imbibition when the equivalent pore size drops below 2nm in size. If we have not yet found the physical phenomenon at play in this particular situation, we record that the imbibition kinetics were greatly influenced by the presence or absence of adsorbed liquid layers at the pore walls.

Conclusion and suggestion

We carried out a multi-scale study of the physics of fluid flow within model homogeneous and heterogeneous porous media with pore sizes ranging from the millimeter scale to the nanoscale during imbibition or drying. This work probes, through 1D MRI and EM imaging, the existence of novel flowing regimes and regime transitions and contributes to the understanding of the new phenomena observed.

Specific to convective drying, we firstly found that under particular conditions of saturation, i.e. if entirely saturated, a material that deforms (shrink and crack) may find its drying kinetics modified. These variations consist in the decrease, the maintenance or the enhancement of the drying rate of the material; inevitably for samples that crack this results in a shorter overall process. If such variations in the drying kinetics were found in the past, their origins were simply assumed to be due to the variation of the surface area available to evaporation; this was without considering the airflow pattern near the sample free surface. Taking great care to fit the cracking and shrinking dynamics of nano-porous gels during drying, and measuring the velocity field of a tangential airflow over and within the vicinity of a model crack by means of a numerical simulation in 2D, we probed the existence of 2 drying regimes depending on the width of the gap between gel fragments and their aspect ratio. Eventually we established a scaling approach enabling to predict the drying rate of such materials when they crack knowing their final number of fragments.

In the aim of understanding the deformation induced in heterogeneous porous media during drying, we studied desiccation of sponges. The two sponges studied showed different width for their pore-size distribution and different surface affinities with water. On one hand we showed that a sudden contraction (short extent saturation) was observed during drying of the hydrophilic sponge presenting a wide pore size distribution (millimeter to micrometer scale) and the classical scaling laws for drying applied (CRP followed by an FRP). This contraction was attributed to the emptying of the tiniest fraction of the porosity. On the other hand, with a narrower pore size distribution, we observed the development of a dry region from the sponge free surface, from the beginning of the test. The drying kinetics were seen independent of the surface property of the liquid and the extent of the dry region appeared uncorrelated to the classic drying scaling law. In fact, the water distribution suggested the presence of liquid films at the pore wall that might play a role in the kinetics observed but further analysis is needed to conclude on the mechanisms that actually govern the drying kinetics in this particular sample.

Looking at the water distribution along a horizontal axis of both sponges, we managed to measure, for the first time with NMR, the fluctuating process of capillary equilibration. If further analysis is needed to build a physical model for flow and quantitatively describe the dynamic of this process, this measurement enabled to see that capillary equilibration also occurs during the FRP for these samples. In fact, the measurement of the concentration of water along the vertical axis of sponges, confirmed this finding showing that the saturation within the wet region during the FRP decreases but still remains homogeneous. Such an extent for this process was unexpected as the classical scheme for water distribution during drying suggests that rapidly after the CRP, the liquid network becomes discontinuous (pendular regime) and desaturation occurs by means of removal of moisture in successive layer from the free surface.

To verify if these findings were generalizable to all porous media and to contribute to the need for a generalist approach on the drying phenomenon, we designed and studied desiccation in homogeneous porous structures, synthesized through viscous sintering, with pore sizes ranging from a couple of microns to a few nanometers. In the same drying conditions, the classical scheme for the drying kinetics was found to apply: at first a CRP took place, its duration decreased with decreasing pore size and eventually disappeared for very small pores (trend expected from the substantial decrease of the permeability of confined networks) and an FRP was triggered. For porous media with particle diameter superior to 12nm (count roughly 1/6 of the particle diameter as the equivalent pore size) the water distribution we observed was relevant to the drying kinetics expected for coarse grain packings i.e. during the CRP the water appeared homogeneously distributed throughout the sample probing the existence of a continuous liquid network capable of draining water to the sample free surface, by means of capillary equilibration, for the process to remain boundary layer controlled. The end of this CRP matched with the development of an apparent dry region and the drying kinetics strongly correlated to vapor diffusion through the height of this region. Surprisingly, during this FRP the diffusion rate of vapor did not bear witness of Knudsen effect when the pore sizes became comparable to the mean free path of a molecule of water in a gaseous phase. Additionally, in this same regime, the same process of desaturation within the wet region was observed as in sponges, i.e. the saturation of this region appeared homogeneous and decreased with the advance in drying. If additional study is needed to clarify the dynamics of water within this wet region, we suggest that local capillary equilibration may take place between neighbouring pores and diffuse to equilibrate the whole region.

For smaller pores (particle diameter inferior to 12nm), we observed an unexpected situation for the water distribution with regards to the drying kinetics. In fact, a continuous liquid distribution, in the shape of a gradient of water was found throughout sample at all time and giving rise to an FRP triggered since the very beginning of the test. In these conditions and assuming that water vapor behaves as a perfect gas, we showed that the kelvin effect governs and limits evaporation. We established a scaling model which accurately depicts the drying kinetics recorded.

Eventually, investigating the field of spontaneous imbibition of water within the variety of homogeneous porous media earlier described, we observed that the rising dynamics of liquid within such structures followed a Washburn type of imbibition even for nano-pores. We recorded these dynamics to be strongly impacted by the existence of adsorbed liquid layer at the pore walls. Particularly, when bead size drop below 12nm, a faster imbibition process than expected otherwise took place. Eventually we showed that imbibition in homogeneous porous media exhibits strong front broadening effect, common to every sample regardless of particle size. This partially saturated region was seen to rise and widen with a \sqrt{t} - dynamic within the sample and to result, in nano-pores, in the apparition of an opalescence at the sample surface likely due to the coexistence of dry regions (air) and liquid-filled pore segments on visible light length scales, scattering light in all directions.

This study has revealed and paved the way to the physical understanding of the rich phenomenology in physical mechanisms encountered during drying and imbibition of submicron porous structures. Specific to nanoscale pores, it showed that liquid transfers may not be governed

by the classical hydrodynamic laws, arousing a plethora of intriguing wonders and perspectives for future investigation.

References:

1. Wang K, W.J., *Composites of nanoporous gold and polymer*. Adv. mater, 2013.
2. Lang X Y, H.A., Fujita T, Chen M W, *Nanoporous metal/oxide hybrid electrodes for electrochemical supercapacitors*. Nat. Nanotechnol., 2011.
3. uan JK, L.X., Akbulut O, Hu JQ, Suib SL, Kong J, Stellacci F *Superwetting nanowire membranes for selective absorption*. Nat. Nanotechnol. , 2008.
4. ruska A, G.M., Sweedler J V, Bohn P W, *Nanofluidics in chemical analysis*. Chem. Soc. Rev., 2010
5. P, B.L.a.T., *Physics and technological aspects of nanofluidics*. Lab Chip 2014.
6. Sadjadi, Z. and H. Rieger, *Scaling theory for spontaneous imbibition in random networks of elongated pores*. Phys Rev Lett, 2013. 110(14): p. 144502.
7. Blasius, H., *Grenzschichten in flüssigkeiten mit kleiner reibung*. 1907, Leipzig: Druck von B.G. Teubner. 39 p., 1 l.
8. Schlunder, E.-U., *On the mechanism of the constant drying rate period and its relevance to diffusion controlled catalytic gas phase reaction*. Chemical Engineering Science, 1987.
9. Coussot, P., *Scaling approach of the convective drying of a porous medium*. Eur. Phys. J. B, 2000. 15(3): p. 557-566.
10. Suzuki, M., *On the mechanism of drying of granular beds*. Journal of chemical engineering of Japan, 1967.
11. Olbricht, K.L., *Pore-scale prototypes of multiphase flow in porous media*. Annu Rev Phys Chem, 1996.
12. Gennes, P.G.d., *Wetting : Statics and dynamics*. Reviews of Modern Physics, 1985.
13. Zisman, W.A., *Relation of the Equilibrium Contact Angle to Liquid and Solid Constitution*. 1964. 43: p. 1-51.
14. gennes, P.G.d., *Capillarity and Wetting Phenomena: Drops, Bubbles, Pearls, Waves*. New York: Springer, 2004: p. 119.
15. Derjaguin, *Structure of water in thin layers*. Langmuir, 1986.
16. Derjaguin, *Direct measurement of molecular forces*. Nature, 1978. 272.
17. Camassel, B., et al., *Evaporation in a capillary tube of square cross-section: application to ion transport*. Chemical Engineering Science, 2005. 60(3): p. 815-826.
18. Chauvet, F., et al., *Three periods of drying of a single square capillary tube*. Phys Rev Lett, 2009. 103(12): p. 124502.
19. Yiotis, A.G., et al., *Effect of liquid films on the drying of porous media*. AIChE Journal, 2004. 50(11): p. 2721-2737.
20. Wong, H., S. Morris, and C.J. Radke, *Three-dimensional menisci in polygonal capillaries*. Journal of Colloid and Interface Science, 1992. 148(2): p. 317-336.
21. Keita, E., et al., *Drying kinetics driven by the shape of the air/water interface in a capillary channel*. Eur Phys J E Soft Matter, 2016. 39(2): p. 23.
22. Shouxiang, *Effect of contact angle on drainage and imbibition in regular polygonal tubes*. Colloids and Surfaces, 1996. 1174: p. 273.
23. CEAGLSKE, *Drying granular solids*. 1937.
24. Costa, A., *Permeability-porosity relationship: A reexamination of the Kozeny-Carman equation based on a fractal pore-space geometry assumption*. Geophysical Research Letters, 2006. 33(2).

25. Dufresne, E.R., et al., *Flow and fracture in drying nanoparticle suspensions*. Phys Rev Lett, 2003. 91(22): p. 224501.
26. Darcy, H., *Les Fontaines Publiques de la Ville de Dijon*, Dalmont, Paris. 1856.
27. Pfitzner, *Poiseuille and his law*. Historical Note, 1976. 31: p. 273-275.
28. Lewis, *The synopsis on drying*. Journal of industrial and engineering chemistry, 1921.
29. Sherwood, *The drying of solids*. Industrial and Engineering Chemistry, 1929. 21(1).
30. Cunningham, *Gasdiffusion: Diffusion in Gases and Porous Media*. Plenum Press, New York und London, 1980.
31. Moyne, *Approche theorique et experimentale de la conductivite thermique des milieux poeux humide*. J Heat Mass Transfer, 1988. 31.
32. de Vries, D.A. and J.R. Philip, *Soil Heat Flux, Thermal Conductivity, and the Null-alignment Method I*. Soil Science Society of America Journal, 1986. 50: p. 12-18.
33. *InternalStress-Scherer*
34. *rayon hydraulique GW Scherer*
35. *JournalOfNonCrystallineSolids - theory of drying I-GW scherer*
36. *JournalOfNonCrystallineSolids-Drying gels VIII G.W Scherer*
37. *JournalOfNonCrystallineSolids-Aging and drying of gels-GW Scherer*
38. Scherer, G.W., *Theory of Drying*. Journal of the American Ceramic Society, 1990. 73(1).
39. Ludviksson, *The Dynamics of Thin Liquid Films in the Presence of Surface-Tension Gradients*. AIChE Journal, 1971.
40. Goyeneche, M., *Etude du transport d'humidite par ecoulement de film lors du sechage d'un milieu capillaro-poreux*. PhD Thesis, 2001.
41. Berg, S., et al., *Real-time 3D imaging of Haines jumps in porous media flow*. Proc Natl Acad Sci U S A, 2013. 110(10): p. 3755-9.
42. Shahidzadeh-Bonn, N., A. Azouni, and P. Coussot, *Effect of wetting properties on the kinetics of drying of porous media*. Journal of Physics: Condensed Matter, 2007. 19(11): p. 112101.
43. Keita, E., *PhD Thesis*. 2013.
44. Yunker, P.J., et al., *Suppression of the coffee-ring effect by shape-dependent capillary interactions*. Nature, 2011. 476(7360): p. 308-11.
45. Brakel, J.V., *Adv. Drying*, 1980. 1: p. 217-267.
46. Coussot, P., *Mouvements capillaires durant le sechage d'une pate granulaire*. Physicochimie, 1999.
47. Lehmann, P., S. Assouline, and D. Or, *Characteristic lengths affecting evaporative drying of porous media*. Phys Rev E Stat Nonlin Soft Matter Phys, 2008. 77(5 Pt 2): p. 056309.
48. Yiotis, A.G., et al., *Effect of liquid films on the isothermal drying of porous media*. Phys Rev E Stat Nonlin Soft Matter Phys, 2003. 68(3 Pt 2): p. 037303.
49. Laurindo, J.B. and M. Prat, *Numerical and experimental network study of evaporation in capillary porous media. Drying rates*. Chemical Engineering Science, 1998. 53(12): p. 2257-2269.
50. Gennes, P.G.d., *Physics of disordered media*. Plenum Press, New York und London, 1985.
51. Yiotis, A.G., et al., *Pore-network study of the characteristic periods in the drying of porous materials*. J Colloid Interface Sci, 2006. 297(2): p. 738-48.
52. Yiotis, A.G., *Analytical solutions of drying in porous media for gravity-stabilized fronts*. Phys Rev E Stat Nonlin Soft Matter Phys, 2012. 85(046308).

53. Prat, M., *On the influence of pore shape, contact angle and film flows on drying of capillary porous media*. International Journal of Heat and Mass Transfer, 2007. 50(7–8): p. 1455-1468.
54. Bhatia, S.K. and D. Nicholson, *Hydrodynamic origin of diffusion in nanopores*. Phys Rev Lett, 2003. 90(1): p. 016105.
55. Keech, *The Determination of drying Kinetics and Equilibrium Characterisation at low Moisture Contents*. PhD Thesis, 1997.
56. Shin, H. and J.C. Santamarina, *Desiccation cracks in saturated fine-grained soils: particle-level phenomena and effective-stress analysis*. Géotechnique, 2011. 61(11): p. 961-972.
57. D., D., *Capillary flow as the cause of ring stains from dried liquid drops*. 1997.
58. Larson, R.G., *Marangoni Effect Reverses Coffee-Ring Depositions*. J. of phys. chem. B Letters, 2006.
59. Giorgiutti-Dauphine, F. and L. Pauchard, *Direct observation of concentration profiles induced by drying of a 2D colloidal dispersion drop*. J Colloid Interface Sci, 2013. 395: p. 263-8.
60. Vodolazskaya, *Mass transfer during drying of colloidal film beneath a patterned mask that contains a hexagonal array of holes*. 2015.
61. Widjaja, E. and M.T. Harris, *Particle deposition study during sessile drop evaporation*. AIChE Journal, 2008. 54(9): p. 2250-2260.
62. Brown, *A brief account of microscopical observations made in the months of June, July and August, 1827, on the particles contained in the pollen of plants; and on the general existence of active molecules in organic and inorganic bodies*. Phil. Mag., 1828. 4: p. 161-173.
63. Jing, G., et al., *Drying of colloidal suspensions and polymer solutions near the contact line: deposit thickness at low capillary number*. Langmuir, 2010. 26(4): p. 2288-93.
64. Sempels, W., et al., *Auto-production of biosurfactants reverses the coffee ring effect in a bacterial system*. Nat Commun, 2013. 4: p. 1757.
65. Larson, R.G., *Analysis of the Microfluid Flow in an Evaporating Sessile Droplet*. Langmuir, 2005.
66. Kim, S., et al., *Drying of the silica/PVA suspension: effect of suspension microstructure*. Langmuir, 2009. 25(11): p. 6155-61.
67. Leng, J., *Drying of a colloidal suspension in confined geometry*. Phys Rev E Stat Nonlin Soft Matter Phys, 2010. 82(2 Pt 1): p. 021405.
68. Tsapis, N., et al., *Onset of buckling in drying droplets of colloidal suspensions*. Phys Rev Lett, 2005. 94(1): p. 018302.
69. HOSOI, A.E., *Marangoni convection in droplets on superhydrophobic surfaces*. J.Fluid.Mech, 2016.
70. E, N.M., *Properties of some Vycor-brand glasses*. J. Am. Ceram. Soc., 1944. 27: p. 299–305.
71. L, D.P.a.C.R., *Flow of liquid hydrocarbons in porous Vycor*. J. Appl. Phys., 1959(30): p. 843.
72. Abeles B, C.L.F., Johnson J Wand Drake J M *Capillary condensation and surface flow in microporous Vycor glass*. Israel J.Chem, 1991.
73. Gelb LD, H.A., *Dynamics of the capillary rise in nanocylinders*. 2002.
74. Dimitrov D I, M.A., Binder K *Capillary rise in nanopores: molecular dynamics evidence for the Lucas–Washburn equation*. Phys Rev Lett, 2007.

75. Quere, D., *Inertial capillarity*. Europhysics Letters (EPL), 1997.
76. Gruener S, H.T., Wallacher D, Kityk A V, Huber P, *Capillary rise of water in hydrophilic nanopores*. Phys Rev E Stat Nonlin Soft Matter Phys, 2009
77. Kusmin A, G.S., Henschel A, Holderer O, Allgaier J, Richter D, Huber P, *Evidence of a sticky boundary layer in nanochannels: a neutron spin echo study of n-hexatriacontane and poly(ethylene oxide) confined in porous silicon*. J Phys Chem Lett, 2010.
78. Kusmin A, G.S., Henschel A, de Souza N, Allgaier J, and H.P. Richter D, *Polymer dynamics in nano channels of porous silicon: a neutron spin echo study*. Macromolecules, 2010
79. Dube M, R.M., Alava M, *Conserved dynamics and interface roughening in spontaneous imbibition: a critical overview*. Eur. Phys. J. B, 2000.
80. Gruener S, S.Z., Hermes H E, Kityk A V, Knorr K, Egelhaaf S U, Rieger, Huber P *Anomalous front broadening during spontaneous imbibition in a matrix with elongated pores*. Proc. Natl Acad. Sci. USA, 2012
81. Callahan P T, C.A., Macgowan D, Packer K J, Zelaya F O, *Diffraction-like effects in NMR diffusion studies of fluids in porous solids* Nature, 1991
82. Perfect E, C.C.L., Kang M, Bilheux H Z, Lamanna J M, and W.D.M. Gragg M J, *Neutron imaging of hydrogen-rich fluids in geomaterials and engineered porous media: a review*. Earth-Sci. Rev, 2014.
83. Lee D S, S.Z., Rieger H L *Lattice model for spontaneous imbibition in porous media: the role of effective tension and universality class*. Phys. Rev. E, 2014.
84. Caupin F, C.M.W., Balibar S, Treiner J *Absolute limit for the capillary rise of a fluid*. Europhys. Lett., 2008.
85. Mecholsky, *Fracture mechanics principles*. 1995.
86. Sadhukhan, S., et al., *Desiccation cracks on different substrates: simulation by a spring network model*. Journal of Physics: Condensed Matter, 2007. 19(35): p. 356206.
87. Peron, H., et al., *Fundamentals of desiccation cracking of fine-grained soils: experimental characterisation and mechanisms identification*. Canadian Geotechnical Journal, 2009. 46(10): p. 1177-1201.
88. Shokri, N., *Liquid-phase continuity and solute concentration dynamics during evaporation from porous media : Pore-scale processes near vaporization surface*. Physical Review E, 2010.
89. Shokri, N., *What determines drying rates at the onset of diffusion control- led stage-2 evaporation from porous media*. Water Resources Research, 2011.
90. Vincent, O., *Capillarity-Driven Flows at the Continuum Limit*. Phys Rev Lett, 2015.
91. Pauchard, L., *Patterns caused by buckle-driven delamination in desiccated colloidal gels*. Europhysics Letters (EPL), 2006. 74(1): p. 188-194.
92. Neda, Z., et al., *Spiral cracks in drying precipitates*. Phys Rev Lett, 2002. 88(9): p. 095502.
93. Lazarus, V. and L. Pauchard, *From craquelures to spiral crack patterns: influence of layer thickness on the crack patterns induced by desiccation*. Soft Matter, 2011. 7(6): p. 2552.
94. Iler, R.K., *The Chemistry of Silica*. Wiley, 1979.
95. Rey, J. and M. Vandamme, *On the Shrinkage and Stiffening of a Cellulose Sponge Upon Drying*. Journal of Applied Mechanics, 2013. 80(2): p. 020908.
96. N, W.R., *Resistance of solid surfaces to wetting by water*. Industrial and engineering chemistry, 1936.

97. Sen, H., *Influence of cross-link density on rheological properties of temperature-sensitive microgel suspensions*. Colloid and Polymer Science, 2000.
98. kamble, S., *Probing Structure and Dynamics of Soft Colloidal Glasses using Rheology and Light Scattering*. PhD Thesis, 2014.
99. Chu, B., *Overlap Concentration of Macromolecules in Solution*. Macromolecules, 1987.
100. KUBOTA, *Molecular Motion and ¹H NMR Relaxation of Aqueous Poly(N-isopropylacrylamide) Solution Under High Pressure*. 1991.
101. Xu, L., et al., *Dynamics of drying in 3D porous media*. Phys Rev Lett, 2008. 101(9): p. 094502.
102. Dittrich, P.S.M., A., *Lab-on-a-chip: microfluidics in drug discovery*. Nat. Rev. Drug Disc, 2006. 5: p. 210–218.
103. Tabeling, P., *Recent progress in the physics of microfluidics and related biotechnological applications*. Biotechnol., 2014. 25: p. 129–134.
104. Simon, P.G., *Materials for electrochemical capacitors*. Nat. Mater, 2008.
105. Lang, X., Hirata, A., Fujita, T. & Chen, M. Nat. , *Nanoporous metal/oxide hybrid electrodes for electrochemical supercapacitors*. Nanotechnol., 2011. 6(232–236).
106. Yuan, J.K. and . , *Superwetting nanowire membranes for selective absorption*. Nat. Nanotechnol, 2008. 3: p. 332–336.
107. Schoch, R.B., Han, J. & Renaud, P., *Transport phenomena in nanofluidics*. Rev. Mod. Phys., 2008. 80(839–883).
108. Humplik, T., et al., *Nanostructured materials for water desalination*. Nanotechnology, 2011. 22(29): p. 292001.
109. Surwade, S.P., et al., *Water desalination using nanoporous single-layer graphene*. Nat Nanotechnol, 2015. 10(5): p. 459-64.
110. Hinrichsen, H., *Non-equilibrium critical phenomena and phase transitions into absorbing states*. Advances in Physics, 2000. 49(7): p. 815-958.
111. Sahimi, M., *Flow phenomena in rocks: from continuum models to fractals, percolation, cellular automata, and simulated annealing*. Reviews of Modern Physics, 1993. 65(4): p. 1393-1534.
112. Alava, M., M. Dubé, and M. Rost, *Imbibition in disordered media*. Advances in Physics, 2004. 53(2): p. 83-175.
113. Gennes, P.G.d., *Faraday Discuss*. 1996. 104.
114. Thompson P.A, R.M.O., Phys Rev Lett, 1989. 63(766).
115. Hoffman, H.R., J. Colloid Interface Sci, 1975. 50 (228).
116. NICOLAS, M, *Écoulements dans les milieux poreux*, Thesis
117. Shokri, N, PhysRevE.81.046308
118. Sendner C, Horinek D, Bocquet L and Netz R R 2009, *Langmuir* 25 10768–81
119. *Eur. Phys. J. E* 12 83
120. Bonnaud P A, Coasne B and Pellenq R J M 2010, *J. Phys.: Condens. Matter* 22 284110
121. Erko M, Findenegg G H, Cade N, Michette A G and Paris O 2011. *Phys. Rev. B*
122. Adrien Lerbret and al. *Water Food Biophysics* (2011) 6:233–240
123. *Europhys. Lett.*, 73 (3), pp. 390–395 (2006)
124. *Nature Materials* 2, 237 - 240 (2003)
125. *Langmuir* 2008, 24, 1165-1172
126. Enoch Kim and George M. Whitesides, *J. Phys. Chem. B* 1997, 101, 855-863
127. de Gennes, P. G. In *Liquids at Interfaces*

128. Capillary Rise in Nanopores, D. I. Dimitrov, A. Milchev, and K. Binder
129. Dimitrov D I, Milchev A and Binder K 2007, *Phys. Rev. Lett.* 99 054501
130. Nanofluidics, from bulk to interfaces, Lydéric Bocquet Elisabeth Charlaix
131. Nanoscale Invest. of Wetting Dynamics with a Surface Force Apparatus, E. Charlaix
132. Effect of Wetting on the Dynamics of Drainage in Porous Media, N. Bonn, A. Tournié, S. Bichon P. Vié, S. Rodts, P. Faure, F. Bertrand, A. Azoun.
133. E. Keita, P. Faure, S. Rodts, and P. Coussot, *Phys. Rev. E* 87, 062303
134. 10.1007/s10853-014-8807-x
135. NMR imaging of moisture transport and ion transport in building materials
136. P. Coussot, P. Faure, *Phys. Rev. E* 82, 036303
137. Callaghan, P. T. (1993). *Principles of Nuclear Magnetic Resonance Microscopy*. Oxford: Clarendon
138. F. Bloch *Phys Rev.* 70, 460 (1946)
139. Hahn, E. L. (1950). Spin echoes. *Physical Review*, 80(4), 580-594.
140. Brownstein, K. R., & Tarr, C. E. (1977). Spin-Lattice relaxation in a system governed by diffusion. *Journal of Magnetic Resonance*, 26, 17-24.
141. Brownstein, K. R., & Tarr, C. E. (1979). Importance of classical diffusion in NMR studies of water in biological cells. *Physical Review A*, 19(6), 2446-2453.
142. M.H. Cohen and K.S. Mendelson, "Nuclear magnetic relaxation and the internal geometry of sedimentary rocks," *J. Appl. Phys.*, vol. 53, pp. 1127–1135, 1982
143. Carr, H. Y., & Purcell, E. M. (1954). Effects of diffusion on free precession in nuclear magnetic resonance experiments. *Physical Review*, 94(3), 630-638.
144. Meiboom, S., & Gill, D. (1958). Modified spin-echo method for measuring nuclear relaxation times. *The Review of Scientific Instruments*, 29(8), 688-691.
145. Mayers, Drew. (2002), *Surfaces, Interfaces, and Colloids: Principles and Applications*,
146. [42] D. A. Weitz and M. Oliveria, *Fractal Structures Formed by Kinetic Aggregation of Aqueous Gold Colloids*, *Phys. Rev. Lett.* 52, 1433 (1984)
147. *Porous Media: Fluid Transport and Pore Structure*, By F. A.L. Dullien
148. Faure, P. F., & Rodts, S. (2008). Proton NMR relaxation as a probe for setting cement pastes. *Magnetic Resonance Imaging*, 26, 1183-1196
149. Brown, R. J. S. (1989). Information available and unavailable from multiexponential relaxation data. *Journal of Magnetic Resonance*, 82, 539-561.
150. G. C. Kuczynski, *J. Appl. Phys.* 20, 1160-1163 (1949)
151. G. W. Scherer, S. Calas, and R. Sempere, *Journal of Non-crystalline solids* 240, 118-130 (1998).
152. *SILICA: VISCOUS SINTERING*, Chap.3 and 4, University of Groningen
153. R. W. Rice, *Journal of Materials Science* 31, 102-118 (1996).
154. Condensation and isothermal water transfer in cement mortar Part I — Pore size distribution, equilibrium water condensation and imbibition, Jean-François Daian.
155. Anton A. Valeev, "Simple Kelvin Equation Applicable in the Critical Point Vicinity" *European Journal of Natural History*, (2014), Issue 5, p. 13-14.
156. O. Vincent, *Capillarity-Driven Flows at the Continuum Limit, soft matter*, 2016

ANNEXES

This section gathers the analyzing tools we used or developed, inventories of detailed measurement parameters as well as unfinished or formatted work.

1 - Pore size analysis software

Program available at: <https://www.mathworks.com/matlabcentral/profile/authors/869576-ohad-gal>

2 - Image and mass acquisition software

Camera: ThorLabs CMOS USB 2.0.
Balance: Classic precision balance.

```
clear all, clc
close all

%=== USER SETTINGS =====%
sample = 'CPD05_GG08_wat_02d'; % enter sample's name
S = 1; % enable save option
% define time scale (as square root function)
t_max = 150; % total time in minutes
nb_frames = 150; % number of frames
square_time = 1; % set linear timescale (0) or square root timescale (1)
%=====

% initialize connection with scale
balance = startBalance(1);

% set camera settings
cam = videoinput('winvideo');
%src = getselectedsource(cam); % establish settings
%set(src, 'HorizontalFlip', 'off', 'VerticalFlip', 'off'); % flip picture

t_max = t_max*60; % total time in seconds
if square_time==1 % square root timescale
    step = t_max^.5/nb_frames;
    time = 0:step:t_max^.5; % time scale in seconds
    time2 = time.^2;
else % linear timescale
    step = t_max/nb_frames;
    time = 0:step:t_max; % time scale in seconds
    time2 = time;
end

% init arrays
eff_time = zeros(1,numel(time)); % effective computer time
```

```

masses = zeros(1,nb_frames);

disp('Camera and balance ready.')
go = 0;
while go~=1
    init = getsnapshot(cam);
    close all
    imagesc(init)
    go = input('Accept camera settings? 0 for no, 1 for yes\n => ');
end
close all
go = input('Press Enter to start study. ');
abs_time = tic; % tic1 : whole study, absolute time
disp('Study started.')

% frames acquisition
for i=1:nb_frames
    % get frame from camera
    frame = getsnapshot(cam);
    t_frame = toc(abs_time); % save absolute time
    eff_time(i) = t_frame;
    frame = frame(:,:,1);
    disp([' > Frame ' num2str(i) ' taken.'])
    % get data from scale
    masses(i) = readBalance(balance);
    disp([' > Mass ' num2str(i) ' taken: ' num2str(masses(i)) ' mg.'])
    % save frames files (png format)
    if S==1
        nb = sprintf('%03d',i);
        title = [sample '_frame' nb '.png'];
        imwrite(frame,title)
        disp([' > File ' num2str(i) ' saved.'])
    end
    % delay
    rel_time = tic; % tic2: delay between frames, relative time
    delay = time2(i+1) - time2(i);
    pause(delay) % pause time in minutes
    eff_delay = toc(rel_time);
    disp([' > Paused ' num2str(eff_delay) 's (' num2str(delay) 's
expected).'])
end

% display total study time
t_study = toc(abs_time);
disp(['End of acquisition. Total time: ' num2str(t_study) 's ('
num2str(t_study/60) 'min).'])
% save mass ant time
if S==1
    masses = masses';
    time2 = time2';
    eff_time = eff_time';
    title = [sample '_time_mass.txt'];
    save(title,'time2','eff_time','masses','-ascii');
    disp(' > Mass and time file saved.')
end
% close balance
fclose(balance);

```

```

catch
    disp('error')
    fclose(balance)
end

```

3 - NMR measurement parameters Chapter 2 sponges

Fig2-22	Resolution (µm)	Echo Time 1 (ms)	Echo Time 2 (ms)	Number of Scans	Recovery time (s)	Sequence time (min)
Graph a - measurement 1	250	5.258610	4.530000	196	7	24.7943
Graph a - measurement 1	600	3.888444	3.130000	196	7	24.7830
Graph b	600	5.830200	5.990000	196	7	24.7986

Fig2-23	Resolution (µm)	Echo Time 1 (ms)	Echo Time 2 (ms)	Number of Scans	Recovery time (s)	Sequence time (min)
Graph a	200	5.781230	4.998000	320	12	67.1551
Graph b	250	5.845823	5.130000	320	12	67.1540

Figure 5-1: MRI measurement parameters for the green sponge in Fig2-22 (green table), and the blue sponge Fig2-23 (blue table).

4 - NMR 1D profiling measurement parameters Chapter 4.

	Time (min)	Resolution (microns)	TE1 (ms)	TE2 (ms)	Nbr scans	Sample height	Profile Nbr
6nm	34.61	120	7.803202	7.130000	1400	1cm	All
12nm	15.50	157	6.628775	5.930000	800	5mm	All
40nm	28.38	120	7.803202	7.130000	800	1cm	All
80nm	32.10	170	6.335168	5.63000	1200	1cm	1-16
	60.55	300	4.867134	4.13	4000	1cm	16-end
300nm	32.58	270	7.803202	7.130000	700	1cm	1-35
	34.44	170	5.104123	4.398747	1300	1cm	36-51
	49.45	520	4.041107	3.281251	2500	1cm	52-end
1000nm	39.35	240	5.356478	4.630000	1200	1cm	1-17
	45.75	480	4.133116	3.380000	1800	1cm	18-end
1500nm	37.6	310	5.030200	5.330000	600	1cm	All
45000nm	32.3691	200	6.830200	7.130000	600	2.5cm	1-55
	45.7869	400	4.330200	4.630000	2500	2.5cm	55-end

Figure 5-2: MRI measurement parameters for the porous media presented in chapter 4

5 - Dimensions of the samples presented in Chapter 5, Fig5-2

	6mn	40nm	80nm	300nm	750nm	1500nm
Length x Width x Height (mm)	17 x 6 x 32 and 18 x 6 x 21	29 x 6 x 30 and 31 x 4 x 32 and 27 x 8 x 28	23 x 9 x 33 and 25 x 8 x 35	19 x 12 x 22	25 x 9 x 35	25 x 8 x 41 and 12 x 8 x 40

Figure 5-3: Dimensions of samples presented in the imbibition curves in chapter 5

6 - NMR 1D profiling measurement parameters Chapter 5

	Time (min)	Resolution (microns)	TE1 (ms)	TE2 (ms)	Nbr scans	Sample size (length x width x height)	Profile Nbr
6nm	3min5sec	660	3.40	2.63	1000	X	1-12
	6min6sec	660	3.35	2.58	2000	X	12-27
	12min12sec	660	3.35	2.58	4000	X	27-end
40nm	5min02sec	660	3.35	2.58	1200	2.67x0.8x2.75	All
	10min05sec	660	3.35	2.58	2400	2.67x0.8x2.75	All
80nm	1min45	660	3.35	2.58	160	X	All
300nm	1min54sec	869	3.21	3.28	160	1.9x1.2x2.2	All
750nm	1min58sec	600	3.41	3.63	120	3.66x0.8x4.3	All
1500nm	1min39sec	410	4.23	4.53	40	2.5x0.8x4.12	All

Figure 5-4: MRI measurement parameters for the porous media presented in chapter 5

